Morphological Modelling and Transport Properties of Mesoporous Alumina

Haisheng Wang

THÈSE DE DOCTORAT

de l'Université de recherche Paris Sciences et Lettres
PSL Research University

Préparée à MINES ParisTech

Modélisation Morphologique et Propriétés de Transport d'Alumines Mésoporeuses

Ecole doctorale n°432

SCIENCES DES METIERS DE L'INGENIEUR

Spécialité MORPHOLOGIE MATHEMATIQUE

COMPOSITION DU JURY :

M. Pierre LEVITZ
Université Pierre et Marie Curie, Rapporteur

M. Karam SAB
Ecole des Ponts ParisTech, Rapporteur

M. Volker SCHMIDT
Université d'Ulm, Rapporteur

M. Dominique BERNARD
ICMCB-CNRS, Examinateur, Président du jury

M. Renaud DENOYEL
Université d'Aix-Marseille, CNRS, Examinateur

M. Loïc SORBIER
IFP Energies Nouvelles, Examinateur

M. Dominique JEULIN
MINES ParisTech, Examinateur

M. François WILLOT
MINES ParisTech, Examinateur

Soutenue par Haisheng WANG
le 23/09/2016

Dirigée par **Dominique JEULIN**

MINES ParisTech | PSL RESEARCH UNIVERSITY PARIS

子曰：有朋自远方来，不亦乐乎？

How delightful we are, to have friends from afar.
Confucius (551 - 479 BC)

Remerciements

Ce travail est effectué au sein du Centre de Morphologie Mathématique de l'École des Mines de Paris, en collaboration avec IFP Energies Nouvelles. Dans les deux endroits, pendant les trois ans de thèse, j'ai rencontré les personnes qui ont créé de beaus souvenirs dans ma vie, et sans qui cette thèse n'était pas possible.

Tout d'abord, je remercie mon directeur de thèse, Dominique Jeulin, et mon maître de thèse, François Willot, grâce à qui j'ai pu bénéficier d'un encadrement hors pair.

François m'a suivi dans la recherche quotidienne. Il m'amène petit à petit dans le domaine de modélisation morphologique et d'homogénéisation. Dans la plupart des cas, c'est lui qui vient dans mon bureau pour des discussions, au moins deux fois par semaine, même si son agenda est très chargé. Il vient toujours en souriant, et me demande les avancements ou si j'ai des difficultés. On discute et résout les problèmes ensemble. Il connaît presque tous les petits obstacles que j'ai rencontrés pendant les trois ans. Il m'a appris à rédiger les rapports, les articles, et les présentations de manière rigoureuse et scientifique. Dans chaque pas de mon avancement pendant les trois ans, il y a ses contributions. Je l'en remercie.

Dominique m'a pris comme son dernier doctorant officiel, c'est un immense honneur. Il passe à mon bureau chaque fois qu'il est venu au CMM, et me dit bonjour chaleureusement. Il répond mes mails toujours au premier temps, quel que soit le jour ou le soir. Il dirige la direction du travail. Son expérience et son expertise m'aident à voir plus loin. J'ai écouté, regardé et appris comment développer un projet scientifique, comment faire des compromis, et comment diriger avec des conditions limitées. Dominique est très encourageant, cela me donne confiance et courage à avancer au fond. Je l'en remercie.

Je remercie mes encadrants à IFP Energies Nouvelle - mes promoteurs de thèse, Loïc Sorbier et Maxime Moreaud. On se voit chaque un ou deux mois par visioconférence, ou physiquement à Paris ou à Solaize. Ils examinent et dirigent mon travail dans une vision industrielle. Loïc m'a amené dans le domaine du catalyseur, m'a introduit les contextes industriels, et m'a expliqué les données expérimentales. Maxime est un expert sur l'imagerie de catalyseur, et m'a donné des avis très précieux sur le traitement d'images MET et sur la modélisation morphologique. Nous réfléchissons ensemble aux désaccords entre résultats numériques et expérimentaux, cherchons des explications possibles, et proposons des pistes potentielles à améliorer les résultats. Ils sont tous les deux très agréables et toujours encourageants.

Je remercie le jury de thèse, sans qui la conclusion de ces travaux aurait été impossible. Je remercie les rapporteurs de thèse, Pr Pierre Levitz, Pr Karam Sab et Pr Volker Schmidt. Ils ont lu mon écrit en détail attentivement et formulé des critiques constructives. Je remercie également Dominique Bernard et Renaud Denoyel pour leur présence à ma soutenance de thèse, et leurs félicitations chaleureuses.

Durant les trois ans de thèse, j'ai obtenu beaucoup de soutiens des collègues du centre. Je les remercie de leur accueil chaleureux depuis le premier jour de ma thèse. Matthieu Faessel m'a donné d'encadrement très précieux durant la première année. Beatriez Marcotegui m'a donné le cours fondamental de morphologie mathématique. Catherine Moysan et Anne-Marie De Castro m'ont accompagné dans toutes les

démarches administratives, et plus important encore, elles unissent la famille CMM. Michel Bilodeau et Serge Koudoro m'ont aidé sur les outils informatiques. Je remercie aussi Petr Dokladal, Fernand Meyer, Bruno Figliuzzi, Étienne Decencière, Jesús Angulo, et Santiago Velasco-Forero pour leurs aides précieuses à la résolution des problèmes ponctuels.

Je remercie également les autres collègues de la direction de Physique et Analyse d'IFPEN. Ils ont synthétisé les trois échantillons, et pris les images MET. Ils ont fait les mesures par porosimétrie et par RMN-GCP. Je n'ai pas beaucoup de communication directe avec eux, mais je sens leurs soutiens.

Je remercie IFP Energies Nouvelles de m'avoir donné cette opportunité de thèse précieuse, et pour le financement du projet. Merci à la direction de Formation Doctorale et IFP Training pour les stages de très haute qualité.

Merci à Pierre Jouvelot, mon tuteur de stage au CRI en été de 2013, pour m'avoir amené du loin à ce campus agréable. Nous avons fait un projet très cool et créé la Faustine ensemble. Je me souviens toujours le beau paysage au fenêtre de mon bureau.

Je remercie mon "team de printemps/été/automn/hiver", mes chère et cher voisins, Vaïa Machairas et Sebastien Drouyer. Vaïa, qui assoit en face de moi, m'a accompagné depuis le début de ma thèse, et tout au long des trois ans. Elle est jolie et sympathique, elle prend soin des autres. Comme Catherine, elle a la magie à unir des gens. Sebastien, qui assoit à ma droite, m'a beaucoup aidé à bien intégrer. Nous avons beaucoup d'intérêt commun, les jeux, les saucissons, et le style de baby-foot. Le team de printemps fait des mini-séminaires et des Missions de Sapin. Il y a tellement beaucoup de beaux moments entre nous, que ce mémoire est trop court pour tous enregistrer.

Merci au team de baby-foot, Theodore, Pierre, Sebastien, Jean-Charles, Robin, Amin, Borja, Nelson, Adrian et Daniele. Vive la pissette et vive la reprise.

Merci au team de salsa, notamment Vaïa et Joris, qui sont excellents professeurs de salsa. Les soirées de salsa m'ont laissé des belles mémoires.

Merci au team de pérudo, Enguerrand, Luc, Bassam, Theodore, Pierre, Nelson, Robin, Sebastien, Angélique, Jean-Baptiste et Gianni. Un pérudo sous l'arbre avec un café est le meilleur moment en été.

Merci à Dopamines, notamment Sebastien Drouyer, pour organiser le voyage à Normandie, la semaine du ski et toutes les soirées.

Je te remercie Fang de ton accompagnement durant la thèse, et de ce que tu apportes dans ma vie. Nous avons fait une aventure ensemble avec des belles vues. Nous avons fait beaucoup de choses intéressantes. Je remercie mes parents et mon frère, vous êtes loin d'ici, mais je sens toujours vos soutiens et vos amours sans conditions (谢谢我的爸爸妈妈和哥哥，虽然你们离这儿很远，我也总能感受到你们的支持和无条件的爱).

Abstract

In a work made at Centre de Morphologie Mathématique and IFPEN, we study the microstructure and physical properties of mesoporous γ-alumina. This is a catalyst carrier used in the petroleum refining industry. Highly porous, it contains disordered "platelets" at the nanoscale. The mass transport properties of the catalyst carrier are strongly influenced by the morphology of the porous microstructure. We focus on the modeling of the microstructure and of transport properties of mesoporous alumina, using numerical and theoretical tools derived from image analysis and random sets models. On the one hand, methods are developed to characterize and model the microstructure, by extracting and combining information from transmission electron microscope (TEM) images and nitrogen porosimetry curves, among others. On the other hand, the numerical homogenization relies on full-field Fourier transform computations (FFT).

The material is first characterized experimentally by nitrogen porosimetry and pulse-field gradient nuclear magnetic resonance (PFG-NMR). TEM images, obtained on samples of various thicknesses are filtered and measured in terms of correlation function. The high-frequency noise caused by carbon membrane support is identified and integrated in the TEM image model. Based on the 2D TEM images, a two-scale random set model of 3D microstructure is developed. It takes into account the platelet shape, platelet size, local alignments and aggregations effects which are numerically identified. The procedure is validated by comparing the model and experimental images in terms of correlation function and specific surface area estimated by nitrogen porosimetry.

Next, a procedure is proposed to simulate porosimetry isotherms in general porous media, including random microstructures. Based on simple morphological operations, it extends an earlier approach of mercury porosimetry. Multilayer adsorption at low pressure is simulated by a dilation operation whereas the menisci of the vapor-liquid interface occurring during adsorption are simulated by closing the solid phase with spherical structuring elements. To simulate desorption, a combination of closing and hole-filling operations is used. The desorption threshold is obtained from a percolation analysis of the gaseous phase. The method, validated first on simple geometries, is compared to previous results of the literature, allowing us to predict the hysteresis and pore size distribution associated to porosimetry. It is applied on 3D microstructures of mesoporous alumina. To account for the pressure threshold during desorption, we propose a refined three-scale model for mesoporous alumina, that reproduces the correlation function and the desorption branch of porosimetry isotherms.

Finally, Fick diffusion, Darcy permeability, and elastic moduli are numerically predicted using the FFT method and the two-scale and three-scale models of mesoporous alumina. The hindering effects in diffusion are estimated by the Renkin's equation. The effective diffusion coefficients and the tortuosity factors are estimated from the flux field, taking into account hindering effects. The effects of platelet shape, alignment and aggregation on the diffusion property are studied. The numerical estimation is validated from experimental PFG-NMR results.

Résumé

Dans ce travail réalisé au Centre de Morphologie Mathématique and IFPEN, on s'intéresse à la microstructure et aux propriétés physiques d'alumines γ mésoporeuses. Il s'agit d'un support de catalyseur utilisé notamment dans les procédés industriels de raffinage du pétrole. Fortement poreux, ce matériau est formé de "plaquettes" distribuées de manière désordonnée à l'échelle de la dizaine de nanomètres. Les propriétés de transport de masse du support de catalyseur sont fortement influencées par la morphologie de la microstructure poreuse. Ce travail porte sur la modélisation de la microstructure et des propriétés de transport des alumines mésoporeuses, à l'aide d'outils numériques et théoriques dérivés de l'analyse d'image et de la théorie des ensembles aléatoires. D'une part, on met en place des méthodes de caractérisation et de modélisation des microstructures, qui s'appuient sur, entre autre, des images obtenues par microscopie électronique en transmission (MET) et des courbes de porosimétrie azote. D'autre part, on utilise des méthodes d'homogénéisation numérique à champs complets par transformées de Fourier rapide (FFT).

Dans un premier temps, le matériau est caractérisé expérimentalement par porosimétrie azote et résonance magnétique nucléaire à gradient de champ pulsé (RMN-GCP). Les images MET sont obtenues sur des échantillons d'épaisseur variable, filtrées et caractérisés par des fonctions de corrélation, notamment. Le bruit à haute fréquence issu de la membrane de carbone est identifié et pris en compte dans la modélisation de l'imagerie MET. À partir des images MET 2D, un modèle aléatoire à deux échelles est proposé pour représenter la microstructure 3D. Il prend en compte la forme des plaquettes d'alumine, leurs tailles, les effets d'alignement locaux et d'agrégation, qui sont identifiés numériquement. La procédure est validée à l'aide de comparaisons entre modèles et images expérimentales, en terme notamment de fonctions de corrélation et de surface spécifique mesurées par porosimétrie azote.

Dans un deuxième temps, une méthode de simulation des courbes d'isotherme de porosimétrie dans des milieux poreux périodiques ou aléatoires est développée. Basée sur des opérations morphologiques simples, elle étend un travail antérieur sur la porosimétrie au mercure. L'adsorption multicouche à basse pression est simulée à l'aide d'une dilatation tandis que les ménisques de l'interface vapeur-liquide intervenant pendant l'adsorption sont simulés à l'aide de fermetures de la phase solide par des éléments structurants sphériques. Pour simuler la désorption, une combinaison de fermetures et de bouchages de trou est utilisée. Le seuil de désorption est obtenu par une analyse de la percolation de la phase gazeuse. La méthode, d'abord validée sur des géométries simples, est comparée à des résultats antérieurs. Elle prédit une hystérésis et les distributions de pores associées à la porosimétrie. Nous l'appliquons aux modèles de microstructures 3D d'alumines mésoporeuses et proposons un modèle à trois échelles afin de rendre compte du seuil de pression pendant la désorption. En plus de la courbe de désorption, ce modèle reproduit les fonctions de corrélation mesurées sur les images MET.

Dans un troisième temps, la diffusion de Fick, la perméabilité de Darcy, et les propriétés élastiques sont prédites à l'aide de calculs de champs complets par FFT sur des réalisations des modèles d'alumines mésoporeuses à deux et trois échelles. Les coefficients de diffusion effectifs et les facteurs de tortuosité sont prédits à partir de l'estimation du flux. Sont étudiés les effets de forme, d'alignement et

d'agrégation des plaquettes sur les propriétés de diffusion à grande échelle. Les prédictions numériques sont validées au moyen des résultats expérimentaux obtenus par méthode RMN-GCP.

Contents

Chapter 1

Introduction

1.1 Context

Mesoporous alumina is a class of porous material made-up by an assemblage of alumina (Al_2O_3) grains at the nanometric scale and is widely used in industry as catalyst supports (Misra, 1986). A catalyst support provides a reaction interface to active sites and reagents by its porosity. The catalytic performance and more generally transport properties of mesoporous materials are strongly influenced by the morphology of the porous phase, including the porosity, specific surface area and connectivity properties (Levitz, 1993; Wernert et al., 2010). This influence of the morphology of the support is experimentally observed for activity (Khodakov et al., 2002; Rana et al., 2011), selectivity (Khodakov et al., 2002) or deactivation (Prieto et al., 2014) for important industrial processes such as methanol synthesis (Prieto et al., 2014), Fischer-Tropsch synthesis (Khodakov et al., 2002) or hydrotreating of heavy oil fractions (Rana et al., 2011). The preparation method and synthesis conditions, especially temperature and type of solvent influence the morphology of the alumina porous structure at the nanoscale (Trimm & Stanislaus, 1986; Chiche et al., 2008). A fine description of the microstructure is required to predict and optimize the adsorption and catalytic performance of these materials.

Different characterization techniques allow one to extract information about the inner microstructure or the spatial organization of grains at the nanoscale. These techniques include nitrogen porosimetry, X-ray diffraction (XRD), Small Angle X-ray Scattering (SAXS), transmission electron microscopy (TEM) and tomography (Kim et al., 2003; Zecevic et al, 2013). Nitrogen porosimetry provides information about the porosity at the macroscale. XRD methods provide information of the mean structuring crystallites and on morphological characteristics such as size and shape, less on pore connectivity or structure at higher length-scale (Chiche et al., 2008). SAXS provides measurement of specific surface area, porous volume and correlation at different length scale of the mass distribution. TEM methods produce transmission 2D images on a thin slice of material, from which 3D reconstruction is difficult. Electron tomographic techniques may provide 3D images of the pore space at the nanoscale but at the expense of long acquisition and reconstruction time and at poor representativeness (volume sides limited to a few hundred nanometers).

Morphological modelling is a key procedure in the design, development and optimization of catalyst supports. On the one hand, simple models are created using

deterministic microstructures such as periodic arrays (Mu et al., 2008). On the other hand, more elaborate modelling relies on stochastic microstructures to mimic real materials (Adler et al., 1990; Koci et al., 2006; Diaz et al., 2004). With the reconstructed microstructures, simulations of adsorption (Štěpánek et al., 2007) have been performed, as well as heat conduction (Kohout et al., 2004) and reaction-diffusion processes (Koci et al., 2007).

1.2 Goal of the thesis

The goal of this thesis is twofold. The prediction of the transport properties of mesoporous alumina are warranted by an accurate description of its porous network. Accordingly, 3D morphological microstructures that are representative of the material will be derived first and employed to estimate and predict the transport properties of these materials in a second step.

The study aims at enriching our knowledge on the relation between the morphology of the microstructure and the transport properties of mesoporous alumina. Combined with the knowledge of synthesis, it will allow us to propose microstructural ways to optimize the architecture of alumina catalysts supports.

1.3 Approach

First, information is extracted using large field of view TEM images of thin alumina samples. A preliminary study (Pietrasanta, 2013) has already characterized the textural fluctuation of these TEM images (in particular the two points correlation function), their Representative Volume Element (RVE) and proposed a two scale Boolean model. However, the identification of the parameters of the model led to platelet size smaller than physically acceptable and consequently to a specific surface area much higher than measured. This preliminary work is the basis for our study. TEM images of thinner specimens at larger magnications are taken, together with TEM images of crushed materials. We have improved the projection model of TEM images, taking into account the noise in the image formation. The two-scale model is reidentified to reproduce both the two points correlation function and the specific surface area.

Second, the nitrogen porosimetry is simulated using morphological operators, including multilayer adsorption, capillary condensation and evaporation. The porosimetry isotherms of digital microstructures are simulated. The method is validated on simple geometries and compared with literature. A detailed parametric study is performed to relate the kind of stochastic model and their parameters with the associated simulated porosimetry curves. A multiscale model based on the former two-scale model is proposed to reproduce the experimental desorption branch, which contains information on specific surface area, pore size distribution, and connectivity of the pores.

Then, the effective diffusion coefficient in the pores, as well as the permeability are computed directly from realisations of the multiscale models developed previously. The transport by diffusion is modeled by Fick law whereas the transport by convection is modelled by Stokes flow. Homogeneization is performed with Fourier-based computational method that allowed us to compute the effective properties as

well as the full-fields response of the materials (Willot et al, 2013; Willot, 2015).

1.4 Project framework

This study has been carried out under a joint collaboration between the Center of Mathematical Morphology (CMM), MINES ParisTech, Fontainebleau and IFP Énergies Nouvelles (IFPEN), Solaize in France. The thesis work has been supervised by F. Willot, D. Jeulin and M. Faessel (Mines ParisTech) and L. Sorbier and M. Moreaud (IFPEN). This work has been made possible by IFPEN. We gratefully acknowledge its financial support.

Part I

State of the Art: Mesoporous γ-Alumina

Chapter 2

Experimental characterization, modeling and effective properties

2.1 Mesoporous alumina

2.1.1 Catalytic performance and morphology

A catalyst support provides a reaction interface to active sites and reagents by its porosity. The catalytic performances are strongly influenced by the morphology of the porous phase. This influence of the morphology of the support is experimentally observed for activity (Khodakov et al., 2002; Rana et al., 2011), selectivity (Khodakov et al., 2002) or deactivation (Prieto et al., 2014) for important industrial processes such as methanol synthesis (Prieto et al., 2014), Fischer-Tropsch synthesis (Khodakov et al., 2002) or hydrotreating of heavy oil fractions (Rana et al., 2011).

Khodakov et al. (2002) studied the effects of pore size on Fischer-Tropsch reaction rate and selectivities over cobalt catalyst on mesoporous silica as catalytic support. The reaction rate was found much higher on cobalt catalyst with the pore diameter exceeding 3 nm than on the narrow pore catalysts. A large pore diameter also led to a higher C_{5+} selectivity.

Prieto et al. (2014) investigated the impact of the support porous texture on the stability of metal nanoparticles on $CuZnO/SiO_2$ methanol synthesis catalyst. The metal particles are confined by the pores, and the growth of metal particles is one of the major deactivation mechanism of supported catalysts. Cagelike pores ensure that the active Cu nanoparticles are exclusively inside the silica pores with short interparticle spacings. The research indicates that catalyst stability is determined by the narrowest characteristic pore dimension, which corresponds to the entrance size of pores.

Rana et al. (2007) systematically studied the support effect in heavy oil hydrotreating catalysts. Both fresh and spent catalysts are characterized, which confirms that coke and metal deposition on the surface of the catalyst is most probably near the pore mouth. The results also indicate that asphaltene conversion depends on the pore diameter of the catalyst.

2.1.2 Synthesis and morphology

In laboratory, mesoporous alumina catalyst support is usually synthesised through thermal treatements of boehmite. In a typical synthesis process, boehmite powder is first dispersed in solvent (e.g. water, ethanol). The suspension is malaxed, and the support pellets are extruded. The extrudates are then calcined under air to obtain porous transition alumina. Pores originate from voids between particles and between aggregates of particles. The preparation method and synthesis conditions influence the morphology of the alumina texture at the nanoscale (Trimm & Stanislaus, 1986; Chiche et al., 2008; Morin, 2014).

Trimm and Stanislaus (1986) summarized the influence of the temperature, the humidity during calcination, and the combination of them on the distribution of pore size, ranging from macropores to mesopores. The empirical experience have become important guidelines to control the porosity for the manufacturers of mesoporous alumina. Chiche et al. (2008) indicate that boehmite nanoparticles synthesized in solvent of different pH values have different morphologies: low pH values produce smaller nanoparticles, while high pH values produce larger or longer nanoparticles. Differences have been observed along the basal face and the thickness of boehmite (see Fig. 2.1). Morin (2014) indicates that the mixture of polar protic solvents has a strong influence on the particle aggregation. The modulation of surface affinity and steric hindrance of the solvent controls the distance between particles, and further controls the porosity and the microstructure.

2.2 Characterization

Once the material is synthesised, different characterization techniques allow one to examinate the microstructure of the material. The main techniques include nitrogen porosimetry, X-ray diffraction (XRD), Small Angle X-ray Scattering (SAXS), transmission electron microscopy (TEM), tomography (Kim et al., 2003; Zecevic et al, 2013) and Nuclear Magnetic Resonance (NMR).

2.2.1 X-ray diffraction

X-ray diffraction has been widely used to determine the microstructure of a crystal at nanoscale. A beam of incident X-rays is diffracted by the alumina lattice. By measuring the angles of the diffracted beams, a 3D image of electron density in the lattice is obtained.

Chiche et al. (2008) used X-ray powder diffraction to determine the shape and size of boehmite particles at the nanoscale. They simulated morphology-dependent diffraction patterns using the Debye formula. These reference patterns are then compared to experimental diffraction pattern. The average particle morphology is then computed by a linear combination of the reference patterns, with weights according to the size distribution. XRD methods provide information of the mean structuring crystallites and on morphological characteristics such as size and shape, but less on structure at higher length-scale like aggregates.

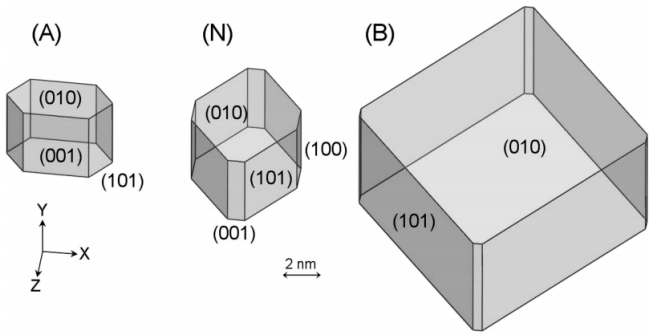

Figure 2.1: Boehmite particle morphology determined by XRD. The three samples are synthesised at different pH values: (A) pH=4.5, (N) pH=6.5 and (B) pH=11.5 (Chiche et al., 2008).

2.2.2 Porosimetry

Nitrogen porosimetry is an important tool to characterize mesoporous material. Material sample is pretreated at high temperature under vacuum to remove adsorbed species and put into a container in vacuum at 77 K. By increasing the nitrogen pressure, nitrogen molecules are progressively adsorbed at the sample surface or condensed in the sample porous volume. The amount of adsorbed or condensed nitrogen is related to the specific surface area and the pores' morphology. The amount of adsorbed nitrogen in function of vapour pressure is termed as nitrogen isotherm.

Nitrogen porosimetry isotherms are generally interpreted as follows. The pressure range is divided into three domains. The low pressure interval corresponds to the thermodynamical multilayer adsorption of nitrogen molecules. The classical Langmuir's model (Langmuir, 1918) regards the monolayer adsorption as a reversible reaction between the solid surface and gas molecules. An equilibrium is built up between the fractions of occupied and non-occupied volume in the monolayer. The gas is assumed to be ideal.

The Brunauer-Emmett-Teller (BET) theory (Brunauer et al., 1938) extends the Langmuir's model to multilayer adsorption. It applies Langmuir's model to each layer, with the assumption of no intersection between layers. The BET equation is:

$$\frac{1}{v[(\frac{1}{\chi})-1]} = \frac{c-1}{v_m c}(\chi) + \frac{1}{v_m c} \tag{2.1}$$

where v is the volume of adsorbed nitrogen gas, $\chi = p/p_0$ is the relative pressure (p is the equilibrium pressure, and p_0 is the saturation pressure), v_m is the volume of one monolayer of adsorbed nitrogen molecules, c is the BET constant determined by the heat of adsorption. In the beginning range of the nitrogen isotherms (about $0.05 < \chi < 0.35$), the relationship between $\frac{1}{v[(1/\chi)-1]}$ and χ is linear. By linear curve fitting, the volume of monolayer v_m is estimated, together with the number of adsorbed nitrogen molecules. With the hypothesis that one molecule occupies an area of $0.16\,\mathrm{nm}^2$, the specific surface area, or more explicitly "BET surface area" denoted S_{BET}, is estimated.

The empirical FHH equation (Frenkel, 1946; Halsey, 1948; Hill, 1952) describes the low pressure part of isotherm. It allows one to deduce the specific surface area,

or more explicitly "FHH surface area". Cimino et al. (2013) indicates that the FHH surface area differs from the BET surface area by 15% or less on various materials.

The intermediate range is interpreted as the capillary condensation and evaporation, together with multilayer adsorption. Capillary condensation occurs from highly curved interface to less curved interface with increasing pressure, while the evaporation occurs in the opposite way. The relationship between the equilibrium pressure and local curvature is described by the Kelvin equation.

The BJH method (Barrett et al., 1951), which combines the capillary condensation and multilayer adsorption, is used to deduce the pore size distribution. The method analyzes the desorption branch, and is based on the assumption of cylindrical pore.

The high pressure part is interpreted as the liquid compression. This part is fitted by a linear function of pressure (Cimino et al., 2013).

Mercury intrusion and helium pycnometry are also widely used techniques to charaterize porous material. Helium pycnometry provides the structural density d_s (in $\mathrm{g\,cm^{-3}}$) of the sample, while mercury intrusion provides the grain density d_g (in $\mathrm{g\,cm^{-3}}$). The pore volume fraction ϵ is then obtained from:

$$\epsilon = 1 - \frac{d_g}{d_s} \tag{2.2}$$

2.2.3 Transmission electron microscopy

Transmission electron microscope (TEM) emits a large uniform beam of electrons to a thin slice of the sample. The electron beam intensity attenuates when hitting the materials, essentially by small angle scattering. Transmission electrons are then caught by detectors and form a 2D image (Williams & Carter, 2009). TEM image is the 2D projection of a 3D microstructure. Each pixel contains information along the vertical axis of the sample slice. Typical resolution of standard microscope is a few Å.

Reimer and Kohl (2008) modeled the bright field TEM image by the Lambert-Beer law:

$$Y(x_1, x_2) = a + b\,exp\left[-c\int_0^f \mathrm{dx}_3\,\chi_S(x_1, x_2, x_3)\right], \tag{2.3}$$

where f is the sample thickness, a and b are constants that depend on the acquisition process, c is the inverse scattering length of the solid phase and χ_S is the characteristic function of the solid phase in 3D, i.e. $\chi_S(x, y, z) = 1$ if and only if point (x, y, z) is in the solid phase.

The TEM images are often blurry and noisy, because of the particle overlapping and the noise during image formation. Moreaud et al. (2009) proposed a method to reduce the noise and to remove the artefacts on TEM images of boehmite nanoparticles. First, a median filter of small size is used to reduce the high frequency electronic noise. Then, a bilateral filter is applied to smoothen and reduce the remaining noise while maintaining the edges information. Third, the artefacts of small thickness around the particles due to Fresnel diffraction are removed by a morphological opening by reconstruction. After the image filtering, they employed a dilution model to simulate the boehmite sample. By adjusting the simulated covariance to the experimental one, the average particle size is estimated, and is found in agreement with the result obtained by XRD analysis.

Local orientations are often visualized in TEM images of mesoporous alumina. Jeulin et Moreaud (Jeulin & Moreaud, 2008) proposed a method to estimate the local orientations in 2D TEM images. First, the vector field of the image gradient is calculated, noted $v(x)$. Second, a sub-domain $W(x)$, e.g. a square in 2D, is located around every point x. Third, a point cloud connected to the origin by the vectors $v(x_i)$ for each point x_i in the sub-domain $x_i \in W(x)$ is generated. Finally, the matrix of inertia of the cloud of points is calculated, from which the main axis is obtained by eigenvectors decomposition. The method is applied on TEM images of cellulose, who has similar alignments as observed in mesoporous alumina.

TEM images are often employed for the reconstruction of 3D microstructure by different models. More details are presented in Sec. 2.3.

2.2.4 Electron tomography

Electron tomography is a technique for the 3D reconstruction of microstructures at nanoscale. It uses a series of 2D TEM images, acquired by tilting the specimen at varying angles around an axis perpendicular to the electron beam (Frank & Joachim, 1992). The 3D reconstruction is based on the discrete Radon transform (Radon & Parks, 1986), which transforms linearly a 2D function to its 1D projection according to the angle rotated. Tran et al. (2014) proposed a robust method based on inverse problem approach to align maker-free projections. The method was applied to a mesoporous alumina sample, and allowed the reconstruction of the 3D microstructure (see details in Chap. 5). The disadvantage of electron tomography is the time consumption for acquisition and reconstruction. Besides, it cannot reconstruct microstructures of large volume (volume size limited to a few hundred nanometers), so it lacks representativity.

2.3 Microstructure Modeling

Microstructure modeling is useful for the design and the optimization of porous media. In literature, many models of porous media have been proposed (see the reviews of Sahimi (1993) for rocks and of Kosek (2005) for catalysts). Among them, we have identified the following models that are of interest for mesoporous alumina of similar materials:

- stochastic reconstruction algorithm (Gaussian field) (Adler et al., 1990).
- grain models (Jeulin, 1991)
- diagenesis process simulation (Štěpánek and Ansari, 2005)
- models obtained from simulated annealing (Yeong & Torquato, 1998)
- pore network model extracted from 3D imaging (Youssef et al, 2007)
- fractal model (Rigby & Gladden, 1999)

For the disordered porous network in mesoporous alumina, the first three types of model are more frequently used.

2.3.1 Grain models

Moreaud et al. (2012) use a dilution model (Serra, 1968; Jeulin, 1991) of grains to simulate experimental TEM images of boehmite. It assumes that the specimen is made of nanoparticles by sequentially letting particles fall from the top of the specimen and stopping them when hitting the bottom. The particles have random orientations uniformly distributed on the unit sphere. The resulting microstructure is a pack of non-overlapping objects in contact. The TEM image is simulated by performing a 2D projection on the microstructure. The parameters of the dilution model are identified by minimizing the quadratic difference between the simulated and the experimental covariance. The scale of the material and the context of the research is similar to our work with mesoporous alumina.

Moreaud, M. (2006) modeled the spatial dispersion of carbon black nanocomposites by a three-scale model. First, the exclusion zones are modeled by a Boolean model of spheres with a radius distribution. Second, the inclusion zones are located by another independent Boolean model of spheres with a radius distribution. Then, the primary particles of carbon black are modeled by a third Boolean model of spheres with a radius distribution inside the inclusion zones. The parameters (the radius distribution and volume fraction of each zone and particles) are identified by minimizing the difference of image statistics between experimental TEM images and simulated ones. The statistics include the covariance, the third order moment and the area fractions measured on TEM images. The multiscale structure, like aggregation, observed in this example is close to the one expected in mesoporous alumina.

Diagenetic model is another type of grain model, which make use of the process occurring during material synthesis, e.g. deposition and sintering process. This method requires prior knowledge on the diagenetic process. Roberts et al., (1985) generated a microstructure model of porous glasses through a simulation of grain consolidation. On the same material, Gelb et al. (1998) proposed the dynamic simulation of spinodal decomposition process, which is the main process occurring during the formation of porous glasses.

Koci et al. (2010) used random packing of particles (Pt and Al_2O_3) together with sintering to simulate the generation of γ-alumina. The packing process (Štěpánek and Ansari, 2005) simulates the diagenesis of grains and the layering growth mechanism. The particles are modeled by cylinders with hemispherical caps. The agglomerates are modeled by the packing of $n \times m$ particles. The level of sintering is described by the intersection fraction between the particles. The parameters are optimized to reproduce the pore volume fraction, pore size distribution and correlation length of the material.

2.3.2 Stochastic reconstruction algorithm

The stochastic modeling algorithm is widely used for the reconstruction of 3D microstructure of porous material from 2D images. The algorithm was originally proposed by Joshi (1974), and was extended into three dimensions by Adler (1990). The basic idea of the method is to smoothen a Gaussian random fields to reproduce the pore volume fraction and the covariance function of the TEM image. First, a 3D space of uncorrelated random variables following Gaussian distribution is generated, noted $X(x)$, with mean equal to 0 and standard deviation equal to 1. An

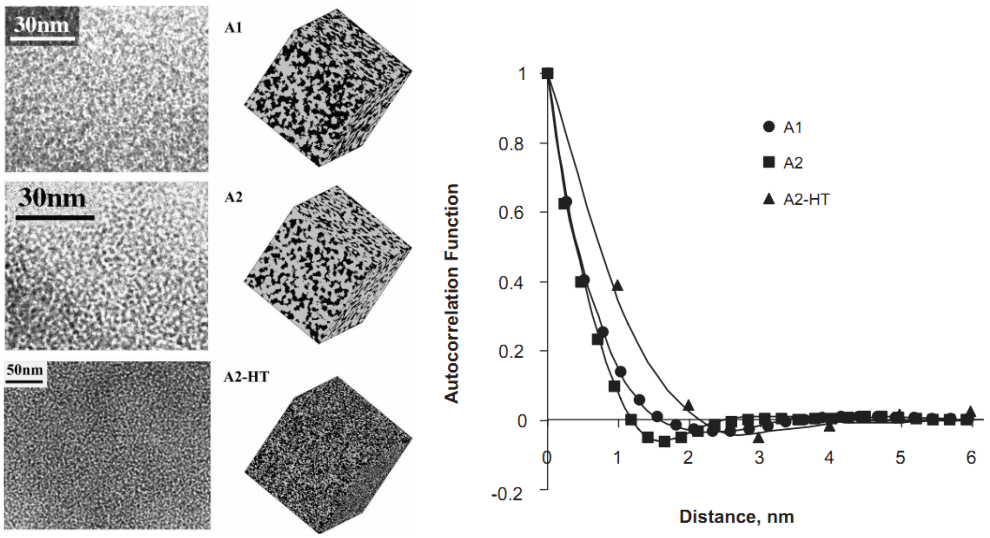

Figure 2.2: Left: 2D experimental TEM images and 3D reconstructed microstructure of mesoporous alumina with porosity in black. Right: Two-point covariance function of reconstructed model and of TEM images (Diaz et al., 2004).

intermediate field, denoted $Y(x)$, is generated from the $X(x)$ random field by the inverse Fourier transform:

$$Y(x) = N^{3/2} \sum_k [\hat{C}_y(k)]^{\frac{1}{2}} \hat{X}(k) e^{-2i\pi kx/N} \tag{2.4}$$

where N is the size of the space, $\hat{C}_y(k)$ and $\hat{X}(k)$ are respectively the discrete Fourier transform of $C_y(x)$ and $X(x)$. The $C_y(x)$ is the covariance function of the field $Y(x)$, deduced from the covariance function of the TEM image. The intermediate field $Y(x)$ generated in this way has a distribution function $P(y)$:

$$P(y) = (2\pi)^{-1/2} \int_{-\infty}^{y} e^{-t^2/2} dt \tag{2.5}$$

The field $Y(x)$ is then thresholded according to its distribution function and the pore volume fraction of the material, to produce the final microstructure. Since the covariance function and the pore volume fraction are both inputs of the modeling process, the generated microstructure inherits the properties.

Adler et al. (1990) used the algorithm to generate the 3D microstructure of Fontainebleau sandstones. Simulated cross-sections of the simulated media are compared to thin sections of real media, and are visually satisfactory. The generated microstructure is used for the simulation of fluid flow. The permeabilities at various porosities are computed numerically and validated with experimental data.

Diaz et al. (2004) used the stochastic reconstruction algorithm to model three samples of γ-alumina from TEM images. With the 3D microstructure, the chord length distribution measured on TEM images was reproduced. The permeability and effective diffusion coefficients are estimated on the 3D microstructure by solving the diffusion and momentum equations, which turned out to be close to experimental measurements with relative error less than 10%.

Kainourgiakis et al. (2005) used the stochastic reconstruction algorithm to model the mesoporous Vycor glass at nanoscale and North Sea chalk at micrometer scale.

Flow in Darcy's regime and diffusion in Knudsen regime was simulated in the microstructure. The estimated permeabilities are in good agreement with experiments.

The main advantage of the stochastic reconstruction algorithm is that it uses correlation function as input and inherits this property in the generated microstructure. The method is also robust without many parameters, except the correlation function and pore volume fraction. The main disadvantage is that microstructures generated in this way do not have morphological features, like particles or the spatial dispersion of particles. These features are important for the synthesis optimization of mesoporous alumina.

2.3.3 Texture measurement on 3D microstructure

Once the microstructure is reconstructed, the geometric quantities of interest, e.g. specific surface area, pore size distribution, chord-length distribution and tortuosity factor are available from the 3D digital microstructure.

The specific surface area (S_V) may be determined from the slope at the origin of the 3D model's covariance (Matheron, 1971). Lindblad (2005) proposed a method to estimate the surface area of a 3D digital model by local configurations. He has defined 14 configurations of a cube of 8 points. Each point can be occupied by solid or void. Each configuration is assigned with an area weight. The algorithm scans the 3D space with the 8 points cubes, determining local weights. The sum of weights is the total surface area of the microstructure. The method is efficient and easily implemented. The weights were further optimized by Ziegel and Kiderlen (2010).

The chord length distribution function is another useful characteristic property of porous structure. It gives the probability for a chord, to lay in pores of the structure. Diaz et al. (2004) computed the chord-length distribution functions of TEM images and of the 3D digital model generated from the TEM images. They confirmed that their reconstruction process preserved this statistics.

2.4 Physical properties of mesoporous alumina

One of the main objectives of microstructure modeling is to predict the physical properties of the material. Physical properties of materials similar to mesoporous alumina have been studied on gas sorption (Štěpánek et al., 2007), Elasticity (Staub, 2014; Digne et al., 2004), permeability (Kainourgiakis et al., 2005; Adler et al., 1990), heat conduction (Kohout et al., 2004) and reaction-diffusion (Koci et al., 2007, 2010). Numerical methods, including finite elements, finite difference, Fast Fourier Transform (FFT), were used to solve the homogenization problem (Kainourgiakis et al., 2005; Willot, 2015).

2.4.1 Elasticity

In industry, manufacturers tend to increase the pore volume fraction and the specific surface area of mesoporous alumina. However, with increasing pore volume fraction, the mechanical rigidity should be maintained. For a two phase material, Hashin-Shtrikman bounds (Hashin & Shtrikman, 1963) are the tightest bounds for the estimation of elastic moduli of isotropic media. The bounds are estimated through the elastic moduli of each phase and their volume fractions.

Author and method	porosity	Alumina particles			Mesoporous alumina		
		Ka (GPa)	Ea (GPa)	Va	K (GPa)	E (GPa)	V
Digne et al. 2004 (by calculation)		171					
Staub 2014 (by experiment)	66.5% (monomodal)					6.4	
Staub 2014 (by experiment)	72.5% (bimodal)					3.6	
Gallas et al. 1994 (by experiment)		162±14	253±22	0.24±0.2			

Table 2.1: Elasticity parameters for mesoporous alumina from bibliography. K is Bulk modulus, G is Young's modulus and V is the Poisson's coefficient.

Experiments were performed to measure the mechanical response of alumina particles (Gallas et al., 1994) as well as that of mesoporous alumina (Staub, 2014). Staub (2014) worked on two different γ-alumina samples with macro pores – unimodal and bimodal. Digne et al. (2004) has calculated the elasticity properties of γ-alumina crystals based on density functional theory. The elasticity parameters for mesoporous alumina mentioned in the bibliography are summarized in Table 2.1.

2.4.2 Permeability

The permeability of a porous medium can be estimated with the Carman-Kozeny equation (Carman, 1937; Kozeny, 1927):

$$\kappa^{CK} = \frac{f^3}{c\gamma^2} \tag{2.6}$$

where κ^{CK} is the estimated permeability, f the pore volume fraction, γ the specific surface area and c an empirical constant.

Kainourgiakis et al. (2005) studied the Stokes flow in Darcy's regime on microstructures of γ-alumina membrane, Vycor glass and North Sea chalk. The microstructure of alumina membrane is modeled by a ballistic deposition of spheres with radius 10 nm. The Stokes equation is solved numerically by a finite-difference scheme, with periodic boundary conditions for the velocity field. The effective permeability is numerically estimated at 4.3×10^{-19} m^2. The result is close to the estimation by the Blake-Kozeny equation (Bird, 1976), with a relative error less than 13%.

2.4.3 Diffusion

The Hashin-Shtrikman lower bound for the effective diffusion coefficient of a porous medium is zero. The upper bound is determined by the pore volume fraction and the free diffusion coefficient of the gas.

Kainourgiakis et al. (2005) simulated the molecule diffusion by blind random walk in the microstructure of a γ-alumina membrane. A sufficient number of point-like molecules are injected into the 3D microstructures. The trajectories are recorded, and the molecules displacements are measured. The diffusion coefficient is calculated using the equation:

$$D = \lim_{t\to\infty} \frac{<\mathbf{r}^2>}{6t} \tag{2.7}$$

where t is the travel time, $\mathbf{r}$ the displacement. In Knudsen regime, the travel time t is replaced by s/u, where s is the travel distance and u the thermal speed. The simulated diffusion coefficient of He, 7.7×10^{-3} $\mathrm{cm^2\,s^{-1}}$ is close to the experimental reference (Papadopoulos, 1993) of 8.0×10^{-3} $\mathrm{cm^2\,s^{-1}}$. The ratio of effective diffusion coefficient to the free diffusion coefficient is 0.25, close to the value 0.25 obtained by Kim and Torquato (1992). The pore volume fraction of alumina sample used in this work is 0.42.

Diaz et al. (2004) also estimate the effective diffusion coefficient of inert tracers by random walk simulation, on the microstructure generated by the stochastic reconstruction algorithm. The simulated diffusion coefficient of He is 6.3×10^{-4} $\mathrm{cm^2\,s^{-1}}$, with pore volume fraction 0.487.

The dependence of the diffusion coefficients on the morphological nature of a porous material is also a hot topic in the field. Derjaguin et al. (1965) proposed the self-diffusion coefficient based on the statistical properties of a set of consecutive chords. Streider et al. (1967) proposed an upper bound on the self-diffusion coefficient by using a variational technique. The upper bound coincides with the coefficients proposed by Derjaguin, when the porous media have an exponential chord-length distribution function. Mu et al. (2008) have examined the influence of connectivity and pore size distribution on the effective diffusion coefficient in Knudsen regime, based on a periodic 3D bond pore network model.

Wernert et al. (2010) studied experimentaly the mass transfer kinetics of toluene and polystyrenes by Inverse Size-Exclusion Chromatography (ISEC). The study is based on an assumption of cylindrical pores, taking into account size effects. An equation was proposed to estimate the effective diffusion coefficient:

$$D_p^{\mathbf{eff}}(r_m) = \frac{\epsilon_p(1-\lambda)^2(1-2.1\lambda+2.1\lambda^3-1.0\lambda^5)D_m}{1-2.4\log\left[\epsilon_p(1-\lambda)^2\right]} \tag{2.8}$$

where $D_p^{\mathbf{eff}}$ is the effective diffusion coefficient, r_m the molecule radius, λ the ratio of molecule radius to pore radius, D_m the molecular diffusion coefficient and ϵ_p volume fraction of open pores.

2.4.4 Fourier-based homogenization method

Fourier-based homogenization algorithms, or "FFT methods" for short, were introduced by Moulinec & Suquet (1994). They were a breakthrough in numerical methods for computing the mechanical response of composite materials. It has been successfully applied to compute the dielectric (Moreaud, 2006; Delarue & Jeulin, 2002), mechanical (Willot, 2015), electrical (Willot et al, 2013) and optical (Azzimonti, 2013) response of composites. The method can be applied to compute the physical response of complex and large microstructures, e.g. multi-scale nano-composites (Jean et al., 2011), granular medium (Willot et al, 2013) or polycrystals (Prakash et al, 2009). In FFT methods, the microstructure is defined by 2D or 3D images, and the local fields are computed on each pixel or voxel in the image. In elasticity, stress and strain field maps are obtained at the scale of microstructure, which enables us to study in detail the effects of microstructure on local fields. Such fields are representative of the material behavior if the resolution is fine enough and the simulated microstructure is large enough.

FFT methods applied in different contexts proceed all from Lippmann-Schwinger's equation (Moulinec & Suquet, 1994):

$$E_i = \bar{E}_i - G^0_{ij} * P_j, \qquad P_j = J_j - \sigma^0 E_j, \tag{2.9}$$

where σ^0 is an arbitrary reference property of a homogeneous medium (conductivity for electrical response, stiffness tensor for linear elasticity media, permeability for flow in porous media), E is the field of the driving force (electric field, concentration gradient, ...), J is the field of response (current, mass flux, ...), P is the polarization field, G^0 is the Green operator and "$*$" is the convolution product. The convolution product can be calculated by a standard product in the Fourier space, using FFT. The iteration of the two equations in Eq. 2.9 leads to the convergence of the full field.

In contrast to the finite element method, no meshing is required by the FFT method. With the software Morph-Hom developed by Willot in CMM, simulated microstructures of large sizes with a high contrast of properties can be handled. The software has been validated on Boolean models of spheres with all volume fractions for elastic properties and conductivity (Willot & Jeulin, 2009).

2.5 Discussion

Microstructure modeling In the literature, microstructures of mesoporous alumina are modeled by ballistic deposition model (Kainourgiakis et al., 2005), cylindrical particle packing with sintering simulation (Koci et al., 2010) and stochastic reconstruction (Diaz et al., 2004). The size of grains are in the same length order: 10 nm (radius) for the ballistic deposition model, and 4 nm (diameter), 12 nm (length) for the cylindrical particles. Diffusion property is the common interest of the three models. The diffusion property of Kainourgiakis's model has the best match with experimental data or literature reference.

The common disadvantage of these models is the accuracy. The stochastic reconstruction model does not preserve neither the particles shape nor their local organization. The grains described in the other two models are simplified to be spherical or cylindrical, which are far from the geometrical accuracy we may expect. Indeed, current characterization techniques (e.g. TEM images (Moreaud et al., 2012) and XRD (Chiche et al., 2008)) enable us to identify the shape and size of alumina nano-particles. An accurate information on the particle morphology is important for the synthesis optimization (Trimm & Stanislaus, 1986; Morin, 2014).

Furthermore, the ballistic deposition model simplifies strongly the aggregation of grains. Koci's model simulates the particle aggregation by aligned packing and intersecting, which is a simplification of the feature. The aggregation is expected to play an important role for γ-alumina as it can produce large pores.

The three models are all identified with the correlation function of 2D microscopy images. However, microscopy image processing and measurements are not presented in detail in the three papers. In fact, the high resolution TEM images are often noisy and blurry (as shown in Moreaud et al., 2009), which leads to inaccuracy in the correlation function estimation.

Physical properties The gas sorption property is also addressed for Koci's model and Diaz's model. Diaz et al. present the experimental isotherms of the alumina

samples. Koci uses the method of virtual capillary condensation (Štěpánek et al., 2007) to evaluate the pore size distribution of the reconstructed microstructures. However, no comparison between simulation and experiment has been made. The gas sorption property is so important for the characterization of mesoporous alumina that it should become a criterion for the model validation.

On the elasticity of mesoporous alumina, numerical calculation of precise local field with the FFT method is well developed (Willot, 2015). No experimental reference or simulation on the same material has been found, which makes the model validation by elasticity difficult.

On the permeability, finite-difference scheme (Kainourgiakis et al., 2005) and FFT method (Abdallah et al., 2015) have both been developed. The effective permeability estimated in (Kainourgiakis et al., 2005) is a rough reference for our estimation, because our samples have a much higher pore volume fraction.

To estimate the diffusion coefficient of a gas in porous media, the widely-used method is random walk simulation. The FFT method to solve Fick's diffusion in porous media is also well developed (Willot et al, 2013). The effective diffusion coefficient and the tortuosity estimated in (Kainourgiakis et al., 2005) is a rough reference for our estimation. Experiments on gas diffusion are required for more accurate validation.

Summary In summary, to advance further from the current literature, and to meet the requirements in refining industry, a model involving details in particle shape, aggregation and other potential features is needed. To support the details in modeling, experimental characterization and data processing with high precision is required. The effective physical properties should be estimated for model validation and for property prediction. The relation between the microstructure morphology and the transport properties should be studied, in order to create links between synthesis and effective properties.

Accordingly, our work focus on two main aspects: i) the extraction, modeling and validation of material's microstructure morphology; ii) its reconstruction and the phenomenological study of the relation between the morphology of microstructure and the transport and sorption properties of mesoporous alumina.

Part II

State of the Art: Mathematical Morphology in Image Processing and Random Models

Chapter 3

Morphological tools in images processing and measurements

Morphological tools are used in the image processing and measurements of the TEM images of mesoporous alumina and in the simulation of capillary condensation and evaporation. In this chapter, the basic notions and operations involved in this work are concisely presented. More details are available in (Serra J., 1982) and (Soille P., 1999).

3.1 Notion of image

An image of dimension d of values in dimension n can be generally defined as a function $\mathbb{R}^n \times \mathbb{R}^d$. In our work, 2D or 3D grayscale images defined in discrete spaces are considered. An image I defined in domain X of values in set Y is defined:

$$I : X \subset \mathbb{Z}^d \to Y \subset \mathbb{Z}, \quad d \in \{2, 3\}. \tag{3.1}$$

3.2 Morphological operations in image processing

3.2.1 Structuring element

I is an image defined in $X \subset \mathbb{Z}^d$. We call any subset B of $\mathbb{Z}^d$ a structuring element (SE): $B \subset \mathbb{Z}^d$. For $x \in X$, we denote B_x the translation of SE B by vector x, defined by:

$$B_x = \{b + x \mid b \in B\}, \quad \forall x \in X \tag{3.2}$$

The symmetric SE of B is denoted $\check{B}$, defined by:

$$\check{B} = \{-b \mid b \in B\} \tag{3.3}$$

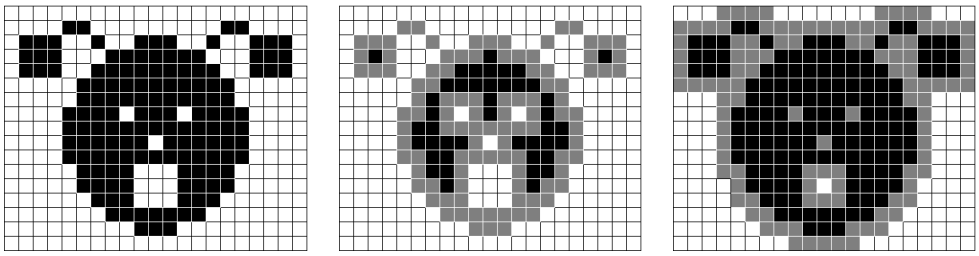

(A) (B) (C)

Figure 3.1: Illustration of morphological dilation and erosion operations on a binary image. Pixels of value 1 is in white. Pixels of value 0 are in black. Pixels have different values before and after the operation are in gray. (A) Original image. (B) Dilation by a square structuring element of size 3×3. Pixels in white and in gray have the same value 1. (C) Erosion by a square structuring element of size 3×3. Pixels in black and in gray have the same value 0. (Image source: E. Decencière, free access in the item *Morphologie Mathématique*, Wikipédia.)

3.2.2 Minkowski addition and subtraction

In binary images or sets, Minkowski addition and subtraction (Serra J., 1982) between two sets A and B are defined:

$$\begin{aligned} A \oplus B &= \bigcup_{b \in B} A_b \\ A \ominus B &= \bigcap_{b \in B} A_{-b} = (A^c \oplus B)^c \end{aligned} \tag{3.4}$$

The Minkowski addition and subtraction constitute the basis of mathematical morphology. The two operators correspond to morphological dilation and erosion in binary images.

3.2.3 Erosion and dilation

The dilation δ and erosion ϵ of a set A by a structuring element B is defined by:

$$\begin{aligned} \delta_B(A) &= A \oplus B \\ \epsilon_B(A) &= A \ominus B \end{aligned} \tag{3.5}$$

Erosion and dilation are the two basic operations of mathematical morphology. The effects of two operations are illustrated in Fig. 3.1. They modify the value of a pixel according to the information in its neighborhood. The neighborhood is defined by the structuring element.

For grayscale images, the dilation and erosion operations by a flat structuring element B is:

$$\begin{aligned} \delta_B(I)(x) &= \sup_{y \in \check{B}}(I(x-y)) \\ \epsilon_B(I)(x) &= \inf_{y \in \check{B}}(I(x-y)) \end{aligned} \tag{3.6}$$

where sup and inf are supremum and infimum operators respectively. The dilation operation enlarge the areas of higher values, while the erosion functions in the inverse way.

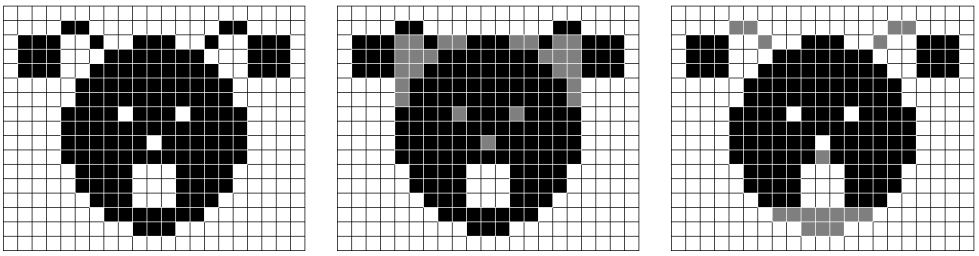

(A) (B) (C)

Figure 3.2: Illustration of morphological opening and closing operations on a binary image. Pixels of value 1 is in white. Pixels of value 0 are in black. Pixels have different values before and after the operation are in gray. (A) Original image. (B) Opening by a square structuring element of size 3×3. Pixels in black and in gray have the same value 0. (C) Closing by a square structuring element of size 3×3. Pixels in white and in gray have the same value 1. (Image source: E. Decencière, free access in the item *Morphologie Mathématique*, Wikipédia.)

3.2.4 Opening and closing

The opening γ and closing φ operations are defined as the combination of dilation and erosion:

$$\begin{aligned} \gamma_B(I) &= \delta_B(\epsilon_B(I)) \\ \varphi_B(I) &= \epsilon_B(\delta_B(I)) \end{aligned} \tag{3.7}$$

The effects of the two operations are illustrated in Fig. 3.2. In binary images, the opening operation erodes the areas of higher values and of size smaller than the structuring element. The areas larger than the structuring element remain unchanged. The closing operation functions in the inverse way: it fills the areas of lower values and of size smaller than the structuring element.

3.2.5 Geodesic dilation and erosion

Geodesic operations are used to constrain the morphological operations, when we expect the operation functions only in a specific domain or in a specific value range. Assuming that X and Y are two subsets of a domain D, it is expected to dilate the set Y, while the result of dilation remains in X. Geodesic dilation and erosion for compact sets or binary images are defined by:

$$\begin{aligned} \delta_X(Y) &= \delta(Y) \cap X \\ \epsilon_X(Y) &= \epsilon(X^c \cup Y) \cap X \end{aligned} \tag{3.8}$$

where X is called mask, Y is called marker, and the structuring element is implicit.

The marker and the mask can be both extended in grayscale. The values in the dilation $\delta(Y)(x)$ remains inferior to the values of $X(x)$. The geodesic dilation and erosion for grayscale images are defined by:

$$\begin{aligned} \delta_f(g)(x) &= \inf\{\delta(g)(x), f(x)\} \\ \epsilon_f(g)(x) &= \sup\{\epsilon(g)(x), f(x)\} \end{aligned} \tag{3.9}$$

3.2.6 Reconstruction

We denote $\delta_X^n(Y)$ the successive geodesic dilations of Y in mask X by n iterations:

$$\delta_X^n(Y) = \delta_X(...\delta_X(\delta_X(Y))) \tag{3.10}$$

where X and Y can be binary images or grayscale images. For binary images or sets, this equation is equivalent:

$$\delta_X^n(Y) = \delta(...\delta(\delta(Y) \cap X) \cap X)... \cap X \tag{3.11}$$

The reconstruction of a binary image or a grayscale image Y is defined as successive geodesic dilations by infinite iterations:

$$R_X(Y) = \lim_{n \to +\infty} \delta_X^n(Y) \tag{3.12}$$

The reconstruction operation dilates the image Y to the maximum under constraint X. The reconstruction operation combined with erosion is called opening by erosion-reconstruction, denoted by $R_f(\epsilon_B(f))$. It filters the small structures of higher values, but at the same time conserves the edge information.

3.2.7 Connected components

A compact set X is said to be connected by arcs, if and only if any two points in X are joined by a path contained in X. Given a point y in a set Y, the largest compact set connected by arcs containing y is called the connected component of y in Y, denoted by $C_y(Y)$. The class of all disjoint connected components in set Y is called the connected components of Y, denoted by $C(Y)$. In binary images or sets, a connected component $C_y(Y)$ can be obtained by reconstruction with the point y as marker:

$$C_y(Y) = R_Y(y). \tag{3.13}$$

3.2.8 Hole-filling

Connected components non-connected to the boundary of the image are called isolated holes. For a set or a binary image X, the boundary is denoted by ∂X. Grains denoted by G are in the image X: $G \subset X$. It is assumed that isolated holes exist in the porous phase G^c. The holes are filled by a reconstruction from the boundary of the image:

$$F = [R_{G^c}(\partial X \cap G^c)]^c \tag{3.14}$$

where F is the set of grains with filled pores.

3.3 Morphological measurements

Morphological measurements play an important role in the characterization of 2D TEM images and of 3D random models. Information like volume fractions of different composites, the distribution of pixel values and the spatial correlation, serve the microstructure modeling of mesoporous alumina.

3.3.1 Volume fraction

The volume fraction f of a random set A in domain $D \subset \mathbb{R}^3$ is the proportion of volume of A. For a stationary random set, it is given by the probability:

$$f = P\{x \in A\}, \quad x \in D \tag{3.15}$$

In practice, f is equal to the ratio of Lebesgue measure of A to that of D.

3.3.2 Histogram

We consider an image $I : X \to Y$. The histogram of the image, denoted by $H^I(y)$ is defined by:

$$H^I(y) = \frac{\#\{\mathbf{x} : I(\mathbf{x}) = y, \mathbf{x} \in X\}}{\#\{X\}}, \quad \mathbf{y} \in Y \tag{3.16}$$

where # is the Cardinal operator for sets, representing the number of elements in a set. The volume fraction is a specific value in histogram.

3.3.3 Covariance

The covariance of a random set or a grayscale image allows one to characterize the spatial dispersion of objects and structures. It is related to the characteristic scales of objects, aggregations and exclusions. It is also sensitive to the isotropy (or anisotropy) and the specific surface area. The rich information contained in the covariance makes it a privileged tool in the characterization of random models.

The covariance of a random set A, denoted by $C(\mathbf{h})$ is defined as:

$$C(\mathbf{h}) = P\{\mathbf{x} \in A, \mathbf{x} + \mathbf{h} \in A\} \tag{3.17}$$

where $\mathbf{h}$ is a coordinate shift. It represents the probability of that a pair of points with shift $\mathbf{h}$ does not hit A^c.

For $\mathbf{h} = \mathbf{0}$, we have $C(\mathbf{0}) = f$. For an ergodic stationary random set, when the shift tends to infinity, we get:

$$C(\infty) = f^2 \tag{3.18}$$

The covariance of a grayscale image Y can be estimated by:

$$C(\mathbf{h}) = \langle Y(\mathbf{x} + \mathbf{h})Y(\mathbf{x})\rangle - \langle Y(\mathbf{x} + \mathbf{h})\rangle\langle Y(\mathbf{x})\rangle, \tag{3.19}$$

where $\langle . \rangle$ mean space average. In practice, the normalized covariance, or the correlation function is also often used, with the same notation $C(\mathbf{h})$ by convention:

$$C(\mathbf{h}) = \frac{\langle Y(\mathbf{x} + \mathbf{h})Y(\mathbf{x})\rangle - \langle Y(\mathbf{x} + \mathbf{h})\rangle\langle Y(\mathbf{x})\rangle}{\langle Y^2(\mathbf{x})\rangle - \langle Y(\mathbf{x})\rangle^2}, \tag{3.20}$$

The normalized covariance satisfies $C(\mathbf{0}) = 1$ and $C(\infty) = 0$.

3.3.4 Specific surface area

The specific surface area is defined as the ratio of surface area to volume, denoted by S_V. The specific surface of a random model is deduced from the slope at the origin of the covariance. For an isotropic medium, the relation is (Matheron, 1967):

$$S_V = 4 \left(\frac{\partial C}{\partial |\mathbf{h}|} \right)_{\mathbf{h}=\mathbf{0}} \tag{3.21}$$

3.3.5 Representative volume element (RVE)

The analysis of the representative volume element allows one to evaluate the statistical quality of the numerical homogenization of an effective property. It evaluates the error of estimation, and further predicts the necessary volume for a given relative error. The RVE analysis focus on a scalar field of a property, denoted by P, e.g. a component of the stress field, a component of the velocity field, etc. In order to homogenize the property P, the average over a volume V is used $\langle P \rangle_V$. The larger the volume for estimation is, the smaller the estimation error is. We define $D_P^2(V)$ the variance of estimates over n random realizations of volume V. The relative error ϵ_P of the estimation $\langle P \rangle_V$ is:

$$\epsilon_P = \frac{2D_P(V)}{\sqrt{n}\langle P \rangle_V} \tag{3.22}$$

Matheron (1971) proved that the asymptotic expansion of $D_P^2(V)$ is proportional to the reciprocal of the volume V when $V \gg A_d^P$:

$$D_P^2(V) \propto \frac{D_P^2 A_d^P}{V} \tag{3.23}$$

where D_P^2 is the point variance ($V = 1$ voxel in discrete space), and A_d^P is the integral range defined by:

$$A_d^P = \int_{\mathbb{R}^d} \mathrm{d}\mathbf{h}\, C(\mathbf{h}), \quad d \in \{2, 3\}. \tag{3.24}$$

where $C(\mathbf{h})$ is the normalized covariance. In practice, a single realization of a large enough volume V_0 is sufficient. The volume is divided into disjoint subdomains of volume V. By plotting the variance $D_P^2(V)$ in function of V, the integral range A_d^P is estimated by curve fitting.

When V_0 is large enough, we use the $\langle P \rangle_{V_0}$ to approximate the property P. In this case, $n = 1$. The Eq. 3.23 is used to estimate the variance $D_P^2(V_0)$, and the relative error of the estimation becomes:

$$\epsilon_P^2 = \frac{4D_P^2 A_d^P}{V_0 \langle P \rangle_{V_0}} \tag{3.25}$$

In the inverse way, with a given relative error ϵ_P, the required minimum volume is:

$$V_{VER} = \frac{4D_P^2 A_d^P}{\epsilon_P^2 \langle P \rangle_{V_0}} \tag{3.26}$$

Chapter 4

Morphological models of random media

Morphological modeling enables us to generate realistic 3D microstructures. It handles the heterogeneity, which exists in materials at various scales, through a probabilistic approach.

4.1 Presentation of random media

For a two-phase material as mesoporous alumina, one phase is modeled by a random closed set A, and the other phase by its complementary A^c. A is fully characterized by its Choquet capacity $T(K)$ in a probabilistic view (Eq. 4.1) (Matheron, 1967):

$$T(K) = P(K \cap A \neq \emptyset) = 1 - P(K \subset A^c) \tag{4.1}$$

where K is a compact set, P denotes the probability. In practice, $T(K)$ can be estimated by volume fraction on 3D images after a morphological dilation of the set A by the set K: $A \oplus K = \cup_{x \in K} A_x$. The Choquet capacity is a general characteristic of the random set A, from which other morphological properties can be deduced. When the set K is a single point, the volume fraction V_V is deduced from eq. 4.1. When the set K is made of a pair of points, the Choquet capacity becomes the covariance. When K is a 3D ball, the distribution of distance of a point in A^c to the boundary of A is deduced.

4.2 Poisson point process

Poisson point process is a typical random point process, which generates points homogeneously and randomly distributed in the 3D domain. The probability that a compact set K contains n points of the process is:

$$P_n(K) = P\{N(K) = n\} = \frac{(\theta\mu(K))^n}{n!} \exp\left[-\theta\mu(K)\right] \tag{4.2}$$

where θ is the intensity (average number of points per unit volume in 3D), $\mu(K)$ is the Lebesgue measure (volume in 3D) of the compact set K.

Starting from random point process, models of random structures can be generated, e.g. the Boolean model (Matheron, 1967), dead leaves model (Jeulin, 1987), mosaic model (Matheron, 1968; Jeulin, 1987) and dilution model (Serra, 1968; Jeulin,

1991). Multi-scale models are also generated from intersections of basic random sets (Moreaud, 2006; Jeulin, 2012). In practice, these models incorporate information from characterization tools and respect physical assumptions (on e.g. crystallography for the grains shape). The parameters of the model are identified by numerical or (semi-)analytical optimization (Moreaud et al., 2012; Couka et al., 2015; Jeulin, 2014; Jean et al., 2010).

4.3 Boolean model

The Boolean model was proposed by (Matheron, 1967), to simulate simple distribution of overlapping objects. It is obtained by implantation of random primary grains A' (with possible overlaps) on Poisson points x_k:

$$A = \cup_{x_k} A'_{x_k}. \tag{4.3}$$

The Choquet capacity of Boolean model is:

$$T(K) = 1 - \exp\left(-\theta\mu(A' \oplus \check{K})\right) \tag{4.4}$$

Any shape (convex or non convex, and even non connected) can be used for the grain A'. Most often in the literature Boolean models of spheres are considered.

4.4 Hardcore model

A hardcore model guarantees a repulsion distance h between all the point pairs of a random point process. Compared to a Poisson point process, the intensity is modified as:

$$\theta_{HC} = \frac{1 - \exp -\theta h^2 \pi}{h^2 \pi} \tag{4.5}$$

In practice, the hardcore points are generated by removing points from Poisson point process – the points of distance smaller than h to any other point are removed. When the repulsion distance h is larger than the gyration radius of the grain A', the objects in the hardcore model do not have intersection.

4.5 Multi-scale models

In mesoporous alumina, the pores' sizes are in different scales. The aggregates or clusters of primary grains have also been observed in TEM or SEM images. Starting from the basic one-scale models, the superposition of scales and the fluctuation of local volume fraction can be used to model multi-scale features. The union or intersection of random sets is a common and simple way to realize multi-scale models (Jeulin, 1979; Greco et al, 1979).

Cox point process is a generalization of the Poisson point process. It generates non-homogeneous distribution of random grains. Instead of the homogeneous intensity, a positive random function is used to describe the local intensity $\theta(x)$ (Jeulin, 1996). The number of points in a domain D follows a Poisson distribution with average $\theta(D) = \int_D \theta(dx)$:

$$P_n(D) = P\{N(D) = n\} = \frac{\theta(D)^n}{n!} \exp\{-\theta(D)\} \tag{4.6}$$

The Choquet capacity of the Cox point process is:

$$T(K) = 1 - E_\theta\{\exp\left(-E_{A'}\{\theta(\check{A}' \oplus K)\}\right)\} \tag{4.7}$$

where E_θ is the mathematical expectation with respect to $\theta(x)$, and $E_{A'}$ is the mathematical expectation with respect to the random set A'. The non-homogeneous distribution of intensity provides a way to generate multi-scale random model.

Part III

Characterization of the Mesoporous γ-Alumina samples

Chapter 5

Experimental Characterization

5.1 Sample preparation

Three different mesoporous alumina samples, with different expected platelet shapes were synthetized. Sample 1 and 2 originated from commercial boehmite powders (provided by *Axens*, Salindres) whereas sample 3 was synthesized in a laboratory scale from solution of aluminum nitrate ($Al(NO_3)_3$,$9H_2O$ from *Sigma Aldrich*) and sodium aluminate ($NaAlO_2$ from *Sigma Aldrich*).

The boehmite powder is dispersed in water to obtain a 10 *wt*% solution. The suspension is stirred for 2 hours and put in an autoclave. The autoclave is sealed and heated at T_A for t_A hours. The suspension is filtered and dried at 393 K overnight. The powder is shaped in trilobed extrudates, the extrudates are dried at 353 K overnight and calcined under dry air (923 K, 4 h) then wet air (temperature T_S, 2 h, X_S *wt*% water). Origin of samples and parameters of the thermal treatments are reported in table 5.1. Such thermal treatments allows to obtain a coherent sample series with very close specific surface and porous volume but different expected platelet shapes.

Sample	Origin	Initial S_{BET} $m^2\,g^{-1}$	T_A K	t_A h	T_S K	X_S %
1	Axens	350	423	7	973	6
2	Sasol	330	403	4	923	1
3	Laboratory	330	403	24	923	1

Table 5.1: Synthesis conditions for the three samples of mesoporous alumina.

The obtained calcined extrudates are translucent, indicating no scattering by light, that is to say, negligible density fluctuation at the scale of visible light wavelength (few hundred nanometers).

5.2 Porosimetry and pycnometry

Structural density d_s (in $g\,cm^{-3}$) is measured by He pycnometry. The sample is pretreated at 523 K for 3 h. Expected relative uncertainty is about 0.5%.

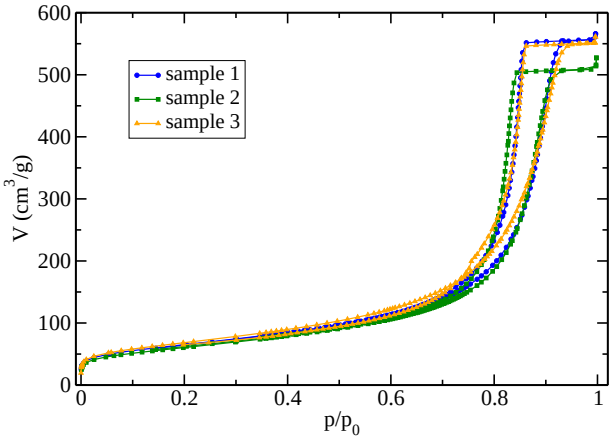

Figure 5.1: Nitrogen porosimetry isotherm on the three samples of mesoporous alumina.

	Sample 1	Sample 2	Sample 3	Relative uncertainty
d_g ($\mathrm{g\,cm^{-3}}$)	1.04	0.95	0.88	2.5%
d_s ($\mathrm{g\,cm^{-3}}$)	3.33	3.26	3.26	0.5%
S_{BET} ($\mathrm{m^2\,g^{-1}}$)	240	223	247	5%
ε	0.688	0.708	0.730	3.6%
S_V ($\mathrm{nm^{-1}}$)	0.232	0.213	0.218	5.6%

Table 5.2: Textural properties and their uncertainties obtained from the porosimetry measurements.

Grain density d_g (in $\mathrm{g\,cm^{-3}}$) is measured by mercury intrusion after a pretreatment (523 K for 2 h). The grain density is obtained at a 0.2 MPa intrusion pressure where mercury fills only inter-grain porosity but not intra-grain porosity. Expected relative uncertainty is 2.5% (Tab. 5.2).

The porosity ε (void volume fraction) is obtained from :

$$\varepsilon = 1 - \frac{d_g}{d_s}$$

Gas sorption properties are characterized by nitrogen porosimetry. Extrudates are pretreated at 623 K for 3 h under vacuum (10^{-4} Pa) before measurement. Adsorbed gas volume is measured under standard temperature and pressure (STP) in $\mathrm{cm^3\,g^{-1}}$. The sorption isotherms are shown in Fig. 5.1. Specific surface area S_{BET} (in $\mathrm{m^2\,g^{-1}}$) is estimated from the isotherm with the Brunauer–Emmett–Teller (BET) method (Brunauer et al., 1938). Relative uncertainty of the obtained specific surface area is estimated to be 5%. Specific surface area S_V in $\mathrm{nm^{-1}}$ is obtained by :

$$S_V = 10^{-3} d_g S_{BET}$$

Relative uncertainties for ε and S_V are then respectively 3.6% and 5.6%. More details are shown in table 5.2.

5.3 Transmission Electron Microscopy (TEM)

For TEM imaging, an extrudate has been put in an oven at 353 K overnight and embedded in araldite resin (*EMbed 812*, provided by *Electron Microscopy Sciences*, Hatfield, PA, USA). The included sample has been trimmed to obtain a trapezoidal surface and then cut in thin slices using an ultramicrotome (*Reicherd*). Slices thickness has been targeted to 300 nm. Only slices with homogeneous color (homogeneous thickness) were withdrawn to a lacey carbon grid. Images were taken with a TEM (*JEM-2100F*, provided by *JEOL*, Peabody, MA, USA) operating at 200 kV, in bright field mode, without objective diaphragm, using a CCD camera (*UltraScan*, provided by *Gatan*, Pleasanton, CA, USA). This camera has a four quadrant CCD captor and 2048 by 2048 pixels maximum resolution. Before taking the images, the gain and dark noise of the camera was calibrated respectively in a hole and in absence of electron beam. Images were taken at full resolution (2048 by 2048 pixels), with a 2 s exposure time at an indicated magnification of 15000. This magnification yields a field of view of 1130 by 1130 nm^2 and a pixel size of 0.552 nm.

Twelve images were taken for different slices and different non overlapping zones where neither the edge of the slices, nor cutting artifacts, nor lacey carbon were apparent. Some of them are presented in Fig. (5.2). Local alignments and textured patterns are somehow visible in the images, but information of platelets shapes and platelets organization in the TEM images is hidden (and lost) by the attenuation of the electron beam along the samples's thickness.

Slices at 70 nm thick were prepared at a second round. An objective diaphragm of 120 µm diameter was used. Images were taken at full resolution (2048 by 2048 pixels), with a 2 s exposure time at indicated magnifications of 20000 and 30000. The magnification of 20000 yields a field of view of 1003 by 1003 nm^2 and a pixel size of 0.49 nm. For the magnification of 30000, the field of view is 676 by 676 nm^2 and a pixel size is 0.33 nm. Ten images were taken for each sample, at each magnification, on non overlapping zones. Some of them are shown in Fig. (5.3).

The three alumina samples were crushed into powders at a third round. Images were taken at higher magnification of 100000, with field of view of 205 by 205 nm^2 and a pixel size of 0.10 nm. Five images were taken for each sample, some of which are shown in Fig. (5.4).

5.4 Electron Tomography

For electron tomography, few calcined extrudates were crushed in a mortar and the obtained powder was dispersed in ethanol. A drop of the suspension was put on a holey carbon grid that was dried. Tilt series projections were acquired on the *JEOL JEM-2100F* fitted with the *Gatan Ultrascan* CCD camera, in bright field mode at 200 kV. 143 projections with an indicated magnification of 40000 times (0.21 nm pixel size) were acquired at full camera resolution (2048 by 2048 pixels). The 143 tilt angles ranged between $-71°$ to $+71°$ with a Saxton spacing scheme. No fiducial marker was put on the grid to avoid the artifacts induced in their vicinity. Prior to reconstruction, images were binned twice to obtain a 1024 by 1024 pixels tilt series. The 3D volume was reconstructed with the robust method based on inverse problem approach to align marker-free projections and reconstruct 3D volume (Tran et al., 2014). A 3D view of the tomographic reconstruction is shown in Fig. (5.5).

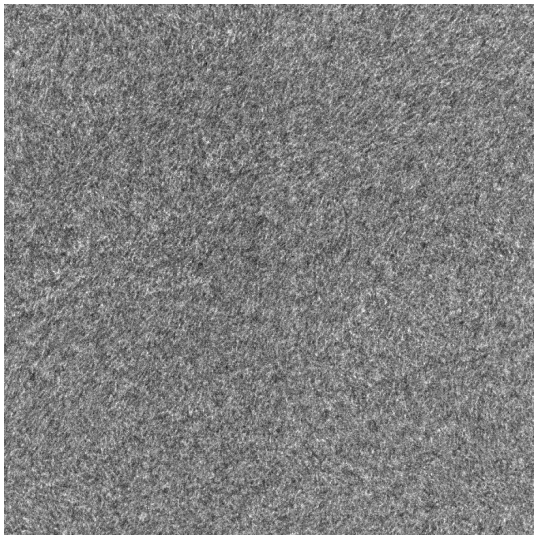

(A) sample 1

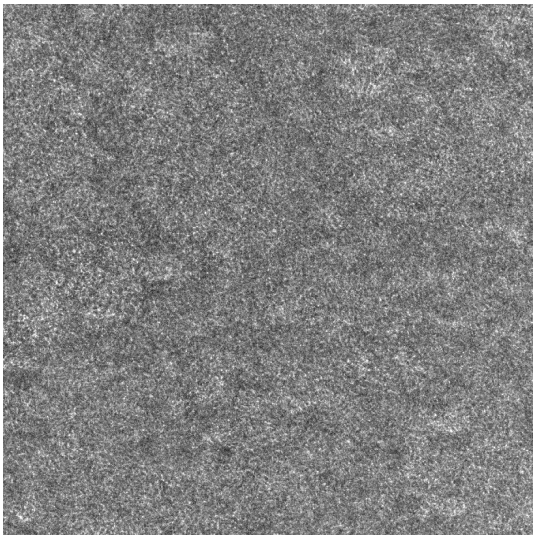

(B) sample 2

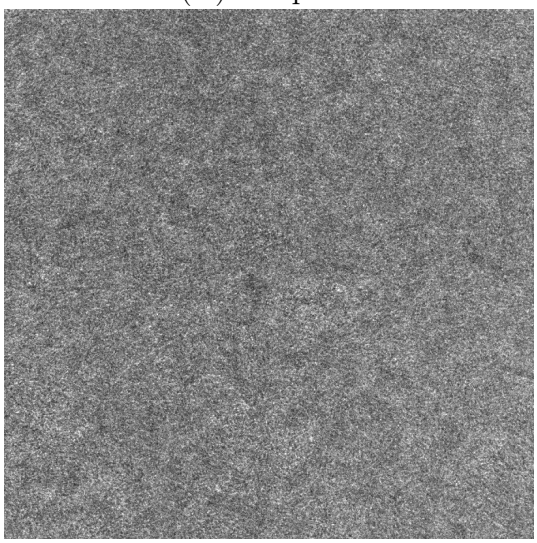

(C) sample 3

Figure 5.2: TEM images of 300 nm thick specimen of mesoporous alumina at magnification of 15000 (1130 nm × 1130 nm).

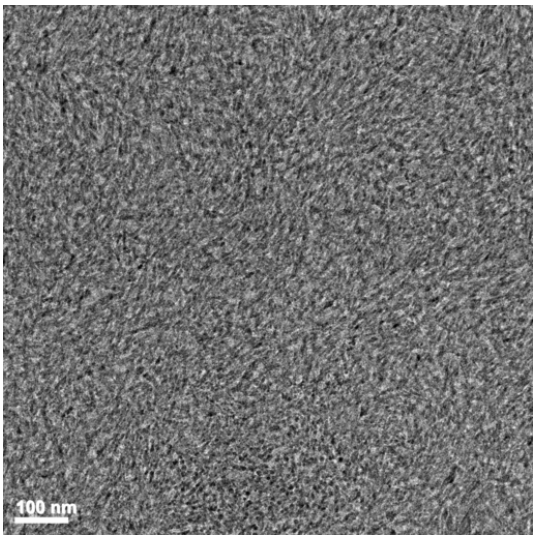

(A) sample 1 at 20K

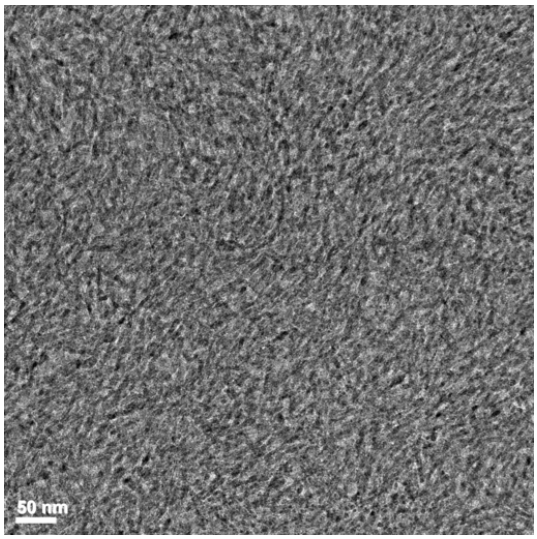

(B) sample 1 at 30K

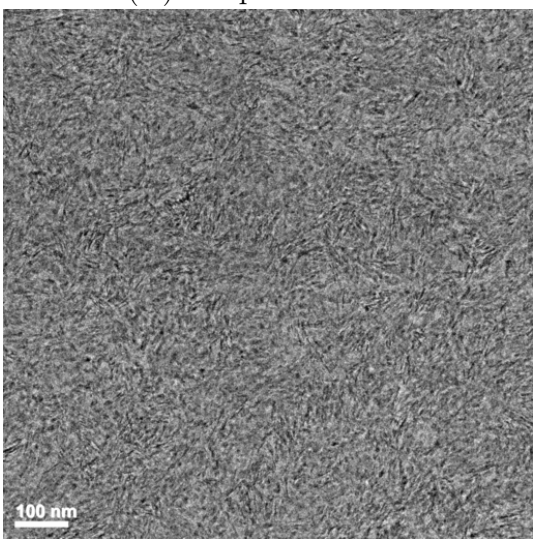

(C) sample 2 at 20K

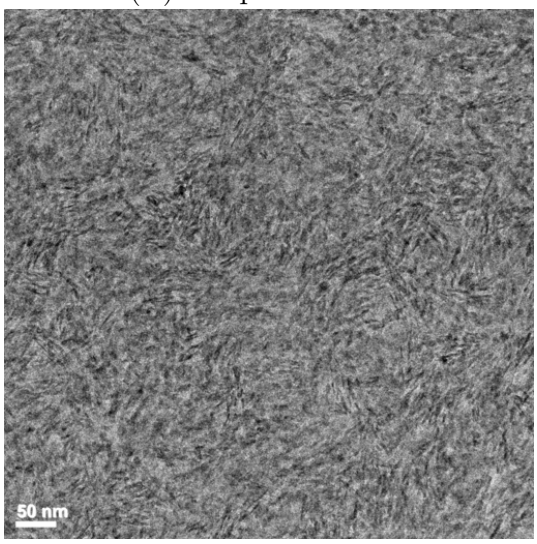

(D) sample 2 at 30K

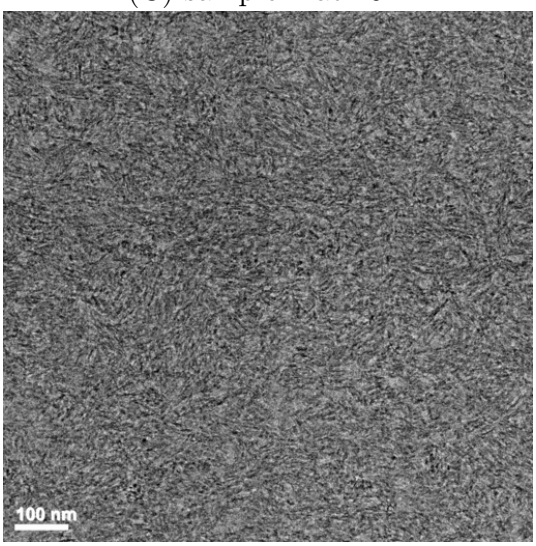

(C) sample 3 at 20K

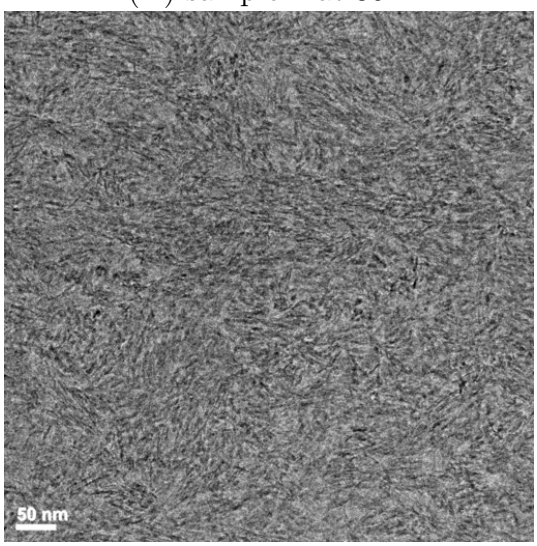

(D) sample 3 at 30K

Figure 5.3: TEM images of 70 nm thick specimen of mesoporous alumina. The field of view for images at 20000 magnification is 1003 nm × 1003 nm, and 676 nm × 676 nm for 30000 magnification.

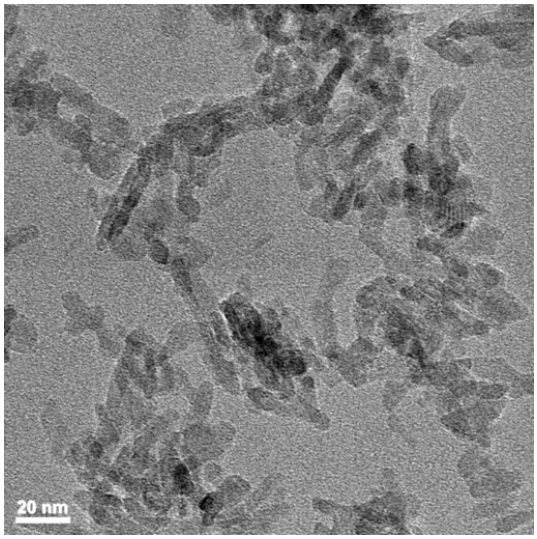

(A) sample 1

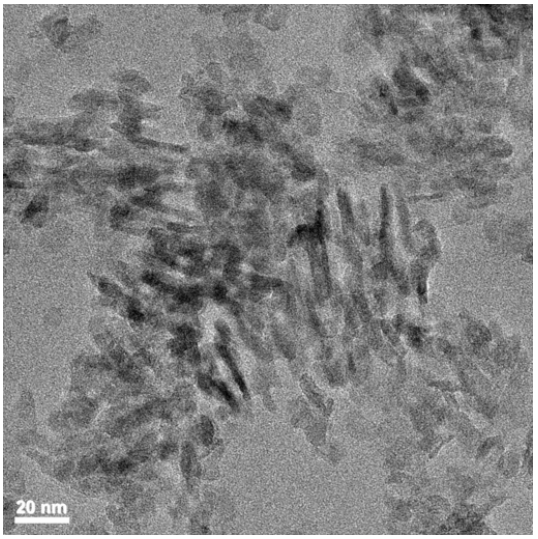

(B) sample 2

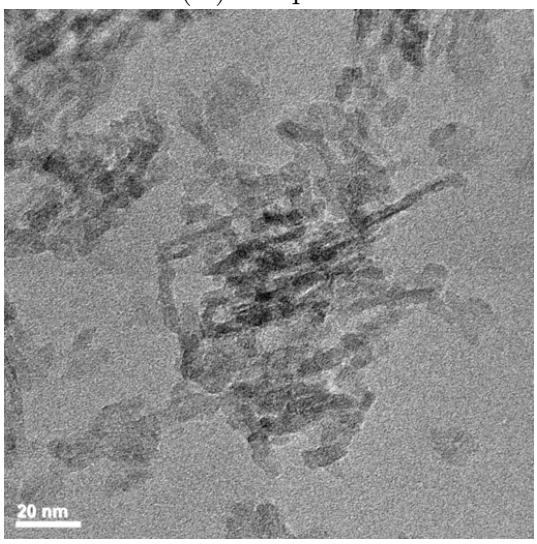

(C) sample 3

Figure 5.4: TEM images of crushed mesoporous alumina (field of view 205 nm × 205 nm).

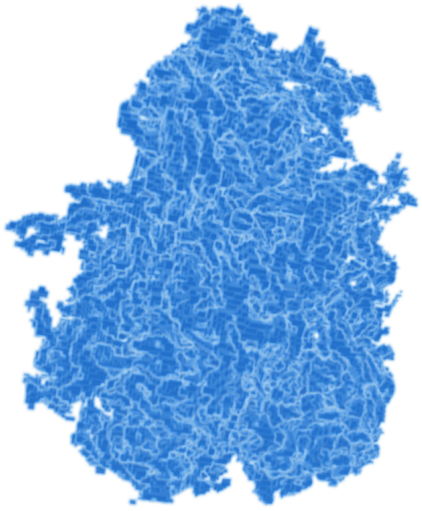

Figure 5.5: 3D view of the tomographic reconstruction of a small portion of mesoporous alumina. The image has a 0.87 nm voxel size, and the image field of view is 328 nm× 290 nm× 257 nm.

Chapter 6

TEM image processing and morphological measurements of 300 nm thick specimen

Slices at 300 nm thick were prepared at the first round. Since the images are noisy and blurry, statistical tools are used to analyze the representativity of the images (Sec. 6.2), and to measure the correlation functions (Sec. 6.3). The image drift and filtering is talked about in Sec. 6.4.

This work was originally realized by Pietrasanta (2013), then was completed and published in Wang et al (2015).

6.1 TEM image model

In TEM, electrons are directed along the thickness of the specimen and smallest dimension, normal to the surface layer. Structure information is carried on transmitted electrons after attenuation. These electrons are then detected and produce an image. The electron direction is hereafter denoted by $\mathbf{e}_3$. We introduce Cartesian axis $\mathbf{e}_1$ and $\mathbf{e}_2$ normal to $\mathbf{e}_3$ and parallel to the surface of the sample. Referring to the coordinates x_1, x_2 and x_3 in the Cartesian basis, 2D TEM images of porous media are modeled by the Lambert-Beer law (Reimer & Kohl, 2008, p.36):

$$Y(x_1, x_2) = a + b \exp\left[-c \int_0^f \mathrm{d}x_3 \, \chi_S(x_1, x_2, x_3)\right], \tag{6.1}$$

where $Y(x_1, x_2)$ is the greylevel TEM image at location (x_1, x_2), $f = 300\,\mathrm{nm}$ is the sample thickness, a and b are constants related to the offset and gain of the camera, c is the inverse scattering length of the solid phase and χ_S is the characteristic function of the solid phase in 3D, i.e. $\chi_S(x, y, z) = 1$ if point (x, y, z) is in the solid (alumina) phase, 0 otherwise.

Monte-Carlo simulations of 200 keV electrons trajectories across alumina embedded in resin selected by a 120 µm objective diaphragm give a value $c = 2.40\ 10^{-3} \pm 2.05\ 10^{-6}\ \mathrm{nm}^{-1}$. Furthermore, the integral is bounded by f and the sample has a high porosity ε, therefore the Eq. (6.1) can be approximated by:

$$Y(x_1, x_2) \approx (a + b) - bc \int_0^f \mathrm{d}x_3 \, \chi_S(x_1, x_2, x_3). \tag{6.2}$$

This approximation is used for the simulation of TEM images from digital 3D microstructures afterwards (Chap. 8).

A typical histogram P_Y of 32-bit TEM image is represented in Fig. (6.1). Most of the values $Y(x_1, x_2)$ lie in-between $y_1 = 405$ and $y_2 = 660$. To visualize the TEM images, we threshold all values larger than y_2 or smaller than y_1, and normalize the result in the range $[0; 255]$. This amounts to replace Y with:

$$\widetilde{Y} = \frac{255}{y_2 - y_1} \left(\max \left\{ \min \left[Y(x_1, x_2), y_2 \right], y_1 \right\} - y_1 \right). \tag{6.3}$$

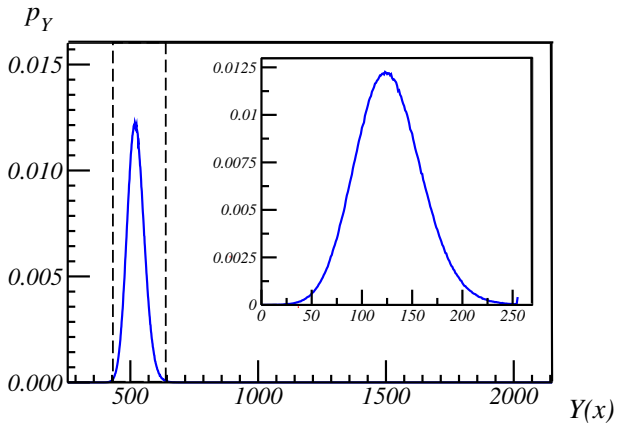

Figure 6.1: Histogram of the raw data in the range $[0; 2140]$. The vertical dotted lines denote y_1 and y_2. Top-right: histogram of $\widetilde{Y}$ (Eq. 6.3) in the range $[0; 255]$.

All TEM images of our samples have similar histogram as in Figure 6.1, which presents only one mode. It is not possible to segment the image using only this information.

6.2 Integral range

We propose to follow the approach of Matheron (1971); Kanit et al. (2003); Jeulin (2011) to estimate the integral range. We define the variance $D^2(S)$ of the means $\langle Y \rangle_S$ of the function Y over a compact subset of area (Lebesgue measure) S by:

$$D^2(S) = E\left\{ \langle Y \rangle_S^2 \right\} - \left(E\left\{ \langle Y \rangle_S \right\} \right)^2, \tag{6.4}$$

with $E\{\cdot\}$ expectation operator (estimated here by averaging). When the area reaches the limit of a single point, we obtain the point variance D_1^2:

$$D_1^2 = \langle Y^2 \rangle - \langle Y \rangle^2. \tag{6.5}$$

The following asymptotic expansion holds (Matheron, 1989; Lantuejoul, 1991):

$$D^2(S) \sim \frac{D_1^2 A_2}{S}, \tag{6.6}$$

where:

$$A_2 = \int_{\mathcal{I}} C(\mathbf{h}) \mathrm{d}\mathbf{h}, \tag{6.7}$$

as long as A_2, the integral range over the support of the image $\mathcal{I}$, is finite. The integral range gives the typical surface area of the microstructure. In practice, use of the correlation function $C(\mathbf{h})$ in (6.7) can hardly be used to estimate A_2, due to fluctuations in the function $C(\mathbf{h})$ when $|\mathbf{h}|$ is large. Instead, the expansion (6.6) is generaly used (Altendorf et al., 2014), provided that numerical data follows the theoretical law (6.6). Hereafter, we need to check if this law is verified. The variances $D^2(S)$ are estimated at increasing values of S. This is done by dividing the TEM image into non-overlapping squares of equal area S, and measuring the variance of the mean over the subdomains (Eq. 6.4). The results are given in Fig. (6.2), in log-log scale for 5 images. An extra point representing $D^2(S)$ for $S = 2048 \times 2048$ pixels is computed using all 12 images. The data follows the scaling law $D^2(S) \sim S^{-0.5}$, with an exponent less than 1, i.e. a much slower decrease than that in (6.6). Similar conclusions hold for the other 11 TEM images of the same sample. This is not consistent with the asymptotic result of Eq. (6.6), which is valid for any ergodic stationary random function with a finite integral range. The slowly-decreasing scaling law of the variance will be explained by a drift in the image, as detailed in Sec. 6.4.

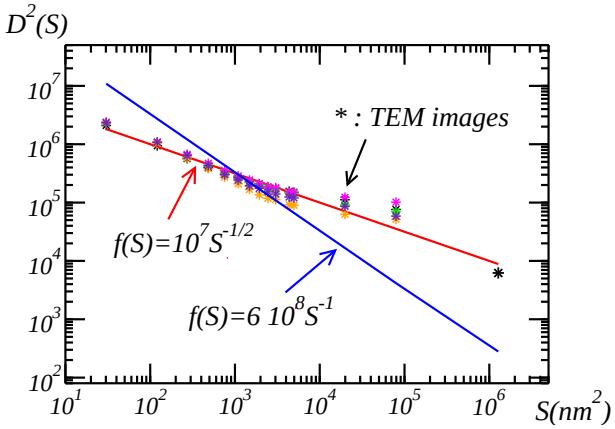

Figure 6.2: Variance $D^2(S)$ of the means over areas of surface S in the image Y, computed using (6.4). Stars of different colors are used to distinguish between the 5 TEM images. Solid lines: numerical fit of the data $D^2(S) \sim S^{-0.5}$ (red), using all 5 samples, and, for comparison, scaling law $D^2(S) \sim 1/S$ (blue) predicted by (6.6).

6.3 Covariance

Referring to a point $\mathbf{x} = (x_1; x_2)$ and a vector $\mathbf{h} = (h_1; h_2)$, the empirical correlation function of Y is the 2D function estimated from the space average denoted by $\langle . \rangle$:

$$C(\mathbf{h}) = \frac{\langle Y(\mathbf{x}+\mathbf{h})Y(\mathbf{x})\rangle - \langle Y(\mathbf{x}+\mathbf{h})\rangle\langle Y(\mathbf{x})\rangle}{\langle Y^2(\mathbf{x})\rangle - \langle Y(\mathbf{x})\rangle^2}, \tag{6.8}$$

so that $C(\mathbf{0}) = 1$ and $C(\infty) = 0$ for a stationary field. Note that the correlation function does not depend on the values of a, b and c in (6.1) and that $C(\mathbf{h})$ in general depends on the norm and orientation of $\mathbf{h}$.

The function $C(h)$ in (6.8) is computed using Fourier transforms (Koch et al., 2003), which comes to periodize the image. The profiles $C(h\mathbf{e}_{1,2})$ along $\mathbf{e}_1$ and $\mathbf{e}_2$,

for $h > 0$, are presented in Fig. (6.3) for two arbitrary TEM images. For the first image, the two profiles are sensibly different, underlying image anisotropy. The anisotropy is more apparent on the 2D representation of $C(h_1, h_2)$ at long distance $h \gg 1$ (Fig. 6.4). The anisotropy generally appears in most of the TEM images of the three samples. The effect is stronger in some images like Fig. 6.3 (a), while less strong in some others like Fig. 6.3 (b). The anisotropy is introduced by the detector drift, which is further discussed in Sec. 6.4.

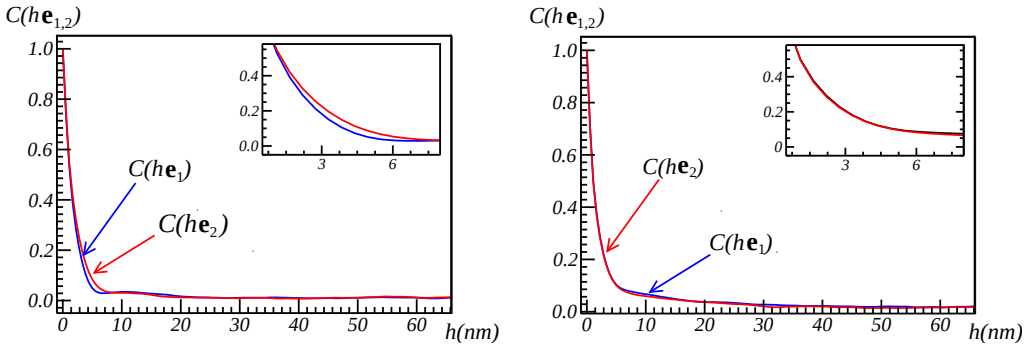

Figure 6.3: Correlation function profiles along the horizontal and vertical axis, for two TEM images (a and b).

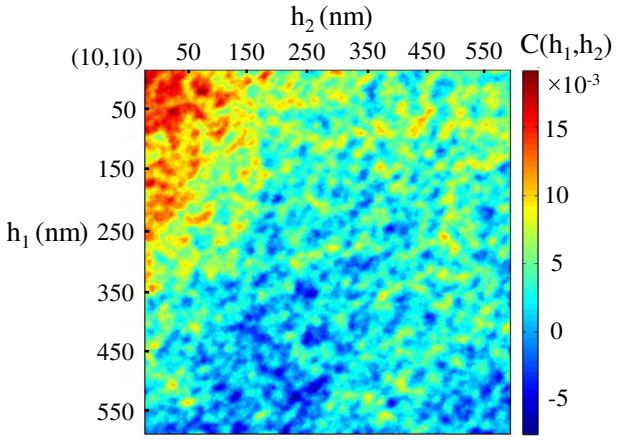

Figure 6.4: 2D correlation function $C(h_1, h_2)$ of a TEM image of sample 1. The function is cropped with top-left corner's coordinate at (10 nm, 10 nm). Highest values are in red and lowest values in blue.

6.4 Drift filtering

To visualize variations in the images over large scales, we divide it into a set of non-overlapping square subdomains of size 140 nm × 140 nm. The means over each square are represented in Fig. (6.5), for two arbitrary images. A drift appears on the two images, roughly oriented along the diagonal from the top-left to the bottom-right. This non-uniform averaged field can be interpreted as the result of a non-uniform detection on the camera or a non-constant thickness of the slices. Indeed, the four quadrants of the camera can be guessed from Fig. (6.5). This

indicates that the correction of the gain of the camera performed before recording the images is not accurate enough to correct for the camera detection discrepancies. This is confirmed by the display of moving averages on more images of the sample, as shown in Fig. (6.6).

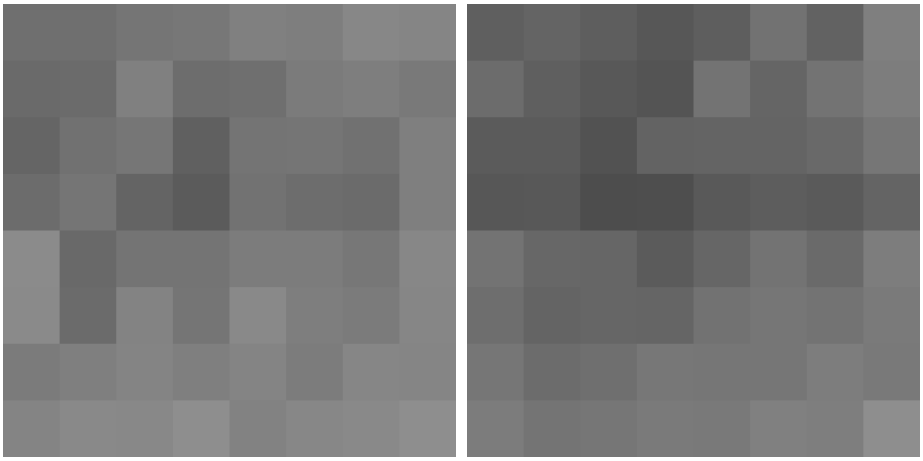

Figure 6.5: Local means computed over a set of non-overlapping square subdomains in two TEM images.

To remove the drift, a moving average is subtracted to each image, computed as the mean of a disk of radius ℓ centered on each pixel. Accordingly Y is replaced by

$$Y'(\mathbf{x}) = Y(\mathbf{x}) - \frac{1}{\pi \ell^2} \int_{|\mathbf{x}-\mathbf{x}'|<\ell} \mathrm{d}\,\mathbf{x}'\, Y(\mathbf{x}'), \tag{6.9}$$

where $\mathbf{x} = (x_1, x_2)$ is a point in the image. The value of ℓ is now chosen so that the integral range A_2' of the convoluted field becomes finite. Equivalently, ℓ is chosen so that the variance $D^2_{Y'}(S)$ of the means over subdomains of size S decreases with a scaling law $\sim 1/S$, as in Eq. (6.6). The variance is computed on the corrected image Y', rather than on the moving average itself. We find numerically that $D^2_{Y'}(S) \sim 1/S^\alpha$ with $\alpha < 1$ (resp. $\alpha > 1$) when $\ell < 110$ nm (resp. $\ell > 110$ nm) and $D^2_{Y'}(S) \sim 1/S$ when $\ell \approx 110$ nm (Fig. 6.7). Accordingly we set $\ell = 110$ nm and replace Y with Y' in the following of this study. The moving average is represented in Fig. (6.6).

After removing the drift, the anisotropy observed in the correlation function becomes weak and negligible. In the following of the thesis, it is approximated by an isotropic correlation function, denoted by $C_{TEM}(h)$, averaging over all directions and over the 12 TEM images. Additionally the integral range of the 12 images is estimated, giving $A_2' \approx 30\,\mathrm{nm}^2$.

6.5 Conclusion

In this chapter, TEM images of 300 nm thick specimens were processed and measured. The covariance of the images were estimated. The systematic drifts appearing in most of the images were identified and removed by moving average. After the filtering, the image representativity is confirmed by the integral range.

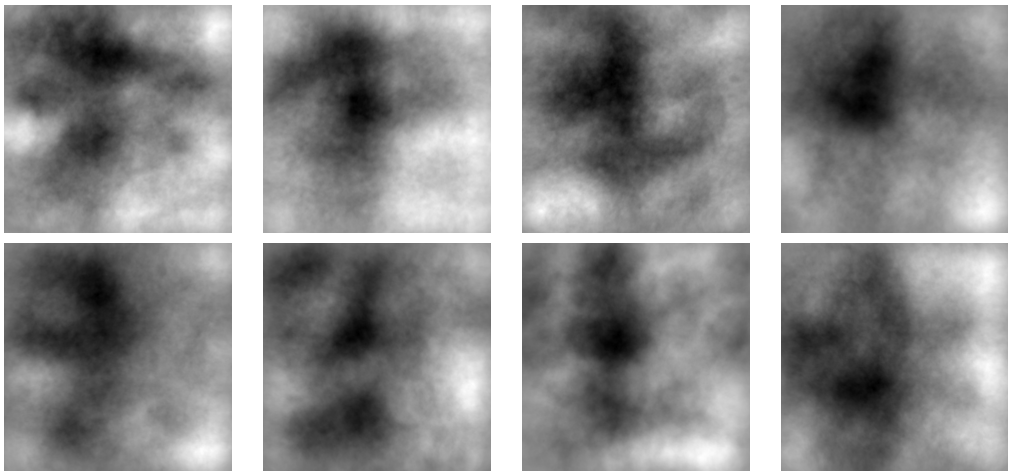

Figure 6.6: Moving average of 8 TEM images of the sample, using Eq. (6.9) with disk radius 110 nm

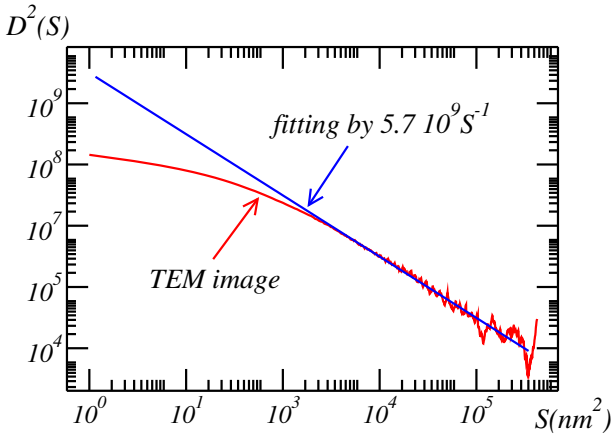

Figure 6.7: Variance $D^2_{Y'}(S)$ of the means of image Y' over subdomains of area S, with respect to S (red). Blue: numerical fit $D^2_{Y'}(S) \sim 1/S$ for large areas $S \gg A'_2$.

Chapter 7

TEM image processing and morphological measurements of 70 nm thick specimen

Slices at 70 nm thick were prepared at a second round. Compared to 300 nm thick specimens, the fluctuation caused by platelet overlapping decreases. Images were taken at higher magnifications, with better resolution. Some platelets in the TEM images of crushed material have clear edges. In this chapter, information of better precision on the noise, correlation function, platelet size and platelet alignments is extracted from the TEM images.

7.1 TEM images of vacuum

TEM images of vacuum are taken at the same condition as the 70 nm thick specimen. Three images at each magnification 20000 and 30000 have been taken.

7.1.1 Histogram

The histograms P_V of the 32-bit TEM images are shown in Fig. 7.1. Their greyscale means and standard deviations are represented in Tab. 7.1. Shifts between the three histograms at the same magnification are observed in Fig. 7.1. The shifts are sometimes higher than the standard deviation, indicating time-variant gain drift and offset drift of the electron detectors or changes in beam illumination.

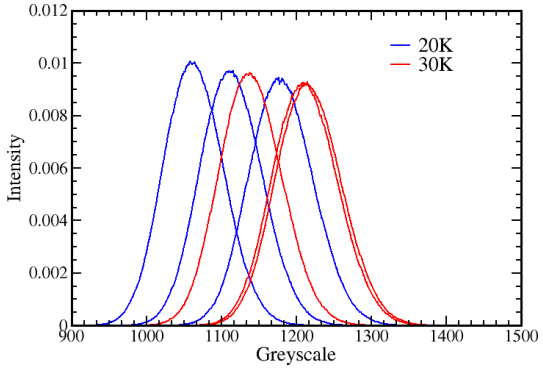

Figure 7.1: Histograms of TEM images of vacuum. Their greyscale means and standard deviations are listed in Tab. 7.1.

	20K			30K		
	N°.1	N°.2	N°.3	N°.4	N°.5	N°.6
Mean	1181	1064	1114	1218	1212	1140
Standard deviation	42	40	41	43	43	41

Table 7.1: Greyscale mean and standard deviation of the TEM images of vacuum. Their histograms are shown in Fig. 7.1.

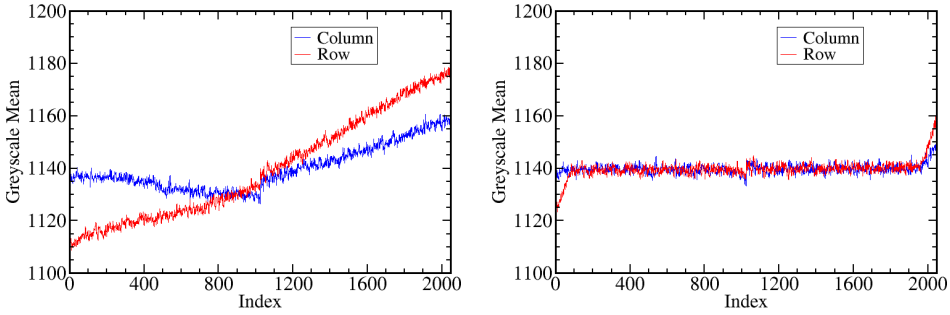

(A) (B)

Figure 7.2: Greyscale mean along the columns (red) and along the rows (blue) of (A) TEM image of vacuum. (B) TEM image of vacuum filtered by moving average (Eq. 6.9) with disk radius 33 nm.

7.1.2 Drift filtering

Four quadrants can be slightly observed in TEM images of vaccum (Fig. 7.3 A). It is consistent with the four-quadrant structure of the electron detector. The greyscale means are then estimated along the columns and rows, shown in Fig. 7.2. It indicates that the drift exists not only between the four quadrants, but also between regions in the same quadrant.

The moving average (Eq. 6.9) is used to remove the drift. In practice, a convolution is used to calculate the average. The drifts are shown in Fig. 7.2 (B) and Fig. 7.3 (B). The filtered image is cropped to remove the boundary effect brought in by the convolution.

(A) (B) (C)

Figure 7.3: (A) TEM image of vacuum. (B) Moving average using Eq. 6.9 with disk radius 33 nm. (C) Filtered image Y'.

7.1.3 Correlation

The correlations of the filtered TEM images of vacuum are estimated with the same equation as Eq. 6.8:

$$C(\mathbf{h}) = \frac{\langle Y(\mathbf{x}+\mathbf{h})Y(\mathbf{x})\rangle - \langle Y(\mathbf{x}+\mathbf{h})\rangle\langle Y(\mathbf{x})\rangle}{\langle Y^2(\mathbf{x})\rangle - \langle Y(\mathbf{x})\rangle^2}, \tag{7.1}$$

The average correlation is shown in Fig. 7.4. The correlation range with $0 < \mathbf{h} < 2$ nm indicates that it is not a pure Poisson noise. The profiles along the two directions are exactly the same, indicating isotropy.

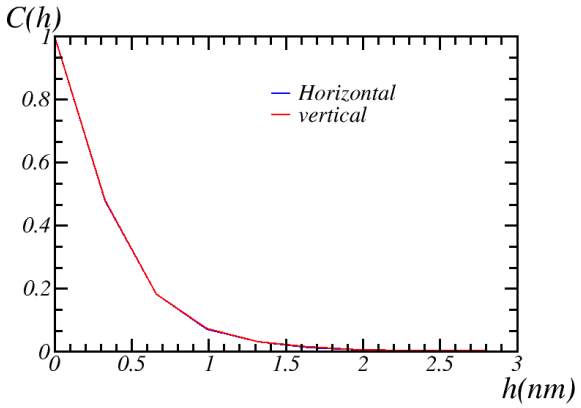

Figure 7.4: Average correlation function $C(\mathbf{h})$ of the filtered TEM image of vacuum.

7.2 TEM images of carbon membrane

TEM images of carbon membrane are taken at the same condition as the 70 nm thick specimen. Three images at each magnification 20000 and 30000 have been taken.

7.2.1 Histogram

The histograms P_C of the 32-bit TEM images are shown in Fig. 7.5, with greyscale means and standard deviations represented in Tab. 7.2. The greyscale means are lower than the image of vacuum, consistent with the electron attenuation by carbon membrane.

	20K			30K		
image N°.	1	2	3	4	5	6
Mean	1046	997	1076	1049	1136	1088
Standard deviation	40	39	41	43	46	45

Table 7.2: Greyscale mean and standard deviation of the TEM images of carbon membrane. Their histograms are shown in Fig. 7.5.

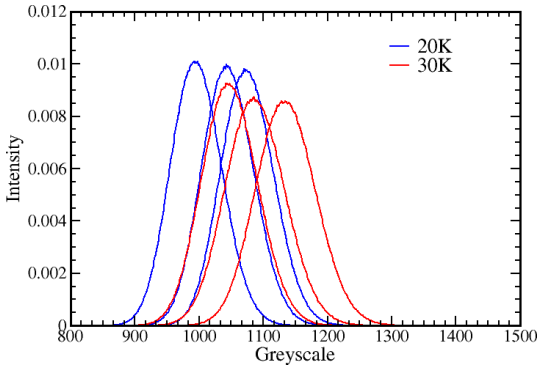

Figure 7.5: Histograms of TEM images of carbon membrane. Their greyscale means and standard deviations are listed in Tab. 7.2.

7.2.2 Drift filtering

Drifts can also be observed in the TEM images of carbon membrane. The drifts are removed using moving average (Eq. 6.9) with disk radius 110 nm. A filtered TEM image of carbon membrane is shown in Fig. 7.6 (A). A TEM image of alumina (Fig. 7.6 B) is compared with the filtered image carbon membrane. We can notice that the images have similar textures.

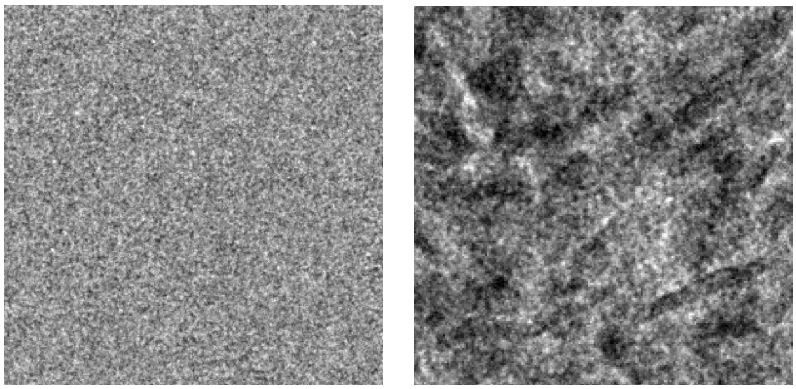

(A) (B)

Figure 7.6: Comparison between the textures of (A) filtered TEM image of carbon membrane and (B) TEM image of alumina sample 2. The image size is 100×100 nm^2.

7.2.3 Correlation

The correlations of the filtered TEM images of carbon membrane are estimated with Eq. 6.8. The average correlation is shown in Fig. 7.7. The correlation range is $0 < \mathbf{h} < 2.5$ nm, with a slight rise in $1.4 < \mathbf{h} < 2.3$ nm. Compared to the correlation of vacuum (in Fig. 7.4), the slight rise is caused by carbon membrane microstructure. Isotropy can be observed regarding the similaity of profiles obtained for differents orientations.

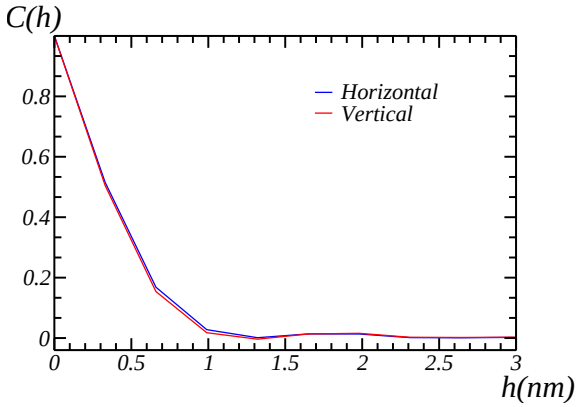

Figure 7.7: Correlation function $C(\mathbf{h})$ of the filtered TEM image of carbon membrane.

7.3 TEM images of 70 nm samples

7.3.1 Histogram

A histogram P_Y of a 32-bit TEM image is shown in Fig. 7.8. The average greyscale means and the average standard deviations over the images are shown in Tab. 7.3. No significant difference between the three samples on the histogram can be observed. The greyscale means at magnification 20K are generally lower than those at 30K. Furthermore, the means are both lower than the images of carbon membrane, which is consistent with the electron attenuation model.

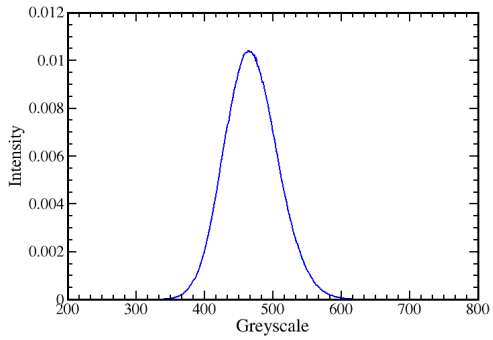

Figure 7.8: Histogram of a TEM image of alumina sample 1. Its greyscale mean is 469, with standard deviation 39.

	20K			30K		
Sample	1	2	3	1	2	3
average mean	428	408	392	435	456	439
average standard deviation	37	35	39	38	36	39

Table 7.3: Average greyscale mean and average standard deviation over the ten TEM images of 70 nm thick specimens for each sample at each magnification.

7.3.2 Drift and integral range

Drifts are observed slightly in the TEM images of mesoporous alumina (Fig. 7.9 A). Observing the integral range curve (Fig. 7.10 A), the existence of large-scale drift is confirmed. The drift is removed using a moving average (Eq. 6.9) with disk radius 110 nm. The filtered TEM image is shown in Fig. 7.9 (B).

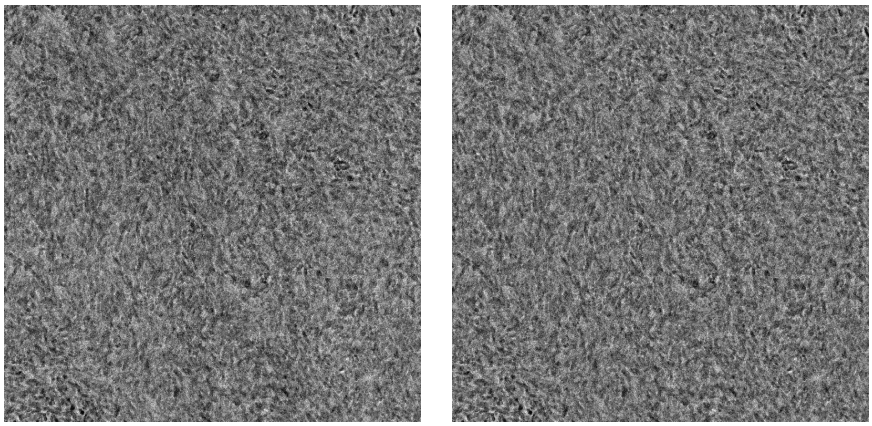

(A) (B)

Figure 7.9: A TEM image of 70 nm mesoporous alumina sample 1. (A) Original image (B) Filtered image.

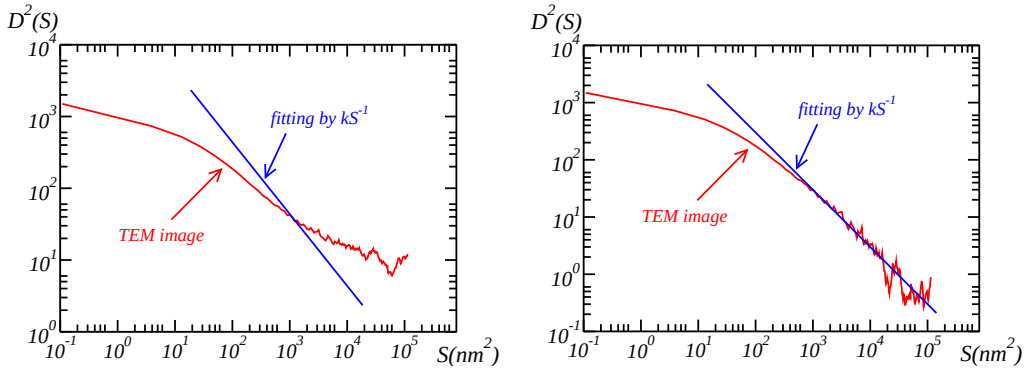

(A) (B)

Figure 7.10: Integral range of a TEM image of mesoporous alumina sample 1. (A) Original image (B) Filtered image.

7.3.3 Correlation

The correlations of the filtered TEM images of the 70 nm thick specimen of mesoporous alumina are estimated with Eq. 6.8, and shown in Fig. 7.11. The correlation range is $0 < \mathbf{h} < 10$ nm. The two profiles of the correlation function in Fig. 7.11 (A) are close, indicating the isotropy of the microstructure of γ-alumina. The correlation functions are then averaged over the images of sample 1, respectively at magnification 20K and 30K.

The images with magnification 20K have slightly higher correlation in the range $0 < \mathbf{h} < 6$ nm (Fig. 7.11 B). This is consistent with the pixel-wise noise brought

in by the electron detector. The slope at the origin of the correlation function corresponds to the pixel size. The pixel-wise noise has stronger effects on images of high magnification.

We calculate the average correlation over all the TEM images at magnification 30K for each alumina sample. The comparison is shown in Fig. 7.11 (C). The slopes at the origin of the correlation function are the same. The sample 1 has higher correlation than the other two at the range $0.8 < \mathbf{h} < 4.8$ nm, but lower than sample 2 at the range $4.8 < \mathbf{h} < 8$ nm. The sample 2 has higher correlation than sample 3 at the range $1 < \mathbf{h} < 10$ nm. Despite these difference, the three samples are quite close in terms of correlation function. In this work, the average correlation of sample 1 at magnification 30K is used as the experimental reference.

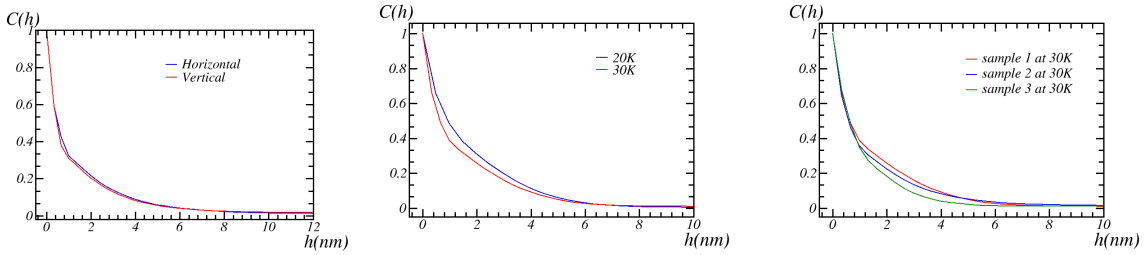

(A) (B) (C)

Figure 7.11: Correlation functions of TEM images of mesoporous alumina. (A) Profiles of the correlation of a TEM image of sample 1 at magnification 30K. (B) Average correlation function over the TEM images of sample 1. (C) Average correlation functions of the three samples.

7.4 TEM images of mesoporous alumina powders

TEM images of alumina powders allow us to distinguish and to segment some of the platelets. We fit ellipses manually over distinguishable platelets for each sample (Fig. 7.12). The platelets with less overlapping and clear contours are selected and encircled in red. The length and width of the ellipses are then measured. Statistics are shown in Tab. 7.4, providing a rough estimation of the platelet size.

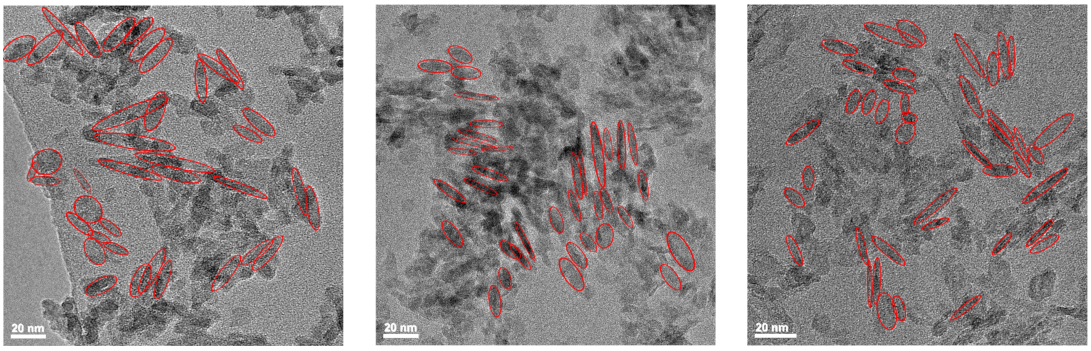

(A) sample 1 (B) sample 2 (C) sample 3

Figure 7.12: TEM images of crushed mesoporous alumina. Measured platelets are encircled in red.

	sample 1		sample 2		sample 3	
dimension (nm)	length	width	length	width	length	width
mean	24.0	6.8	18.8	4.7	20.3	5.3
standard deviation	8.6	2.5	5.2	2.0	6.2	1.9

Table 7.4: Estimated length and width of the 2D projections of platelets of the three samples of mesoporous alumina. The estimation is based on the manually measured platelets in the TEM images of crushed material.

It needs to be mentioned that the estimation is biased, for the following reasons.

- First, some of the platelets may be broken during material crushing, even if the damage process is much less favorable than breaking of contact zone between platelets. This leads to an underestimation of platelet size.
- Second, the platelets observed in TEM images are 2D projections, which leads to the underestimation of their length and overestimation of their width.
- Third, the platelets are overlapped one upon another, which makes the segmentation difficult. The big, elongated and sideways monocrystals have more chance to be distinguished. It leads to overestimation of platelet length.

7.5 Local alignments

Local alignments and platelet aggregation have been observed in the images of crushed material (Fig. 5.4) and the images of 70 nm thick specimen (Fig. 5.3). In order to study the orientation distribution, we segment the aligned platelets and measure their orientations.

We use one of the TEM images of sample 2 at magnification 30K. For better visualization, the image is normalized between $[0; 255]$ and reversed with platelets in bright, denoted $Y(x_1, x_2)$. A median filter of size 1×1 nm^2 is used to remove Poisson noise. A Gaussian filter with $\sigma = 1$ nm is used to smooth the fluctuations caused by the carbon membrane. The filtered image denoted Y_f is shown in Fig. 7.13 (A).

The aligned elongated platelets are in bright, together with small fluctuations also in bright. To remove the fluctuations, opening by reconstruction is used. First, a threshold is applied to extract the bright regions:

$$M_1 = \begin{cases} 255 & Y_f > 150 \\ 0 & Y_f < 150 \end{cases} \tag{7.2}$$

A binary image, denoted M_1, is obtained (Fig. 7.14 A). M_1 is then eroded with square struturing element of size 5×5 pixel (1.65×1.65 nm^2):

$$M_1' = \epsilon^5 (M_1) \tag{7.3}$$

Only large bright regions are left in M_1'. The greyscale image is then reconstructed with M_1' as markers:

$$Y_1 = R_{Y_f}(M_1') \tag{7.4}$$

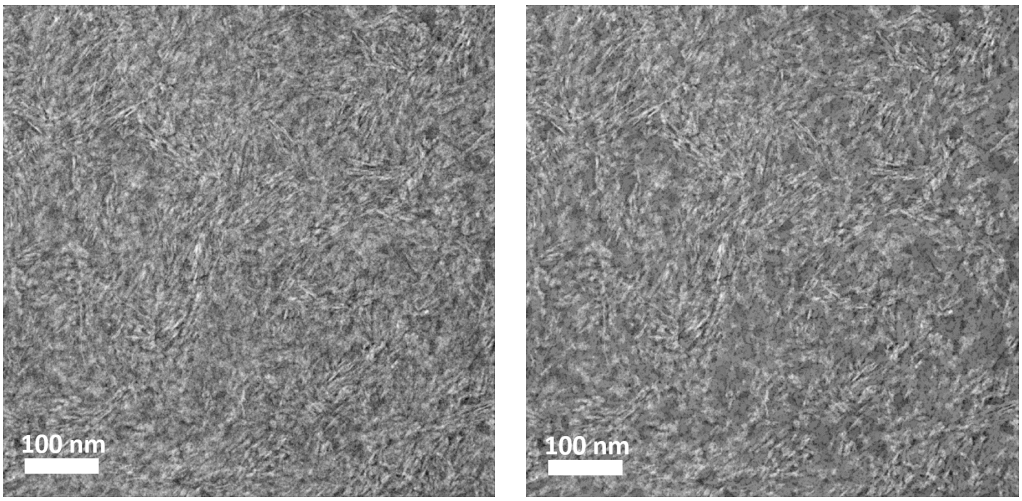

(A) (B)

Figure 7.13: A TEM image of the 70 nm thick specimen of sample 2. (A) Filtered by a median filter and a Gaussian filter. (B) Reconstructed TEM image with eroded markers.

The reconstructed greyscale image is shown in Fig. 7.13 (B). In Y_1, only big bright regions are reconstructed, but some of these regions do not have elongated structure.

To obtain only the elongated structures in the image, a second opening by reconstruction is performed. The binary image, denoted M_2 is obtained by applying a threshold of 150 on Y_1 (Fig. 7.14 B). M_2 is opened with segments of size 15 nm with various orientations θ from $-90°$ to $90°$ with step $1°$. The union of the opened images, denoted M_2' is shown in Fig. 7.14 (C).

$$M_2' = \bigcup_{\theta} \varphi^{\theta}(M_2) \tag{7.5}$$

The greyscale image is reconstructed with M_2' as markers, shown in Fig. 7.15.

$$Y_2 = R_{Y_1}(M_2') \tag{7.6}$$

In Y_2, only the elongated bright regions are kept.

To determine the orientation of the platelets, another binary image, denoted M_3 is obtained by applying a threshold of 150 on Y_2. The connected components in the binary image M_3 are labeled. For each connected component, the orientation is determined by the eigenvector corresponding to the largest eigenvalue of the covariance matrix (Jeulin & Moreaud, 2008). We associate the orientation degree of each connected component to the binary image M_3, and obtain the orientation map (Fig. 7.16). The orientation distribution based on surface fraction is represented in Fig. 7.17.

To summarize, we observe some zones with local alignment of the platelets at a small scale (about 30 nm), but a global random orientation at larger scale.

7.6 Conclusion

In this chapter, TEM images of vacuum, carbon membrane, 70 nm thick specimens and crushed alumina were processed and measured. First, the drift brought in by

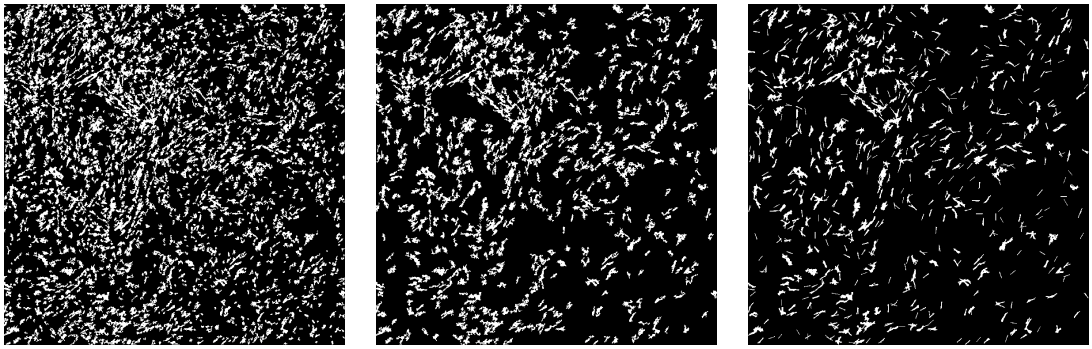

(A) (B) (C)

Figure 7.14: Reconstruction markers. (A) Marker thresholded from Y_f. (B) Marker thresholded from Fig. 7.13 (B). (C) Marker opened with segments as structuring element.

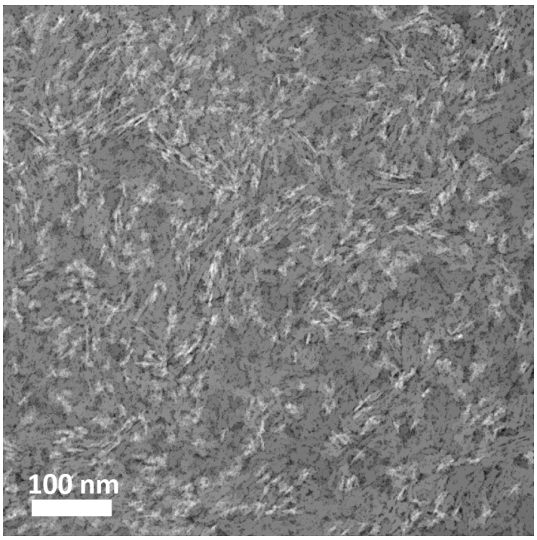

Figure 7.15: Reconstructed TEM image of alumina with elongated platelets highlighted.

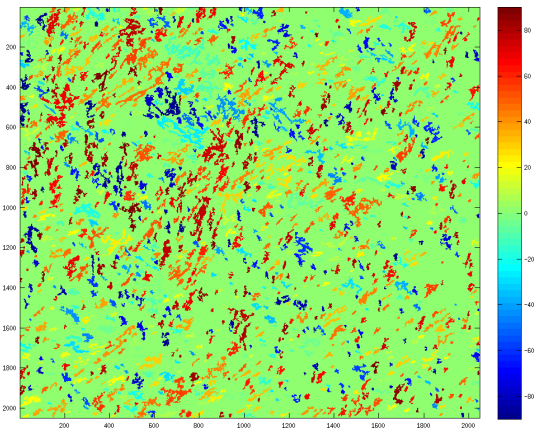

Figure 7.16: A TEM image of mesoporous alumina with elongated platelets segmented. Platelets are highlighted in color presenting orientation from -90 deg to 90 deg.

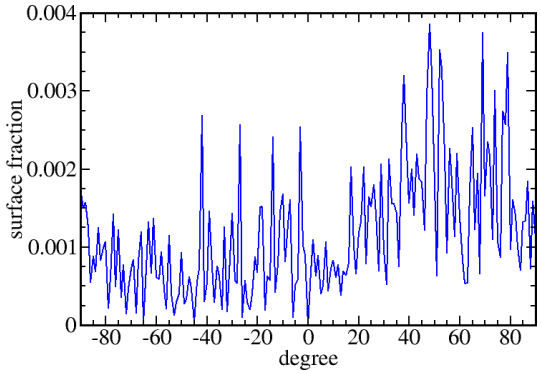

Figure 7.17: Orientation distribution of Fig. 7.16.

the electron detectors was confirmed with the TEM images of vacuum and carbon membrane. The high-frequency noise was characterized in terms of histogram and correlation. Second, the correlation functions of TEM images of 70 nm thick slices were estimated for each sample with each magnification. The difference between correlation functions of 20000 magnification and 30000 magnification supports the speculate of pixel-wise noise. Then, visible platelets in the TEM images of crushed alumina were measured manually. It provides a rough estimation of the platelet size. Finally, we filtered a TEM image of a 70 nm thick specimen and extract the elongated objects with opening by reconstruction. The orientation distribution of the extracted platelets were measured.

Part IV

Morphological Modeling of the 3D Microstructure of Mesoporous γ-Alumina from the 2D Images

Chapter 8

Random model of platelets

Through the physical characterizations, the porosity and the specific surface area of the microstructure of mesoporous alumina are obtained from He pycnometer and nitrogen porosimetry. From the TEM image processing and the morphological measurement, the correlation and the size of primary grains are estimated. Based on the known information, mesoporous alumina is a material consisting of monocrystals.

In this chapter, random models of platelets are proposed to model the 3D microstructure. A one-scale model is first talked about in Sec. 8.1. The aggregation phenomenon is then taken into account, with a two-scale model proposed in Sec. 8.2. The model is compared with the tomographic reconstruction in terms of specific surface area in Sec. 8.3. In Sec. 8.4, the TEM image model is re-considered with noise taken into account. The random model of platelets is re-identified with the new TEM image model in Sec. 8.5.

The work in Sec. 8.1 and Sec. 8.2 was originally realized by Pietrasanta (2013). It was then completed and published in Wang et al (2015).

8.1 One-scale Boolean model of platelets

8.1.1 Modeling

Mesoporous γ-alumina is a material which consists of primary grains, or monocrystals. The monocrystals are observed in dark shadows in the TEM images, but their accurate shape and size in 3D at the nanometric scale remains unknown. A similar material – boemite (Chiche et al., 2008), consisting of prisms with irregular octagonal basis is considered (Fig. 8.1). The basis is made up of three sides with lengths D_1, D_2 and D_3. The angles, equal to $127.8°$ and $270 - 127.8 = 142.2°$, are fixed by crystallography. With the prism's height D_4, the platelets shape is parametrized by $(D_i)_{1\leq i\leq 4}$. X-ray diffraction data for the oxide nanoparticles (Chiche et al., 2008) indicate $D_1 = 3.4\,\text{nm}$, $D_2 = 1.4\,\text{nm}$, $D_3 = 0.4\,\text{nm}$ and $D_4 = 3.7\,\text{nm}$ (Fig. 8.1). These values do not necessarily correspond to the material we consider, so that we let $(D_i)_{1\leq i\leq 4}$ vary.

Nevertheless, for consistency with XRD measurements, we fix the ratios $D_2/D_1 = 0.41$ and $D_3/D_1 = 0.12$, as obtained in (Chiche et al., 2008). With these constraints, the prism shape is fully parametrized by the two variables D_1 and D_4. Hereafter, we call the primary grain in prism shape "platelet". The work of Chiche (Chiche et al.,

2008) indicates that materials synthesized in solvent of different pH values have different particle morphologies, in other words, varying shape of octagonal basis and varying width. For the sample we use in this work, the pH value is already known.

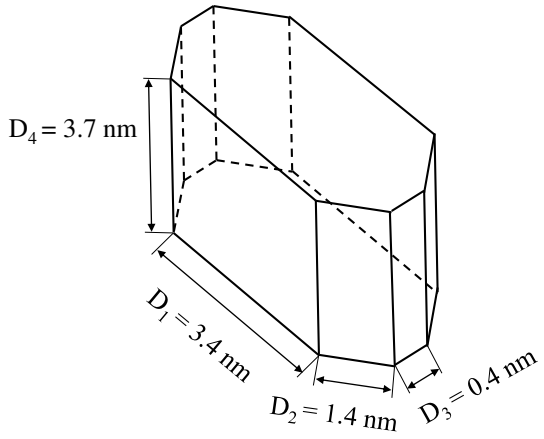

Figure 8.1: Alumina platelet shape, following (Chiche et al., 2008).

To model the microstructure, we first consider a Boolean model of randomly-oriented platelets. We take first the octagonal prism presented in Fig. 8.1 as the shape of platelets. Microstructures are generated in two steps (Matheron, 1967; Jeulin, 2000):

- First, a realization of a Poisson random point process is generated with a prescribed point density, determined by the microstructure overall porosity, and the volume of the platelet.
- Second, an octagonal prism is translated at each Poisson point. The prism main axis orientation is uniform on the sphere.

This model should be considered as a one-scale model in the sense that it is based on a *homogeneous* Poisson point process. The Boolean model depends on the shape of the prisms and on the porosity. The latter pore volume fraction is set to 69%, according to porosimetry data.

Realizations of the model are generated in a window consisting of $400 \times 400 \times 546$ voxels with resolution 0.55 nm per voxel. The upper surface of the microstructure $(\mathbf{e}_1; \mathbf{e}_2)$ is discretized on a 400×400 voxels grid, and the thickness along $\mathbf{e}_3$ by 546 voxels. The microstructures have the same thickness as the specimen material (300 nm). A 2D section of the 3D model is shown in Fig. (8.2). Transmission images in 2D are readily computed by performing an integral along the vertical axis ($\mathbf{e}_3$) on the generated microstructure (the same equation as Eq. 6.2):

$$Y(x_1, x_2) \approx (a + b) - bc \int_0^f \mathrm{d}x_3 \, \chi_S(x_1, x_2, x_3). \tag{8.1}$$

From the simulated transmission images, we obtain the corresponding 2D correlation function $C_M(\mathbf{h})$, who is confirmed to be isotropic. Since the correlation is normalized, the choice of the parameters a, b and c does not influence the estimation of correlation function. The 1-D profile of $C_M(\mathbf{h})$ is hereafter denoted by $C_M(h)$. A comparison with the correlation functions of the TEM images $C_{TEM}(h)$ is represented in Fig. (8.3).

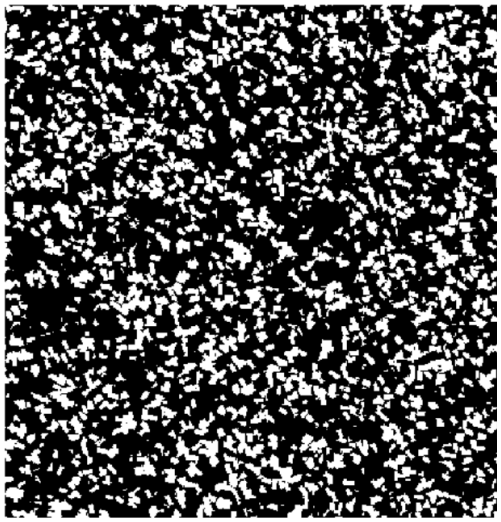

Figure 8.2: 2D section of a Boolean model of octagonal prisms. Solid phase in white.

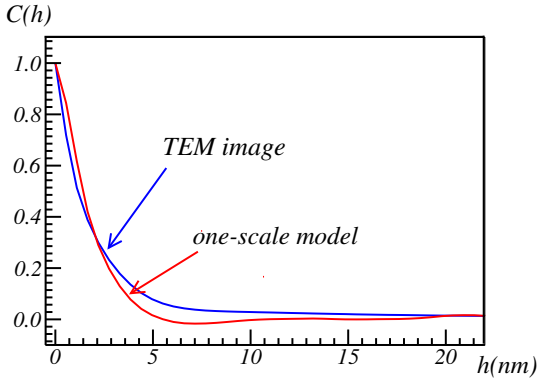

Figure 8.3: correlation of TEM images and of a computer-generated one-scale Boolean model.

8.1.2 Parameter identification

The parameters of the one-scale Boolean model are estimated by minimizing some distance between the correlation functions measured on TEM and on simulated images:

$$\inf_{M} \left\{ \sum_{h=0}^{N} w_h \left[C_{TEM}(h) - C_M(h) \right]^2 \right\}, \tag{8.2}$$

where h is given in pixels units, w_h are weights given by:

$$w_h = \frac{a_h}{\sum_{i=0}^{N} a_i}, \quad a_h = \frac{1}{1 + 0.2h}, \tag{8.3}$$

and $N = 29$ defines a (finite) domain of comparison of the two correlation functions. The decreasing weights with h are used to give more importance to the correlation function for small values of h, which is more reliable than when h is large.

Previous findings (Chiche et al., 2008) indicate that the basis of the primary grain is octagonal. Under this assumption, the length D_1 and width D_4 of the octagonal grains vary independently, while the shape of the basis is fixed. Accordingly, the prism is parametrized by two variables. To examine the effects of both parameters on the correlation function, we fix one and let the other vary (Fig. 8.4). The slope at the origin ($h = 0$) of the correlation is driven by the platelet's shape: the thicker the platelet is (D_4 increases), the smaller the slope of correlation will be. For an isotropic random set, it is related to the specific surface area S_V (Matheron, 1967):

$$\left| \frac{\mathrm{d}\, C_M(h)}{\mathrm{d}\, h} \right|_{h=0} = \frac{1}{4} S_V, \tag{8.4}$$

For a Boolean model with primary grain A', $S_V = -q \log(q) \frac{S_{A'}}{V_{A'}}$ where q is the volume fraction of void, $S_{A'}$ and $V_{A'}$ are respectively the average surface area and average volume of primary grains. This can be used as an additional constraint to the optimization problem. Under this constraint, the width D_4 is fixed by the length D_1 or vice-versa. Therefore Boolean models following the additional constraint are generated and the resulting correlation functions are compared in Fig. (8.5). As expected, with the additional constraint, the models reproduce the correct slope at the origin for the correlation function, irrespective of the shape. However, the long-range of the correlation function is not reproduced except for very thin and highly elongated platelets (in red, in Fig. 8.5). These platelets shapes, with sizes smaller than 1 nm, are hardly physical and must be rejected. Accordingly, models with larger correlation ranges must be used to approach the TEM images correlation function. Hereafter, a two-scales model is considered.

8.2 Two-scale model of platelets

8.2.1 Aggregates and local alignments

As previously seen, the one-scale model of random platelets cannot reproduce the correlation function of the TEM images in the range larger than the size of the platelets. Indeed, crushed powder of mesoporous alumina exhibits local alignments

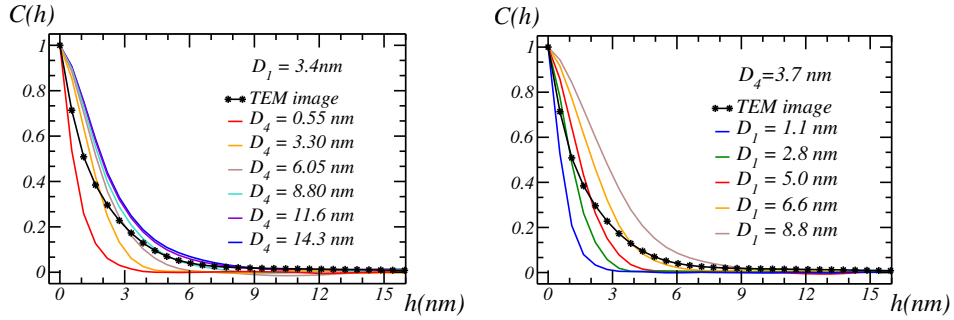

(a) (b)

Figure 8.4: Effect of the grain shape on the correlation function of the one-scale model: with $D_1 = 3.4\,\text{nm}$ and D_4 varying from 0.55 nm to 14.3 nm (a); with $D_4 = 3.7\,\text{nm}$ and D_1 varying from 1.1 nm to 8.8 nm (b). The correlation function of the TEM images is shown in blue.

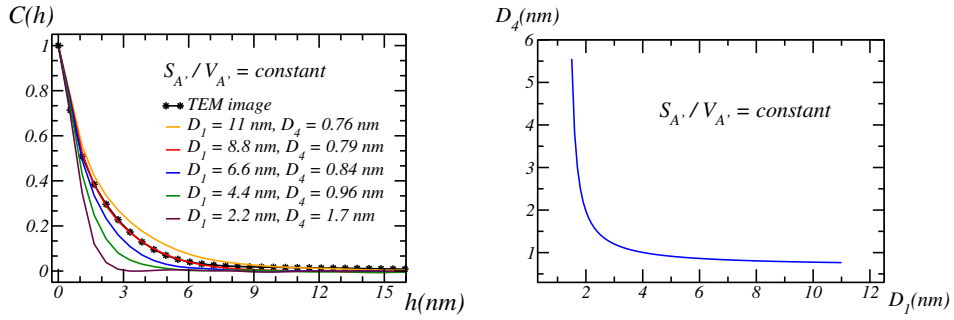

(a) (b)

Figure 8.5: Correlation function of one-scale Boolean models of octagonal prisms with fixed surface density S_V and increasing platelet width D_4 (a). Length D_1 with respect to width D_4 under the constraint in Eq. (8.4) (b).

(Fig. 8.6). The aggregation of alumina platelets is well known (Euzen et al, 2002) and originates from the behavior of the boehmite precursor in solution (Fukusawa & Tsujii, 1988). This aggregation is expected to be highly anisotropic due to the anisotropy of the platelet shape and the degree of hydroxylation of platelet faces (Digne et al., 2004). The alignments suggest the existence of at least one larger scale, which correspond to the size of aggregates of platelets. The size of these aggregates is in-between 2 to 3 times the size of platelets, according to Fig. 8.6. Thus, the local dispersion of the platelets should be taken into account.

8.2.2 Modeling

Accordingly a simple two-scales Boolean model, more general than the previous one-scale model, is defined as follows:

- First, a Boolean model of spheres is used to generate a field of orientations: to each sphere is associated a random principal direction uniformly distributed on the unit sphere.
- Then, two Poisson point processes with two densities are generated inside and outside the spheres.

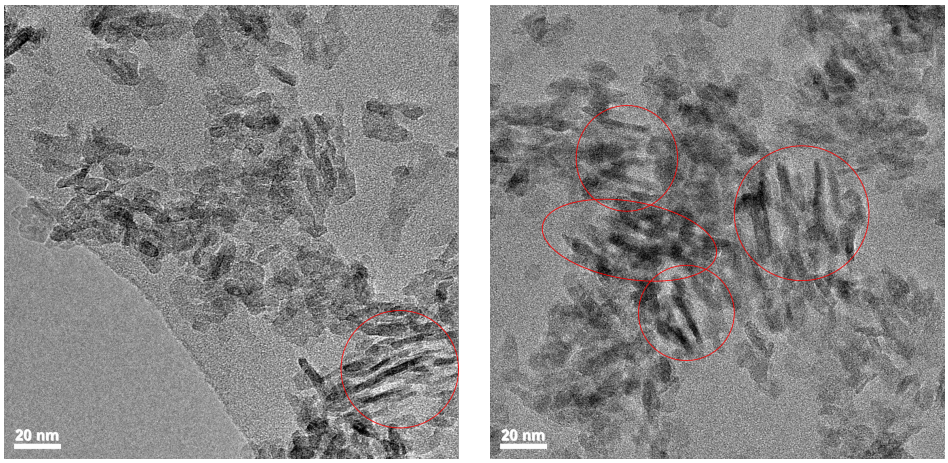

(a) (b)

Figure 8.6: TEM image of crushed powder of mesoporous alumina. Local alignments are encircled in red.

- Third, a platelet with fixed shape is located at each Poisson point. When the point is outside the spheres, the platelet orientation is uniformly random, as in the previous one-scale model. When the point is inside a sphere, the platelet orientation is given by that of the sphere. If a point is located in two or more spheres, one of the corresponding orientations is chosen at random.

This type of model is a variant of a Cox Boolean model (Jeulin, 2012). The two-scales Boolean model has 5 parameters: the shape parameters D_1 and D_4 (Fig. 8.1) and 3 other variables that control the spatial dispersion of platelets. The latter are the volume fraction of spheres at the larger scale p_S, the radius of the spheres r_S and the volume fraction of platelets inside spheres p_A. The volume fraction of platelets outside the spheres p'_S is prescribed by the overall porosity, fixed to 69%, by:

$$p'_S(1 - p_S) + p_A p_S = 1 - 0.69. \tag{8.5}$$

An example of realization of a two-scales model is shown in Fig. (8.7). The volume of the microstructure is $400 \times 400 \times 546$ voxels at resolution 0.55 nm per voxel. The size of the 2D section is 400×400 pixels. The shape and size of the platelet is chosen the same as the prism shown in Fig. (8.1). The volume fraction of spheres p_S is 0.5, with sphere radius fixed at 8 nm. The volume fraction of aligned platelets inside the spheres p_A is 0.5. In the generated microstructure, there are 5713 spherical aggregates, 165629 platelets aligned in the aggregates and 30364 randomly oriented platelets outside the aggregates. Local alignments are distinguished and encircled in red. We checked that the microstructure is macroscopicaly isotropic with respect to the correlation function. Hereafter, we let the 5 paremeters $D_{1,4}$, $p_{S,A}$ and r_S vary. We optimize them to approach the TEM images' correlation function.

8.2.3 Parameters identification

The effect of each parameter on the correlation function has firstly been examined numerically. Simulations are performed by fixing two of the three parameters, and

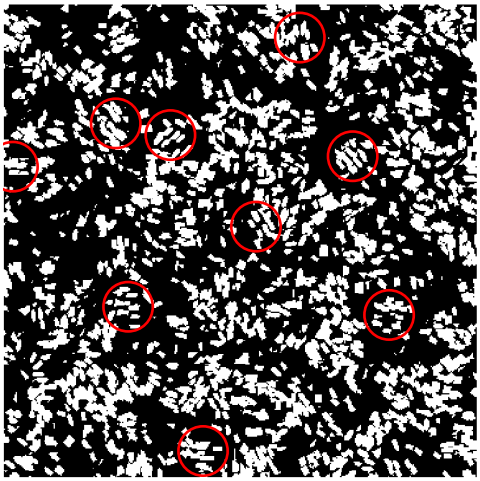

Figure 8.7: 2D section of a realization of the two-scales Boolean model with locally-aligned platelets (some of them encircled in red).

letting the third parameter vary (Fig. 8.8). As expected, the slope at the origin of the correlation is not sensitive to the parameters governing large scale effects p_S and r_S (Figs. 8.8a and 8.8b). Their values however greatly affect the correlation range from 1.1 nm to 5.5 nm. On the contrary, the slope at the origin of the correlation is sensitive to the volume fractions of platelets inside the grains p_A (Fig. 8.8c), in particular for high values of p_A larger than 50%. In this regime, platelets often intersect, which greatly reduces their specific surface area. In the optimization process detailed below, the two parameters p_S and r_S are adjusted to control the correlation range, the other one being chosen to adjust the slope at the origin.

Hereafter, the parameters of the two-scales Boolean model are estimated by optimization, to approach the correlation function of the TEM images. The same criterion is used as in the one-scale Boolean model (Eq. 8.2). First, a standard conjugate gradient descent method was tested. The method was ineffective, due to the high variability in the estimate of the gradient, especially for such two-scales model. The more robust Nelder-Mead method, which does not require the computation of a gradient (Nelder & Mead, 1965), was also used. In most of our numerical simulations, the algorithm very slowly converges. Furthermore, the microstructure was found to be sub-optimal. This is presumably an effect of variability.

Finally, a random "point cloud"simulations based on a Monte Carlo method (Hammersley & Handscomb, 1964) was tested. To initialize the point cloud method, the shape parameters D_1 and D_4 are fixed, as in the optimized one-scale model. The cloud zone for the other parameters (p_A, p_S and r_S) is initially a large domain ($0.1 < p_A < 0.9$, $0.1 < p_S < 0.9$ and $2.6\,\text{nm} < r_s < 21\,\text{nm}$). In this domain, the specific surface area is not sensitive to p_A and controlled by the values of D_1 and D_4 initially chosen. After random simulations, the zone of interest is reduced to a region where the objective function is lower. The process is repeated until convergence to a single point. The method, which tends to explore larger regions in the parameters space, was found to significantly reduce variability compared to the Nelder-Mead method, and also provided the best local minima. After 3 iterations, the algorithm provides good-enough microstructures and was stopped.

The cloud optimization was repeated with varying shape parameters D_1 and D_4, following the specific surface area constraint (Eq. 8.4). A series of optimal two-

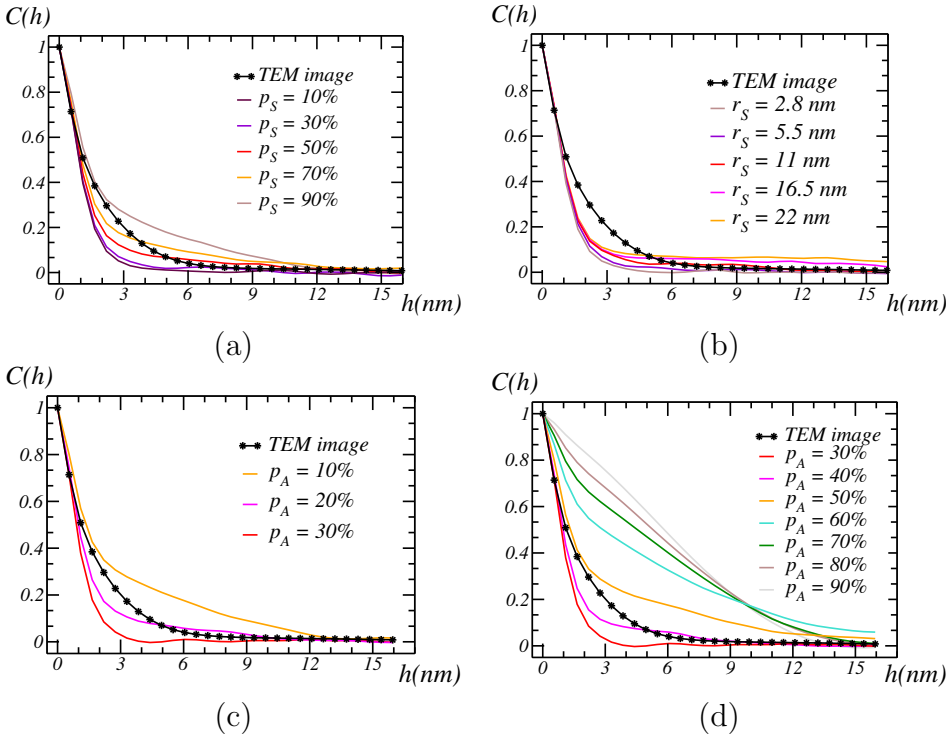

Figure 8.8: Effects of the spatial dispersion parameters p_S, r_S and p_A on the correlation function.

scale models with respect to D_1 (or equivalently, D_4) is obtained. The correlation functions of two such models are represented in Fig. (8.9) and compared with that of the TEM images. For each set of parameters, the two correlation functions are in excellent agreement. We pick one of the two optimal models, corresponding to $D_1 = 3.3$ nm, and used in Fig. (8.9). This model is compared to the TEM image in Fig. (8.10). Image (8.10b) is simulated using (6.2) and a normalization similar to (6.3). For the sake of comparison, all values are comprised beteen 0 and 255. Note that the parameters a, b and c entering (6.2) are irrelevant due to (6.3).

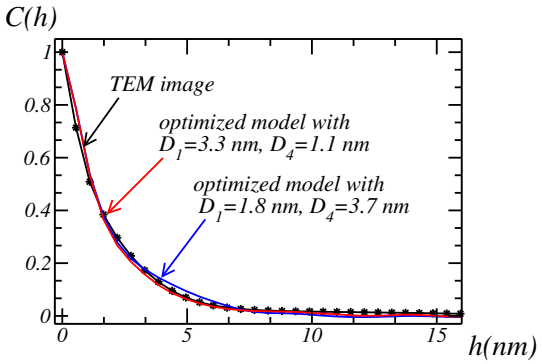

Figure 8.9: Correlation functions of two optimized two-scales models with different shape parameters for the grains: comparison with the correlation function of TEM images.

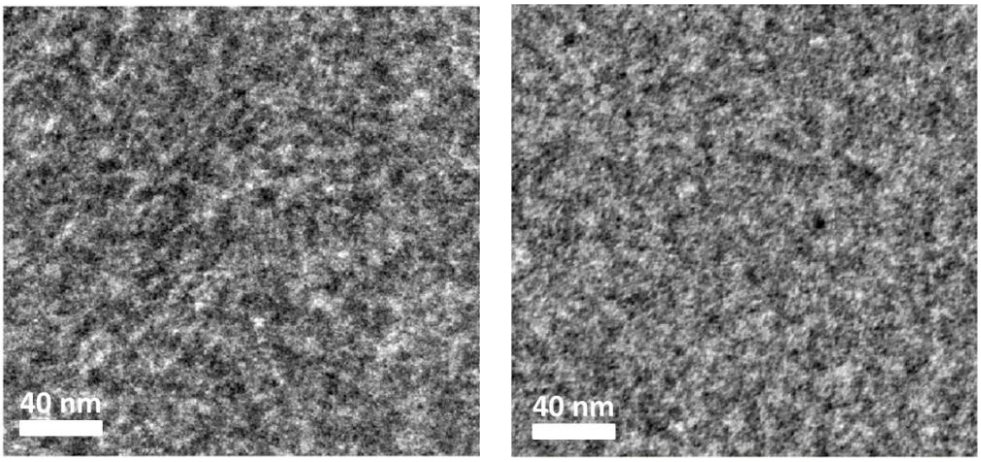

(a) (b)

Figure 8.10: Comparison between (a) the TEM image and (b) the simulated transmission image using one of the optimal two-scales models with $D_1 = 3.3$ nm (see Fig. 8.9). Image (b) is generated from Eq. (6.2) and a normalization similar to (6.3).

8.3 Validation with specific surface area

In this section, the specific surface area of the optimized models and obtained from available porosimetry data are compared. Nitrogen porosimetry on the sample gives a specific surface area of 0.232 nm^{-1}.

8.3.1 Specific surface area estimation

For an arbitrary random set A, the specific surface area S_V of A is given by the slope at the origin of the correlation $Q(h)$, as reminded in equation 8.4. For two-scales models B written as:

$$B = (A_0 \cap A_1) \cup (A_0^c \cap A_2)\,, \tag{8.6}$$

where A_i ($i = 0,\ 1,\ 2$) are independent random set with volume fraction p_i and specific surface area $S_V^{(i)}$, and A_0^c is the complementary of A_0, the specific surface area S_V^B of the random set B is given by (Jeulin, 2014):

$$S_V^B = S_V^{(0)}(p_1 + p_2 - 2p_1p_2) + p_0 S_V^{(1)} + (1 - p_0)S_V^{(2)}. \tag{8.7}$$

The first term in the right-hand side represents the specific surface of the set B cut by that of A_0. The next terms are the specific surface in the interior and exterior of A_0. This equation is exact for platelets that are cut off at the boundary of primary grains. It can be applied to the two-scales Boolean model as follows:

$$\begin{aligned} S_V^{(0)} &= -\frac{3}{r_S}(1 - p_S)\log(1 - p_S), \quad S_V^{(1)} = -\frac{S_p}{V_p}(1 - p_A)\log(1 - p_A), \\ S_V^{(2)} &= -\frac{S_p}{V_p}(1 - p'_S)\log(1 - p'_S), \end{aligned}$$

where $\frac{S_p}{V_p}$ is the surface/volume ratio of the platelets, determined by D_1 and D_4 by simple geometric considerations. The resulting estimation for S_V^B is only an

approximation, since Eq. (8.6) is not exact for the Cox Boolean model. However, the approximation is correct if a large scale-separation $r_S \gg D_1$ and $r_S \gg D_4$ is assumed (Jeulin, 2012). In the present two-scales model, r_S/D_1 and r_S/D_4 are at least equal to 2.

In a first step, a particular optimized two-scales microstructure with $D_1 = 3.3\,\text{nm}$ and $D_4 = 1.1\,\text{nm}$ (corresponding to Fig. 8.9) is considered. The porosimetry results depend on the size of the molecules used for adsorption experiments (Thommes et al., 2000; Wernert et al., 2010). The estimated specific surface areas are higher (resp. lower) when small (resp. large) molecules are used. This effect is especially important in nanomaterials. To roughly model the nitrogen adsorption, morphological closings (dilation followed by erosion) by a cube, a 3D cross and a rhombicuboctahedron of increasing sizes are first performed. The rhombicuboctahedron better approximates the shape of molecules on a digitized image, and offers a good compromise between performance and exactness. Its size corresponds to the radius of an equivalent sphere. Second, closed pores that are not accessible to nitrogen are removed. 3D views of one optimized two-scales microstructure after closing are represented in Fig. (8.11). Results for the estimates of the specific surface areas are given in Tab. (8.1). We denote by S_V^{cov} the estimate of the slope of the tangent line to the correlation function at $h = 0$ (Eq. 8.4). For comparison purposes, we also give estimates obtained by the method of weighted local configurations proposed in (Ziegel & Kiderlen, 2010) and analytical estimates from Eq. (8.7), denoted S_V^Z and S_V^B respectively. The method in (Ziegel & Kiderlen, 2010) makes use of 5 weights which depend on two parameters s and r. We follow (Ziegel & Kiderlen, 2010) and set $s = 1.7452$ and $r = 1$. These two values are given for cylinders. They give nearly optimal estimates with the platelets used in the present work.

The estimates S_V^{cov}, S_V^Z are measured on the original microstructure (M), its closing by a cube (M') and by a 3D cross (M'') of size 1 pixel (0.55 nm). We also remove closed pores by a hole filling operation on the three microstructures and estimate their specific surface area $S_V^{Z'}$, using the method of Ziegel.

Numerical results for the specific surface are of the same order of magnitude than experimental ones (about $0.232\,\text{nm}^{-1}$) and yet, significantly higher. Closing also significantly influences the specific surface area. Furthermore, numerical results indicate that the latter is affected by the shape of the structuring element. There are very few closed pores in the microstructure, as indicated by the values of $S_V^{Z'}$, very close to S_V^Z.

	S_V^B (nm^{-1})	S_V^{cov} (nm^{-1})	S_V^Z (nm^{-1})	$S_V^{Z'}$ (nm^{-1})
M	0.8104	0.6611	0.5533	0.5527
M'		0.4225	0.4299	0.4277
M''		0.5796	0.4878	0.4871

Table 8.1: Specific surface areas of the two-scales optimized Boolean model M, and of its closing M' and M'', computed using the analytical estimate (Eq. 8.7), the correlation function and the method of weighted local configurations in (Ziegel & Kiderlen, 2010). The analytical estimate (Eq. 8.7) is relevant for model M only.

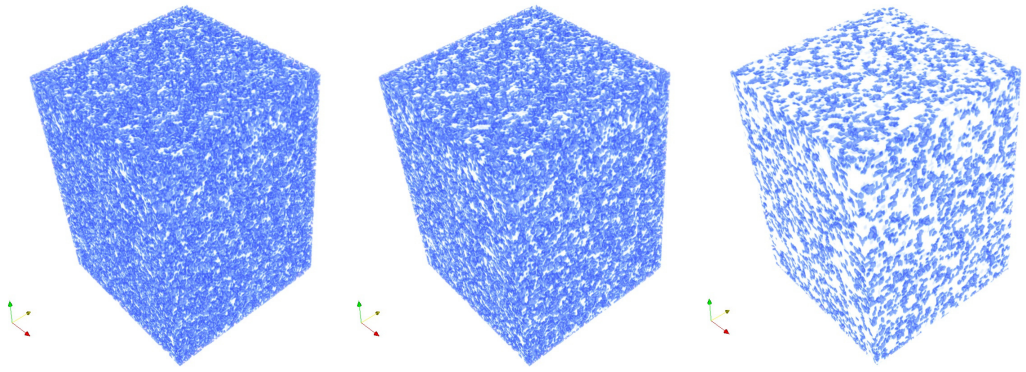

$\delta = 0$ $\delta = 1$ $\delta = 2$

Figure 8.11: 3D views of the closings of an optimized two-scales Boolean model with increasing structuring element size (left to right). Porosity in blue and platelets in white. The structuring element is a rhombicuboctahedron of size δ (in voxels).

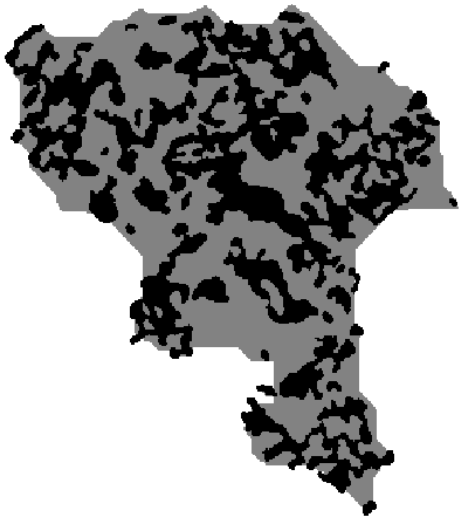

Figure 8.12: Porous volume of the tomography image after closing with rhombicuboctahedron of 30 voxels and erosion by 3 voxels (2D section). Alumina grains are in dark, while in grey is the porosity.

8.3.2 Electron tomography reconstruction

Hereafter, the two-scales models of platelets are compared to the tomographic model in terms of porosimetry. The porous volume of the tomographic model is extracted by using a series of morphological operations proposed by Moreaud et al (Moreaud et al., 2008). First, a closing operation by a sufficient size (here we take 30 voxels) together with a hole filling operation is performed to remove all pores in its interior. Next, a geodesic erosion is performed on the 3D image in order to maintain the surface irregularity (Fig. 8.12). The global volume and the external surface contour of the tomographic model are emerged after the erosion.

Then, closings of increasing sizes are performed with rhombicuboctahedra on both the tomographic model and the two-scales microstructure models, to simulate the nitrogen adsorption. The structuring element roughly mimics the role of nitrogen molecules. Isolated pores are removed using hole filling operations to extract the accessible porosity. Specific surface area measurement results are given in Fig. (8.13),

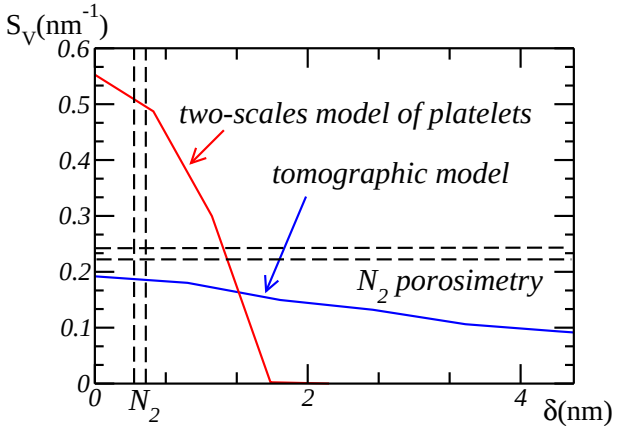

Figure 8.13: Specific surface areas with respect to the size of the closing: comparison between one two-scales model of platelets (red), the tomographic model (blue) and porosimetry data in confidence interval (horizontal black dotted lines). The sizes of nitrogen molecules are indicated by the two vertical black dotted lines.

in red for the area of accessible specific surface in the two-scales model, and in blue for the area of accessible specific surface in the tomographic model. These values have been corrected by subtracting the exterior surface area of the specimen. Finally, the nitrogen porosimetry data ($0.232\,\mathrm{nm}^{-1}$) is indicated by the dotted black horizontal lines. The nitrogen molecules whose shapes are anisotropic are indicated by vertical black dotted lines.

8.3.3 Comparison

As shown in Fig. (8.13), the specific surface area in the two-scales microstructure agrees with porosimetry data when the size of the structuring element is about 1.2 nm. This value is quite higher than the nitrogen size, of about 0.3 and 0.4 nm. For a structuring element of this size, the estimated specific surface area is about 2 to 3 times higher for the two-scales model compared to porosimetry data and to the tomographic model. However, the difference between model and porosimetry data is much less of the same order than usually observed when comparing image analysis results to molecular porosimetry.

Some differences between the two-scales optimized Boolean model and tomographic image are also observed. The decrease of the specific surface area with respect to the size of the structuring element is much steeper in the two-scales model than in the tomographic image. The difference between accessible and overall properties is also more important in the two-scales model, for large structuring elements. The accessible porosity globally follows the same trend as the specific surface area when the size of the structuring element increases (Fig. 8.14).

Also, our results are nearly insensitive to the shape of the platelets in the two-scales model. Nearly identical results have been obtained when considering other two-scales optimized models with varying shape parameters (not shown). This is because the size of the platelets in the two-scale models is constrained by the slope at the origin of the correlation, in other words, constrained by the specific surface area. As indicated in the equation 8.4, the slope at the origin of the correlation of the 3D microstructure is directly related to its specific surface area. In our study, even

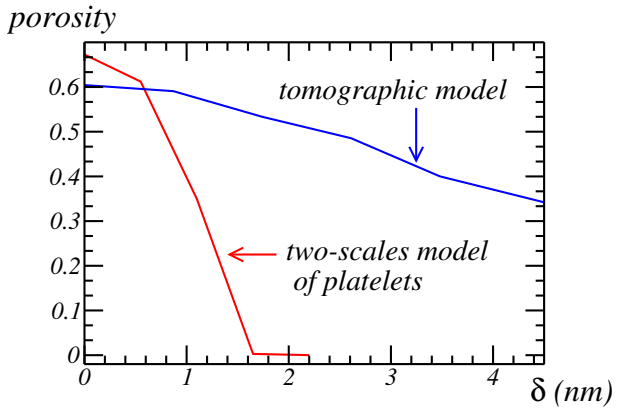

Figure 8.14: Accessible porosity V_V after closings by rhombicuboctahedra of increasing size, for the two-scales optimized and tomographic models (red and blue, resp.).

though only the 2D projections of the microstructure (TEM images) are available, the correlation of the 2D projection still dominates the specific surface area.

To conclude, the specific surface area of the optimized two-scale models are 2 or 3 times higher than the results measured by nitrogen porosimetry. The difference is essentially due to the conflict between the high-frequency information on the TEM images and the nitrogen porosimetry. As a independent third-party reference, the size of platelets measured on the TEM images of crushed material (section 7.4) are much larger than the optimized platelets for the two-scale model. The large platelets support the lower specific surface area, in favour of the nitrogen porosimetry results.

The high-frequency information in the TEM images are possibly coupled with noise or projection of carbon membrane. The idea is proved in section 8.4, together with the proposition of a corrected model for TEM image simulation. Larger platelets are then used in the two-scale model identification with the new TEM image model in section 8.5.

8.4 TEM image simulation

8.4.1 Noise and carbon membrane

In previous sections, the TEM images were simulated from the 3D microstructure by 2D projection. In the comparison between experiment and simulation, the noise in the TEM images were not taken into account. A comparison between the 2D projections of a microstructure with and without Poisson noise is shown in Fig. 8.15. The noise influences the correlation function, especially the slope at the origin of the correlation function.

In reality, the noise is more complex than the pure Poisson noise. The TEM images of vacuum show correlation in the range $0 < h < 2$ nm (Sec. 7.1). Where the noise in the TEM images comes from? Despite the complex electron emission system and the lens system, only the electron detector brings quite a lot of noise (Meyer & Kirkland, 2000).

The electron detector consists of a layer of scintillator, an optical coupling system and a grid of CCD photon detectors. The transmitted electrons hit and are scattered

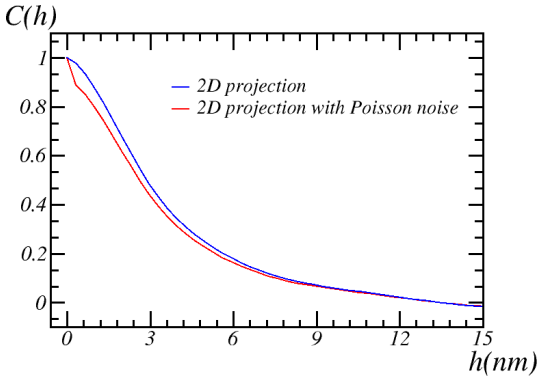

Figure 8.15: Correlation functions of the 2D projections of a microstructure with and without Poisson noise.

in the scintillator. Photons are emitted along the trajectory of electrons. Some of the photons go through the optical coupling system and are captured by the CCD. During the process, noise source includes:

- Scattering of electrons in the scintillator, which brings spatial correlation.
- Emission of photons in the scintillator, which brings Poisson noise.
- Scattering of photons in the scintillator, which brings spatial correlation.

In the Lambert-Beer law (Reimer & Kohl, 2008, p.36) for the modeling of 2D TEM images of porous media, only the electron attenuation caused by the specimen is taken into account (Eq. 8.10). In reality, besides the alumina specimen, the carbon membrane is also projected on the TEM images. Eventhough the carbon membrane is thin and nearly transparent for electrons, it still influences high-frequency information of the TEM image, in other words, the slope at the origin of the correlation function. Accordingly, it influences the estimation of platelet size. The effect is more important when the specimen is thin and the platelets are small.

8.4.2 TEM image model

There are two ways to compensate the noise effects – to remove it by filtering or to add it into the simulation. The noise in the TEM images are difficult to filter, because its correlation range is $0 < h < 2$ nm, very close to the scale of the platelets. Especially when the platelets overlap, the details in the intersections are removed together with the noise.

The solution we choose is to integrate the main features of TEM image formation into the simulation model. The "main features" here explicitly refer to the features who influence the correlation function, which include the electron attenuation, the Poisson noise and the carbon membrane.

How to integrate the noise features to the TEM image model? The TEM image formation is complex, and it is difficult to simulate the physics of the entire system. Our first try is to add the Poisson noise to the Lambert-Beer law (Eq. 6.1), and then to convolute with the point spread function. The point spread function is estimated from the TEM images of vacuum. However, the resulting TEM images are too blurry (not shown), compared to the experimental images. In the experimental images, the

contours of the platelets are much more clear, which shows a weak point spreading. The difference is due to that the transfer functions for noise and for signal are not the same, as talked about in (Meyer & Kirkland, 2000). From the current pack of TEM images, we do not have means to measure the point spread function for the signal. Moreover, this approach cannot take the carbon membrane into account, whose microstructure remains unknown.

Our second approach is based on the assumption that the noise is superposed on the signal. The model is described as an additive noise term:

$$Y(x_1, x_2) = a(x_1, x_2) + b \exp\left[-c_1 \int_0^f \mathrm{d}x_3\, \chi_S(x_1, x_2, x_3) - c_2 \int_{-f_c}^0 \mathrm{d}x_3\, \chi_C(x_1, x_2, x_3)\right] \tag{8.8}$$

where $a(x_1, x_2)$ is no longer a constant, but a noise term, b is a positive constant coefficient, c_2 is the attenuation coefficient of the carbon membrane, f_c is the thickness of the carbon membrane, χ_C is the microstructure of carbon membrane.

Since both the thickness and the attenuation coefficient of the carbon membrane are much smaller than those of alumina specimen, the relation $c_2 f_c < c_1 f \ll 1$ holds. The equation 8.8 is approximated by:

$$Y(x_1, x_2) \approx a(x_1, x_2) + b - b\left[c_1 \int_0^f \mathrm{d}x_3\, \chi_S(x_1, x_2, x_3) + c_2 \int_{-f_c}^0 \mathrm{d}x_3\, \chi_C(x_1, x_2, x_3)\right] \tag{8.9}$$

The noise term $a(x_1, x_2)$, the coefficient b, the attenuation coefficient c_2 and the microstructure χ_C of carbon membrane remain unknown. Fortunately, the TEM images of the carbon membrane is available. The above equation is then evaluated as:

$$\begin{aligned} Y(x_1, x_2) &= \left[a(x_1, x_2) + b - bc_2 \int_{-f_c}^0 \mathrm{d}x_3\, \chi_C(x_1, x_2, x_3)\right] - bc_1 \int_0^f \mathrm{d}x_3\, \chi_S(x_1, x_2, x_3) \\ &= Y_C(x_1, x_2) - bc_1 \int_0^f \mathrm{d}x_3\, \chi_S(x_1, x_2, x_3) \end{aligned} \tag{8.10}$$

where Y_C is the TEM image of the carbon membrane. The remaining problem is to identify the coefficient b.

We take the mean value of greyscale on the both sides of Eq. 8.10, and obtain:

$$\langle Y \rangle = \langle Y_C \rangle - bc_1 pf \tag{8.11}$$

where p is the volume fraction of solid phase in the alumina specimen fixed at 31%, f is the specimen thickness fixed at 70 nm or 300 nm and the attenuation coefficient of electron through alumina c_1 is estimated in Sec. 6.1 with the value 2.40 10^{-3} nm^{-1}. The coefficient b is then obtained by:

$$b = \frac{\langle Y_C \rangle - \langle Y \rangle}{c_1 pf} \tag{8.12}$$

The means of the TEM images of mesoporous alumina were estimated in chapter 7. With the images of 70 nm thick specimen at magnification 20K, the value of b is estimated to be 13270 ± 1665 with 95% confidence interval. With the images of 70 nm thick specimen at magnification 30K, the estimation is 12933 ± 1511 with the

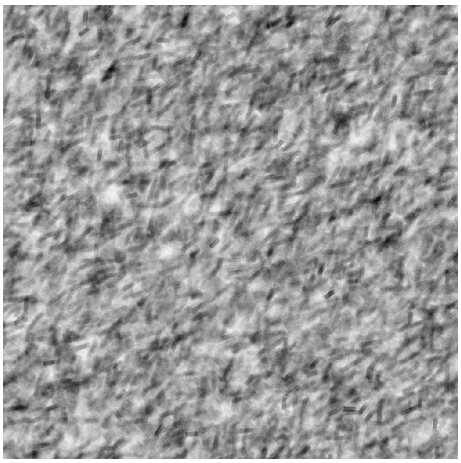

Figure 8.16: TEM image simulation with a one-scale model of platelets using the model in Eq. 8.10.

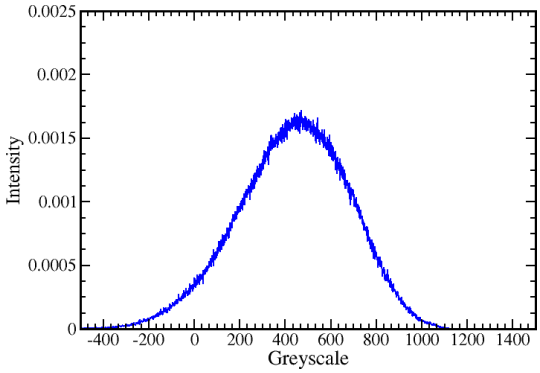

Figure 8.17: Histogram of the simulated TEM image in Fig. 8.16.

same confidence interval. We take the average of the two estimations $b = 13101$. The TEM image simulation model is then tested with a one-scale model of platelets (shown in Fig. 8.16). The platelet size comes from the measurement on the TEM image of crushed sample (Sec. 7.4). The length and width of platelets measured are converted to the side lengths $D_{i,1\leq i\leq 4}$ of the similar octagonal prisms with constraint of equal width and thickness.

In the simulated TEM image, the noise is weak compared to experimental TEM images. Furthermore, the greyscale variance of the simulated TEM image (Fig. 8.17) is much higher than that of the TEM images (Sec. 7.3). The difference is because in Eq.8.10, the variance of greyscale in the pure carbon membrane image $\sigma^2(Y_C)$ is high. The second term on the right of the equation also brings variance, constrained by b. In the formation of TEM images of alumina, the intensity of the noise term is lower than Y_C. The intensity difference of noise in TEM image of alumina and of pure carbon membrane is interpreted by the electron detector's gain drift in the two processes.

Accordingly, a coefficient $\alpha \in \mathbb{R}$ is added into the TEM image model (Eq. 8.10), in order to correct the detector gain and to constrain the noise intensity:

$$Y(x_1, x_2) = \alpha Y_C(x_1, x_2) - bc_1 \int_0^f \mathrm{d}x_3 \, \chi_S(x_1, x_2, x_3) \tag{8.13}$$

The histograms of the two components are shown in Fig. 8.18, together with the

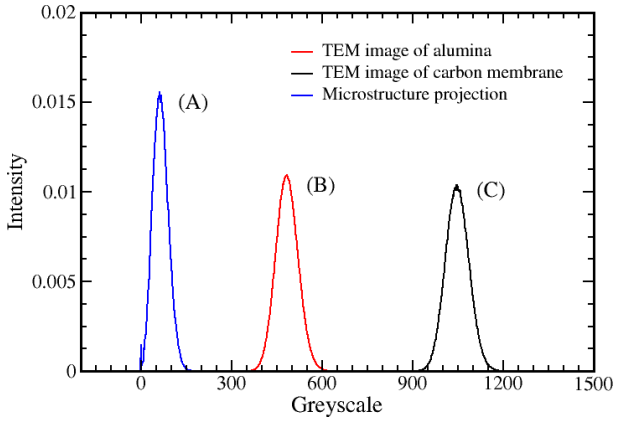

Figure 8.18: Histograms of (A) the 2D projection of a microstructure $\int_0^f \mathrm{d}x_3\, \chi_S(x_1, x_2, x_3)$ (B) the TEM image of alumina Y (C) the TEM image of carbon membrane Y_C. The microstructure in (A) is a realization of the one-scale model of platelet with platelet size measured in section 7.4.

objective histogram.

Parameter identification is performed by searching for α and b to reproduce the experimental histogram using the two constraints on the mean and variance of the image:

$$\begin{cases} \langle Y \rangle = \alpha \langle Y_C \rangle - bc_1 pf \\ \sigma_Y^2 = \alpha^2 \sigma_{Y_C}^2 + (bc_1)^2 \sigma_M^2 \end{cases} \tag{8.14}$$

where σ_M^2 is the variance of the 2D projection of the microstructure. Unfortunately, no real solution is found for the Eq. 8.14. This is because the variance of the carbon membrane image is so high that the coefficient α cannot restrict $\sigma_{Y_C}^2$ while at the same time maintaining a high mean value $\langle Y_C \rangle$.

In the Fig. 7.5, the histograms of the TEM images of carbon membrane for the same condition (magnification, exposure time, etc.) show shifts between them. The shift cannot be explained quantitatively by the detector gain drift only. Except the detector gain drift, the offset drift also exists if we compare the second and the third peaks in Fig. 7.5. Therefore, a linear transform of the carbon membrane image is considered as the noise component in the alumina TEM images. A constant term β is then added to the model:

$$Y(x_1, x_2) = \alpha Y_C(x_1, x_2) + \beta - bc_1 \int_0^f \mathrm{d}x_3\, \chi_S(x_1, x_2, x_3) \tag{8.15}$$

To identify the three parameters – α, β and b, the mean and the variance are used as two constrains:

$$\begin{cases} \langle Y \rangle = \alpha \langle Y_C \rangle + \beta - bc_1 pf \\ \sigma_Y^2 = \alpha^2 \sigma_{Y_C}^2 + (bc_1)^2 \sigma_M^2 \end{cases} \tag{8.16}$$

Obviously, the two equations are not sufficient to identify the three parameters. In our first try, the skewness is used as the third constraint. However, it does not deduce parameters in the correct range $b > 0$. In fact, the skewness in the experimental TEM images is very weak, and is not significant enough for model identification.

Instead, we consider the following constraints:

$$\begin{cases} b > 0 \\ \sigma_Y^2 > \alpha^2 \sigma_{Y_C}^2 \\ \Delta > 0 \end{cases} \tag{8.17}$$

where Δ is the discriminant of the quadratic equation. The term σ_M^2 is estimated from the one-scale of platelets with histogram shown in Fig. 8.18 (A). The solution for the inequations 8.17 is then obtained:

$$\alpha\langle Y_C\rangle + \beta \in (434, 528) \tag{8.18}$$

where 434 is the mean $\langle Y\rangle$ of the objective image. The inequation constrains the greyscale mean of the noise term. Based on it, we define t to be:

$$t = \frac{\alpha\langle Y_C\rangle + \beta - 434}{528 - 434} \in (0, 1) \tag{8.19}$$

When t tends to 0, the value of b should be small, and the noise component dominates the resulting TEM image. When t tends to 1, the discriminant Δ and α tends to 0, thus the signal component dominates the resulting TEM image. Therefore, the variable t is a normalized descriptor of the signal-to-noise ratio.

Now we need to know the signal-to-noise ratio in the TEM images of mesoporous alumina.

8.4.3 Signal-to-noise ratio

We have TEM image for pure noise, but not for the pure signal. The intensity of pure signal in the TEM images of alumina remains unknown. However, the signal-to-noise ratio t influence the texture of the TEM images, as shown in Fig. 8.19. The ratio t dominates the high-frequency information in the simulated TEM images, in other words, dominates their autocorrelation at low shift. This feature is then used to identify the signal-to-noise ratio.

The correlation functions are estimated and compared with experimental TEM images in Fig. 8.20. As expected, the correlation is very sensitive to the signal-to-noise ratio. When $t = 0.68$ (Fig. 8.20 (B) blue dotted line), the simulation fits the experimental curve at the range $0 < h < 1$ nm. This range corresponds to the correlation range of the carbon membrane images.

With the identified signal-to-noise ratio $t = 0.68$, the equations Eq. 8.16 and Eq. 8.19 are solved. The TEM image model (Eq. 8.15) is identified with the following parameters: $\alpha = 0.717$, $\beta = -253$ and $b = 1208$. It coordinates the criteria: greyscale mean, greyscale variance and the correlation function at low shift $0 < h < 1$ nm.

The textures of the experimental and simulated TEM images are visually close, as shown in Fig. 8.21. The dark areas (solid phase, or platelets) in the two images have close shapes and sizes. The small fluctuations homogeneously dispersed in the images come from the projection of the carbon membrane and the noise.

It needs to be noted that the signal-to-noise ratio t is estimated with platelets of measured size. The size is supposed to be overestimated (details in Sec. 7.4), and the model does not have features in local alignment. The overestimated size and

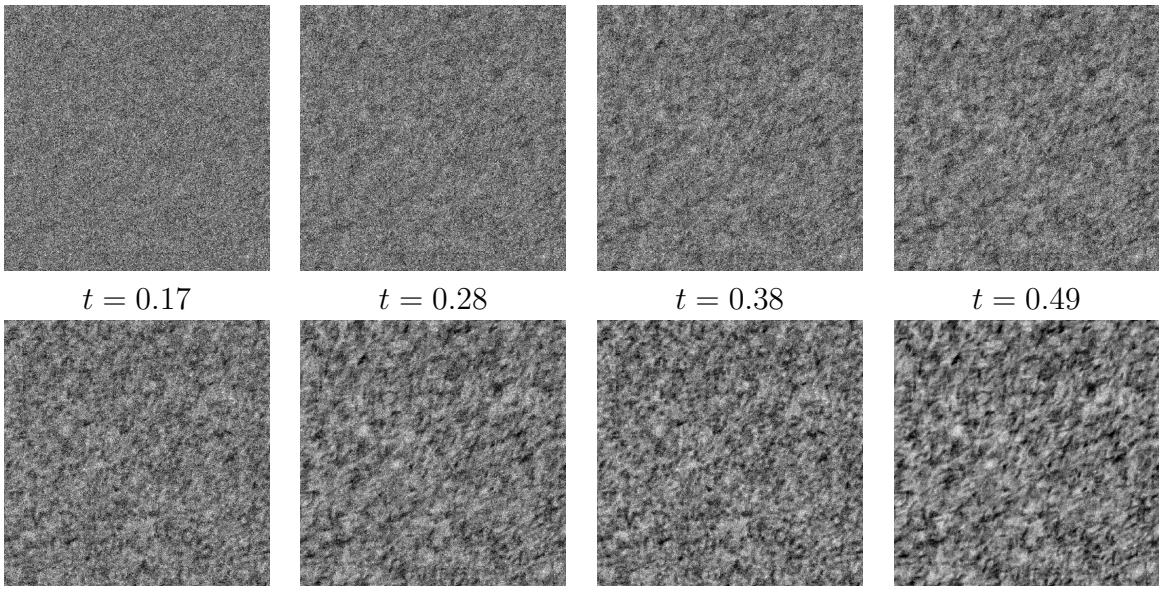

Figure 8.19: Simulated TEM images with different signal-to-noise ratios. The one-scale model of platelets is used to generate the microstructure. The platelets have the same size as the measurements in Sec. 7.4.

the non-alignment feature both bring bias to the estimation. However, they have opposite effects on the correlation function. Therefore, the value $t = 0.68$ is basically a reliable estimation. In the re-identification of the two-scale model (Sec. 8.5), the two effects are both taken into account.

8.5 Two-scale model identification

The re-identification is based on the two-scale model of platelets and the new TEM image model (Eq. 8.15). The platelet size and the spatial dispersion are free to vary. The constraints for identification include the experimental correlation function $C(h)$ and the specific surface area S_{BET} ($0.232\,\mathrm{nm}^{-1}$).

The effects of the parameters on the correlation function are studied in Sec. 8.2. The relation between the platelet size and specific surface area is described by Eq. 8.4. With the known information, a parameter searching process is performed.

We have already the correlation function estimated on the one-scale model in Fig. 8.20. The correlation at low shift fits well the experimental reference, but in long range it is higher. In addition, the specific surface area of this one-scale model is $0.2\,\mathrm{nm}^{-1}$, slightly less than the experimental BET surface area of $0.232\,\mathrm{nm}^{-1}$. The specific surface area further confirms the overestimation of the platelet sizes.

Accordingly, the general searching direction is to decrease the platelet volume and to add the aggregation features. A smaller platelet decreases the correlation $C(h)$, and makes room for the addition of aggregates. On the other side, it increases the specific surface area.

Along with this direction, five microstructures are generated (Tab. 8.2), with different platelet sizes and spatial dispersions. The sizes are chosen randomly around the initial parameters. The spatial dispersion parameters are initially taken from the

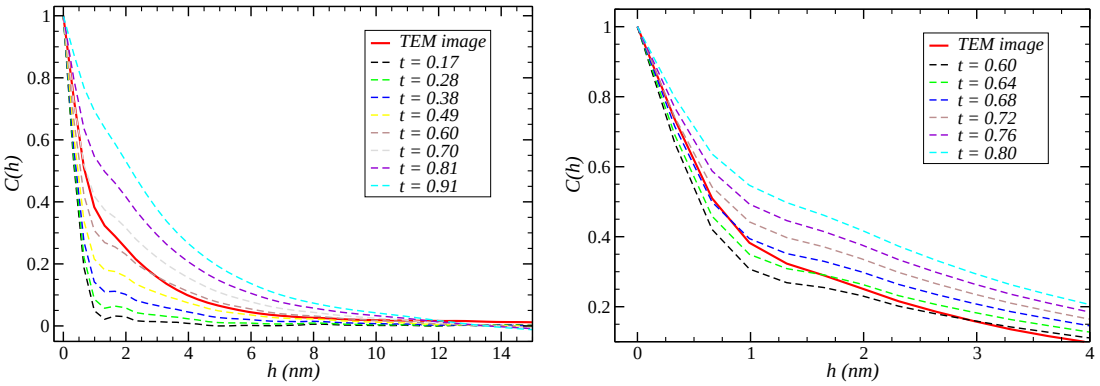

(A) (B)

Figure 8.20: Correlation functions of the simulated TEM images with different signal-to-noise ratios. The simulated TEM images are shown in Fig. 8.19. The one-scale model of platelets is used to generate the microstructure.

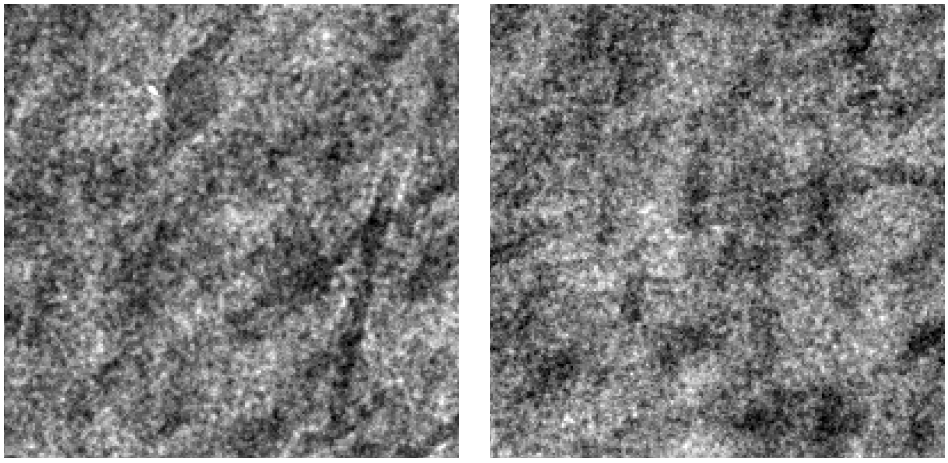

(A) (B)

Figure 8.21: Comparison between the texture on (A) a TEM image of sample N°.2 and (B) a simulated image with $t = 0.68$ by the TEM image model in Eq. 8.15. The image size is 100×100 nm^2.

identified two-scale model of Sec. 8.2, and are then adjusted to adapt to the correlation in long range. The correlation functions estimated from these microstructures are shown in Fig. 8.22.

Since the correlation of the initial one-scale model of platelets is already quite close to the experimental reference, the parameter searching in around is not difficult. It is quickly found that in the five realizations, the microstructure (B) and (E) (Fig. 8.22 dotted orange line and dotted blue line) both produce acceptable correlation functions. The microstructure (E) has the best specific surface area compared to the experimental data. The TEM image simulated from the microstructure (E) is compared with an experimental TEM image of sample N°. 1 in Fig. 8.23.

The solution for the identification of the two-scale model of platelets is not unique. The correlation function and the specific surface area does not constrain the two-scale model of platelets to a specific point, but a zone in the parameter space. It explains why the three alumina samples have close correlation functions,

Microstructure	Platelets (nm) D_1	D_2	D_3	D_4	Aggregates p_{A1}	p_S	r_S (nm)	Specific surface area S_V (nm^{-1})
Initial	14.8	3.3	4.0	3.0	0	0	0	0.201
(A)	17.4	1.6	4.0	3.0	0.6	0.2	8	0.221
(B)	17.4	1.6	4.0	3.0	0.3	0.2	20	0.225
(C)	11.6	4.1	3.0	3.0	0.3	0.2	40	0.212
(D)	15.4	1.6	2.0	3.0	0.3	0.2	30	0.261
(E)	14.3	2.4	2.0	3.3	0.3	0.2	30	0.231

Table 8.2: Parameter identification of the two-scale model of platelets for mesoporous alumina. The corresponding correlation functions of the simulated TEM images are shown in Fig. 8.22.

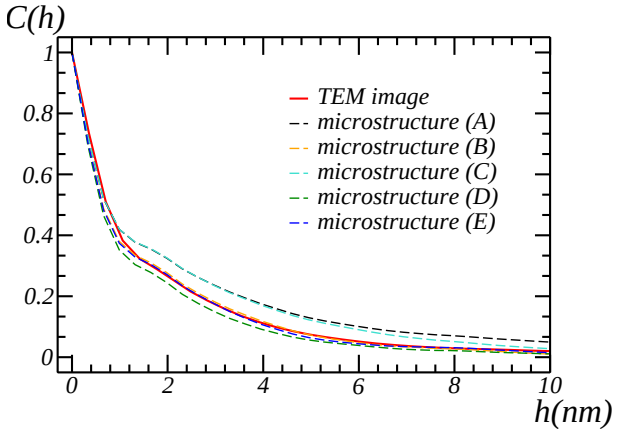

Figure 8.22: Correlation functions of simulated TEM images from microstructures shown in Tab. 8.2.

but different visual appearance (Fig. 5.2).

At present, we cannot sketch the shape of the zone, due to the lack of analytic model and the numerous parameters. However, during the parameter searching, some key factors which constrain the zone have been found.

- First, the surface-to-volume ratio of the platelets is important to obtain the right correlation at low shift, and to obtain the objective specific surface area.
- Second, the aggregates are useful to increase the correlation in long range. It is achieved by increasing the density of the aggregates (p_S). The radius of the aggregates should always be higher than the platelet length (from 1 to 2 times).
- Third, the density of aligned platelets in aggregates (p_A) should be close to or a bit higher than the average platelet density in the medium. A relatively high p_A simulates the bonding between aligned platelets. It helps increase the correlation function in the entire range.

Through the above approach, more parameter sets that satisfy the correlation function and the specific surface area can be found. Under the current constraints, the two-scale model of platelets still has degrees of freedom. More information should be extracted from the material to constrain the model. The degrees of freedom also provide potential for the material optimization.

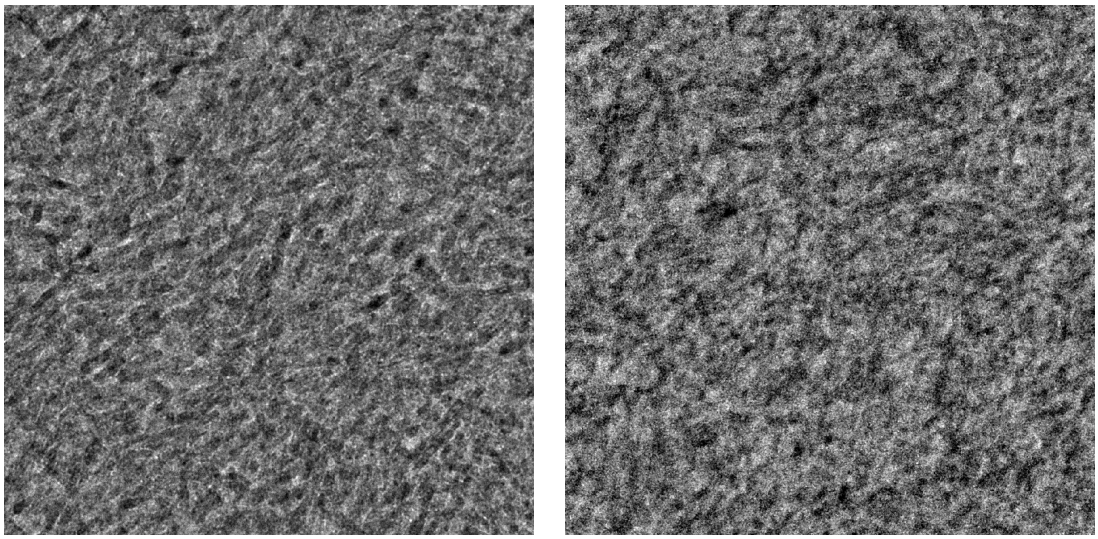

(A) (B)

Figure 8.23: Comparison between (A) experimental TEM image of sample N°.1 and (B) simulated TEM image with the identified microstructure shown in Tab. 8.2 (E).

8.6 Conclusion

In this chapter, random models are proposed to model the 3D microstructure of mesoporous alumina. A Boolean model of random-oriented octagonal prisms, or platelets is first considered. TEM images are simulated with the digital microstructures by integration along the thickness axis. The length and width of the platelets are identified with the correlation functions of the simulated TEM images. However, the identified platelets are too thin compared to observations.

A two-scale model of platelets integrating the features of platelet aggregation is then proposed. The aggregates are modeled with a Boolean model of spheres. The platelets inside the aggregates have same orientations. The platelet size and the spatial dispersion in the two-scale model are identified with correlation function. The identified model is compared with the tomographic reconstruction and porosimetry data in terms of specific surface area. The specific surface area of the two-scale model is in-between 2 to 3 times higher than the BET specific surface area.

The noise and carbon membrane are then taken into account in the TEM image simulation. The intensity of the noise in the TEM images are identified with histogram and correlation. The platelet size and the parameters for spatial dispersion in the two-scale model of platelets are identified again, with correlation as constraint. The identified platelet size is consistent with experimental observations. Furthermore, the solution for the identification is not unique. The identified model is validated with the BET specific surface area from the porosimetry test.

Part V

Morphological Simulation of Capillary Condensation and Evaporation

Chapter 9

Simulations of capillary condensation and evaporation on random materials

9.1 Introduction

This work focuses on the modelling of the capillary condensation and evaporation phenomena in porous media The phenomena of capillary condensation and evaporation is locally described by the Kelvin equation. The latter relates the equilibrium vapour pressure to the morphology of the pores: the more curved the local vapour/liquid interface is, the lower the equilibrium vapour pressure is. Accordingly, capillary condensation occurs first along highly curved interfaces. Porosimetry isotherm represents the amount of liquid (or equivalently, the remaining porosity filled by gas) as a function of pressure. When represented as a function of curvature radius, the isotherm is frequently interpreted as a cumulative size distribution for the porous phase (Barrett et al., 1951). Accordingly, the simulation of the capillary condensation and evaporation is important to study the relation between morphology of the material microstructure and experimental porosimetry data. Nevertheless, the question of determining the main microstructure parameters that influence the porosimetry remains open. It is of clear interest to microstructure modeling.

To numerically simulate the capillary condensation/evaporation on 3D disordered porous media requires a high efficiency of the algorithm. Here we highlight the method of virtual capillary condensation method by Stepanek (Štěpánek et al., 2007) and the MIP simulation method by Münch (Münch & Holzer, 2008).

9.1.1 Method of virtual capillary condensation

Stepanek et al. (2007) proposed the method of "virtual capillary condensation" to simulate the nitrogen adsorption and desorption process. The method focuses on the propagation of liquid-vapour interface. At a given temperature and at a given pressure, the Kelvin equation provides a relationship between radius of curvature and pressure. The method measures the local radius of curvature on the solid-vapour or the liquid-vapour interface. Wherever the local radius of curvature is less than the minimum radius, nitrogen liquid is condensed. With liquid condensation and filling, the curved interfaces becomes smooth and less curved. The algorithm converges when the radius of curvature of vapour-liquid interface is equal to the

minimum value and the radius of curvature of vapour-solid interface is equal to or larger than the minimum value. At equilibrium, a point in the porosimetry isotherm is obtained. The pressure is then increased, to achieve other equilibrium points in the isotherm. The method is validated for simple geometries like ink-bottle pore, and is also applied to microstructures generated by Gaussian random fields and microstructures of nano-agglomerates and open-cell foams. The pore size distributions of these models are then estimated from the isotherm. It should be noted that the numerical computation of procedure of interface propagation requires much computing power. Porous media are considered for volumes of size 100^3 voxels.

9.1.2 Mercury intrusion simulation

In many cases, it is sufficient to compute equilibrium states during nitrogen condensation. These states are obtained experimentally by increasing and decreasing pressure very slowly, so that equilibrium is met at all time. The equilibrium states are governed by the Kelvin equation, which replaces the physical problem by geometrical considerations. In this request, a similar geometrical problem arises in the simulation of Mercury Intrusion Porosimetry (MIP). The analysis of MIP is based on the Washburn equation, which relates the pressure to the radius of intruded cylindrical pores, whose role is similar to the curvature radius in the Kelvin equation. In MIP, mercury intrudes largest pores first, and then, with increasing pressure, intrudes gradually into pores of smaller size. Garboczi and Bentz (1991) simulated the MIP in 2D porous structures by the propagation of disc-shape elements from the external borders to the center of the 2D space. The disc element of a given radius, which is determined by mercury pressure, occupies the maximum amount of space without overlapping with the solid phase. When the pressure increases, the radius of the disc decreases, and more space is intruded by mercury. Bentz (1994) used the method in 3D space and estimated the pore size distribution. At nearly the same time, Thovert et al. (1993) proposed the notion of critical sphere in the geometrical characterization of porous media: the sphere of maximum radius fitted in the porous phase in function of coordinates. Critical spheres are used to probe the pore size at each point. Based on that, Münch and Holzer (2008) proposed the notion of "continuous PSD": the amount of pore volume that can be covered by critical spheres. The critical spheres are simulated using double Euclidean distance transforms and thresholds, while the radius of the spheres is equal to the threshold. The "continuous PSD" is then applied to simulate the MIP: despite the "continuous PSD" operation, a regular region growth is performed. The region growth takes the connectivity of the mercury phase into account, and the ink-bottle effect emerges in the simulated isotherm.

9.1.3 Discussion

In 1967, Matheron introduced the morphological closing operator – a combination of morphological dilation and erosion, and noted its equivalence with the capillary condensation with spherical structuring element (Matheron, 1967). Münch's method in MIP simulation is similar to Matheron's idea, and they both solve physical problems by geometrical means. Furthermore, the double distance transform plus threshold is a specific case of the closing operator when a spherical structuring element is used.

Other thermodynamic effects, e.g. solid/liquid interaction (Kierlik et al., 2001) and physical multilayer adsorption (Brunauer et al., 1938) have been addressed in the literature. Nevertheless, the geometry or the morphology of the porosity dominates the capillary behavior in meso-pores. For disordered porous media as γ-alumina, the 3D porous microstructure is complex, and the representative volume for the capillary behavior of such disordered porous media is also much larger than ordered porous media. In order to predict the capillary behavior of a random porous model, numerical simulation methods should be able to handle large volumes to ensure the representativity of the simulated result.

In this chapter, we propose a novel method that draws on the geometrical MIP simulation described by (Münch & Holzer, 2008). It extends to nitrogen porosimetry simulation, in particular, adsorption and percolation analysis. The method is described from a mathematical morphological point of view in Section 9.2, together with illustrations on simple geometries in Section 9.3. The representativity of the simulated isotherm is then discussed on Boolean models in Section 9.5. The method is then applied to more general random models with different morphologies, like multi-scale models and 3D tomography images in Section 9.6.

9.2 Simulation using morphological operations

9.2.1 Capillary condensation and evaporation

The Kelvin equation is:

$$p_c = p_s \exp\left(-\frac{2\gamma}{r_p}\frac{V_m}{RT}\right) \tag{9.1}$$

where p_c (in Pa) the equilibrium vapour pressure above a curved interface, r_p (in m) the local curvature radius of the interface, γ (in $\mathrm{N\,m^{-1}}$) the interfacial tension, R (in $\mathrm{J\,K^{-1}\,mol^{-1}}$) the universal gas constant, V_m (in $\mathrm{m^3\,mol^{-1}}$) the molar volume of liquid nitrogen, T (in K) the absolute temperature and p_s (in Pa) is the saturation vapour pressure if the liquid-vapour interface is flat. The Kelvin equation is valid for pores of radius above 2 nm (Takei et al., 1997). Hereafter, we denote r_p the curvature radius corresponding to the vapour pressure "Kelvin radius".

9.2.2 Representation of porous media

The structure of porous media (denoted by χ) in 3D space is represented by a function of two phases – solid and pore:

$$\chi(x) = \begin{cases} 1 & \text{if } x \text{ is in the solid phase} \\ 0 & \text{otherwise} \end{cases} \tag{9.2}$$

9.2.3 Condensation

We denote S and S^c the solid and porous phase respectively:

$$S = \{x \in D \quad \| \quad \chi(x) = 1\}, \qquad S^c = D \backslash S \tag{9.3}$$

where $D = S \cup S^c$ is the simulation domain. For simplicity D is a cube of length l. When the porous media is put into vapour atmosphere, condensation and evaporation occur, and the pore is filled by vapour and condensed liquid. However, not all the pore volume is accessible for vapour from exterior, and there exists pores totally closed by the solid phase. Therefore, before the condensation simulation, a preprocessing is needed to fill the isolated pores. We denote the accessible pores by P. It is obtained by a hole-filling morphological operation $H(\cdot)$ so that $P = H(S)^c$. The hole-filling operation $H(S)$ is realized using connected components (Serra J., 1982) of the porous phase S^c: components unconnected to any border of the domain are filled.

Capillary condensation and evaporation occurs in P, more specifically, in areas of a high curvature, e.g. corners, narrow slit pores. During the adsorption process in porosimetry, vapour pressure starts from nearly zero, and increases until the saturation vapour pressure. At any given pressure, an equilibrium between the condensation and the evaporation is established. The criterion of the equilibrium is the radius of curvature, indicated by the Kelvin equation. The maximum radius of curvature of vapour-liquid interface at position x is determined by the maximum sphere in the porous phase that it can reach (Štěpánek et al., 2007). The menisci of condensed liquid-vapour interface is formed along the spheres' borders. The filling of areas of high curvature and narrow space, and the forming of meniscus can be realized using a morphological operation – closing with a sphere as structuring element.

$$L(r_p) = \varphi_{r_p}(S) \cap P \tag{9.4}$$

where L the liquid phase and φ_{r_p} is the closing operation, which is expressed by:

$$\varphi_r(S) = S \oplus S_B(r) \ominus S_B(r) \tag{9.5}$$

where $S_B(r)$ is the structuring element of sphere of radius r, $\ominus$ is the Minkowski substraction (or erosion). In this work, we assume that the system is perfectly wetted and the contact angle is 0°.

A textbook example is provided in Fig. 9.1: capillary condensation in a conical pore. In a conical pore, the curvature radius decreases linearly in function of pore depth. According to the Kelvin equation, the apex region is filled first with condensed liquid at low pressure. The local curvature radius of liquid-vapour interface and solid-vapour interface should be equal or greater than the Kelvin radius.

As shown in the figure, the closing operation fills the regions of small curvature radius first, and a spherical-cap meniscus is formed on the vapour-liquid interface (Fig. 9.1 (A)). The curvature radius of every point on the spherical meniscus equals the Kelvin radius. The spherical cap is tangent to the conic solid wall, so the curvature radius at the boundary of the meniscus is also equal or greater than the Kelvin radius. The curvature radius of the remaining vapour-solid interface is greater than the Kelvin radius. Accordingly, the interface resulting from the closing operation satisfies the Kelvin equation, and the capillary condensation phenomenon is simulated.

With increasing pressure, the Kelvin radius increases, the meniscus propagates, and fills the space of large size (Fig. 9.1 (B)). Even when Kelvin radius is larger than the radius of the cone base, the meniscus becomes the arc of a larger pore outside the conical pore (Fig. 9.1 (C)). The contact angles are no longer 0°, but the

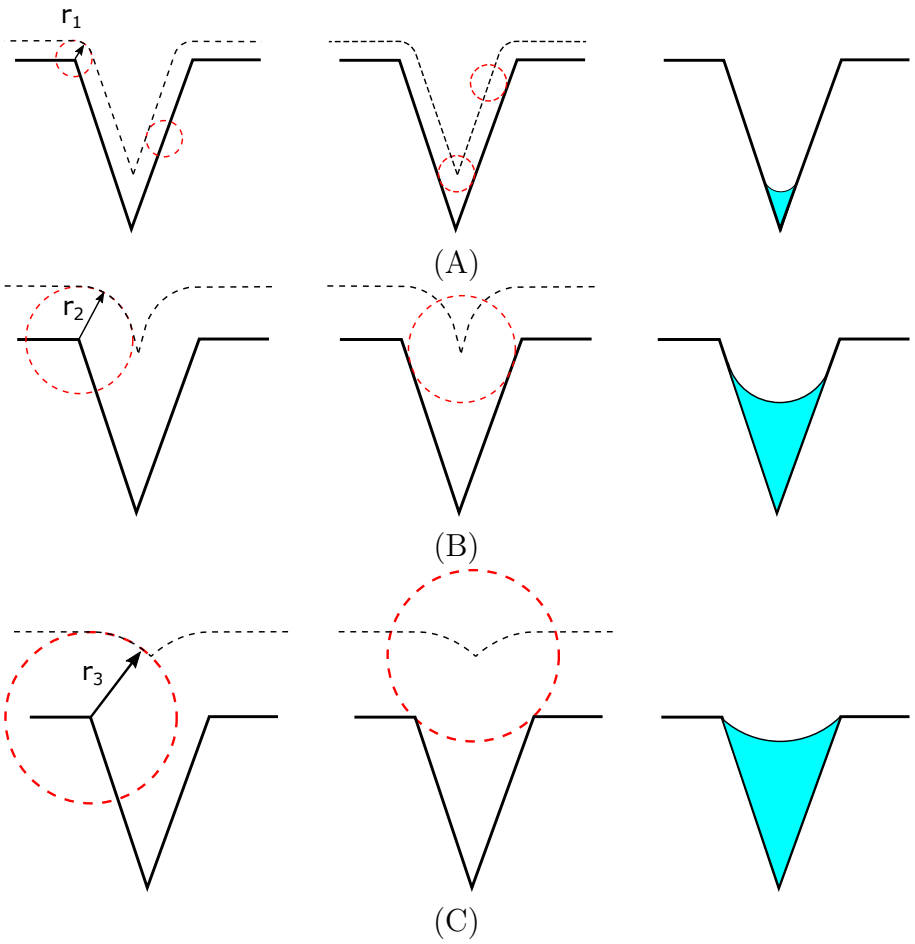

Figure 9.1: 2D sections of closing operations in a conical pore (solid black line). The dilation operation is shown with dotted black line in the left column. The erosion operation is shown in the middle column. The resulting liquid condensation is shown in blue in the right column. (A),(B) and (C) correspond to increasing size of the spherical structuring element (dotted red line).

curvature radius becomes negative at the borders of the arc and does not change the satisfaction to Kelvin equation.

Another typical example of capillary condensation is the cylindrical pore. Fig. 9.2 is a cylindrical pore with one side open and the other side closed. Capillary condensation occurs first at the corners, where condensed liquid flatten and smoothen the vapour/liquid interface. The main space of the porosity remains empty until the pressure reaches the critical radius, and the pore space is filled all at once.

In practice, approximate spherical structuring elements are used in a discrete grid. The approximations, like rhombicuboctahedron, are not accurate to probe the pore size and to reproduce the menisci. Alternatively, the closing operation with spheres can be realized using Euclidean distance transforms (Maurer et al., 2003), as the implementation in (Münch & Holzer, 2008). The distance map, denoted by $d_S(x), x \in P$, is the distance from a coordinate x to the closest solid-pore interface. The dilation $\delta_r(S)$ of the solid phase is obtained simply by an inferior threshold:

$$\delta_r(S) = S \oplus S_B(r) = \{x | x \in P, d_S(x) < r\} \tag{9.6}$$

For the following erosion, the distance map is recalculated from the pores Dil^c, and

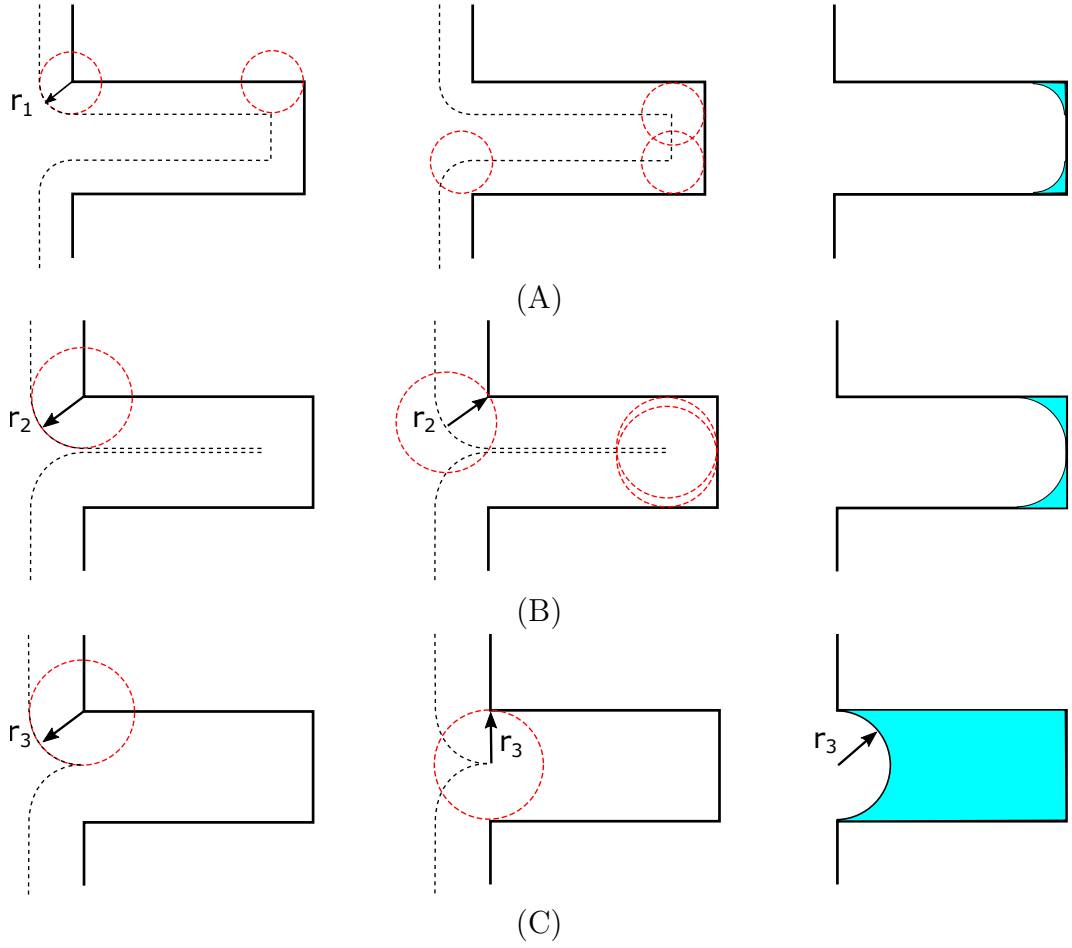

Figure 9.2: 2D sections of closing operations in a cylindrical pore (solid black line). The dilation operation is shown with dotted black line in the left column. The erosion operation is shown in the middle column. The resulting liquid condensation is shown in blue in the right column. (A),(B) and (C) correspond to increasing size of the spherical structuring element (dotted red line).

a superior threshold is taken to form the condensed liquid.

$$\varphi_r(S) = \delta_r(S) \ominus S_B(r) = \{x | x \in \delta_r(S), d_{\delta_r(S)^c}(x) > r\} \tag{9.7}$$

The distance map for dilation is calculated only once during the whole process, but that for erosion should be recalculated for each radius r. After the closing operation, the areas where the curvature radius is inferior to r_p are filled, the Kelvin equation is locally satisfied, and we obtain an equilibrium state in the adsorption process. The increasing pressure during adsorption corresponds to increasing sphere radius. The procedure is repeated with increasing sphere radius to obtain all equilibrium states.

The volume of condensed liquid at equilibrium state, denoted by $\Psi(r_p)$, makes a point on the nitrogen isotherm:

$$\Psi(r_p) = \mathcal{L}(L(r_p)) \tag{9.8}$$

where $\mathcal{L}(\cdot)$ is the Lebesgue measure. The total volume of adsorbed liquid at saturated pressure is $\Psi_\infty = \lim_{r \to +\infty} \Psi(r)$. In porosimetry isotherm plot, the normalized volume of condensed liquid (denoted by ψ) in function of relative pressure (denoted by p/p_0) or the equivalent Kelvin radius is often used.

$$\psi(r_p) = \Psi(r_p)/\Psi_\infty \tag{9.9}$$

Once we obtain the whole branch of adsorption $\psi(r_p)$, the continuous pore size distribution – the normalized intensity of pore volume in function of pore size, denoted by $I(r_p)$, is evaluated using differentiation (Münch & Holzer, 2008; Štěpánek et al., 2007):

$$I(r_p) = \frac{\mathrm{d}\psi(r_p)}{\mathrm{d}r_p} \tag{9.10}$$

9.2.4 Evaporation

During the adsorption process, each equilibrium state depends only on the pressure and on the solid's morphology, and is independent of previous states of the condensation. However during the desorption process, the evaporation depends on the previous state of condensed liquid. Due to the ink-bottle effect, small "neck pores" block the large pores from evaporation. A blocked large pore remains filled until at least one of the small "neck pores" is released. In practice, when the geometry is disordered and the porous structure is complex, it is difficult to judge the role of "neck pore".

We notice that the evaporation occurs only from exterior to interior. It depends both on the local curvature radius and on the connection to the exterior vapour reserve. A criterion is then proposed: at a given pressure, after the closing operation, if a pore is still connected to the exterior vapour reserve, it is released; if the pore is blocked by condensed liquid or by the solid phase, then it should remain filled.

The above criterion is fulfilled using a morphological operation – hole-filling. We assume that the borders of the domain ∂D is the vapour reserve. The operation follows the closing operation, and fills the pores that are not connected to any border of the domain. Indeed, this operation just eliminates some vapour-liquid interface and some vapour-solid interface around the blocked large pores, and does not change the remaining interface. It is still consistent with the Kelvin equation.

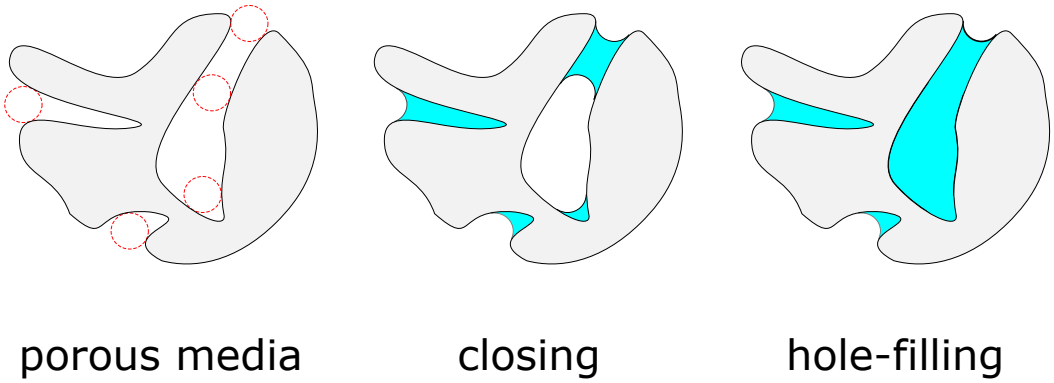

Figure 9.3: Closing operation followed by a hole filling operation to block the inner pores due to ink-bottle effect.

Therefore, there are two steps to obtain an equilibrium state during desorption: closing and hole-filling. The liquid phase as a function of sphere radius:

$$L(r_p) = H(\varphi_{r_p}(S)) \cap P \tag{9.11}$$

where $H(\cdot)$ is the hole-filling operator defined as:

$$H(A) = [R_{A^c}(\partial D \cap A^c)]^c \tag{9.12}$$

where R is the reconstruction operator. The decreasing pressure during the desorption process corresponds to the decreasing radius of the spherical structuring element. An equilibrium state during the evaporation is simulated, as shown in Fig. 9.3. The volume filled by the hole-filling operation creates a gap between the adsorption and the desorption branches, and is the origin of hysteresis. The width of the gap is the volume of blocked pores.

The morphological simulation of capillary condensation/evaporation have been validated on some simple geometries – narrow slit pore, ink-bottle pore and cylinder-sphere grid pore. We now apply our method on random models – Boolean models and multi-scale models. The discretization effects on the isotherms and the representativity of the resulting isotherms have been studied.

9.3 Capillary behavior of simple geometries

9.3.1 Slit pore

Capillary condensation occurs in a narrow slit pore and forms menisci at the edges of the pore. Even between two flat solid surfaces, where the local vapour-solid interface already satisfies the Kelvin equation, the condensation still occurs to achieve a lower energy state. The curvature radius of the menisci follows the Kelvin equation.

We consider a slit pore between two flat surfaces (Fig. 9.4 (A)). When nitrogen vapour pressure is low, or more precisely, when the Kelvin radius is less than half of the pore width, no condensation occurs at this stage. When the vapour pressure increases, the equivalent curvature radius becomes larger than half of the pore width, condensation occurs and the menisci is formed (Fig. 9.4 (B)).

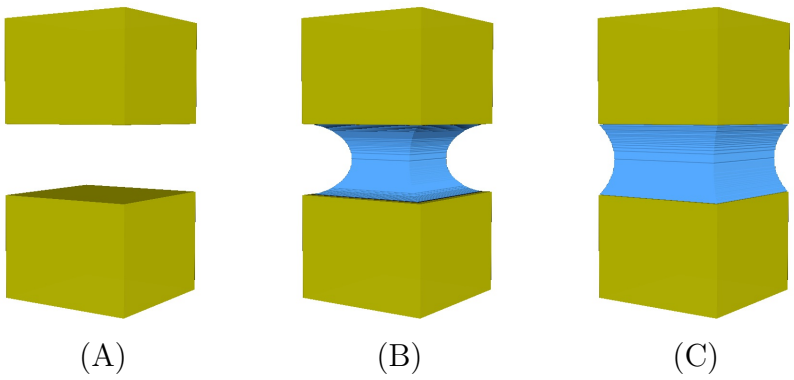

Figure 9.4: Condensation of liquid between two flat surface.

Since the pore is open, without ink-bottle effect, there is no hysteresis loop in the condensation isotherm, and the adsorption-desorption process is completely reversible. As shown in Fig. 9.5, fluctuations of the liquid volume, occurring when the curvature radius is large, are due to discretization effects.

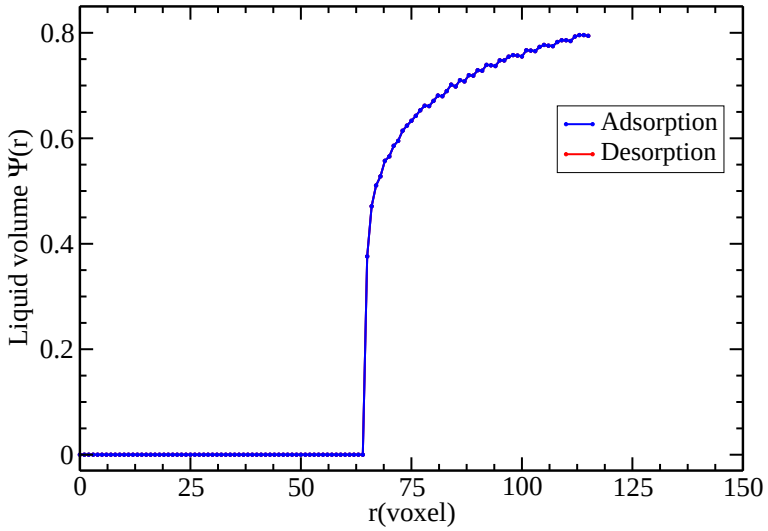

Figure 9.5: Nitrogen adsorption-desorption hysteresis curve simulated between two flat surfaces.

It should be mentioned that, according to the Kelvin equation, the narrow slit pore between two convex or flat obstacles are not necessarily filled by liquid, because the local vapour-solid interface curvature is zero or negative, which already satisfies the Kelvin equation. In this case, there are two different equilibrium states that both satisfy the Kelvin equation: condensation or no-condensation. The Kelvin equation cannot tell the choice of the two states. The thermodynamics during condensation and the energy states have strong influence on the choice. In terms of surface energy, for a wetting solid/liquid interface, the capillary condensation may occur between two close surfaces to achieve a lower energy state. However, the formation of the condensed liquid and the meniscus between two surfaces needs an activation energy, which depends on the distance between them. When the slit pore is narrow enough, the obtained condensed liquid is realistic – the result predicted by our approach. If we use the "virtual capillary condensation" method proposed by Stepanek et al. (2007), whose condensation depends only on the local curvature, there is no

condensation in the slit pore, This is one of the main differences between the two approaches. In this work, we focus only on the capillary behavior governed by the Kelvin equation. The choice between different equilibrium states remains an open question, which requires further study with the thermodynamic effects taken into account.

9.3.2 Ink-bottle pore

An ink-bottle pore consists of two embedded cylindrical pores having the same center axis (Fig. 9.6). Here we take diameters and heights of the cylinders measured manually from the paper of Stepanek et al (2007). The radius of the outer cylinder, denoted by r_1, is 50 voxels and that of the inner pore, denoted by r_2, is 100 voxels. We apply the capillary condensation simulation on the ink-bottle pore (3D view in Fig. 9.6 and obtain the condensation isotherm (Fig. 9.7).

The condensation occurs first at the corners of the inner pore, when the Kelvin radius r_p is inferior to the radius of the outer cylinder pore r_1 (Fig. 9.6A). When the Kelvin radius is larger than r_1, the outer pore is filled by condensed liquid, and the hemispherical menisci is formed with sphere radius r_1 (Fig. 9.6B). The condensation continues in the inner pore with increasing curvature radius, until it reaches the radius of the maximum sphere r_{max} that can fit in the pore (Fig. 9.6C). It should be noted that the r_{max} is less than r_2 because the inner pore is not deep enough to fit a larger sphere.

During the evaporation process, the Kelvin radius r_p decreases. When r_p is inferior to the maximum sphere radius r_{max}, the inner pore would not be released because it is not connected to the outer vapour reserve. Vaporization occurs only on the surface of the outer pore. The radius of the menisci decreases (Fig. 9.6E), until it reaches r_1. The outer cylindrical pore is then released, together with the inner pore (Fig. 9.6F). Some condensed liquid remains at the corners of the inner pore. The latter is vaporized with decreasing pressure.

The capillary condensation/evaporation simulation 2D sections on slit pore and ink-bottle pore is compared with that of (Libby & Monson, 2004) obtained by density functional theory. The results are qualitatively consistent (no quantitative data available). The resulting isotherms are also compared with that of Stepanek (Štěpánek et al., 2007) obtained by the virtual capillary condensation method. Isotherms are quantitatively very similar regarding the filling pressure of the inner pore (Fig. 9.7 from point (C) to point (D)), the release pressure of the inner pore (Fig. 9.7 from point (E) to point (F)). However, the obtained pressure when the outer pore is filled (Fig. 9.7 from point (A) to point (B)) is different in the two approaches. This is because the two methods predict two different local minima. Both the hemispherical vapour/liquid interface produced by our method and the cylindrical vapour/solid interface predicted by the virtual condensation method satisfy the Kelvin equation. The choice of the equilibrium states depends on other thermodynamic factors, which needs further investigation. However, our simulation on the ink-bottle pore is consistent with the results obtained by DFT and Monte Carlo simulation by Libby & Monson, contrary to the method of Stepanek.

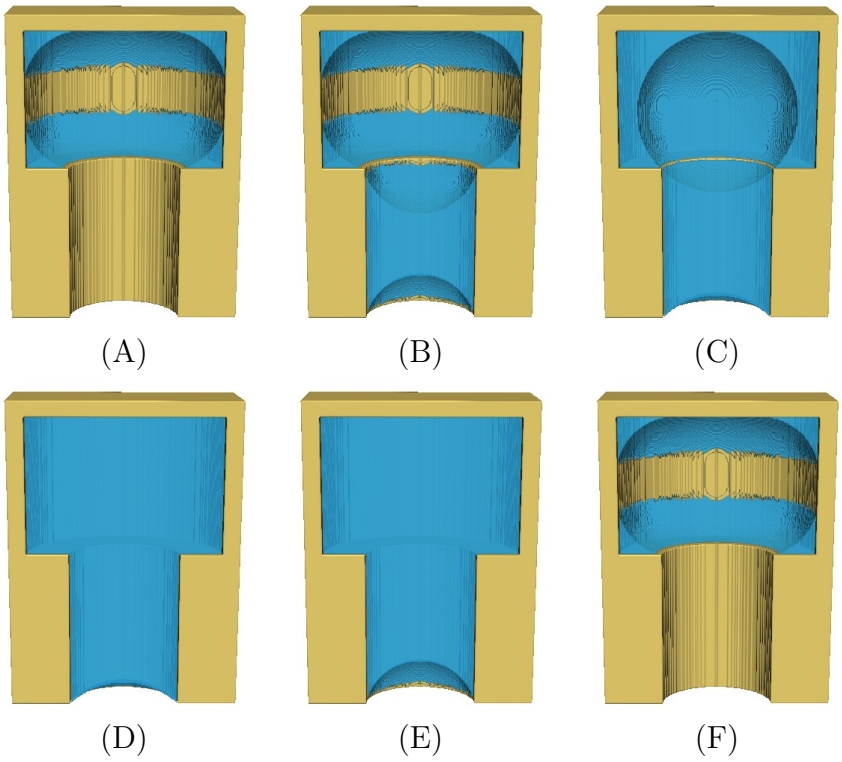

Figure 9.6: Ink-bottle pore with condensed liquid in blue and solid in yellow. The images from (A) to (D) are equilibrium states during adsorption at increasing pressure. The images (E) and (F) are equilibirum states during desorption at decreasing pressure. The pressures are marked in the Fig. 9.7 (A, ..., E).

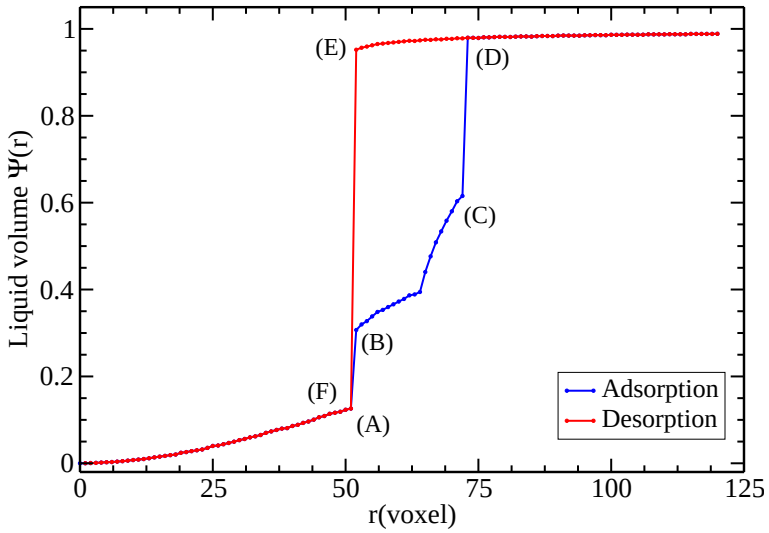

Figure 9.7: Nitrogen adsorption-desorption hysteresis curve simulated on the ink-bottle pore by our approach. The shape of the liquid-vapour interface of each marked pressure point is represented in Fig. 9.6 (A, ..., E).

9.3.3 Cylinder-sphere grid pore

We now consider a periodic porous network that consists of spherical and cylindrical pores (Fig. 9.8A). There are 8 spherical pores in the system, connected by cylindrical pores. Only the cylindrical pores are connected directly to the outer space. This microstructure can be viewed as a porous network with strong ink-bottle effect. The radius of the cylindrical and spherical pores, denoted by r_c and r_s, are respectively 24 voxels and 72 voxels. We accordingly expect two peaks in the pore size distribution.

During the adsorption process, the capillary condensation doesn't occur when the Kelvin radius r_p is inferior to r_c. When $r_s > r_p \geq r_c$, the cylindrical pores are filled (Fig. 9.8 (B) and (C)). When $r_p \geq r_s$, the whole porous network is filled by condensed liquid (Fig. 9.8 (D)). In the simulated isotherm in Fig. 9.9, we see two steps, corresponding to the two pore sizes. The ink-bottle effect is also reproduced in this regular pore grid – the liquid in the spherical pores are released only after the release of the cylindrical pores.

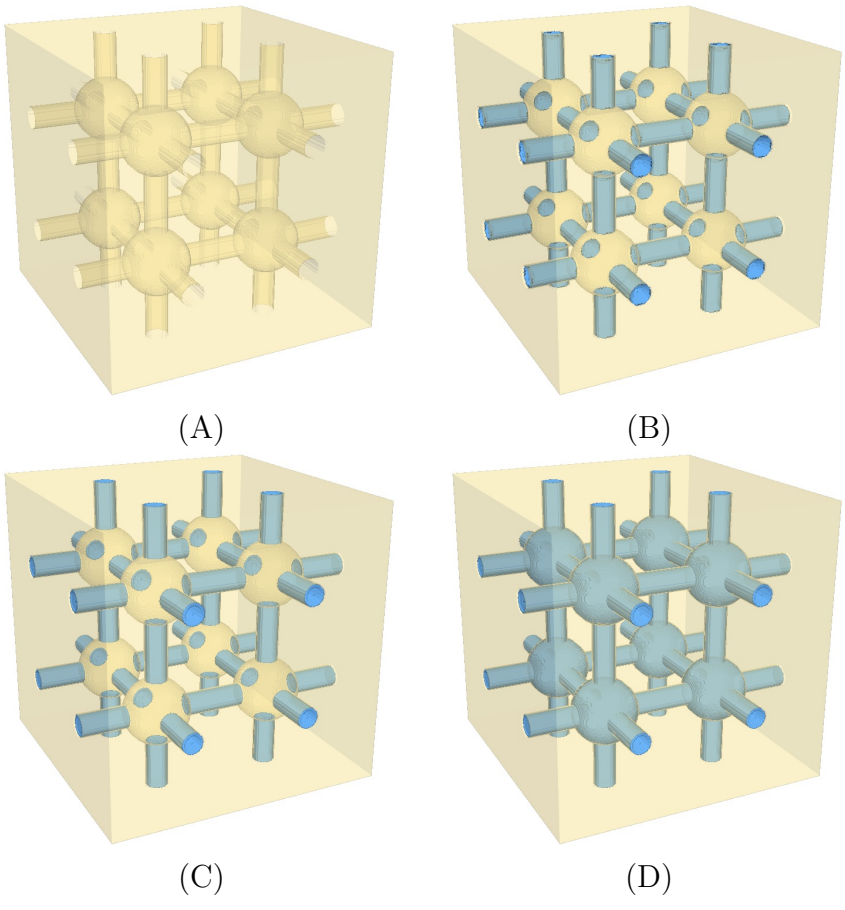

Figure 9.8: Condensation in a regular cylinder-sphere grid pore.

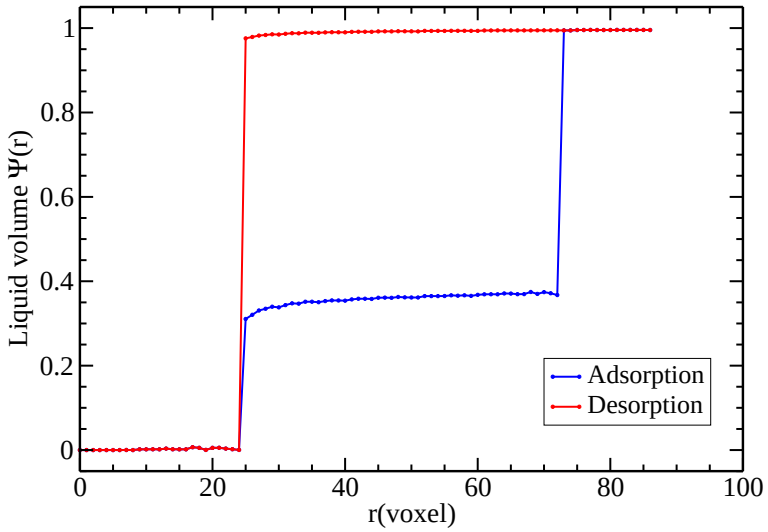

Figure 9.9: Capillary condensation/evaporation isotherm simulated on the regular pore grid.

9.4 Capillary behavior of Boolean models of spheres

We now consider a disordered random porous medium, namely Boolean model of spheres. The porosity is the space between the spheres or obstacles, so that the shape and size of the pore volume fraction is a random distribution. In the simulation, we take spheres of diameter 50 voxels at a volume fraction of 0.5, and system volume $256 \times 256 \times 256$ voxels. The condensation and evaporation processes are shown respectively in Fig. 9.10 and Fig. 9.11, together with the isotherm in Fig. 9.12.

Condensation first occurs at the corners of intersections and in the narrow space between two spheres. With increasing Kelvin radius, small pores are then filled (Fig. 9.10 (B)), and vapour "bubbles" are formed inside the microstructure (Fig. 9.10 (C)). When the pressure is high enough, the Kelvin radius is large enough for the condensed liquid to fill the whole porosity.

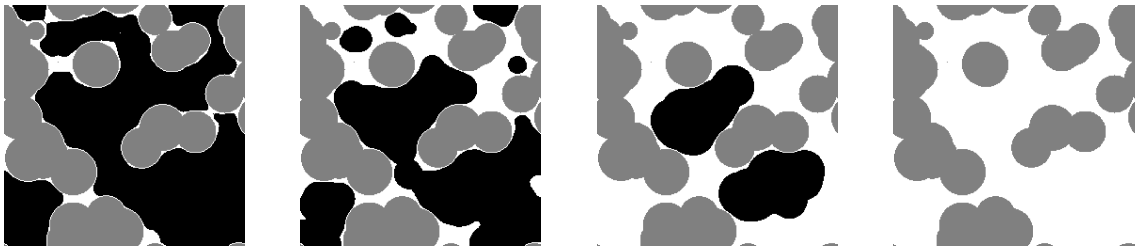

(A) (B) (C) (D)

Figure 9.10: 2D sections of equilibrium states during the capillary condensation. Vapour phase is in black, solid phase is in grey and liquid phase is in white. The four graphics correspond to increasing Kelvin radius.

During the desorption process, large pores at the boundary that are connected to the exterior vapour reserve are released first (Fig. 9.11). Because of the ink-bottle effect, some large pores are blocked inside from releasing. The 3D views of the liquid

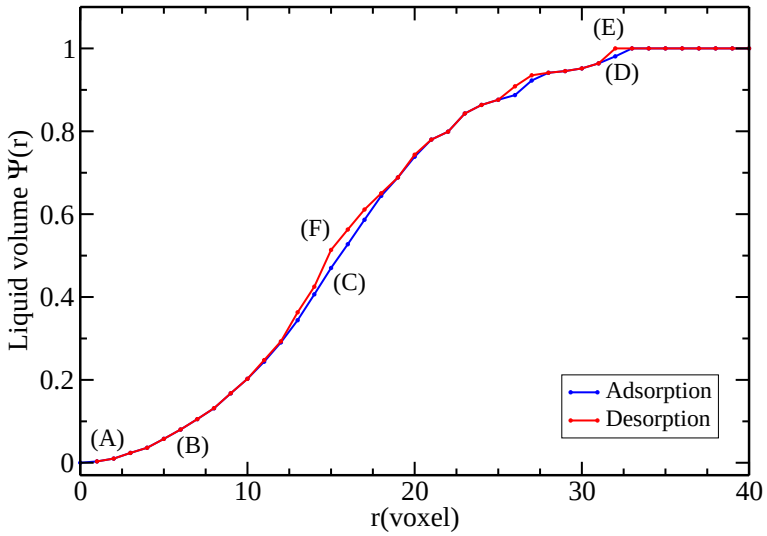

Figure 9.12: Capillary condensation/evaporation isotherms simulated on the Boolean model of spheres. The markers (A F) correspond to the images in Fig. 9.13.

phase condensation and vaporization are presented in Fig. 9.13, together with the isotherm in Fig. 9.12.

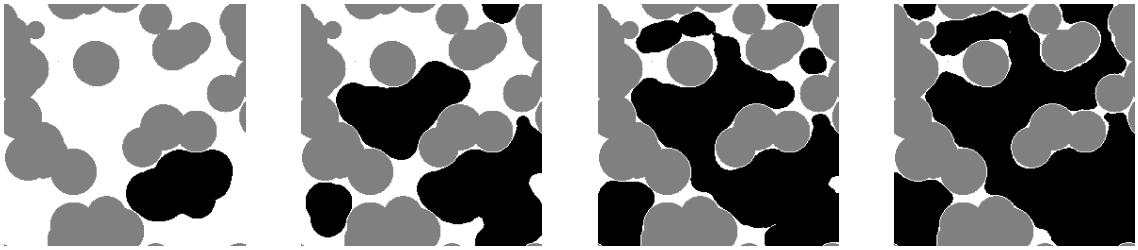

Figure 9.11: 2D sections of equilibrium states during the capillary evaporation. vapour phase is in black, solid phase is in grey and liquid phase is in white. The four graphics correspond to increasing Kelvin radius.

As shown in the isotherm, a very weak hysteresis is obtained for the one-scale Boolean model. We then generate three microstructures of Boolean models with the same system volume, the same volume fraction $f = 0.5$ and different sphere radii. The isotherms of the three microstructures are represented in Fig. 9.14: the smaller the spheres are, the greater the hysteresis is. The difference is an effect of boundary condition. This is discussed in detail in Sec. 9.5 (representative volume element).

9.5 Representative volume element

9.5.1 Finite-size effects

Clearly hysteresis in sorption isotherm is related to the amount of large pores that are not well-connected to the boundary of the volume. The system size plays an important role in determining the connection of the porous network to the exterior vapour reserve. To study the boundary effect of the microstructure on the isotherms,

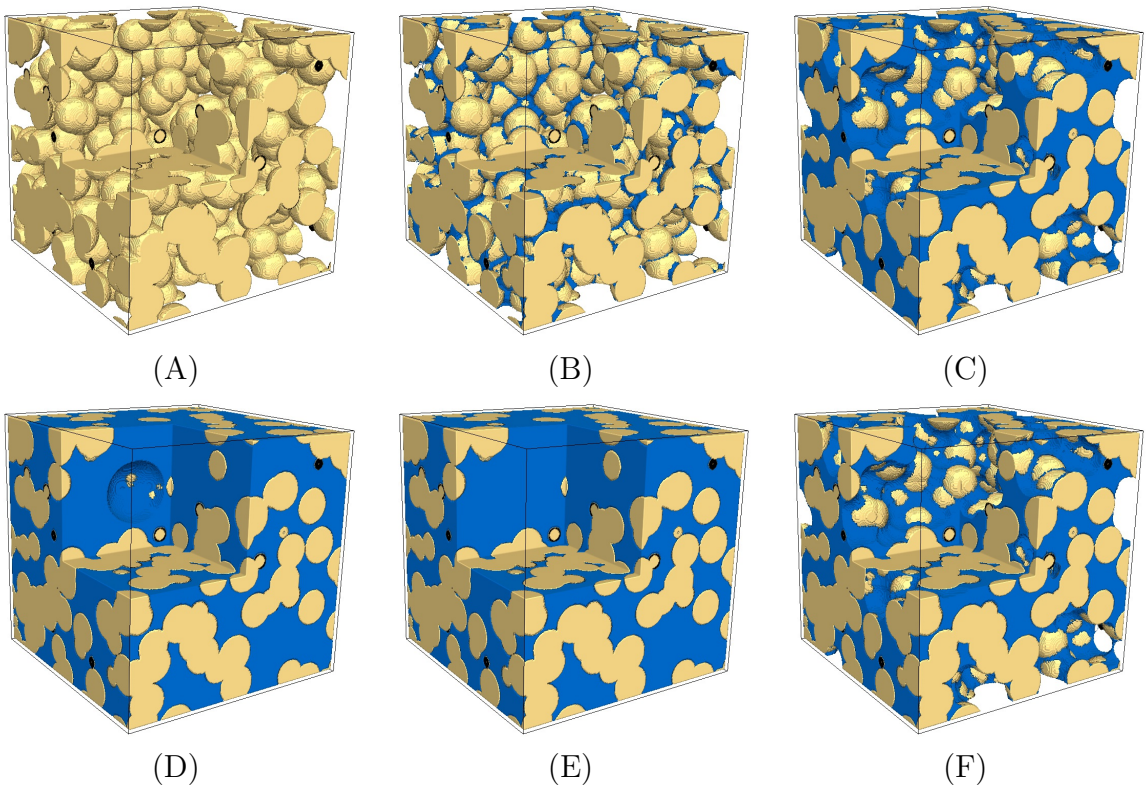

Figure 9.13: Equilibrium states during capillary condensation/evaporation on a Boolean model of spheres. The images correspond to the markers (A F) in Fig. 9.12

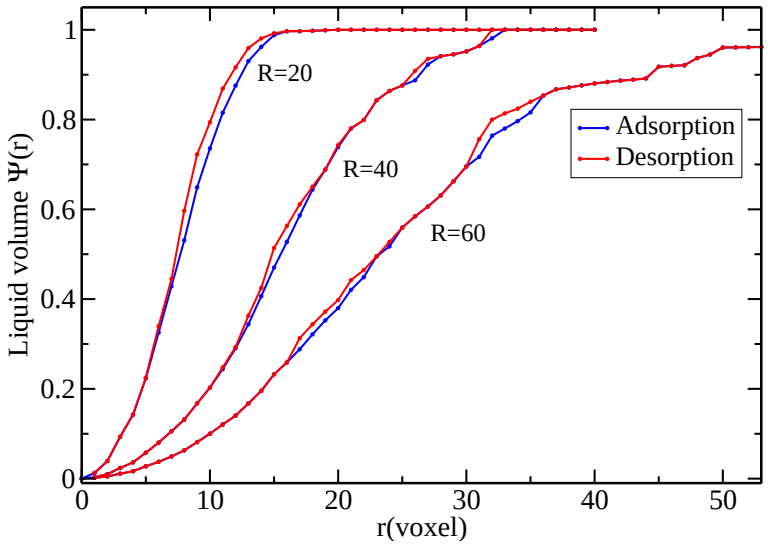

Figure 9.14: Capillary condensation (blue) and evaporation (red) isotherms of Boolean models of spheres, of increasing radius $R = 60$ voxels, $R = 40$ voxels and $R = 20$ voxels (bottom to top).

we consider three realizations of Boolean models of obstacle spheres of radius 20 voxels in different volumes: 256^3 voxels, 512^3 voxels and 1024^3 voxels (Fig. 9.15 (A)). The number of spheres in the three microstructures increase by a factor of 8. A significant difference between the three hysteresis is observed: the hysteresis increases when the number of the spheres increases, i.e. the volume is more representative of a macroscopic sized mesoporous sample. Furthermore, as expected, the desorption branch is also smoother when the microstructure is more representative. The difference is amplified for Boolean models of spheres of radius 10 voxels (Fig. 9.15 (B)). Compared to the desorption branches, the adsorption branches are much less sensitive to the system size.

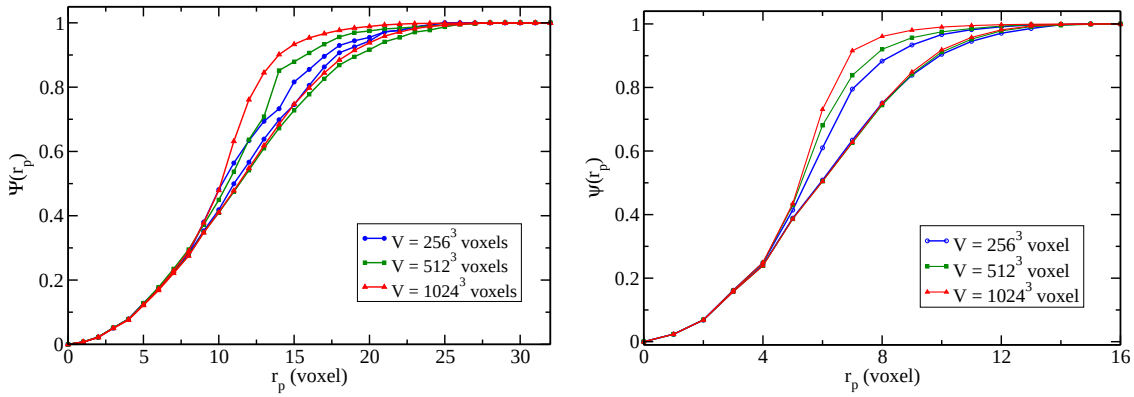

Figure 9.15: Capillary condensation isotherm in three Boolean models of spheres of different sizes. the volume fraction of solid phase is 0.65. (A) The sphere radius is 20 voxels. The number of spheres are 525 (for $V = 256^3$ voxels), 4205 (for $V = 512^3$ voxels) and 33639 (for $V = 1024^3$ voxels). (B) The sphere radius is 10 voxels. The number of spheres are 4205 (for $V = 256^3$ voxels), 33639 (for $V = 512^3$ voxels) and about 2.7×10^5 (for $V = 1024^3$ voxels).

The adsorption branches converge to an asymptotic curve when the number of spheres becomes very large (Fig. 9.15). However, the corresponding asymptotic curve has not been obtained numerically for desorption. Computations were not carried out for samples of size larger than 1024^3 voxels due to the high memory requirements. A solution to this problem is proposed in Subsection 9.5.3. The algorithm is implemented in Matlab script, and the most time and memory consuming process is the distance transform. In our program, the fast algorithm for computing the exact Euclidean distance transform proposed by Maurer et al. is used. A pair of equilibrium states, respectively in the adsorption branch and in the desorption branch at the same Kelvin radius, takes 3 minutes for a system of 1024^3 voxels (with CPU 24×2.67 GHz and RAM 100 GB). To achieve the convergence of the desorption branch, a compromise should be made between the resolution and the volume of microstructure.

9.5.2 Effect of discretization

To study the effect of resolution, we consider a Boolean model of spheres of diameter 40 voxels. A microstructure is realized in volume 1024^3 voxels. Downsampling is

then performed on the microstructure, with decimation factors of 2 and 4. The capillary condensation and vaporization simulation isotherms are shown in Fig. 9.16. The horizontal axis of the isotherms of the downsampled microstructures have been corrected by multiplying by their decimation factors. As shown in Fig. 9.16, at low resolution, the adsorption branches and the desorption branches are both less smooth and are both shifted to the right, which means an overestimation of the pore size.

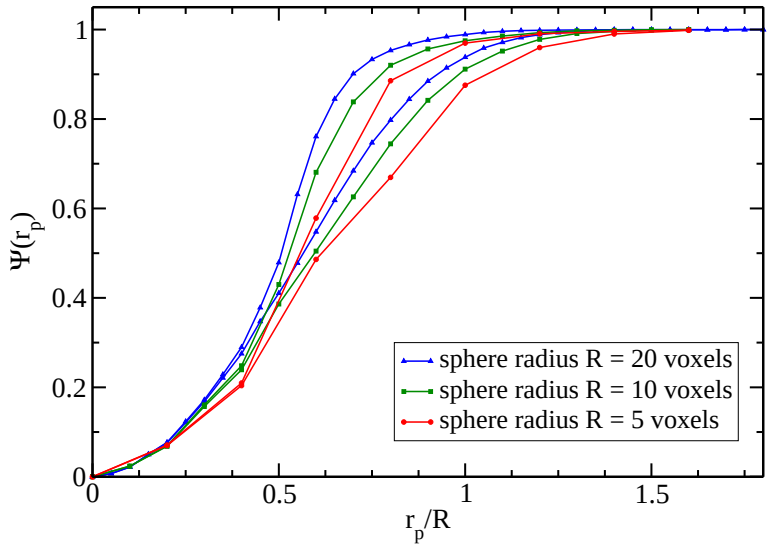

Figure 9.16: Capillary condensation isotherm in a Boolean models of spheres at increasing resolutions.

The simulated isotherms are very sensitive both to the system volume and to the resolution. Computations on very large volumes (more than 2048^3 voxels) are not practical.

Changes of the boundary condition (use of a surface or a point where vapour is injected) and the use of periodic microstructures were considered, but are insufficient to fix this problem. As observed in experimental isotherms (Fig. 5.1), typical type IV isotherm in porosimetry (see Sing et al., 1985), the desorption branches remains at 1 until the decreasing pressure reaches a certain threshold. The same phenomenon has also been observed in the literature (Liu & Seaton, 1994). Therefore, to address the problem, we take into account the desorption threshold of the vapour phase explicitely in the next subsection.

9.5.3 Percolation of the vapour phase

In porosimetry, the pores which are directly connected to the exterior will be released once the local curvature radius satisfies the Kelvin equation. However, most pores will remain filled because of the ink-bottle effect. The proportion of the released exterior pores tends to 0 when the system volume tends to infinity, which is the case in real experiments. In the simulations, due to the finite system size, the desorption branch does not remain at 1, but decreases along with the pressure decreasing. We identify the pressure value when the desorption branch appears to the desorption threshold of the vapour phase. Thus in capillary evaporation simulation, we should consider the percolation of the vapour phase as the beginning of the desorption.

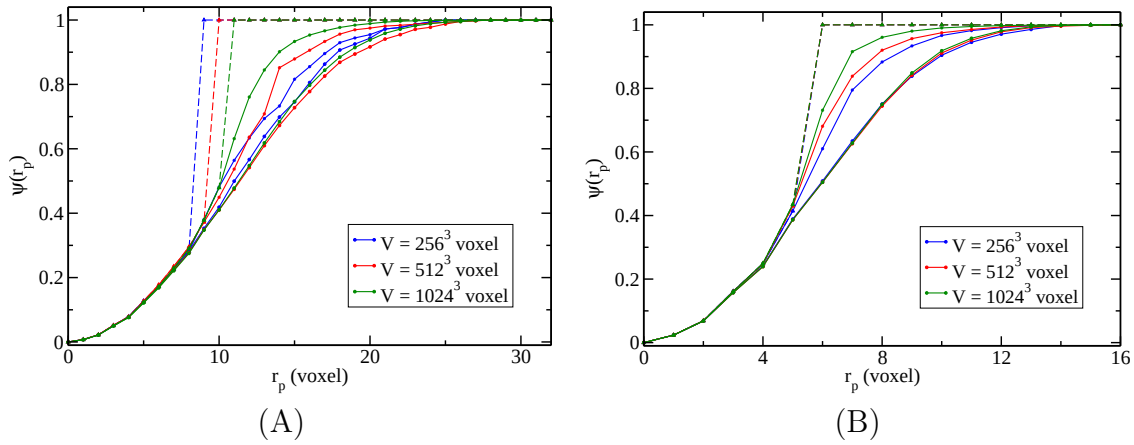

Figure 9.17: Capillary condensation/evaporation isotherms with percolation correction of Boolean models of spheres. The volume fraction of solid phase is 0.65. (A) Sphere radius is 20 voxels. The number of spheres are the same as Fig. 9.15(A). (B) Sphere radius is 10 voxels. The number of spheres are the same as Fig. 9.15(B).

We accordingly check for the percolation of the vapour phase at each equilibrium state. Connected components are used: if there exists a connected component of the vapour phase which reaches the 6 faces of the cube, the vapour phase percolates. It is possible to consider a smaller number of faces to determine the desorption threshold since our material is isotropic. This has not been explored in the present work. Using the information of percolation, the desorption branch is adjusted to simulate the evaporation in an infinite-size system as follows:

$$\psi'(r) = \begin{cases} \psi(r), & \text{if } \exists j, \forall i \in \{1,2,...,6\}, \{C_G(r)\}_j \cap (\partial D)_i \neq \emptyset \\ 1, & \text{otherwise} \end{cases} \tag{9.13}$$

where ψ' is the normalized volume of condensed liquid for an infinite-size system, $(\partial D)_i, i = 1,2,...,6$ are the six faces of the cubic domain and $C_G(r)$ is the set of labeled connected components of the vapour phase $G(r)$, which reads:

$$G(r) = \{P^c \cup L(r)\}^c \tag{9.14}$$

For comparison, we take the same Boolean microstructures as studied in Fig. 9.15, and compute the corrected desorption branch using percolation (Eq. 9.13). The desorption branches of infinite-size systems are shown in dotted lines in Fig. 9.17. Figure 9.17(A) shows that the desorption threshold of the vapour phase in a Boolean model of spheres varies with respect to microstructure size. Fig. 9.17(B) shows that the desorption threshold converges with increasing representativity, and so do the desorption branches.

Does the discretization influence the value of desorption threshold? The desorption thresholds of the microstructures in Fig. 9.16 are estimated by simulation, with corrected desorption branch in dotted lines in Fig. 9.18.

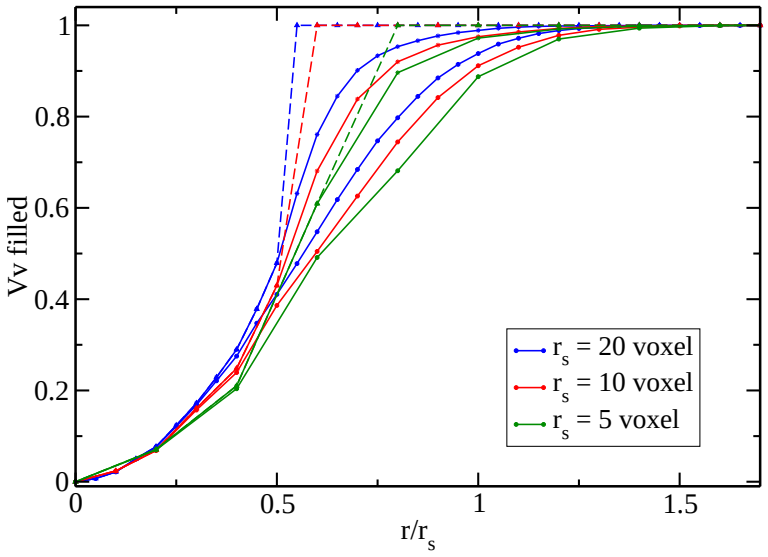

Figure 9.18: Capillary condensation/evaporation isotherms with percolation correction of Boolean models of spheres of difference radius. The volume fraction of solid phase is 0.65. The numbers of spheres are the same 33639.

Results shown in Fig. 9.18 demonstrate that for the same number of spheres, a worse resolution leads to an over-estimation of the desorption threshold. The isotherms obtained with the two higher resolution are close to one another. Smoother curves are obtained for the highest resolution. In the following, we take the highest resolution curves as that representative of a Boolean model of spheres. The latter is used for comparison with other models.

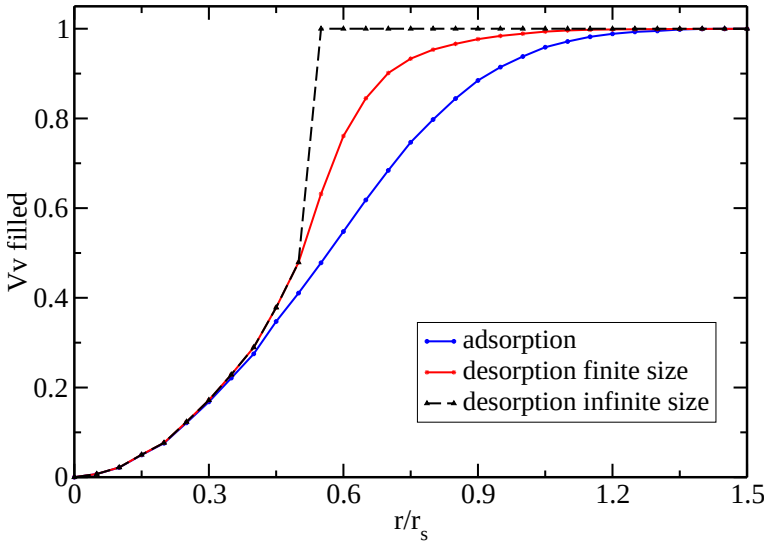

Figure 9.19: Capillary condensation/evaporation isotherms of a Boolean model of spheres with volume fraction of solid phase 0.65. The sphere radius is 20 voxels and the microstructure volume is 1024^3 voxels.

9.6 Capillary behavior of random models

9.6.1 Boolean models

We examine how the obstacle shapes affect the capillary condensation isotherms of Boolean models. Instead of spheres, cylinders with different ratio base/height are considered. These models are compared at the same volume fraction of solid phase p, the same specific surface area S_V, the same microstructure size of 512^3 voxels and the same resolution. The following obstacle shapes are considered:

- spheres of diameter 20 voxels
- oblate cylinders of diameter 40 voxels and height 10 voxels
- intermediate cylinders of diameter 20 voxels and height 20 voxels
- elongated cylinders of radius 15 voxels and height 60 voxels

The isotherms obtained from the condensation/vaporization simulation are rather close (Fig. 9.20). It is explained by the fact that when the obstacles are uniformly dispersed in the 3D space, the pore size in a Boolean model is mainly determined by the number of obstacles in the space, and is not sensitive to the shape of obstacles. When the volume fraction of the obstacles is fixed, the number of obstacles is strongly influenced by the specific surface area, that's to say, the higher the specific surface area is, the smaller the obstacles are, the more obstacles we need to satisfy the volume fraction, and the smaller the pores's sizes are. For a Boolean model, if the volume fraction and the specific surface area are fixed, not much variation in the pore size distribution is observed. It gives us the insight that if we want more freedom in manipulating the pore size distribution by microstructure modeling, a one-scale Boolean model is not sufficient. Multi-scale models should be considered.

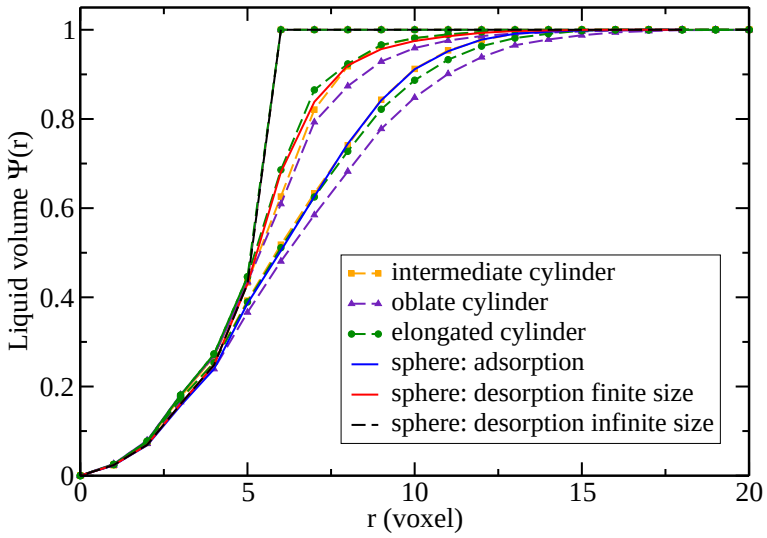

Figure 9.20: Capillary condensation/evaporation isotherms in a Boolean models of different obstacle shapes.

9.6.2 Two-scale model of spherical exclusions

We now focus on the capillary behaviors of multi-scale random models, in order to explore the effects of the different scales and parameters of the microstructure on the simulated isotherm and in particular on the hysteresis. We consider first the intersection of the complementary of two Boolean model of spheres, constructed as follows:

- A Boolean model of spheres of radius 36 voxels, with porous phase in spheres, denoted by X^c, of volume fraction $p_{X^c} = 25\%$
- A Boolean model of spheres of radius 12 voxels, with porous phase in spheres, denoted by Y^c, of volume fraction $p_{Y^c} = 25\%$
- A two-scale model of spherical pores, with porous phase, denoted by A^c and defined by:

$$A^c = X^c \cup Y^c \tag{9.15}$$

The volume fraction of 25% is chosen to make sure that the spheres do not percolate (the desorption threshold of a Boolean model is about 29%). The volume fraction of the porous phase A^c of the two-scale model is therefore $1-(1-25\%)^2 = 43.75\%$. The porous phase presumably percolates, but the small spherical pores will block large pores during the desorption. The model is a probabilist version of the combination of regular sphere-cylinder pores in Fig. 9.8. Its behavior in capillary condensation simulation is shown in Fig. 9.21. The rectangle hysteresis is reproduced, very similar to the curves in Fig. 9.8. The small spherical pores play the role of valves, and the critical pore size of the microstructure is the radius of the small pores.

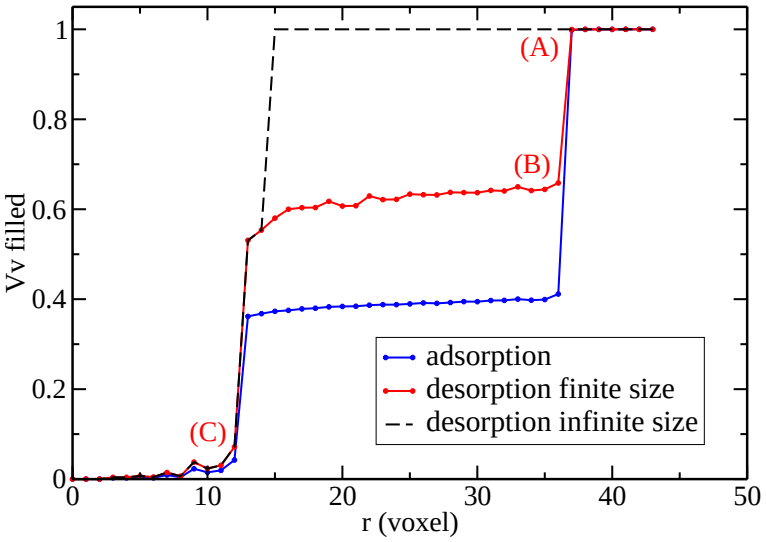

Figure 9.21: Capillary condensation/evaporation isotherm of the two-scale model A. The markers (A, B, C) on the desorption branch of the finite-size model correspond to the images in Fig. 9.22.

From point (A) to (B) in Fig. 9.22, the large pores connected to the exterior are released, but the entire vapour phase does not percolate. Percolation occurs when

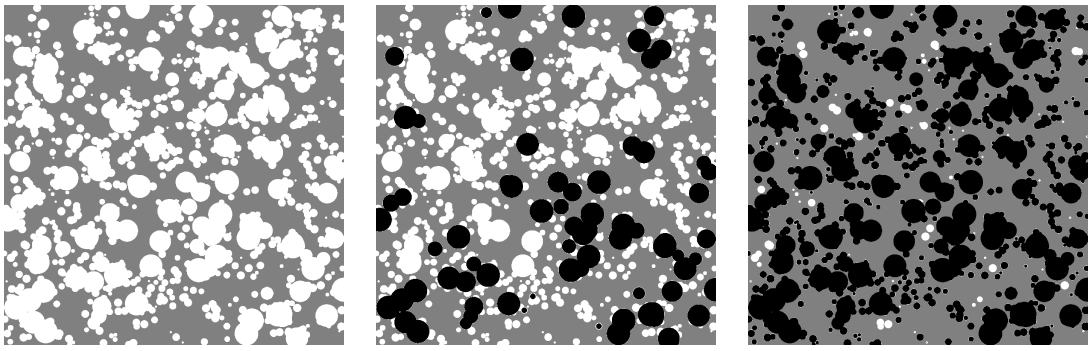

(A) (B) (C)

Figure 9.22: 2D sections at different steps of the desorption process on the two-scale model A. (A) $r_p = 37$ voxels (B) $r_p = 36$ voxels and (C) $r_p = 12$ voxels correspond to the markers on the desorption branch of finite-size model in Fig. 9.21.

the curvature radius reaches $r_p = 14$ voxels, before the release of most of the small pores. Indeed the small pores enlarge the intersection zones between the largest pores and facilitate the pore connections.

9.6.3 Two-scale model with hardcore exclusions

We then try to eliminate the direct connection between the large pores, to highlight the role of the connection functionality of the small pores. We add a repulsion distance between the large spherical pores, and the two-scale model is constructed in the following way:

- A hardcore model of spheres of radius 36 voxels with repulsion distance 36 voxels. The porous phase, denoted by H^c, has volume fraction $p_{H^c} = 25\%$.
- A Boolean model of spheres of radius 12 voxels, with porous phase in spheres, denoted by Y^c, of volume fraction $p_{Y^c} = 25\%$.
- A two-scale model of spherical pores, with porous phase denoted by B^c, is considered. It is defined as:

$$B^c = H^c \cup Y^c \tag{9.16}$$

The capillary condensation isotherms simulated on the two-scale model is shown in Fig. 9.23. From (A) to (B) in the desorption process, only the pores directly connected to the boundaries are released. The interior of the microstructure remains filled by liquid, until the Kelvin radius reaches the radius of the small spherical pores, and then the whole porosity in the microstructure percolates.

The comparison of Fig. 9.24 (B) and Fig. 9.22 (B), shows that the released pores are located along the boundaries of the volume. It means the repulsion distance reduces the connections between the large pores. The isotherms of model B is also smoother with less perturbation.

9.6.4 Two-scale model with Poisson-fiber exclusions

In the above cases, the desorption threshold is determined by the radius of the small pores. The Poisson fibers could also be used to play the role of valves, replacing the

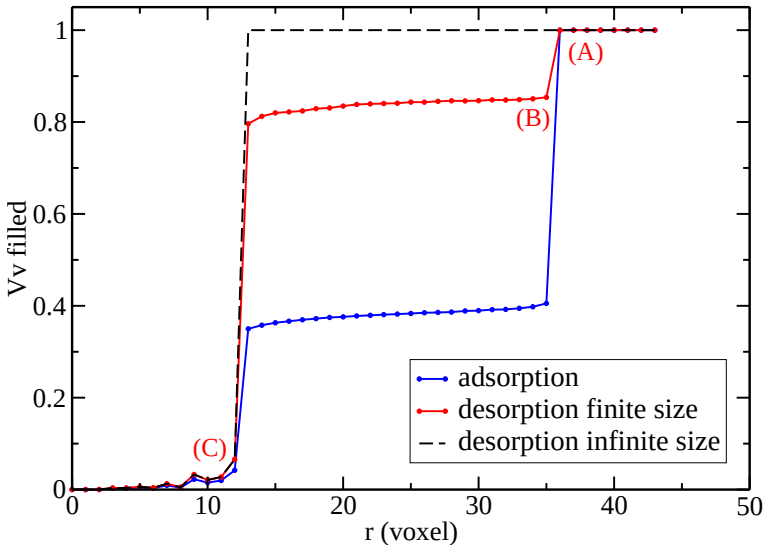

Figure 9.23: Capillary condensation/evaporation isotherm of the two-scale model B. The markers (A, B, C) on the desorption branch of the finite-size model correspond to the images in Fig. 9.24.

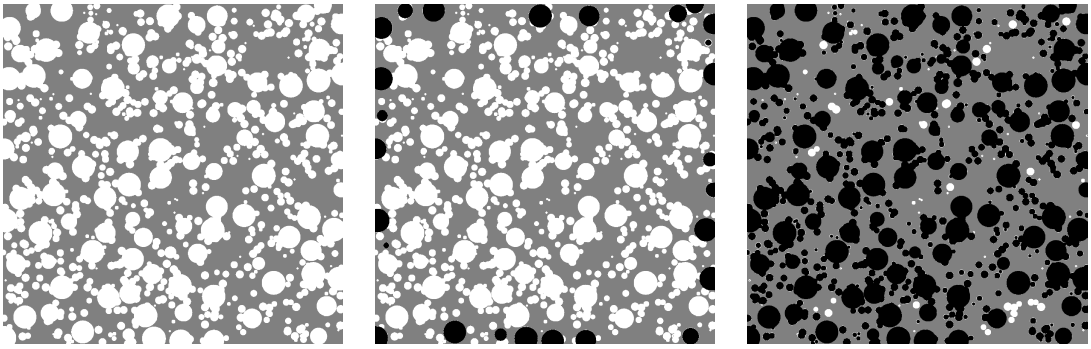

(A) (B) (C)

Figure 9.24: 2D sections at different steps of the desorption process on the two-scale model B. (A) $r_p = 36$ voxels (B) $r_p = 35$ voxels and (C) $r_p = 12$ voxels correspond to the markers on the desorption branch of finite-size model in Fig. 9.23.

spherical pores. We consider the following two-scale model:

- A Boolean model of spheres of radius 36 voxels, with porous phase, denoted by X^c, of volume fraction $p_{X^c} = 25\%$.
- A model of Poisson fibers of circular base radius 12 voxels, with porous phase, denoted by F^c, of volume fraction $p_{F^c} = 25\%$.
- A two-scale model of spherical and cylindrical exclusions, with porous phase denoted by C^c, is considered. It is defined as:

$$C^c = X^c \cup F^c \tag{9.17}$$

The porosimetry isotherm simulated on the two-scale model is shown in Fig. 9.25, together with the 2D sections illustrated in Fig. 9.26.

The capillary behaviors of the above two-scale models of exclusions showed a perspective that pore size distribution can be manipulated using the combination of multiple scales. The method is further developed in Chapter 10.

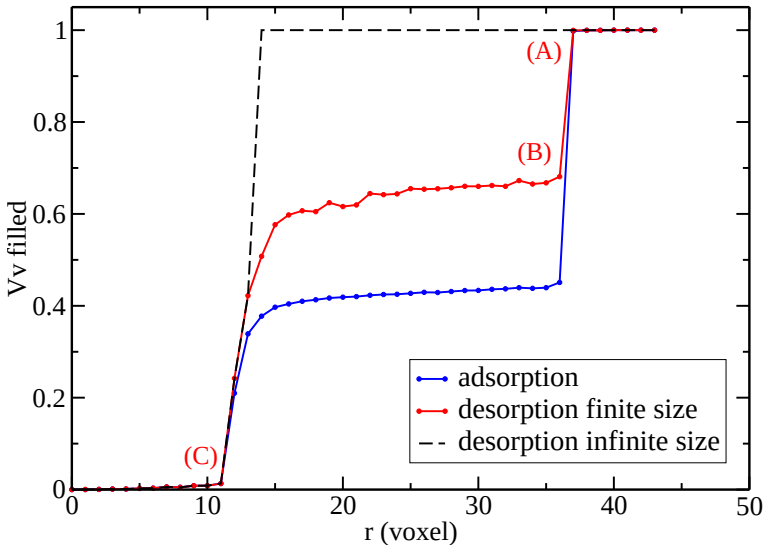

Figure 9.25: Capillary condensation/evaporation isotherm of the two-scale model C.

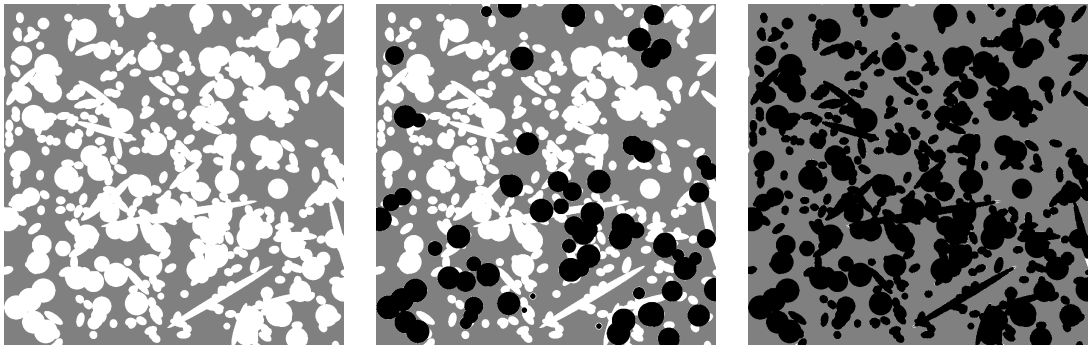

(A) (B) (C)

Figure 9.26: 2D sections during the desorption process of two-scale model C with Poisson fibers. (A) $r_p = 37$ voxels (B) $r_p = 36$ voxels and (C) $r_p = 11$ voxels correspond to the markers on the desorption branch of finite-size model in Fig. 9.25.

9.6.5 Two-scale model of inclusions and exclusions

We consider two two-scale models: First, a two-scale model of the intersection of two Boolean models of spheres of much different scales, with the solid phase denoted by D_1, is constructed. The larger scale plays the role of aggregations, while the small scale plays the role of primary grains. The model is a realistic description for materials like mesoporous alumina (Wang et al, 2015).

$$D_1 = X_1 \cap X_2 \tag{9.18}$$

where X_1 is the solid phase of a Boolean model of spheres of radius 40 voxels, at volume fraction $p_{X_1} = 0.8062$, and X_2 is the solid phase of a Boolean model of spheres of radius 5 voxels, at volume fraction $p_{X_2} = 0.8062$. Therefore, the volume fraction of the solid phase D_1 is: $p_{D_1} = p_{X_1} p_{X_2} = 0.65$.

Second, a two-scale model of the intersection of the complementary of a Boolean model of large spheres and a Boolean model of small spheres, with the solid phase

denoted by D_2, is constructed in the following way:

$$D_2 = Y_1^c \cap Y_2 \tag{9.19}$$

where Y_1 is the solid phase of a Boolean model of spheres of radius 20 voxels, at volume fraction $p_{Y_1} = 0.1$, and Y_2 is the solid phase of a Boolean model of spheres of radius 5 voxels, at volume fraction $p_{Y_2} = 0.7222$. Therefore, the volume fraction of the solid phase D_2 is: $p_{D_2} = (1 - p_{Y_1})p_{Y_2} = 0.65$.

For comparison purpose, we add a one-scale Boolean model of sphere of radius 5 voxels, with the solid phase denoted by D_3 at volume fraction $p_{D_3} = 0.65$. The three models have the same volume fraction of solid phase $p = 0.65$. The parameters of D_1 are chosen so that the number of large spheres in the cubic volume is the same as the number of small spheres in a large sphere. The volume fraction of large spheres in D_2 is chosen so that the large spheres do not percolate.

The simulated condensation/vaporization isotherms are shown in Fig. 9.27. At low pressure, a quick filling of the small pores is observed, and the three models have the similar behavior quantitatively. After that the pore space between small spheres in the model D_1 have been filled, condensed liquid begins a slow filling of the larger pores along with increasing pressure. The isotherm well combines the same behavior of two Boolean models at different scales.

In the model D_2, the scale effect is more evident. After the quick filling of the small pores, the large pores remain empty, until the Kelvin radius reaches the radius of the large spherical pores. At the beginning of the desorption process, the large spherical pores are partially released (those connected to the exterior vapour reserve). The pores between small spheres play the role of valves to control the release of the large spherical pores. Note that the desorption threshold of D_1 is much larger than D_2, because the complementary of a Boolean model is in good connection.

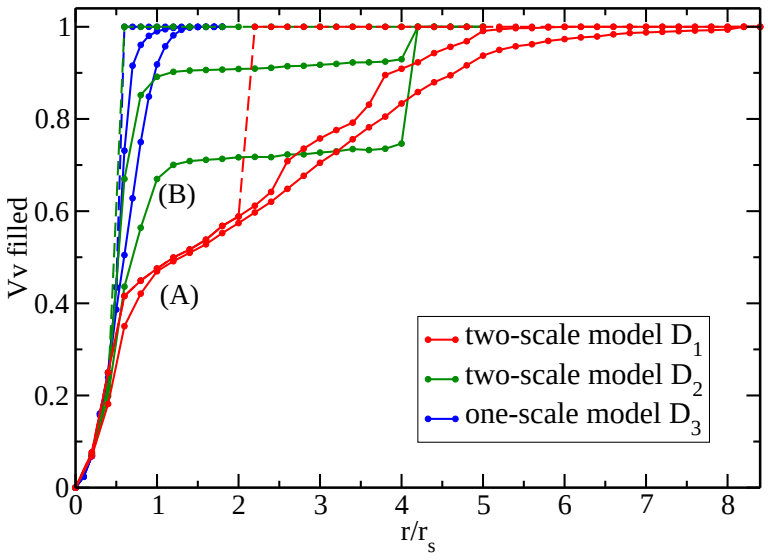

Figure 9.27: Capillary condensation isotherm simulated on one-scale and two-scale models.

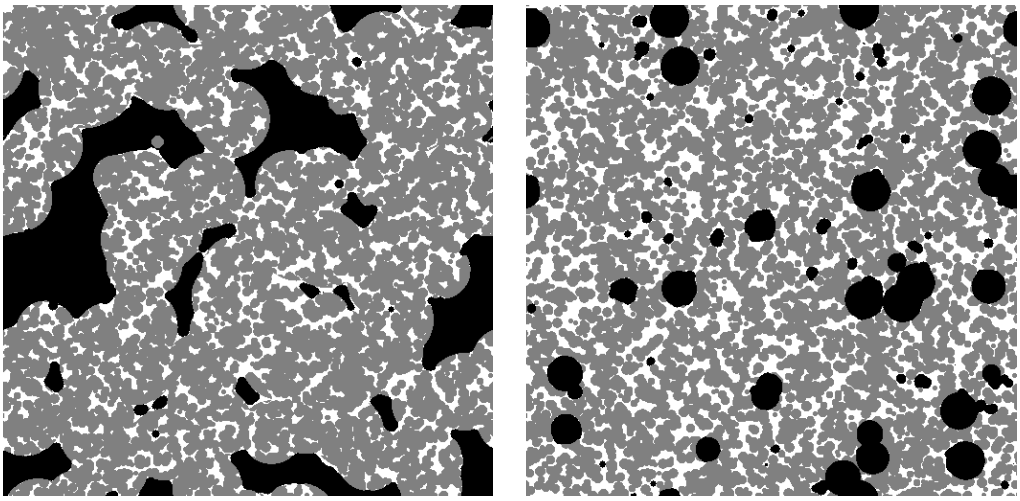

(A) (B)

Figure 9.28: 2D sections of capillary condensation simulation during the adsorption at r_p=7 voxels. (A) Two-scale model D_1. (B) Two-scale model D_2.

9.7 Conclusion

In this chapter, a procedure has been proposed to simulate the capillary condensation and evaporation in porous media. The method is entirely geometrical and relies on morphological operators. The latter is validated on simple geometries like slit pore and ink-bottle pores. The results are in agreement with the literature. The method is also applied to random models of porous media. Boundary effects introduce strong finite-size effects on random media. These effects have been corrected by taking into account the desorption threshold of the vapour phase.

The capillary behaviors of various random models have been simulated and investigated. Isotherms are not sensitive to the shape of obstacles in Boolean models. With the union and intersection of two Boolean models of spherical exclusions of different sizes, the "ink-bottle" effect is reproduced in the 3D disordered porous network. The repulsion distance between the spherical pores helps to control the size of the "neck-pore", and thus controls the desorption threshold. These preliminary results demonstrate perspectives in adjusting multi-scale model parameters to reproduce a prescribed isotherm. The topic is further investigated in Chapter 10.

Chapter 10

Microstructure modeling with porosimetry constraint

In chapter 9, the capillary condensation and evaporation occuring in Boolean models and two-scale Boolean models have been studied. A methodology has been employed to limit microstructure models with prescribed pore size. Use has been made of exclusion pores with spherical shapes.

This chapter further explores ways to control porosimetry isotherms with microstructure modeling. We start with a presentation of the experimental porosimetry isostherms of mesoporous alumina in Sec. 10.1. A multi-scale Boolean model with repulsion is used to reproduce the pore size distribution and the desorption threshold in Sec. 10.2. The behaviors of microstructures of mesoporous alumina are studied in Sec. 10.3. The effect of multilayer adsorption on the solid interface is talked about in Sec. 10.4. A three-scale model of platelets is proposed in Sec. 10.5 aiming at reproducing the experimental isotherms. In the last section, the limitations of the method is discussed. The parameters of the three-scale model are identified again and validated using TEM images.

10.1 Isotherms of mesoporous alumina

10.1.1 Experimental isotherm

The samples of mesoporous alumina under study have been characterized by nitrogen porosimetry at IFPEN, with isotherms shown in Fig. 5.1. The porosimetry curves of the three samples are close to each other. They follow typical type IV isothemrs (Sing et al., 1985) with gradual adsorption branches and steep desorption branches. The pressures for adsorptions and desorptions are also similar, which means that they have similar pore size distribution. The only evident difference is that the pore volume fraction of sample 2 is about 5% lower than two other samples.

10.1.2 Preprocessing with the FHH equation

The experimental isotherms contains information on multilayer adsorption, capillary condensation and liquid compressing. To highlight the capillary condensation, we use the method proposed by Cimono et al. (2013) to preprocess the isotherms.

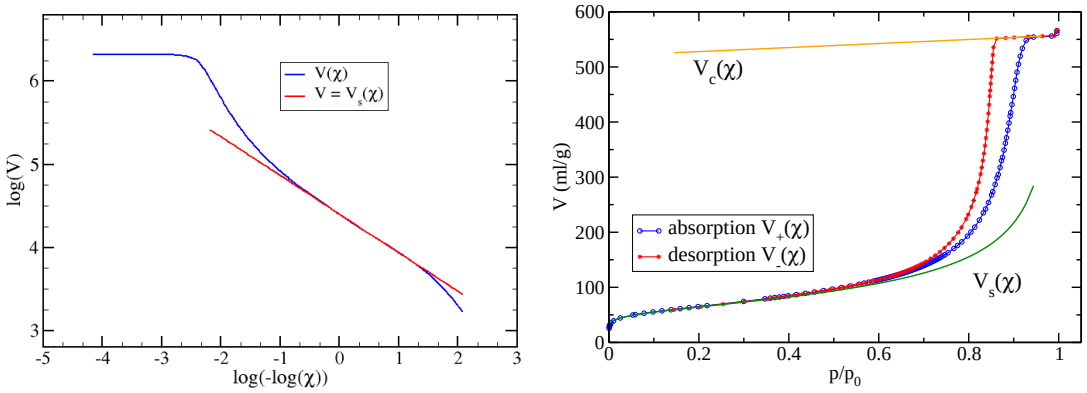

(A) (B)

Figure 10.1: Fit of the adsorption branch in nitrogen porosimetry of sample 1 by Eq. 10.2.

The method removes the effects of liquid compressibility at high pressure with a linear fit, and removes the effects of multilayer nitrogen molecule adsorption at low pressure with the FHH equation. Let us recall the principles of the method. First, a linear fit of the high pressure part of the isotherm is defined, denoted $V_c(\chi) \propto \chi$, where $\chi = p/p_0$ is the relative pressure. Second, the low pressure part is defined as $V_s(\chi) = S \cdot h(\chi)$, where S is the specific surface area, and $h(\chi)$ is the thickness of the multilayer molecule film, usually modelled by the FHH equation (Cimino et al., 2013)

$$h(\chi) = \left[\frac{K}{-\log \chi}\right]^{1/m} \tag{10.1}$$

The prefactor K and exponent m are constants related to the chemical nature of the nitrogen-alumina interface. The equation is identified by curve fitting for each isotherm. Eq. 10.1 is rewritten as:

$$\log V_s(\chi) = -\frac{1}{m} \log\left(-\log \chi\right) + \log S + \frac{1}{m} \log K \tag{10.2}$$

We use Eq. 10.2 to fit the linear part of the original experimental isotherms (denoted $V(\chi)$ shown in Fig. 10.1 A). Therefore, the FHH equation $V_s(\chi)$ with identified parameters is obtained:

$$\begin{aligned} -\frac{1}{m} &= -0.465 \\ \log S + \frac{1}{m} \log K &= 0.402 \end{aligned} \tag{10.3}$$

The result in Eq. 10.3 is sufficient to draw $V_s(\chi)$ with Eq. 10.2, without knowing the exact values of K and m. The linear curve fit result is shown in Fig. 10.1 for sample 1. The same procedure is performed on the other two samples.

Furthermore, in the rest of this work, we denote the filtered and normalized isotherms by:

$$Q(\chi) = \frac{V_c(\chi) - V(\chi)}{V_c(\chi) - V_s(\chi)} \tag{10.4}$$

The quantity $Q(\chi)$ is plotted as a function of χ for the three samples in Fig. 10.2.

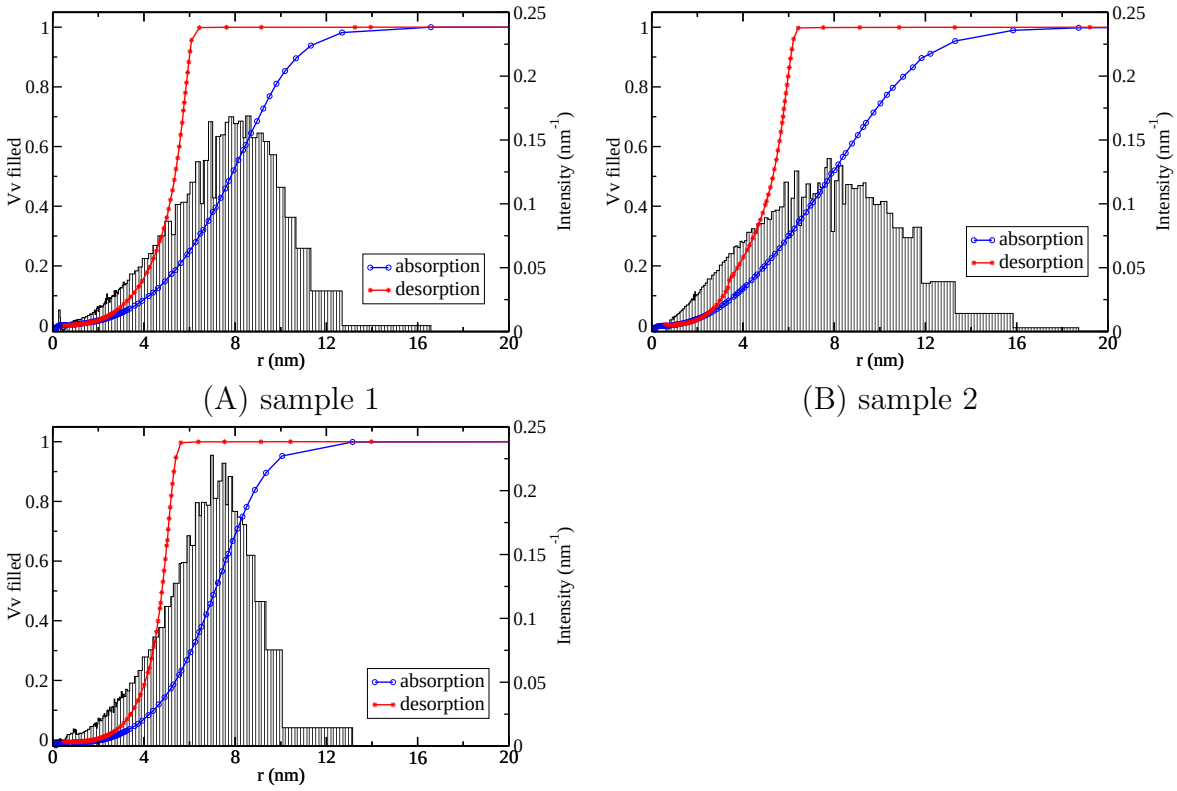

(A) sample 1

(B) sample 2

(C) sample 3

Figure 10.2: Nitrogen porosimetry isotherms of the three samples normalized with Eq. 10.4, together with pore size distribution estimated with Eq. 9.10.

10.1.3 Pore size distribution

The pore size distribution was defined in Eq. 9.10. The pore size distributions of the three samples $I(r)$ are estimated using the normalized isotherm $Q(r)$. The results are shown in Fig. 10.2, and are close to each other. In this work, we take without loss of generality the sample 1 as experimental reference.

10.2 Isotherm simulation with multi-scale Boolean models

10.2.1 Adsorption branch simulation with Boolean models

In the experimental isotherms, the pressures for cumulated volume is discretized. For each pressure p_i, we obtain the corresponding curvature radius r_i from the Kelvin equation. The cumulated volume fraction of condensed liquid is given at a set of values: $Q_i = Q(r_i)$. Therefore, the pore size distribution intensity is: $I_i = \Delta Q_i / \Delta r_i$.

The capillary behavior of two-scales models of spherical exclusions contains two peaks (see Fig. 9.21). It suggests that the union of a series of Boolean models of spherical exclusions with a radius distribution allows one to reproduce various pore size distributions. We thus introduce the microstructure:

$$S = \bigcap_{j=1}^{n} B_j^c \tag{10.5}$$

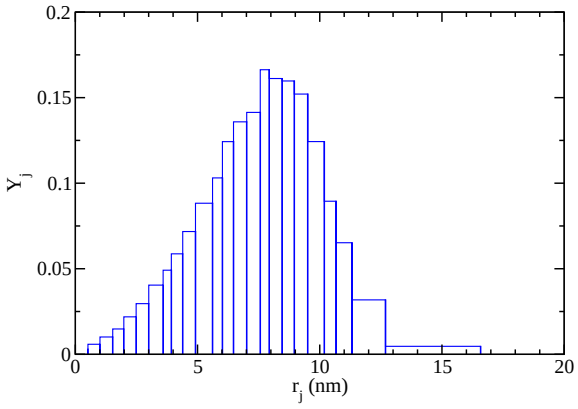

Figure 10.3: Prescribed pore size distribution y_j of a multi-scale model of Boolean models, deduced from the experimental reference of sample 1.

where S is the solid phase, $\Omega \backslash S$ is the porous phase, $B_j, (j = 1, 2, ..., n)$ are Boolean models of spheres. The number n is related to the number of discretized pressure in the experimental isotherms. The sphere radii (denoted by r_j) and the volume fraction (denoted by p_j) for each Boolean model B_j need to be identified. We use information from the experimental pore size distribution (Fig. 10.2) to set these variables r_j and p_j.

In the experimental isotherm $\psi - p/p_0$ plot (Fig. 5.1), the spacing is constant along the relative pressure axis. However in the $\psi - r_p$ plot (Fig. 10.2), the points at low pressure are more dense than that at high pressure (Fig. 10.3 A). We accordingly regularize the spacing by combining close peaks. In the range of r_p, we generate a series of points $\{x_i\}$ with spacing of 0.5 nm. The spacing equal to the voxel length is chosen. The series x_i is then shifted to the closest experimental Kelvin radius. The resulting Kelvin radius serve as the sphere radius $\{r_j\}$ for the Boolean models:

$$r_j = \arg\min_{r_k} |x_j - r_k| \tag{10.6}$$

The same elements in the series $\{r_j\}$ are eliminated and the series is sorted. This preprocessing improves the regularity of the radius spacing and is consistent with the spacing in sparse zones (Fig. 10.3).

The resulting model S is expected to have the same pore size distribution as I_i, with intensity denoted by y_j:

$$y_j = \frac{\sum_{r_{j-1}<r_i<r_j} I_i \Delta r_i}{\sum_{r_{j-1}<r_i<r_j} \Delta r_i} = \frac{Q(r_j) - Q(r_{j-1})}{r_j - r_{j-1}} \tag{10.7}$$

The model (Eq. 10.5) would have the expected pore size distribution y_j with $p_j = y_j$, if there is no intersection between the Boolean models. However, the intersections exist and modify the pore size. The intersected regions between two pores of different sizes belong to the large pore in terms of pore size distribution. To account for the intersection of sphere, we have:

$$y_j(r_j - r_{j-1})q = p_j - p_j \sum_{k=j+1}^{n} y_k(r_k - r_{k-1})q \tag{10.8}$$

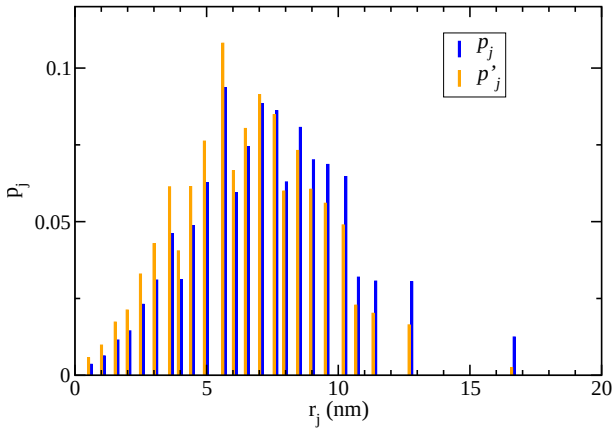

Figure 10.4: Volume fractions of Boolean models of spheres deduced from Eq. 10.10 (blue) and Eq. 10.11 (orange).

where $y_k(r_k - r_{k-1})q$ is the volume fraction of pores of radius r_j, which satisfies:

$$\sum_{k=1}^{n} y_k(r_k - r_{k-1}) = 1 \tag{10.9}$$

and q is the experimental pore volume fraction measured by pycnometry, and is also the pore volume fraction of the multi-scale model S. The second term on the right of Eq. 10.8 represents the intersections. From Eq. 10.8, we obtain the volume fraction p_j for each Boolean model B_j (Fig. 10.4 blue bars):

$$p_j = \frac{y_j(r_j - r_{j-1})q}{1 - \sum_{k=j+1}^{n} y_k(r_k - r_{k-1})q} \tag{10.10}$$

Once we have the r_j and p_j, the multi-scale model S is determined. A microstructure was realized and its capillary behavior is studied. The 2D sections during adsorption and desorption are represented in Fig. 10.5 and Fig. 10.6 respectively, together with isotherms in Fig. 10.7 (a). During the adsorption process, the pores of different sizes are filled gradually from small pores to large pores. The adsorption branch has the same shape as the experimental isotherm, but is shifted to the right. The shift represents an overestimation of the pore size.

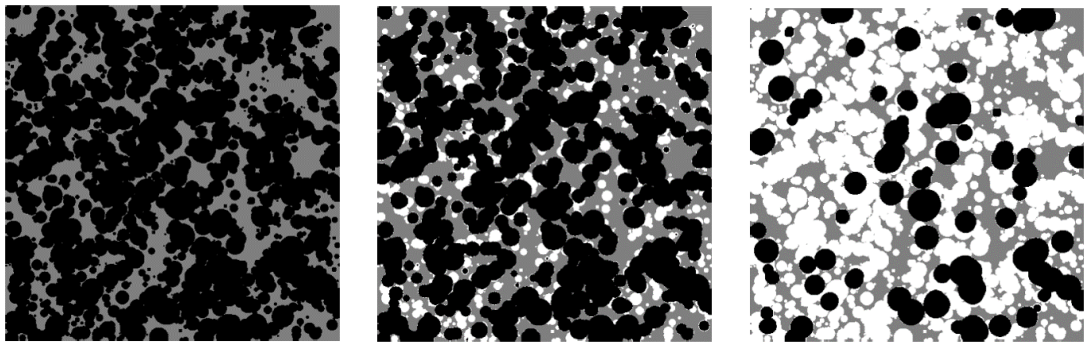

(A) (B) (C)

Figure 10.5: 2D sections during adsorption process. (A) r = 0 nm (B) r = 6 nm and (C) r = 12 nm. Vapour phase is in black, solid phase is in grey and liquid phase is in white.

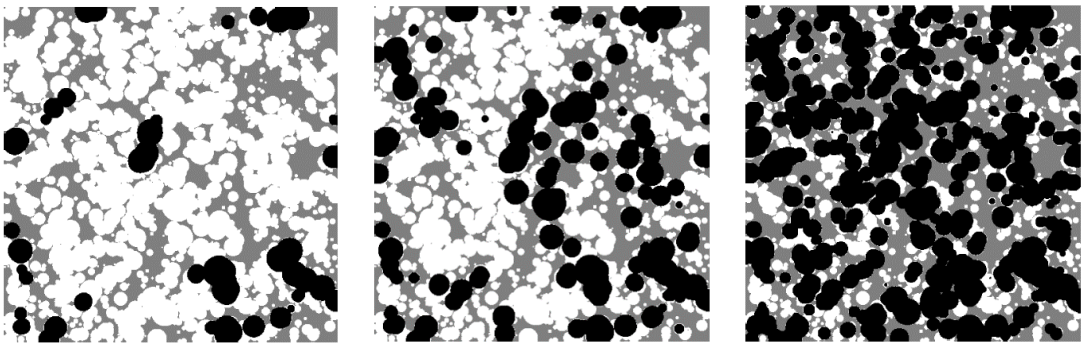

(A) (B) (C)

Figure 10.6: 2D sections during desorption process. (A) r = 9 nm (B) r = 8 nm and (C) r = 6 nm. Vapour phase is in black, solid phase is in grey and liquid phase is in white.

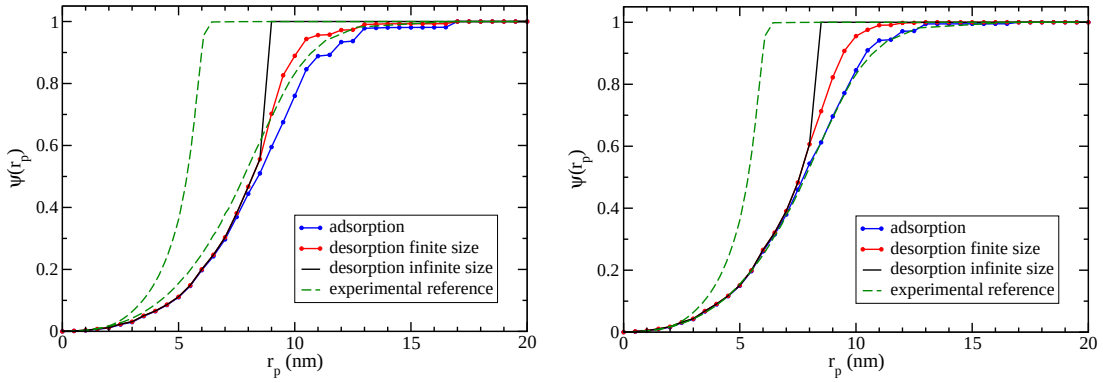

(a) initial (b) identified

Figure 10.7: Isotherms of capillary condensation-evaporation simulated with (a) initial parameters and (b) identified parameters by Eq. 10.11.

Parameters identification

The overestimation of the pore size is because of the approximation by Eq. 10.8, which did not take the change of size in the small pores into account. As shown in Fig. 10.8, the intersections do not only take away a part of the small pores, but also change the pore size distribution inside the small pores (the orange part in Fig. 10.8).

The intersection effect increases the volume of large pores, and decreases that of small pores. To compensate the effect, a linear empirical correction on the volume fractions p_j is proposed:

$$p'_j = c(r_j)p_j \tag{10.11}$$

$$c(r_j) = kr_j + b \tag{10.12}$$

where k and b are empirical parameters. The volume fractions of pores of different sizes is modified accordingly:

$$y'_j(r_j - r_{j-1})q = p'_j - p'_j \sum_{k=j+1}^{n} y'_k(r_k - r_{k-1})q \tag{10.13}$$

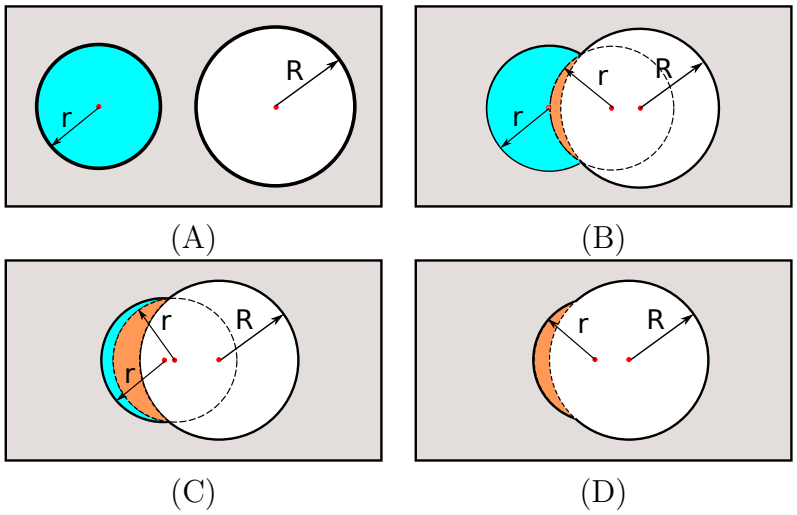

Figure 10.8: Schematic illustration of the intersection effect on the pore size. Grey: solid phase. Blue: porous phase of size r. Orange: porous phase of intermediate size between r and R. White: porous phase of size R.

We now minimize the difference between the simulated adsorption branch and the experimental reference. Manual dichotomy is used to optimize k and b, described as follows. The parameter k is optimized first to increase the volume of small pores and to decrease the volume of large pores. Once the simulated adsorption branch fits the experimental isotherm, the parameter b is adjusted to compensate the total pore volume fraction.

After about 10 rounds of parameter tuning, we fix the values $k = -0.09\,\mathrm{nm}^{-1}$ and $b = 1.64$. The corrected volume fractions p'_j are shown in Fig. 10.4 (orange bars), together with the isotherms of capillary condensation simulation on the model in Fig. 10.7 (b). The adsorption branch is close to the experimental isotherm. However, the desorption branch is still far away, especially the neck-pore size. This problem is addressed in the next subsection.

10.2.2 Desorption branch simulation with hardcore model

In order to reproduce the desorption branch, based on the Boolean model proposed in subsection 10.2.1, it is necessary to reduce the connection of the pores and decrease the neck-pore size. We add a repulsion distance between the large spherical pores. The smallest pores remain connected and play the role of "neck pores". This multi-scale hardcore model is defined as:

$$T = \left(\bigcap_{j=1}^{m} B_j^c \right) \bigcap H^c \tag{10.14}$$

where T is the solid phase of the microstructure, B_j is a Boolean model of spheres of radius r_j and volume fraction p_j, m is the number of Boolean models and H is the solid phase of the multi-scale hardcore model:

$$H = \bigcap_{j=m+1}^{n} R_j^c \tag{10.15}$$

where R_j is a one-scale hardcore model of spheres of radius r_j, and satisfies:

$$R_k \cap R_l = \emptyset, \quad \forall\ k, l \in \mathbb{N} \cap [m+1, n] \quad \text{and} \quad k \neq l \tag{10.16}$$

In practice, one-scale hardcore models are generated in a sequence from the largest pores to the smallest pores. The domain of the repulsive point process for hardcore model R_k is denoted by D_k:

$$D_k = \left\{ \delta_{r_k} \left(\bigcup_{j=k+1}^{n} R_j \right) \right\}^c \tag{10.17}$$

where $\delta_{r_k}(\cdot)$ is the dilation operator by a spherical structuring element of radius r_k. For each repulsive point process, the repulsion distance is set to be the sphere radius r_k. Thus, any two spheres in H do not intersect, which makes it a multi-scale hardcore model. The multi-scale model H is then intersected with the Boolean models of small spheres, and results in the model T. The small spherical pores connects the large repulsive pores and play the role of "bottle neck" as in the ink-bottle pore.

The multi-scale model T have the following parameters: the volume fractions p_j of the Boolean models and of the one-scale hardcore models, and the threshold m from which the spherical pores become repulsive. The volume fractions p_j are determined in a similar way as in Eq. 10.8:

$$y_j q(r_j - r_{j-1}) = \begin{cases} p_j & j \geq m \\ p_j - p_j \sum_{k=j+1}^{n} y_k q(r_k - r_{k-1}) & j < m \end{cases} \tag{10.18}$$

where $y_k(r_k - r_{k-1})$ satisfies always Eq. 10.9. The equation is split into two cases because there is no intersection between the large hardcore pores. Consequently, the volume fractions of the one-scale models are determined by:

$$p_j = \begin{cases} y_j q(r_j - r_{j-1}) & j \geq m \\ \frac{y_j q(r_j - r_{j-1})}{1 - \sum_{k=j+1}^{n} y_k q(r_k - r_{k-1})} & j < m \end{cases} \tag{10.19}$$

We now fix the value of the parameter m for the hardcore model. From the experimental porosimetry isotherms (Fig. 10.2), the desorption threshold is around 6 nm, so the value of r_m is initially set to be 6 nm.

The results of capillary condensation and evaporation simulation is shown in Fig.10.9 (a). As expected, the isotherms show a much lower neck-pore size than that in Fig. 10.7 (b). The low neck-pore size is also observed on the 2D sections during capillary evaporation simulation (Fig. 10.10): the evaporation occurs only at the boundary before the pressure reaches the desorption threshold.

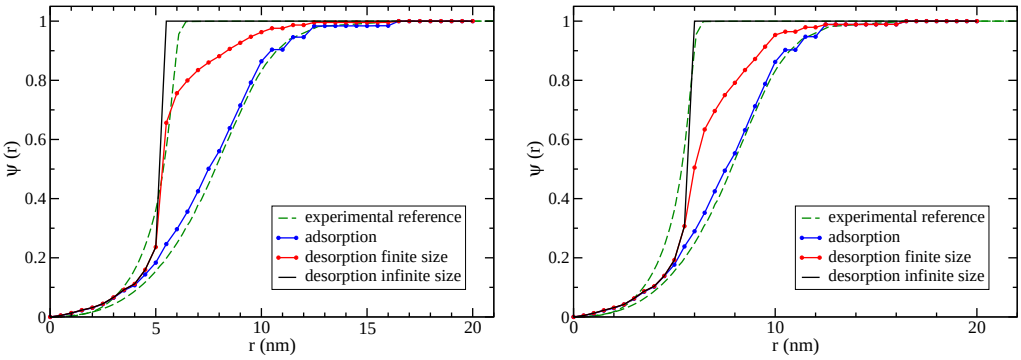

Figure 10.9: Isotherms of capillary condensation-evaporation simulation with (a) initially chosen parameters and (b) optimized parameters by Eq. 10.11.

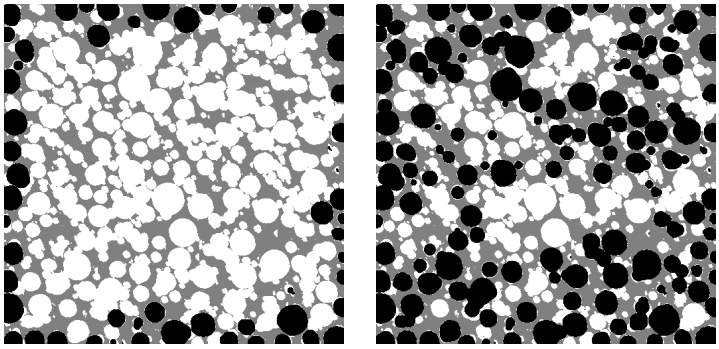

Figure 10.10: 2D sections of capillary evaporation on multi-scale hardcore model. (a) $r_p = 5.5$ nm, (b) $r_p = 5$ nm.

The simulated adsorption and desorption branches of model T are quite close to the experimental data. However, the pore volume fraction of the resulting model is 0.63, lower than the experimental reference of 0.69. Eq. 10.11 is used to adjust the parameters. By manual dichotomy, we find $k = -0.0034\,\mathrm{nm}^{-1}$, $b = 1.18$ and $r_m = 6.4\,\mathrm{nm}$ for the identified multi-scale hardcore model, with a pore volume fraction of 0.69 and isotherms shown in Fig.10.9 (b).

10.3 Capillary behavior of microstructures of mesoporous alumina

Two microstructure models of mesoporous alumina have been previously constructed: the tomographic reconstruction and the two-scale model of platelets. In this section, we study their capillary behaviors.

10.3.1 Tomographic reconstruction

The tomographic 3D image (Fig. 5.5) was reconstructed upon a small piece of crushed sample of sample 1 (Fig. 10.2 A). The reconstruction image size is 328

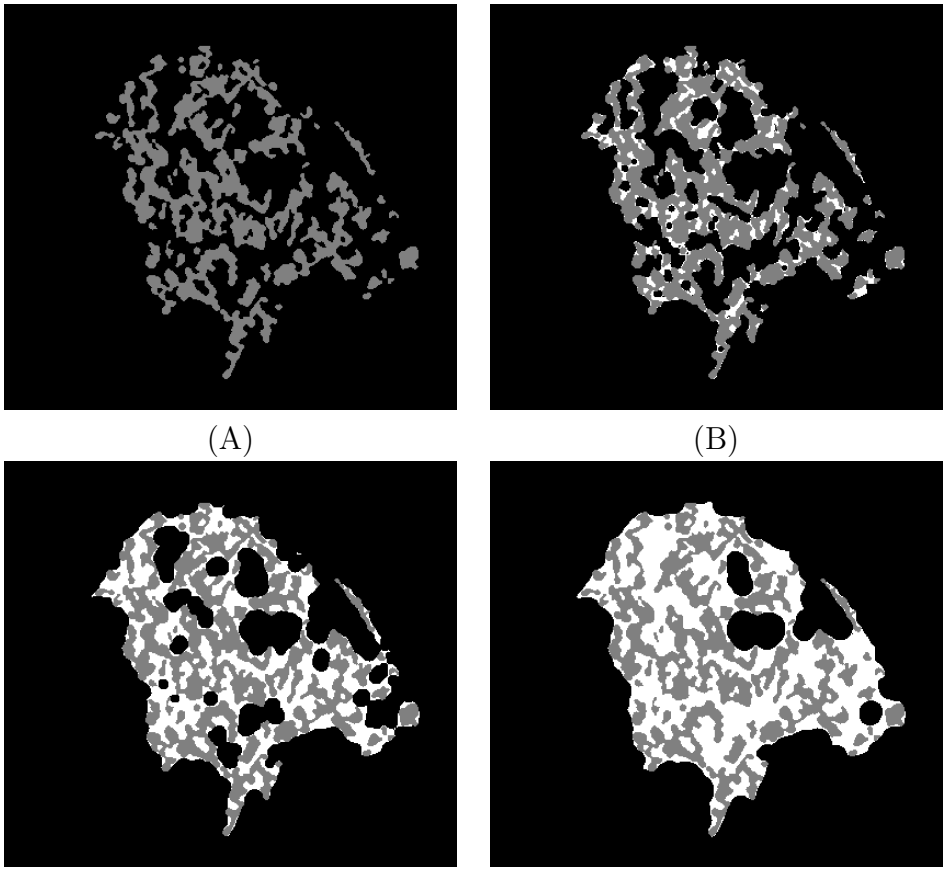

Figure 10.11: 2D sections during the capillary condensation simulation on the tomographic reconstruction of the mesoporous sample. (A) $r_p = 0$ nm, (B) $r_p = 3.5$ nm, (C) $r_p = 7$ nm, (D) $r_p = 10.5$ nm.

nm $\times$290 nm $\times$257 nm at resolution 0.66 nm^3 per voxel. It is a binary image with pore phase in 0 and solid phase in 1. Since the shape of the microstructure is irregular, the cuboid container can not represent the volume of the microstructure. The envelop and the total volume of the microstructure was obtained in chapter 8, by closing and geodesic erosion operations.

The capillary condensation and evaporation simulation was performed on the microstructure, with 2D sections in Fig. 10.11. The morphological simulation method adapts on the tomographic 3D image. The condensation occurs first on the interface of small curvature radius and in the narrow space between solid walls. The meniscus then propagates gradually from the small pores to large pores, until the whole porosity is filled by condensed liquid.

Simulated isotherms are shown in Fig. 10.13 in red. The adsorption branch increases slowly until $r_p = 17$ nm, which means a smooth pore size distribution. However, it is observed on the 2D sections that some of the pores larger than 13 nm, are very close to, or directly part of the contour of the sample. It is possible that some of these pores were formed during the sample crushing by mechanical damage. The weak hysteresis means a good connection of the pore phase to the exterior, because of the small system volume and the irregular shape. For the same reason, it is impossible to obtain any information about desorption thresholds. The

tomographic reconstruction is not representative enough to simulate the capillary condensation and evaporation behavior.

10.3.2 Two-scale model of platelets

A two-scale model of platelets was proposed in chapter 8, based on TEM images. The model consists of aggregates of aligned platelets and individual randomly oriented platelets.

We perform the capillary condensation & evaporation on a realization of the identified model, with 2D sections shown in Fig. 10.12. Fig. 10.12(A) is a 2D section of the microstructure. The capillary condensation occurs first in the concave corners of intersected platelets. Then the narrow slit space between aligned pores are filled by condensed liquid. The meniscus propagates gradually from small pores to large pores. The large pores locates usually between the aggregates (black zones in Fig. 10.12(B)). When the Kelvin radius reaches 10 nm, the whole pore phase is filled.

During the desorption, the pore phase does not percolate until the Kelvin radius reaches 5 nm and lower. In Fig. 10.12(F), only pores at the boundaries are released. The ink-bottle effect prevent the inner pores from releasing. If we compare the 2D sections Fig. 10.12 (B) and (E), when the pore phase percolates at $r_p = 5$ nm, there are still pores that are blocked by the "neck pores", especially the pores surrounded by aggregates.

The isotherms of the identified two-scale model is shown in green in Fig. 10.13. Compared to the experimental isotherms, its pore size distribution is very narrow with smaller average pore size. Indeed, the porosity in the identified two-scale model consists of small regions located in-between platelets, rather than aggregates of platelets. According to the result of subsection 9.6.1, the pore size in a Boolean model is dominated by the pore volume fraction. The pore size distribution inside the aggregates and in the complementary is rather the same. To widen the range of the pore size distribution, we ought to enlarge the difference between the platelet volume fractions inside and outside the aggregates. This way is explored in the next subsection 10.3.3 and further developed in section 10.5.

Another significant difference observed in Fig. 10.13 is that at the origin of the adsorption branches, the slope of the experimental isotherm is zero, but the other two simulated adsorption branches show high slopes. This is because the experimental isotherms have been preprocessed to remove the effects of multilayer adsorption of nitrogen molecules on the solid surface using the FHH equation, while the simulated isotherms have not been preprocessed. Although all isotherms in Fig. 10.13 are related to capillary behavior, the initial step eliminates a non-negligible volume fraction (about 23%) of the porosity. This step changes the morphology of the porous phase. The simulation of multilayer adsorption is studied in section 10.4.

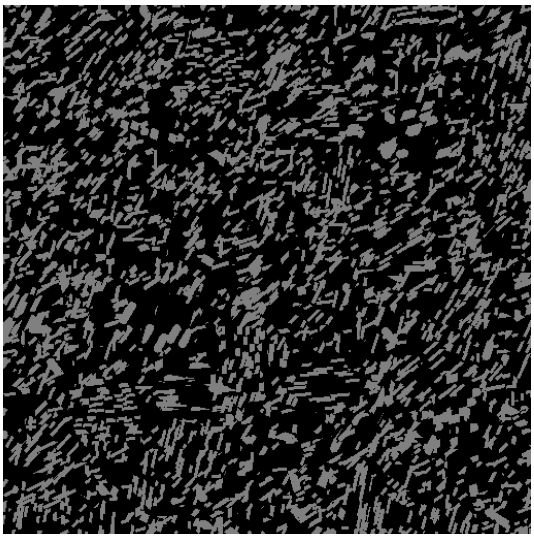

(A) adsorption $r_p = 0$ nm

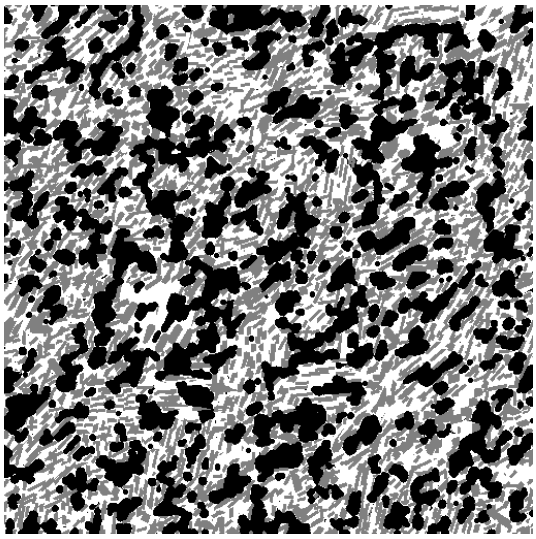

(D) desorption $r_p = 4$ nm

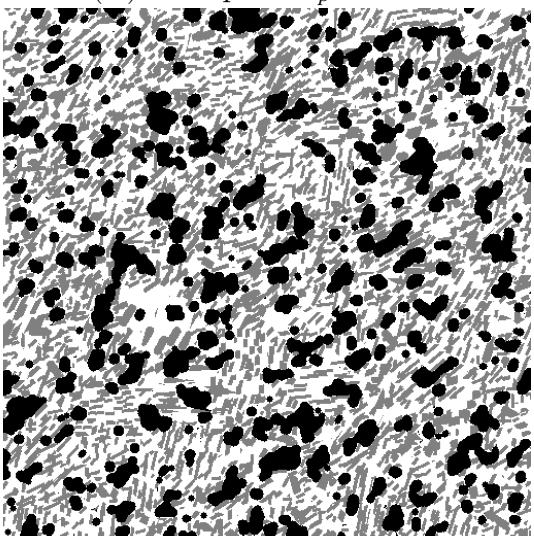

(B) adsorption $r_p = 5$ nm

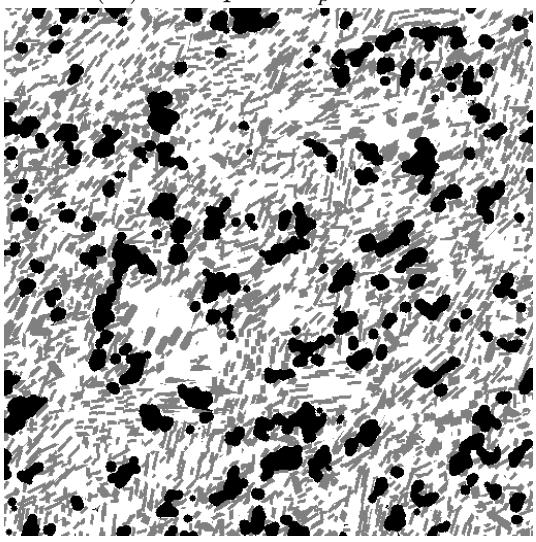

(E) desorption $r_p = 5$ nm

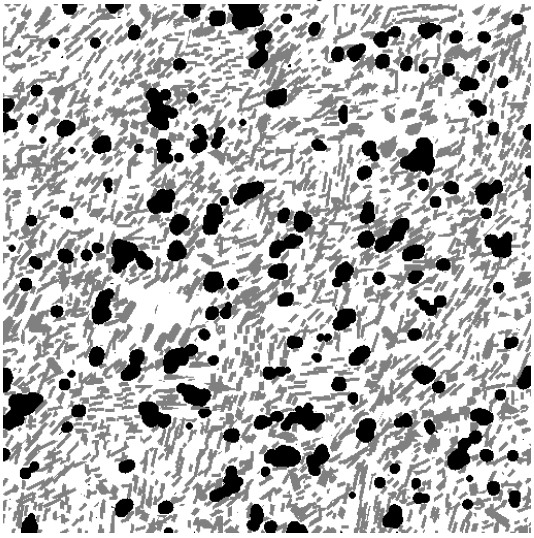

(C) adsorption $r_p = 6$ nm

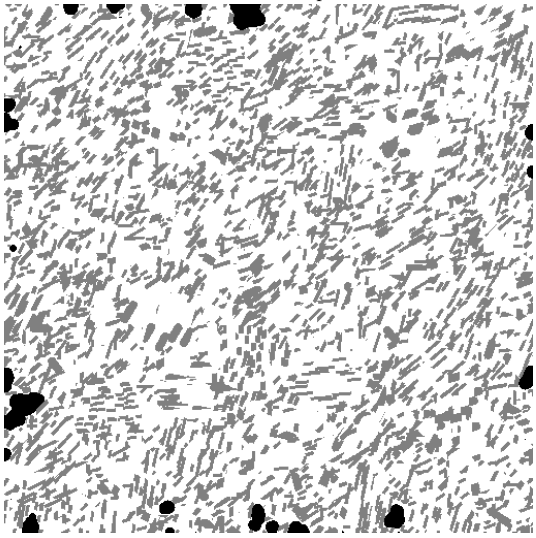

(F) desorption $r_p = 6$ nm

Figure 10.12: 2D sections during the capillary condensation simulation on the identified two-scale model of platelets of mesoporous alumina. Left column: adsorption. Right column: desorption.

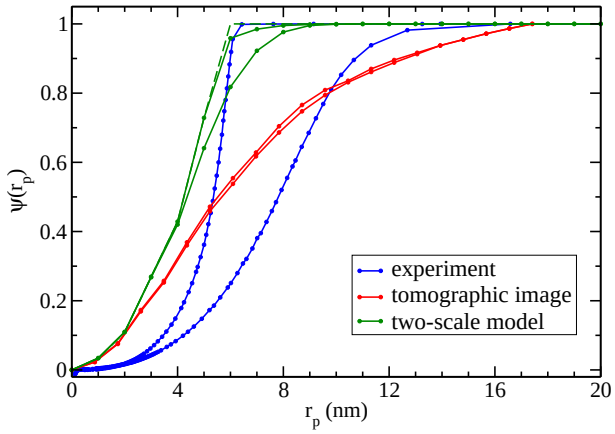

Figure 10.13: Comparison between the hysteresis of experiment and simulations.

10.3.3 Random models of platelets

In order to explore the limits of the two-scale model of platelets proposed in chapter 8 on capillary behavior, we consider the following generalized random models of platelets of the same shape ($D_1 = 6.8$ nm, $D_2 = 3.3$ nm, $D_3 = 2.0$ nm, $D_4 = 2.0$ nm) and of the same pore volume fraction 69%.

1. a two-scale model, denoted by P_1: a Boolean model of spheres is used to model to aggregates, aligned platelets are intersected inside the spheres, the complementary of the aggregates is empty. The parameters on spatial dispersion are $p_A = 0.49$, $p_S = 0.65$, $r_S = 16$ nm. 2D sections are available in Fig. 10.14 (C) and (D).

2. a two-scale model, denoted by P_2: a Boolean model of spheres is used to model to the large pores, randomly-oriented platelets are dispersed in the complementation of the spherical pores. The parameters on spatial dispersion are $p_A = 0$, $p_S = 0.28$, $r_S = 16$ nm. 2D sections are available in (Fig. 10.14) (E) and (F).

3. a reference Boolean model, denoted by P_0, of platelets of random orientation uniformly distributed on the unit sphere. The parameters on spatial dispersion are $p_A = 0$, $p_S = 0$, $r_S = 0$ nm. 2D sections during capillary condensation & evaporation simulation are shown in Fig. 10.14 (A) and (B).

The platelet shape and size are chosen so that the representativities of structures of different scales are ensured to the maximum, and at the same time the microstructures have sufficient resolution.

The capillary isotherms of these microstructures are shown in Fig. 10.15. The porosity in P_0 are the space between the randomly oriented platelets, which are rather small. The range of the pore size distribution is also narrow (from 1 to 5 nm). The percolation is achieved when half of the pores are released ($r_p = 3$ nm). The porosity in P_1 are either the space between the aligned platelets, or the space between the aggregates. The latter is much larger than the former. The distribution range is also larger than the former (from 5 to 15 nm). The vapour phase percolates through the complementary of the aggregates at $r_p = 7$ nm. The pores in P_2 are either the space between the randomly oriented platelets, or the spherical exclusions.

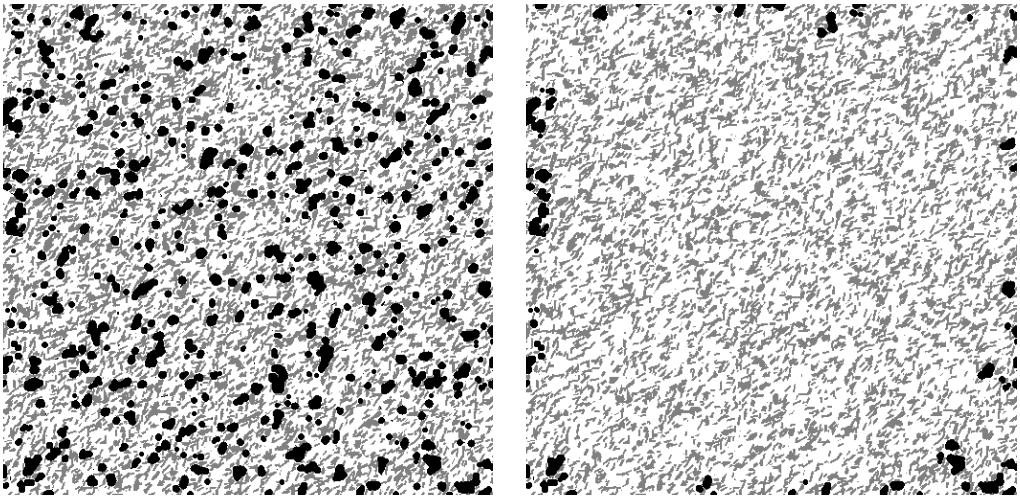

(A) P_0, adsorption, $r_p = 4$ nm (B) P_0, desorption, $r_p = 4$ nm

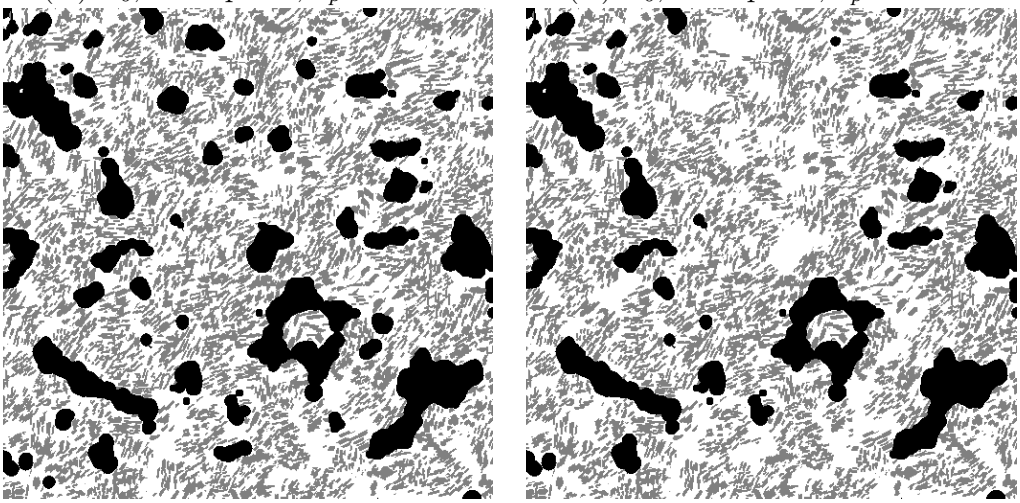

(C) P_1, adsorption, $r_p = 8$ nm (D) P_1, desorption, $r_p = 8$ nm

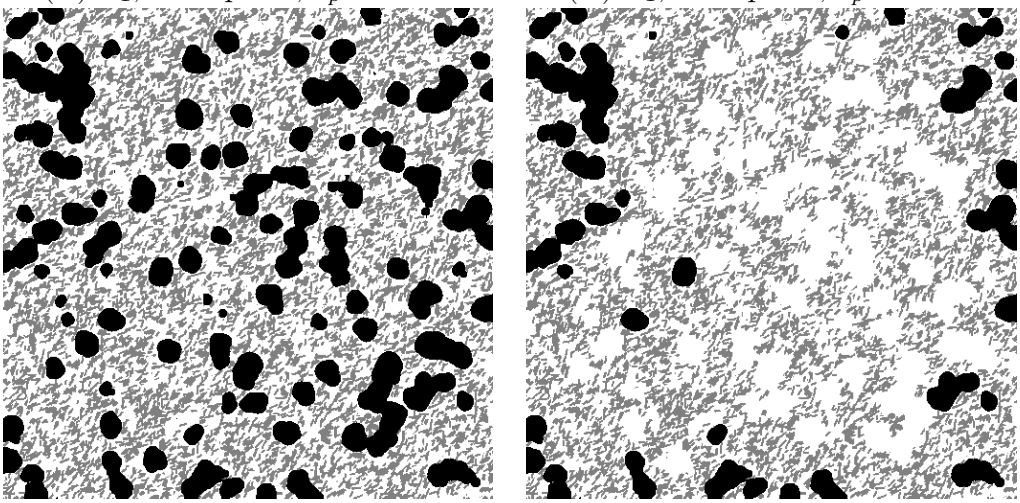

(E) P_2, adsorption, $r_p = 8$ nm (F) P_2, desorption, $r_p = 8$ nm

Figure 10.14: 2D sections of equilibrium states during the condensation & vaporization simulation on random models of platelets P_0, P_1 and P_2.

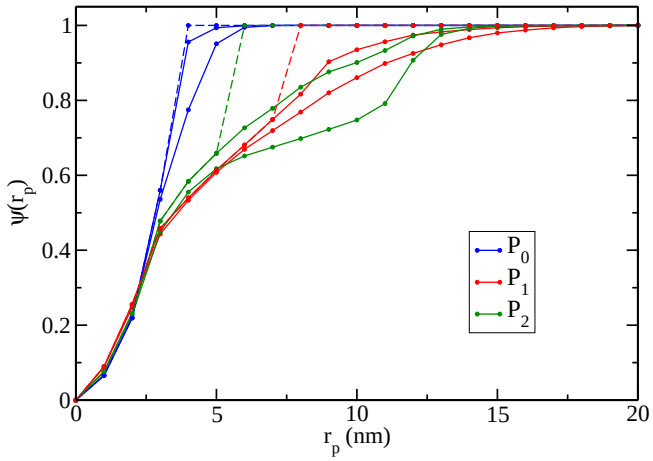

Figure 10.15: Capillary condensation and evaporation isotherms simulated on random models of platelets.

In this model, the adsorption branch increases rapidly with r_p between 0 nm and 3 nm and between 11 nm and 13 nm. They correspond to the space between platelets and the spherical exclusions respectively. The percolation of the vapour phase is more difficult to achieve in P_2 than in P_1. This is because the spherical exclusions are surrounded by the platelets. The small pores play the role of "neck pores", which strengthen the ink-bottle effect.

None of the two-scale models has the same capillary behavior as the experimental isotherm shown in Fig. 10.13 (blue). The main differences include:

- The desorption threshold of the experimental isotherm is so low that more than half of the porosity is blocked by neck pores.
- The adsorption branch of the experimental isotherm is smooth, without significant scale separation in pore size distribution.

The first difference means that there exists structures and pores of large scales, but these pores do not contribute to the percolation of the vapour phase. This phenomenon has not been observed in the two-scale models P_1 and P_2.

The second difference is because the preprocessing eliminates the multilayer adsorption from experimental isotherms with FHH equation. In mesoporous alumina, the multilayer adsorption ($r_j < 2$ nm) takes a non-negligible percentage of condensed liquid at about 25%, as shown in the isotherms without preprocessing in Fig. 10.16. The pore size distribution shows two peaks: one at very low pressure, the other at $r_p = 6$ nm. The first peak corresponds to the multilayer adsorption, the simulation of which is detailed in the next section.

10.4 Multilayer adsorption simulation

The phenomenon of physical adsorption of nitrogen molecules on a solid surface is well known. Nitrogen molecules are adsorbed on the solid walls, to minimize the interface energy. The molecules also approach the existing molecule layers, and forms multilayer molecules on the solid surface, independent of surface curvature. It happens at low pressures, before the Kelvin equation is valid, and the phenomenon

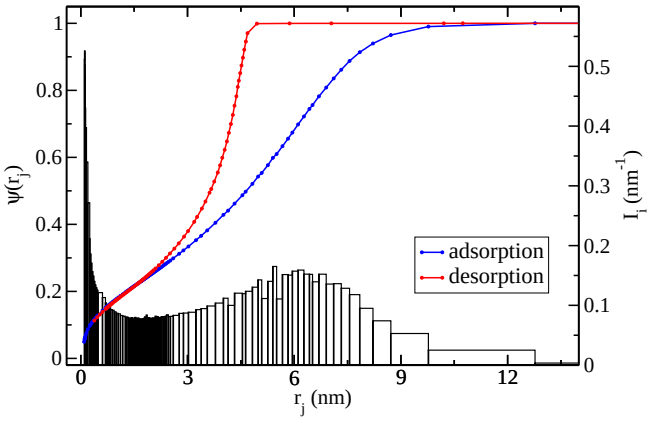

Figure 10.16: Pore size distribution derivative of the experimental adsorption branch of sample N°.1 by Eq. 9.10. The sample is preprocessed with only the linear fitting of liquid compressing $V_c(\chi)$.

still takes effect at high pressure. In the BJH method for pore size distribution analysis, the pore size is determined by both the Kelvin radius and the multilayer thickness.

According to the BET theory, the number of molecules on the solid interface follows a random distribution. The average number of molecules or layers increases with increasing pressure. We use a dilation operation, denoted $\delta(\cdot)$, with a spherical structuring element to simulate the average thickness of the layers, before the simulation of capillary condensation:

$$L_{r_t} = \delta_{r_t}(S) \cap P \tag{10.20}$$

where L_{r_t} is the multilayer nitrogen molecules, S is the solid phase, P is the accessible porosity and r_t is the size of the structuring element, corresponding to the thickness of the multilayer adsorption. In practice, the multilayer adsorption is thin, and the spherical structuring element is small and discretized. The spherical structuring element can be replaced by a 3D cross or by the Euclidean distance transform with threshold. In this work, we choose the latter for a better precision.

The multilayer adsorption is followed by the capillary condensation. Its simulation is performed based on the dilated microstructure $S \cup L_{r_t}$. The liquid phase in the microstructure is then obtained by the closing operator:

$$L(r_p) = \varphi_{r_p}\left(S \cup L_{r_t}\right) \cap P \tag{10.21}$$

It needs to be mentioned that the capillary condensation simulation wouldn't begin from Kelvin radius equal to zero. This is because at low pressure, the thermodynamic multilayer adsorption, not the capillary condensation, dominates the volume of condensed liquid. It is well known that, the Kelvin equation is only valid for Kelvin radius above 2 nm (Takei et al., 1997). The domain of Eq. 10.21 is accordingly set to be $r_p \geq 2$ nm. The local pore size, denoted r, is then determined by both the multilayer thickness and the Kelvin radius:

$$r = r_t + r_p \tag{10.22}$$

The simulation method by dilation is illustrated in a cylindrical pore in Fig. 10.17. This is a cylindrical pore with base radius r_0 and two ends open. At low pressure,

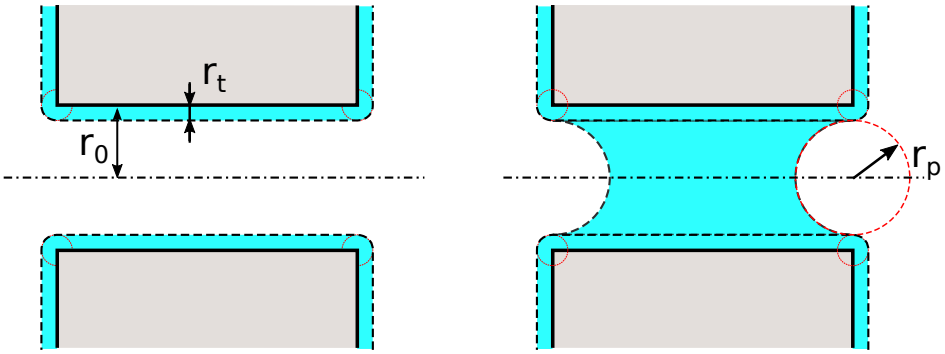

Figure 10.17: 2D section of a cylindrical pore with multilayer adsorption (left) and capillary condensation (right). Solid phase is in grey. Liquid phase is in blue. Red dotted lines are the structuring elements.

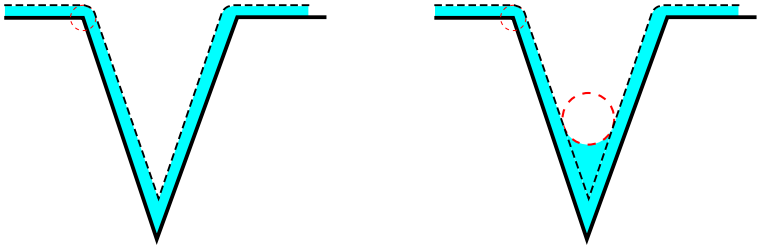

Figure 10.18: 2D section of a conical pore with multilayer adsorption (left) and capillary condensation (right). Solid phase is in grey. Liquid phase is in blue. Dotted red lines are the structuring elements.

only the multilayer of molecules of thickness r_t is adsorbed on the solid interface. With increasing pressure, when the Kelvin radius satisfies $r_p = r_0 - r_t$, the pore is filled and the meniscus is formed at the two ends. The boundaries of the meniscus are tangent to the existing liquid interface. The newly formed vapour/liquid interface is smooth and satisfies the Kelvin equation.

Another schematic illustration of the multilayer adsorption simulation in shown in a conical pore in Fig. 10.18. After the multilayer adsorption on the cone surface, the capillary condensation is simulated with a spherical structuring element of radius 2 nm, instead of radius starting from 0 nm.

To implement the method, the multilayer thickness r_t at low pressure needs to be identified. According to Lippens et al. (1964), the thickness of a nitrogen monolayer is 0.354 nm. To address the question more precisely – how many layers are there before the capillary condensation occurs at $r_p = 2$ nm? According to the Kelvin equation, the Kelvin radius $r_p = 2$ nm corresponds to relative pressure $p/p_0 \approx 0.6$. As mentioned in the experimental isotherms, the volume fraction of condensed liquid in the porosity at $p/p_0 = 0.6$ is 23%. The 23% contains the volume fraction of the multilayer adsorption and the initial volume fraction by capillary condensation at $r_p = 2$ nm. With the BET equation, we obtain the gas quantity adsorbed in a monolayer nitrogen, which takes a volume fraction of the porosity at 8.24%. The proportion $23\%/8.24\% < 3$, which indicates that the average number of adsorbed layers at $p/p_0 = 0.6$ should be less than 3. Thus, in the multilayer adsorption simulation by dilation, the thickness r_t is either 1 or 2 layers. This question is addressed in the following section.

10.5 Microstructure modeling with porosimetry constraint

The two-scale model of platelets and the tomographic reconstruction of mesoporous alumina can not reproduce the experimental isotherms. A microstructure with larger pores and strong ink-bottle effect is considered in this section.

10.5.1 Three-scale model of platelets

We make use of the hardcore exclusions, and combine it with the two-scale model of platelets. The new model has features of large unconnected pores, aggregates as well as platelets. The three-scale model is constructed in the following way.

First, we consider a multi-scale hardcore model of spherical exclusions:

$$H = \bigcap_{j=m+1}^{n} R_j^c \tag{10.23}$$

where R_j is the solid phase of a one-scale hardcore model of spheres of radius r_j at volume fraction p_j. These one-scale hardcore models do not intersect with one another:

$$R_k \cap R_l = \emptyset, \quad \forall\ k, l \in \mathbb{N} \cap [m+1, n] \quad \text{and} \quad k \neq l \tag{10.24}$$

The sphere radius r_j and the corresponding volume fractions p_j are chosen according to the experimental pore size distribution (Fig. 10.16). Only the pores larger than the parameter threshold r_m are taken into account. Since no intersection exists between the spheres, the volume fraction the hardcore exclusion, denoted p_H, is the sum of p_j:

$$p_H = \sum_{j=m+1}^{n} p_j. \tag{10.25}$$

Second, we consider a Boolean model, denoted B, of spheres of radius r_S and volume fraction p_S in the 3D domain D. This Boolean model is used to locate the aggregates of platelets, independent of the exclusions. Each sphere in the Boolean model is associated with a random orientation θ_l, distributed uniformly on unit sphere.

Third, we consider a primary platelet A' and implement it randomly inside and outside the aggregates. A Poisson point process generates random points x_k with volume fraction of platelets p_{A1}, in the aggregates and out of exclusions $B \cap H^c$. At each point, a platelet is implemented A'_{x_k}. The platelet is then rotated along the orientation associated with the sphere that it locates in, denoted A'_{x_k,θ_l}. If the platelet is located in the intersection of multiple spheres, it takes an arbitrary orientation of these spheres. The set of aligned platelets inside the aggregates is then obtained by:

$$A_1 = \bigcup_{x_k} A'_{x_k,\theta_l} \tag{10.26}$$

Note that the Poisson point process of x_k takes place in the domain $B \cap H^c$, but the platelets are implemented in the full domain D.

A homogeneous Poisson point process is simulated outside the aggregates and the exclusions in $B^c \cap H^c$. A platelet A'_{y_k,μ_k} is implanted at each Poisson point

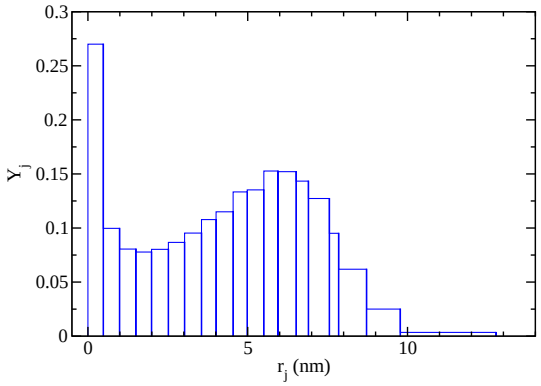

Figure 10.19: Regularized pore size distribution based from the experimental isotherm in Fig. 10.16.

y_k with volume fraction p_B. The orientations μ_k are randomly distributed on unit spheres and are independent. The volume fraction p_B is prescribed by the overall porosity, fixed by experimental to 69%:

$$p_{A2}(1-p_S)(1-p_H)+p_{A1}p_S(1-p_H)=1-0.69 \tag{10.27}$$

The set of randomly oriented platelets is then obtained by:

$$A_2=\bigcup_{y_k} A'_{y_k,\mu_k} \tag{10.28}$$

The three-scale model of platelets, with solid phase denoted by A, is then obtained by:

$$A=A_1\cup A_2 \tag{10.29}$$

The parameters of the three-scale model A include: radius threshold r_m, reference pore size distribution (r_j, p_j), volume fraction p_S and radius r_S of spherical aggregates, volume fraction of aligned platelets p_{A1} and shape of platelets A'. In this work, we take the octagonal prism as the primary platelet, described by the lengths of four sides (Fig. 8.1): D_1, D_2, D_3 and D_4.

In practice, the reference pore size distribution is deduced from the experimental data by regularization (Eq. 10.6). The regularized pore size distribution is shown in Fig. 10.19. The desorption threshold is initially fixed at 6.4 nm as identified in section 10.2.2. The three parameters of the aggregates p_{A1}, p_S and r_S and the four parameters of platelet shape are initially taken the same as the optimized two-scale model in section 8.5. The resolution of the microstructure is chosen to be 0.354 nm per voxel, because it is the size of monolayer nitrogen and it garanties the necessary precision for the simulation of multilayer adsorption. A 2D section of the hardcore spherical exclusion is shown in Fig. 10.20 (a). After inserting platelets, the microstructure of platelets is obtained (with 2D section shown in Fig. 10.20 b).

The multilayer adsorption at low pressure is performed on the three-scale model of platelets (2D sections shown in Fig. 10.21(A)). The number of nitrogen layers on solid interface is fixed at 1 for the initial test. It is observed in Fig. 10.21(A) that the monolayer nitrogen is "pasted" on the solid walls. Few pores are filled by the monolayer nitrogen. The volume fraction of the monolayer in the total porosity is 11.5%.

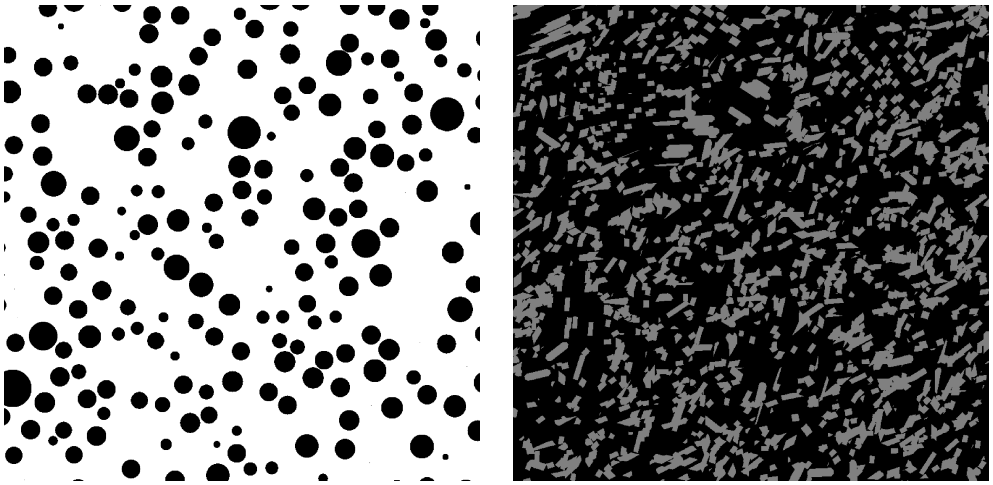

(a) hardcore exclusions (b) three-scale model of platelets

Figure 10.20: 2D sections of (a) the hardcore spherical model H and (b) the three-scale model of platelets. The parameters of the microstructure are shown in Tab. 10.1(B).

After the monolayer adsorption has occurred, the capillary condensation is simulated, starting from Kelvin radius $r_p = 2$ nm. At the corresponding pressure, the small space between platelets begins to be filled. The volume fraction of condensed liquid at this stage is 23%, which is in agreement with the experimental data. Indeed, the volume fraction of condensed liquid at low pressure is mainly determined by the specific surface area and the thickness of multilayer nitrogen. The former is dominated by the platelet size. This agreement validates the assumption of only one layer of nitrogen molecule at relative pressure $p/p_0 = 0.6$. It validates also the platelet size identification in chapter 8.

The simulated isotherms are shown in Fig. 10.22(B). The first point from the origin of the simulated isotherm is the volume fraction of the monolayer at $r_p = 0.354$ nm (note that here it takes approximately the value of r_t). The second point is the volume fraction of condensed liquid by monolayer adsorption and capillary condensation at $r_p = 2$ nm. The two points are connected with dotted line, because the first point is an approximation and the Kelvin equation is not valid at pressure below $r_p = 2$ nm.

The simulated adsorption and desorption branches of the three-scale model are shifted left compared to the experimental isotherms. It means the pores in the three-scale model are smaller than the real material. Compared to the two-scale model of platelets (Fig. 10.22(A)), the exclusions have taken effects to enlarge the pore size. Comparing Fig. 10.20 (a) and Fig. 10.21 (C), it is observed that at $r_p = 4.8$ nm, the remaining unfilled pores are mainly from the spherical exclusions. At the same time, the ink-bottle effect with small desorption threshold has been retained (Fig. 10.21 D).

Note that the exclusions do not explicitly generate spherical pores, but are useful for simulating the repulsion between the platelets in the model. An interpretation of the repulsion is that during the shaping, the neighbouring platelets tend to approach and align with one another. This effect creates aggregates at a larger scale, but also creates hollow space between large-scale structures.

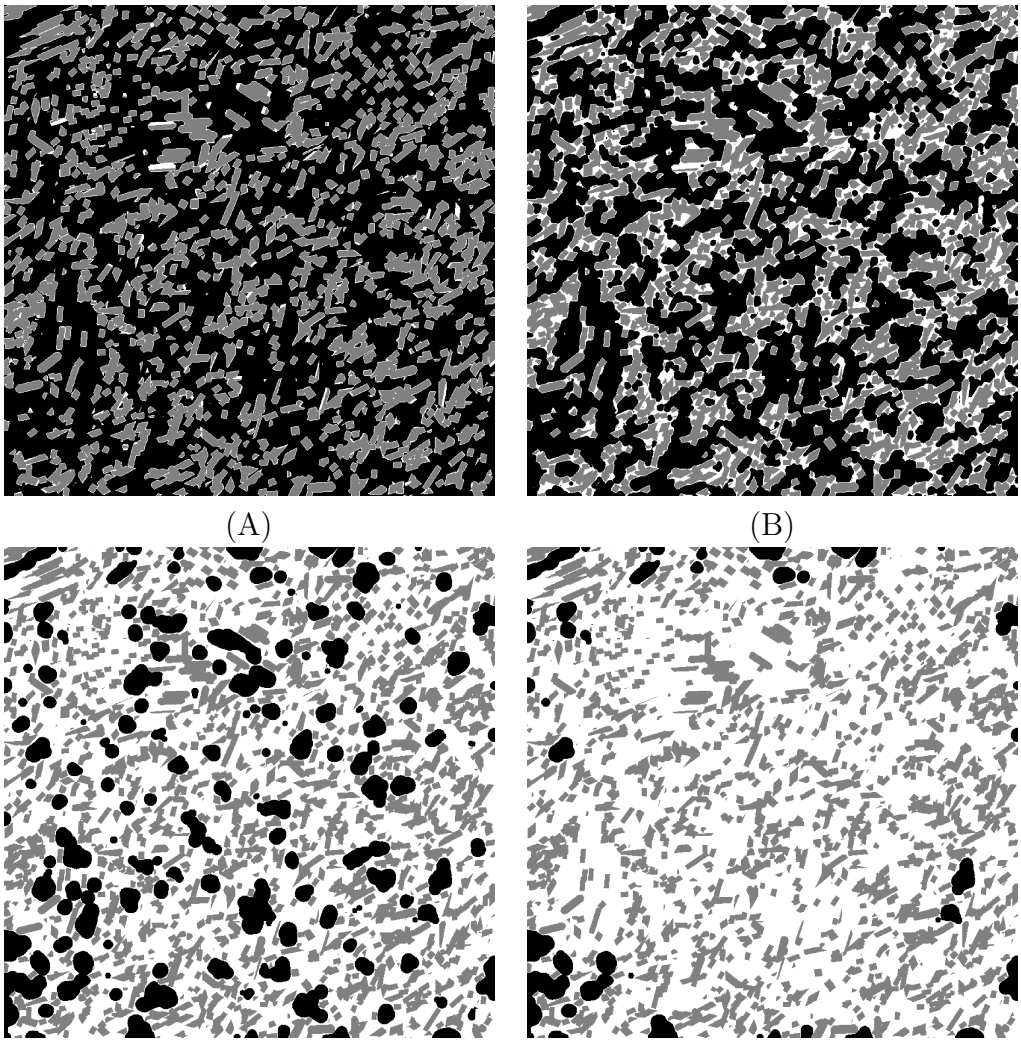

Figure 10.21: 2D sections of equilibrium states during porosimetry simulation on the three-scale model of platelets. The parameters of the microstructure are shown in Tab. 10.1(B). (A) Multilayer adsorption of thickness $r_t = 0.354$ nm. (B) Capillary condensation simulation at $r_p = 2$ nm. (C) Capillary condensation simulation at $r_p = 4.8$ nm. (D) Capillary evaporation simulation at $r_p = 4.8$ nm.

10.5.2 Parameters identification

The platelet size and the aggregates have been identified in chapter 8. Here, we emphasize on the identification of the exclusions. The exclusions in the three-scale model of platelets are described by three parameters: radius threshold r_m in nm, sphere radius r_j in nm and volume fractions p_j. First, we enlarge the radius of spherical exclusions by:

$$r'_j = r_j + r_c \tag{10.30}$$

where r_j is the original radius in the experimental pore size distribution, r'_j is the adjusted radius and r_c is the compensation size.

The value of r_c is determined by manual dichotomy method. The initial value of r_c is set to be 9 nm, half of the platelet length. A microstructure is generated with the new exclusions radius (Tab. 10.1 C) with simulated isotherms shown in Fig. 10.22 (C). The radius compensation is very efficient to increase the large-size pores. Furthermore, it does not change much the desorption threshold of the vapour phase, thanks to the hardcore features. A problem is shown in the adsorption branch that the pores are over enlarged. When the value of r_c is adjusted to be 6 nm (Tab. 10.1 D), the high-radius part (r_p from 8 nm to 12 nm) of the adsorption branch fits the experimental reference (Fig. 10.22 D).

Then we consider the intermediate part of the adsorption branch (r_p from 4 nm to 8 nm). In the microstructure (D), the volume fraction of pores of these sizes is less than that in experimental reference. To increase their volume fraction, we can either decrease the radius threshold r_m or increase their volume fractions p_j. However, the volume fraction of the hardcore spheres is limited to about 60%. The closer it gets to the limit, the more time-consuming the generation process is. We first decrease the radius threshold r_m to 5.5 nm (parameters in Tab. 10.1 E, isotherms in Fig. 10.22 E). It increases the volume fraction of exclusions and helps to facilitate the connections of the vapour phase. Compared to microstructure (D), the adsorption branch gets closer to the experimental isotherm.

To recover the experimental adsorption branch, we have tried to decrease further the radius threshold (not shown). However, the small exclusions take a significant volume fraction, but the do not contribute equally to the pores of corresponding size. Instead of adding more small exclusions, we increase the volume fraction of spherical exclusions of current sizes by a coefficient k:

$$p'_j = kp_j \tag{10.31}$$

where p_j is the original volume fractions in the experimental pore size distribution, p'_j is the adjusted volume fractions and the coefficient k is greater than 1. When the value of k is set to be 1.3, the isotherm in Fig. 10.22F is obtained. The adsorption branch gets closer to the experimental reference. When the volume fraction of exclusions increases, the desorption threshold also becomes higher.

To pull back the desorption threshold without decreasing the volume fraction of exclusions, the size of neck pores is considered. With fixed total number of platelets, we minimize the neck pores size by dispersing the platelets homogeneously in the domain. We let $p_{A1} = p_{A2}$ in Eq. 10.27 and obtain $p_{A1} = 0.47$. The parameters of the microstructure is shown in Tab. 10.1 G, and simulated isotherms in Fig. 10.22 G). As expected, the desorption threshold is decreased and fit the reference.

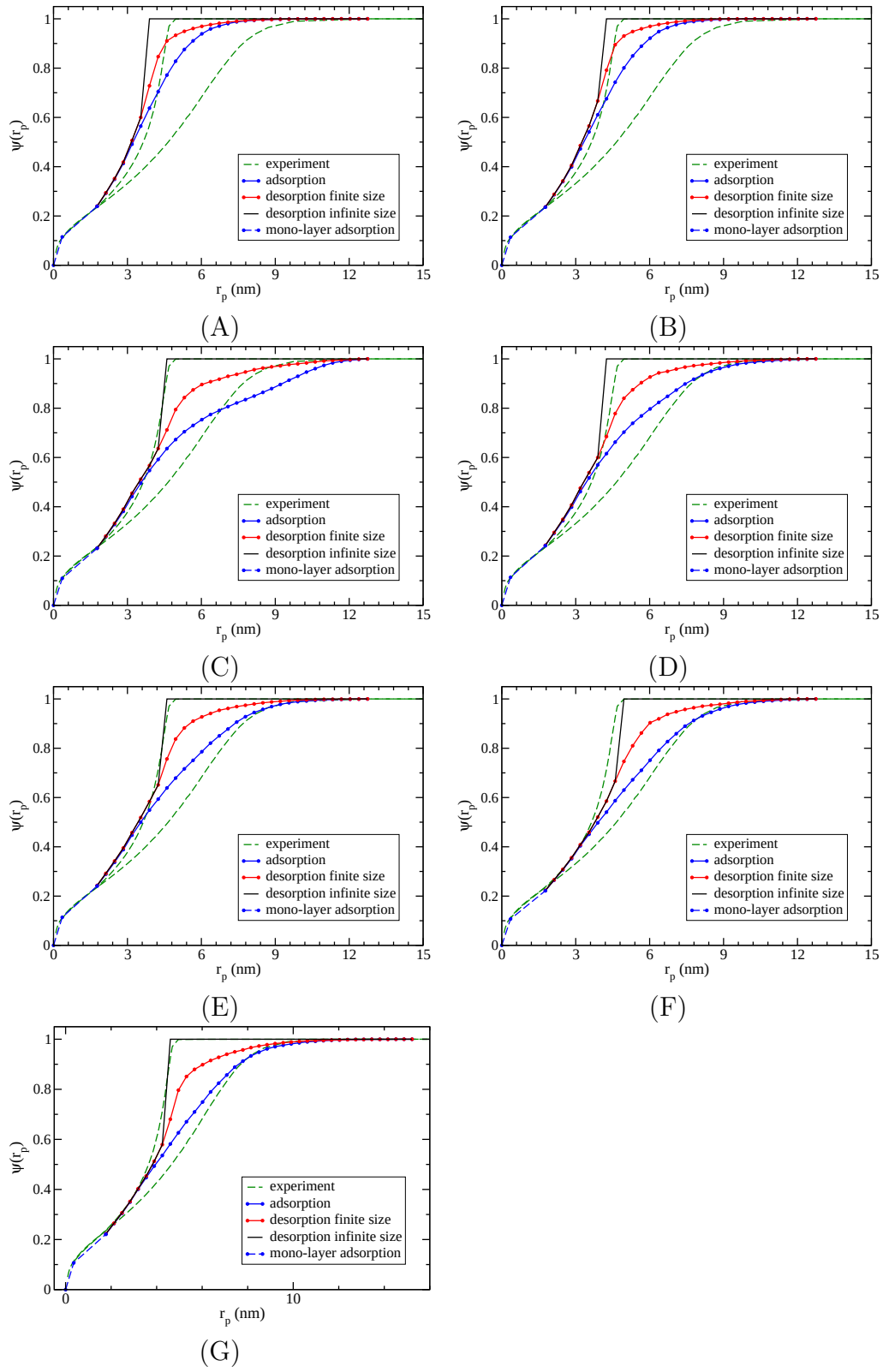

Figure 10.22: Simulated capillary isotherms of the multi-scale model of platelets for mesoporous alumina. The parameters of above microstructures are shown in Tab. 10.1.

Microstructure	Platelets (nm)				Aggregates			Exclusions		
	D_1	D_2	D_3	D_4	p_{A1}	p_S	r_S (nm)	r_m (nm)	r_c (nm)	k
(A)	14.3	2.4	2.0	3.3	0.3	0.2	30	0	0	0
(B)	14.3	2.4	2.0	3.3	0.3	0.2	30	6.4	0	0
(C)	14.3	2.4	2.0	3.3	0.3	0.2	30	6.4	9	0
(D)	14.3	2.4	2.0	3.3	0.3	0.2	30	6.4	6	0
(E)	14.3	2.4	2.0	3.3	0.3	0.2	30	5.5	6	0
(F)	14.3	2.4	2.0	3.3	0.3	0.2	30	5.5	6	1.3
(G)	14.3	2.4	2.0	3.3	0.47	0.2	30	5.5	6	1.3

Table 10.1: Parameter identification of the multi-scale model of platelets for mesoporous alumina. The corresponding simulated isotherms are shown in Fig. 10.22.

The microstructure (G) is sufficient to approximate the behavior of mesoporous alumina in nitrogen porosimetry, both the adsorption and desorption branches. The dichotomy searching process illustrates the effects of each parameter.

10.5.3 TEM image simulation

The TEM image is simulated from the microstructure (G) with the method presented in chapter 8. The simulated image is shown in Fig. 10.23, together with the correlation function shown in Fig. 10.24. Platelets and aggregates are visible in the simulated images in dark, together with the exclusions in bright hollows. Compared to the experimental TEM image, the contrast between solid phase and porous phase is higher. The difference is also shown in the correlation function: the exclusions contribute to the correlation of structures of large scales, and the range of correlation is much farther. The repulsion distance between hardcore exclusions also makes oscillations in long range.

The difference between the simulated TEM image and experimental TEM images originates from the interpretation of porosimetry data and TEM images. The integral range of the experimental TEM images is 30 nm^2 (section 6.4). The range of the correlation function of the TEM images is about 6 nm. In the TEM images, no structures as large as the simulated big hollows has been observed. However, the range of the adsorption branch of the nitrogen porosimetry isotherm is around $r_p = 12$ nm, larger than 6 nm. The porosimetry data shows the existence of structures of large scales that have not been observed in the TEM images.

The conflict between the information extracted from TEM images and nitrogen porosimetry leads to a reconsideration of the capillary condensation-evaporation simulation method. This is further discussed in Sec. 10.6.

10.6 Limitation of the method

10.6.1 Adsorption simulation on simple geometries

In the capillary adsorption simulation, spherical structuring elements are used to probe the local curvature. Where it cannot enter in, the local curvature is supposed to be smaller than the sphere radius. It fills these areas, and produces hemispherical meniscus on the vapour-liquid interface. This probing process describes the

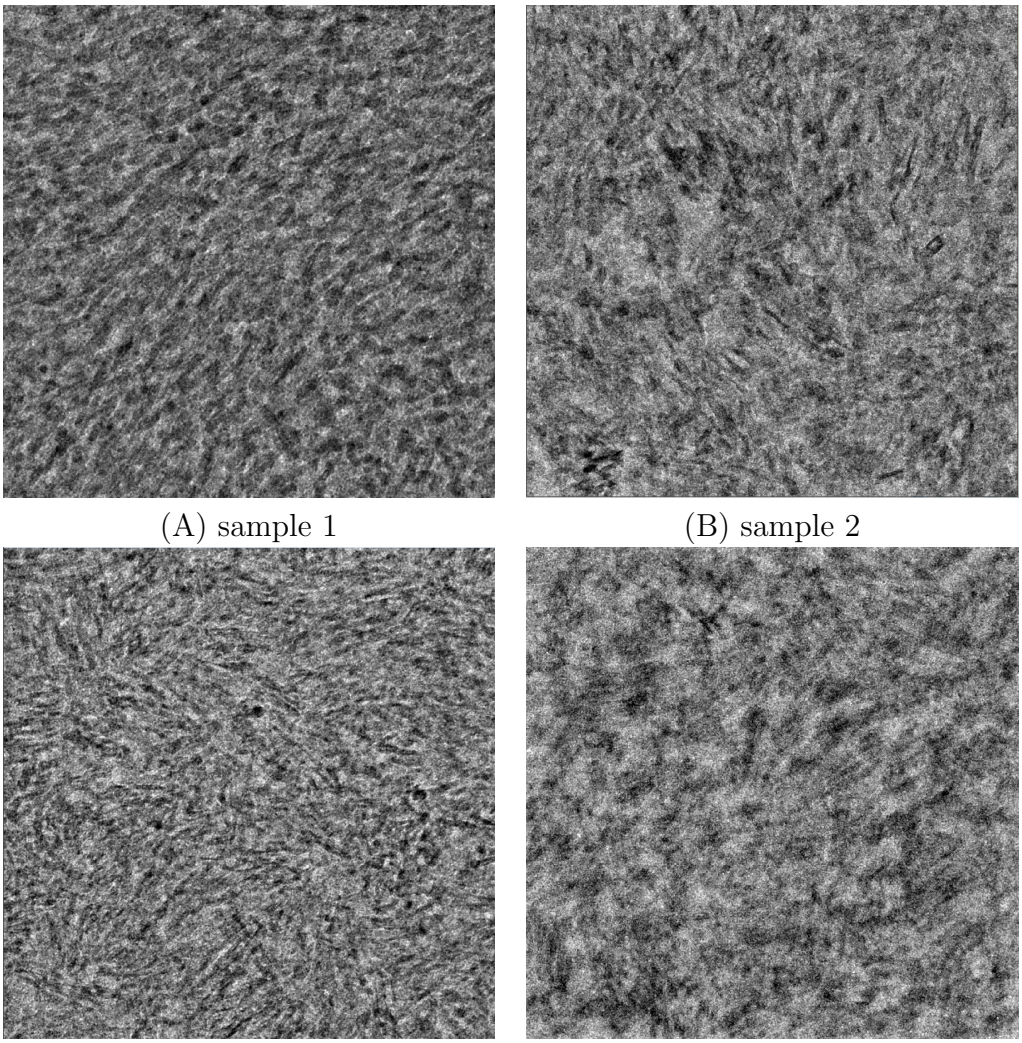

(A) sample 1 (B) sample 2

(C) sample 3 (D) simulation

Figure 10.23: Comparison between TEM image of the three samples and the simulation from the three-scale model of platelets, with parameters shown in Tab. 10.1 (G). The resolution of the four images is the same 0.33 nm per pixel, and the same for the system size 300^3 nm^3.

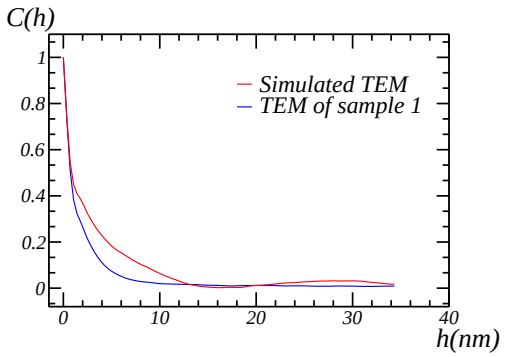

Figure 10.24: Comparison between the correlation functions of the TEM images and of the from the multi-scale model of platelets for mesoporous alumina. The parameters are shown in Tab. 10.1 (G).

reality during the desorption process, because the entire pore has been filled, and the evaporation depends only on the curvature of the vapour-liquid interface. The vapour-liquid interface tend to be spherical for a minimun energy state. However this is not exactly the case for adsorption, because the condensation depends more on the vapour-solid interface.

Cohan's model (Cohan, 1938) is an typical example to demonstrate the difference. In a cylindrical pore with one end closed, the condensation occurs first in the corners where the local curvature is low. With our method, hemispherical meniscus is formed, as predicted by the Kelvin equation. The meniscus propagates from the initial meniscus formed in the corners. The entire pore is filled when the Kelvin radius reach the radius of the cylinder base (denoted by r). In this case, it is right to use a spherical structuring element to probe the local curvature, because the condensation occurs on the hemispherical vapour-liquid interface.

However, in a cylindrical pore with two ends open, the condensation would not occur at the beginning at low pressure. The condensation occurs on the vapour-solid interface. The local curvature on the solid interface inside the pore is $2r$. The entire pore is filled suddenly when the Kelvin radius reach $2r$. Cohan predicts hysteresis for the cylindrical pore with two ends open – condensation at $r_p = 2r$ and evaporation at $r_p = r$. If we use a spherical structuring element to probe the local curvature, the result is r, which leads to pore filling at underestimated pressure.

Cohan's model tells a fact that hysteresis can be produced even without the ink-bottle effect, in the regime of the Kelvin equation. This effect – the difference in local curvature probing has not been taken into account in our method. It explains the different adsorption pressure observed on the isotherms of ink-bottle model between our method and the method of Virtual Capillary Condensation (Štěpánek et al., 2007) in Chapter 9. In a slit pore (Fig. 9.4), this effect is even more important. The curvature of the flat vapour-solid interface is infinite, and the meniscus curvature during desorption is d (where d is the pore width). The condensation occurs at saturated pressure, and the evaporation occurs at $r_p = d$. Being empty and being filled are two equilibrium states that both satisfy the Kelvin equation. However, the adsorption and the desorption have different preferences between the two states, which brings hysteresis.

Accordingly to the above, the pressures obtained during condensation are underestimated.

10.6.2 Identification using the desorption branch only

Since the adsorption branch simulated using spherical structuring element is not reliable, we re-identify the three-scale model with only the desorption branch as constraint.

As observed in the isotherm of Fig. 10.22(B), the black line (the desorption branch for system of infinite size) is quite close to the experimental desorption branch. Small changes are carried out in order to reduce the difference between model and experiment.

We keep the spherical exclusions, but cancel the repulsion distance. The other parameters are exactly the same as the microstructure (B). Therefore, the exclusion is an union of Boolean models of spheres with a radius distribution. The scales of aggregates and platelets remain unchanged. The simulated isotherms is shown

Microstructure	Platelets (nm)				Aggregates			Exclusions		
	D_1	D_2	D_3	D_4	p_{A1}	p_S	r_S	r_m (nm)	r_c (nm)	k
(A′)	14.3	2.4	2.0	3.3	0.3	0.2	30	0	0	0
(B′)	14.3	2.4	2.0	3.3	0.3	0.2	30	6.4	0	0

Table 10.2: Parameter identification of the three-scale model of platelets with only desorption branch. The corresponding simulated isotherms are shown in Fig. 10.25.

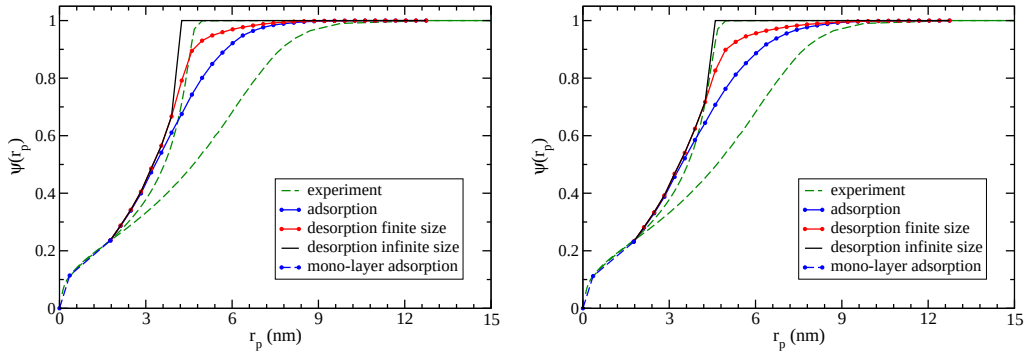

(A′) (B′)

Figure 10.25: Experimental and simulated correlation functions of the three-scale model of platelets for mesoporous alumina. The parameters of the microstructures are shown in Tab. 10.2.

in Fig. 10.25(B′). The desorption isotherm is fitted to the experimental data with the same desorption threshold. A comparison is made between the two microstructures (A′) and (B′) in Fig. 10.25, where microstructure A′ is the identified two-scale model in chapter. 8. The comparison illustrates the effects of the exclusions on the isotherms.

TEM image validation

The TEM image is simulated from the microstructure (B′), as shown in Fig. 10.27, together with the correlation functions shown in Fig. 10.26. The simulated image is also compared with the TEM image simulated from the two-scale model A′. In order to reproduce the correct porosimetry data, exclusions are used to slightly enlarge the pores and the desorption threshold, but it has a side effect that the correlation of the random structure is also slightly increased. At this point of view, the correlation function of the 2D projection (simulated TEM image) of a microstructure is correlated to its capillary behavior.

The two-scale model and the three-scale model of platelets are compared in terms of both capillary condensation-evaporation and image visualization. One is closer to the experimental data in capillary behavior, while the other is closer in TEM image validation. After all, the TEM image simulation and the porosimetry simulation both have been simplified. Their behaviors are similar and are both coherent to the experimental data. The real microstructure of the material is supposed to be a mixture of the two models.

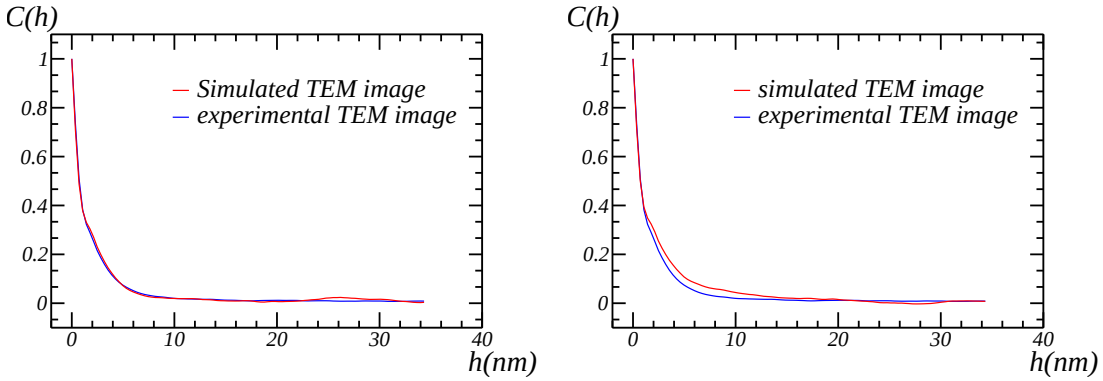

(A′) (B′)

Figure 10.26: Simulated capillary isotherms from (A′) the identified two-scale model of platelets (B′) the three-scale model of platelets for mesoporous alumina. The parameters of the microstructures are shown in Tab. 10.2.

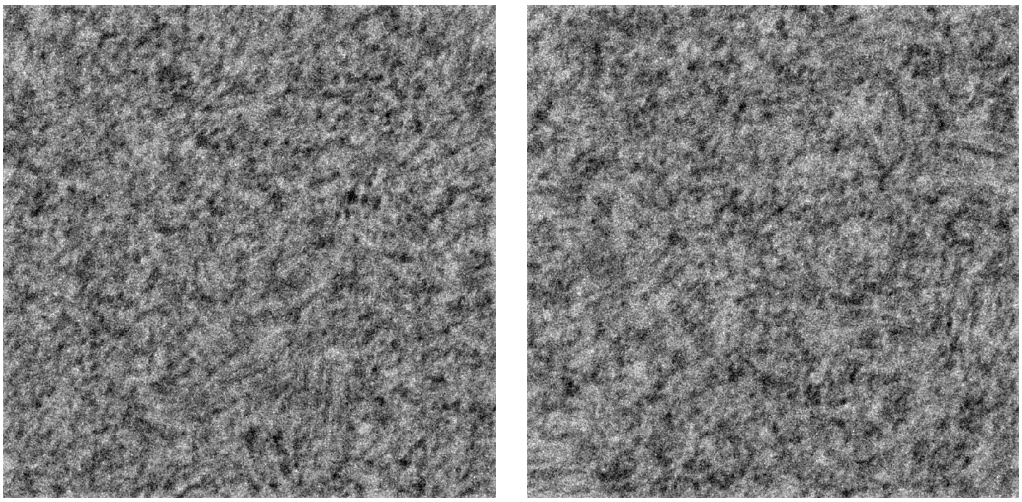

(A′) (B′)

Figure 10.27: Simulated TEM images from (A′) the identified two-scale model of platelets (B′) the three-scale model of platelets for mesoporous alumina. The parameters of the microstructures are shown in Tab. 10.2.

10.7 Conclusion

The objective of this chapter is twofold: model the microstructure of mesoporous alumina, and reproduce its porosimetry isotherms numerically. We developed a multiscale model based on Boolean random sets of spheres. By adjusting the sphere radius and volume fractions, the pore size distribution has been reproduced. Afterwards, by implementing hardcore spherical exclusions, the desorption threshold has been controlled. Then we observed the capillary behaviors of the tomographic reconstruction and of the two-scale model of platelets. The former's volume is too small and lacks representativity. The latter's average pore size was much smaller than the experimental data. Furthermore, it is found for the model of platelets, that the multilayer adsorption of nitrogen molecules occupies an non-negligible amount of liquid volume. The multilayer adsorption was simulated with a dilation operator.

A three-scale model was proposed with hardcore exclusions. The parameters of the three-scale model were identified to reproduce the experimental isotherm. However, the TEM image simulated from the three-scale model could not fit the experimental images in terms of correlation function. The information extracted from the TEM images and the porosimetry isotherms conflicted. This has led us to reconsider the interpretation of the isotherms and TEM images. It is found that the use of spherical structuring element simplifies the complex local geometry during the adsorption, and it causes the underestimation of the condensation pressure. The spherical structuring element is more coherent with the vapour-liquid interface during the desorption. The model has been then re-identified with only the desorption branch as constraint. The resulting three-scale model has the same desorption branch as experimental isotherms, and is validated with the TEM images. A comparison was made between the behaviors of the two-scale model and the three-scale model in terms of porosimetry and TEM image simulation. The comparison shows that through microstructure modeling, the information extracted from the two sources are consistent.

Part VI

Diffusion and Physical Properties

Chapter 11

Hindered diffusion in mesoporous alumina

11.1 Introduction

The mass transport property in nanoporous solid is driven by diffusion. Among important industrial processes under internal diffusional limitation, one finds hydrodemetalation of vacuum residues (Merdrignac et al., 2013), fixed-bed Fischer-Tropsch synthesis (Iglesia et al., 1995) and selective hydrogenation of unsaturated hydrocarbons (Derrien, 1986; Godinez et al., 1995). For these process, diffusion at the catalyst pellet's scale occurs at a lower pace than the chemical reaction, leading to internal diffusional limitations. Increasing the diffusion efficiency may lead to increased catalyst efficiency and overall process conversion.

In this chapter, we study the influence of the microstructure on diffusion properties of mesoporous alumina with a simplified quasistatic diffusion model. The experimental characterizations are presented in Sec. 11.2. The FFT method is used to compute the velocity fields in random models in Sec. 11.3. The effective diffusion coefficient of mesoporous alumina is estimated in Sec. 11.4.

11.1.1 Hindered diffusion

Mass transport of liquids in nanoporous media is a complex process, where hindered diffusion dominates. Hindered diffusion occurs when the gyration radius of the diffusing molecule is not negligible compared to the size of the pores. The ratio λ of the gyration radius r_g of the molecule on the pore radius r_p plays an important role.

$$\lambda = \frac{r_\mathrm{g}}{r_\mathrm{p}} \tag{11.1}$$

Liquid diffusion in nanoporous media occurs at a slower pace in bulk liquids. The effective diffusion coefficient D_e reads (Wernert et al., 2010):

$$D_\mathrm{e} = \frac{\epsilon K_\mathrm{p}(\lambda) K_\mathrm{d}(\lambda)}{\tau(\lambda)} D_0 \tag{11.2}$$

where D_0 is the molecular diffusion coefficient, ϵ the pore volume fraction, τ the tortuosity factor, K_p the partition coefficient, and K_d the drag coefficient. Three phenomena which slow down mass transport have been taken into account in the equation:

- The tortuosity of the porous space that implies that a molecule have to travel a longer path than the Euclidean distance to move from two remote (far away from the pore size) points. This effect is described by a tortuosity factor τ

- The steric hindrance, which describes a the fact that a finite sized molecule can not approach nearer than its gyration radius to the pore walls. This effect is described by a partition coefficient K_p

- A difference in viscous drag of the molecule due the vicinity of the pore walls, modeled by a drag coefficient K_d

For molecules much smaller than the pore size, $K_\mathrm{p} = K_\mathrm{d} = 1$. For a cylindrical pore, a molecule having a giration radius r_g has access to a fraction of the porosity equal to $K_\mathrm{p}\epsilon$, where:

$$K_\mathrm{p} = (1 - \lambda)^2 \tag{11.3}$$

Several expressions have been proposed for the K_d factor depending on the geometry and method of averaging (Deen, 1987; Dechadilok and Deen, 2006). The most employed factor, called the Renkin's equation, has been computed for a geometry made of a hard sphere in a cylindrical pore and reads, for $0 \leq \lambda \leq 0.4$:

$$K_\mathrm{d} = 1 - 2.1044\lambda + 2.089\lambda^3 - 0.948\lambda^5 \tag{11.4}$$

For rather small molecules, an empirical formula has been proposed by Satterfield et al. (1973):

$$K_\mathrm{d}K_\mathrm{p} = \exp(-2\lambda) \tag{11.5}$$

The tortuosity factor τ depends strongly on pore space topology and porosity. A general relation between τ and ϵ in the high porosity regime has been proposed by Comiti and Renaud (1989):

$$\tau = 1 - p\ln\epsilon \tag{11.6}$$

Where p is specific to the pore space topology, hence to the geometry of particles forming the solid. Equation 11.6 with $p = 0.5$ is an upper bound of the effective diffusion coefficient in a random model of overlapping sphere (Weissberg, 1963). Its applicability has been experimentally assessed by permeability (Comiti and Renaud, 1989), electrical conductivity (Barrande et al., 2007) or effective diffusion (Wernert et al., 2010) measurements.

11.1.2 Pulse-Field Gradient Nuclear Magnetic Resonance (PFG-NMR)

Hindered diffusion coefficient in nanoporous solids can be measured by proton Pulse-Field Gradient Nuclear Magnetic Resonance (PFG-NMR) (Hollewand and Gladden, 1995), inverse chromatography (Wernert et al., 2010), membrane permeation or modeling of the kinetics of adsorption of the solute in a batch reactor (Prasher and Ma, 1977; Tayakout et al., 2010). It is worth mentioning that PFG-NMR measures a self-diffusion coefficient, and the measurement is done only in the accessible part

of the pore space by the probe molecule. Then, effective diffusion coefficient probed by NMR D_e^{NMR} is related to molecular diffusion coefficient D_0^{NMR} by:

$$D_e^{\mathrm{NMR}} = \frac{K_{\mathrm{p}}(\lambda)}{\tau(\lambda)} D_0^{\mathrm{NMR}} \tag{11.7}$$

Pulse Gradient Spin Echo (PGSE) Nuclear Magnetic Resonance is a well establish technique to measure effective self-diffusion coefficient in porous media. Proton spins are phase-encoded and decoded by a field gradient impulsion and attenuation of the NMR signal can be related to the effective diffusion coefficient. Indeed, PGSE-NMR allows to map the diffusion propagator in q space, the magnetization wave vector (Callaghan et al., 1990). Assuming long diffusion times Δ and small magnetization wave vector q, the propagator is Gaussian and there is a simple relation between the ratio of echo intensities $S(g)$ with a field gradient over $S(0)$ without gradient, the parameters of the NMR sequence and the effective diffusion coefficient D_e^{NMR}. Using the stimulated echo sequence proposed by Tanner (1970), this relation writes:

$$\ln\left(\frac{S(g)}{S(0)}\right) = -D_e^{\mathrm{NMR}}\gamma^2 g^2 \delta^2 \left(\Delta - \frac{\delta}{3}\right) \tag{11.8}$$

where γ is the gyromagnetic ratio of the nucleus probed, g is the intensity of the field gradient pulses, δ is the duration of the gradient pulses and δ the time between the two gradient pulses (diffusion time). In this case, if $\delta \ll \Delta$ the magnitude of magnetization wave vector q is:

$$q = \frac{\gamma g \delta}{2\pi} \tag{11.9}$$

Following the argument of Callaghan, effective diffusion measurement by PFG-NMR must be performed in the regime $1/q \gg d_{\mathrm{p}}$, where d_{p} is the pore diameter.

PGSE-NMR has been used to study the diffusion of probe molecules in various mesoporous samples: water in silica and alumina (Hollewand and Gladden, 1995) or in mesoprous NaA zeolite (Valiullin and Kärger, 2011), n-pentane and n-heptane in alumina and used hydro-processing catalysts (Wood and Gladden, 2003), n-octane and 1,3,5-triisopropylbenzene in mesoporous Y zeolithe (Kortunov et al., 2005) or n-hexane in micro-mesoporous activated carbon (Kirchner et al., 2012). Hollewand et al. found a $D_0^{\mathrm{NMR}}/D_e^{\mathrm{NMR}}$ ratio equal to 1.8 for water diffusing in a $182\,\mathrm{m}^2/\mathrm{g}$ specific surface area alumina support (Hollewand and Gladden, 1995). Wood et al. have observed such ratio equal for 1.6 and 2.37 respectively for pentane and heptane in a $372\,\mathrm{m}^2/\mathrm{g}$ specific surface area alumina support (Wood and Gladden, 2003). DOSY (Diffusion Ordered SpectroscopY) is a class of NMR sequences that allows the simultaneous measurement of the classical NMR spectrum (chemical shift) with the measurement of the apparent diffusion coefficient. The Fourier transform of the free induced decay signal gives the NMR spectrum whereas the inverse Laplace transform of the echo attenuation yields the apparent diffusion coefficient.

Self-diffusion coefficient in pure toluene measured by PFG-NMR can be found in literature. Extrapolated values at 295 K found are 2.11 (Krüger and Weiss, 1970), 2.22 (Harris et al., 1993) and $2.39 \times 10^{-9}\,\mathrm{m}^2/\mathrm{s}$ (Pickup and Blum, 1989). Using the value of viscosity $\eta = 575.3\,\mu\mathrm{Pa\,s}$ (Santos et al., 2006) and $D_0 = 2.39 \times 10^{-9}\,\mathrm{m}^2/\mathrm{s}$ the Stokes-Einstein formula gives an hydrodynamic radius $r_{\mathrm{g}} = 0.16\,\mathrm{nm}$ at 295 K.

11.1.3 Homogenization of Fick's diffusion

Fick's diffusion

The steady-state diffusion governed by the Fick's first law is considered. Let $J_i(\mathbf{r})$ be the diffusion flux of molecules along the i axis and $c(\mathbf{r})$ the concentration of molecule at point $\mathbf{r}$, The Fick diffusion equation reads, in the permanent regime (time-independent):

$$\begin{cases} J_i(\mathbf{r}) = -D_{ij}(\mathbf{r})\,\partial_j c(\mathbf{r}) \\ \partial_i J_i(\mathbf{r}) = 0 \end{cases} \tag{11.10}$$

where $D_{ij}(\mathbf{r})$ is the local diffusivity tensor. Assuming isotropic media, $D_{ij} = D\delta_{ij}$ where $D(\mathbf{r})$ is a scalar field. The effective diffusion coefficient D_e of a porous medium is defined by:

$$\langle \mathbf{J} \rangle = D_e \langle -\nabla c \rangle. \tag{11.11}$$

Analytical bounds and estimates

The Hashin-Shtrikman lower bound for the effective diffusion coefficient of a porous medium is zero. For 3D medium, the upper bound is (Hashin & Shtrikman, 1963):

$$D_e \leq D_{max}^{HS} = D_0 \left(\frac{2\epsilon}{3-\epsilon} \right) \tag{11.12}$$

Numerical computation: FFT-*Fick* diffusion

We use an auxiliary field $\mathbf{E} = -\nabla c$ and note that the problem of Fick diffusion a mathematically (not physically) equivalent to that of electrical response of materials (Willot, 2015). According to this analogy, diffusion flux is associated with electrical current, the concentration gradient to electric field, concentration to electric potential and diffusion coefficient to conductivity. We now consider a three-dimensional cubic domain $\Omega = [-L/2, L/2]^3$ of width L. The edges of the domain are aligned with the Cartesian unit vectors $\mathbf{e}_i$ with $i \in \{1, 2, 3\}$ and periodic boundary conditions are employed:

$$\mathbf{J}(\mathbf{r}) \cdot \mathbf{n} - \#, \qquad c(\mathbf{r} + L\mathbf{e}_i) \equiv c(\mathbf{r}) - \overline{E}_i L, \qquad \mathbf{r}, \mathbf{r} + L\mathbf{e}_i \in \partial\Omega \tag{11.13}$$

where $-\#$ means anti-periodicity, $\mathbf{n}$ is the outer normal of $\partial\Omega$, and $\overline{\mathbf{E}}$ is an applied concentration gradient.

To apply FFT methods, we rewrite equation 11.10 as the Lippmann-Schwinger's equation:

$$\begin{cases} E_i = \overline{E_i} - \widetilde{G}_{i,j} * P_j \\ P_j = J_j - \widetilde{D} E_j \end{cases} \tag{11.14}$$

where $\widetilde{D}$ is an arbitrary reference diffusion coefficient, $\mathbf{P}$ is the associated polarization field, $\widetilde{\mathrm{G}}$ the Green operator and $*$ the convolution product. The convolution product in equation 11.14 may be advantageously evaluated in the Fourier domain. Simple FFT methods consists in iterating the following equation until convergence:

$$\mathbf{E}^{k+1} = \overline{\mathbf{E}} - \widetilde{\mathrm{G}} * \left[\left(D - \widetilde{D} \right) \mathbf{E}^k \right] \tag{11.15}$$

where $\mathbf{E}^k$ is the opposite of the concentration gradient at iteration k.

The effective diffusion coefficient D_e is obtained from the flux along i axis using:

$$D_e = \frac{\iint_\Omega D(\mathbf{r}) E_i(\mathbf{r}) \, \mathrm{d}x \, \mathrm{d}y}{L^2 \overline{E}_i} \tag{11.16}$$

where $-\overline{E}_i$ is the applied (macroscopic) concentration gradient along axis i.

11.2 Experimental Characterization

The experimental characterization is carried out by IFPEN.

11.2.1 Texture of alumina

Median pore diameter d_p is defined as the diameter where half of the mesoporous volume is contained in pores larger and smaller than d_p. It is obtained from mercury intrusion and from the Barret-Joyner-Halenda (BJH) calculation of the nitrogen desorption branch. The accessible porosity by toluene $\epsilon_t = \epsilon K_\mathrm{p}(\lambda)$ is computed from equation 11.4 using the hydrodynamic radius of toluene and the median pore radius measured from mercury intrusion. Results of texture characterization are summarized in table 11.1.

Table 11.1: Texture characterization of alumina samples. The value of λ is estimated using the average median pore diameter $d_\mathrm{p} = (d_\mathrm{p}^\mathrm{Hg} + d_\mathrm{p}^\mathrm{BJH})/2$. The coefficients K_d and K_p are calculated with Eq. 11.4 and Eq. 11.3 respectively. The accessible pore volume fraction ϵ_t is estimated by ϵK_p.

Sample	S_BET	ϵ	d_p (Hg)	d_p (BJH)	ϵ_t	λ	K_p	K_d
	m^2/g		nm	nm		10^{-2}		
sample 1	240	0.69	11.3	12.9	0.68	2.64	0.948	0.944
sample 2	223	0.71	10.7	15.7	0.70	2.42	0.952	0.949
sample 3	247	0.73	10.7	15.9	0.72	2.41	0.953	0.949

The three alumina have close textural properties. As toluene has a small hydrodynamic radius compared to the mean pore size, most of the porosity is accessible by toluene. Nitrogen desorption and mercury intrusion give slightly different values for the median pore diameter but it does not appreciably change the obtained K_d value and hence the accessible porosity by toluene.

11.2.2 Effective diffusion from PFG-NMR

About 15 extrudates are placed in a 5 mm diameter tube and immersed in 10 % deuterated toluene. The deuterated fraction has the purpose of locking the NMR probe on the deuterium resonance frequency. Measurements were performed with a Brucker Avance 600 spectrometer (600 MHz resonance frequency for proton). Temperature is controlled during the experiments at 295 K. Longitudinal relaxation time T_1 is measured by inversion-recovery sequence and transverse relaxation time T_2 by Carr-Purcell-Meiboom-Gill (CPMG) sequence. The relaxation time measurement

Table 11.2: Diffusion coefficient from NMR measurements

Sample	D_e^{NMR}	D_0^{NMR}	$\tau^{\mathrm{NMR}} = \frac{D_0^{\mathrm{NMR}}}{D_e^{\mathrm{NMR}}}$	$D_e = \epsilon_{\mathrm{t}} D_0 / \tau^{\mathrm{NMR}}$	$\tau = \frac{D_0}{D_e}$
	$10^{-9}\,\mathrm{m}^2/\mathrm{s}$	$10^{-9}\,\mathrm{m}^2/\mathrm{s}$		$10^{-9}\,\mathrm{m}^2/\mathrm{s}$	
Toluene	2.40				
sample 1	1.52	2.36	1.55	1.05	2.29
sample 2	1.57	2.60	1.65	1.02	2.35
sample 3	1.40	2.24	1.60	1.08	2.22

is mandatory to choose the correct PFG sequence and the order of magnitude its parameters.

The echo attenuation coefficients are measured using the bipolar pulse pairs longitudinal-eddy-current delay stimulated echo sequence (BPP-LED-STE) with parameters *delta*=2.5 µs, *Delta*=140 µs and *tau*=0.05 µs (Wu et al, 1995). q space is probed by varying the intensity of the gradient g, in order to obtain 16 values of attenuation from 2 % to 95 %. The values of the parameters are consistent with the small q requirement as $1/q_{\min} = 1.2 \times 10^5\,\mathrm{nm}$. Data are processed by the NMRnotebook software using the maximum entropy algorithm. Both free and hindered toluene diffusion coefficients are measured simultaneously by the DOSY sequence. From the experimental data, the tortuosity factor τ^{NMR} is estimated by:

$$\tau^{\mathrm{NMR}} = \frac{D_0^{\mathrm{NMR}}}{D_e^{\mathrm{NMR}}}. \tag{11.17}$$

Following the expressions of equation 11.2 and 11.7, effective diffusion coefficient D_e is obtained by:

$$D_e = \epsilon_{\mathrm{t}} \frac{D_0}{\tau^{\mathrm{NMR}}} \tag{11.18}$$

A reference measurement is performed on a tube filled with only deuterated toluene to check the field gradient calibration.

DOSY spectra of pure toluene and alumina plunged into toluene are showed in Fig. 11.1. For free toluene (Fig. 11.1 A), the five protons of the aromatic cycle are observed between 7 and 8 ppm, whereas the three proton of the methyl group are observed between 2 and 2.5 ppm. The 5/3 expected ratio of the peaks area is correctly recovered. A single diffusion coefficient is observed $D_0 = 2.40 \times 10^{-9}\,\mathrm{m}^2/\mathrm{s}$, compatible with the value found in literature. For toluene in all alumina, a strong broadening of both aromatic and methyl proton peaks are observed. Chemical shifts of confined toluene protons are shifted to higher values. Two distinct diffusion coefficients for free and confined toluene are systematically observed. Numerical values of diffusion coefficient extracted from DOSY spectra are reported in table 11.2. As expected by the subtle variation in texture, the effective diffusion coefficients of the three alumina are found very close. It should be noticed that the range of diffusion coefficients of free toluene from the three alumina is much greater than the uncertainty of measurement in pure toluene.

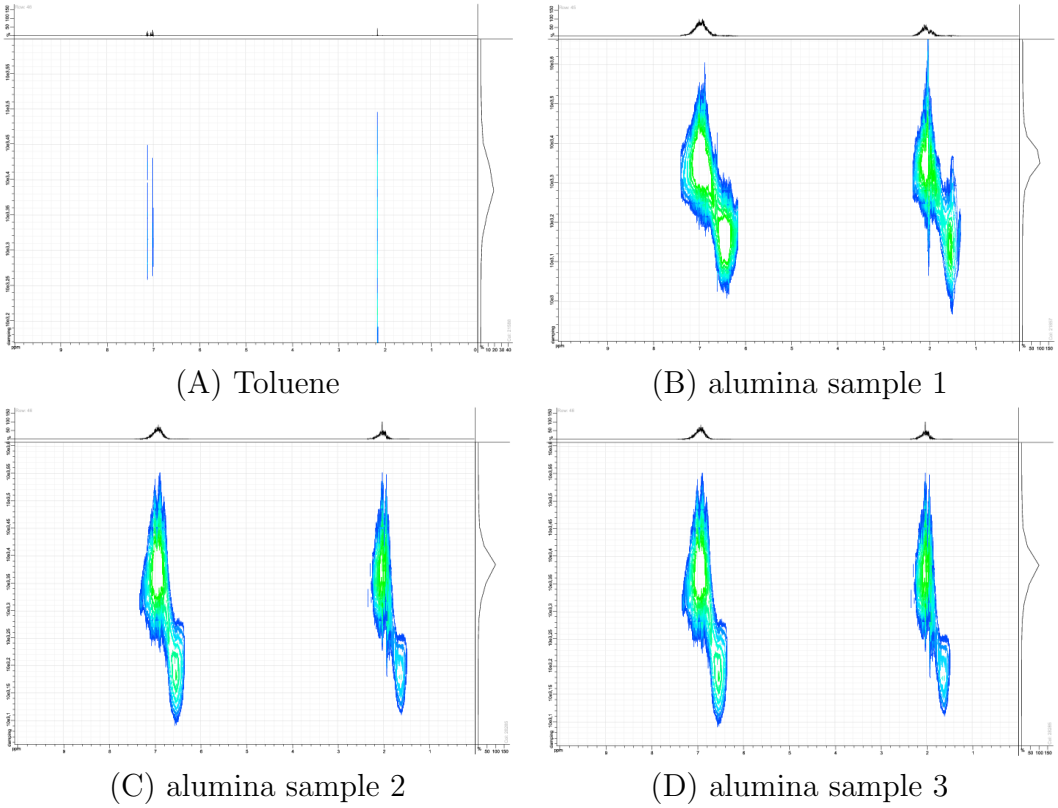

(A) Toluene (B) alumina sample 1

(C) alumina sample 2 (D) alumina sample 3

Figure 11.1: DOSY spectra of pure toluene and toluene in alumina.

11.3 Modeling of tortuosity from random models

Numerically, the effective diffusion coefficient D_e is computed numerically with the FFT-*Fick* diffusion method. Eq. 11.2 is used to estimate the tortuosity factors of random models. The molecule size effects and the viscous drag effects are neglected, so $K_p = K_d = 1$. $D(\mathbf{r})$ is set equal to $D_0 = 1$ in the pore space and $D_S = 0$ in the solid part. The tortuosity factor is then estimated by:

$$\tau = \frac{\epsilon}{D_e} \tag{11.19}$$

Analytically, the self-consistent homogenization method provides the relationship between the pore volume fraction ϵ and the effective diffusion coefficient D_e (Pellegrini & Willot, 2012):

$$\epsilon \frac{D_0 - D_e}{\frac{1}{d}D_0 + (1 - \frac{1}{d})D_e} + (1 - \epsilon)\frac{D_s - D_e}{\frac{1}{d}D_s + (1 - \frac{1}{d})D_e} = 0 \tag{11.20}$$

where d is the dimension factor (fixed at 3 in our case), D_s is the diffusion coefficient in the solid phase (fixed at 0 for alumina grains). Accordingly, we get $D_e = (3\epsilon - 1)/2$, and the tortuosity factor is obtained by:

$$\tau = \frac{2\epsilon}{3\epsilon - 1}. \tag{11.21}$$

11.3.1 Boolean models

In order to study the effects of particle shape on the effective diffusion coefficient and on the tortuosity, two grain shapes for Boolean models are considered: spheres

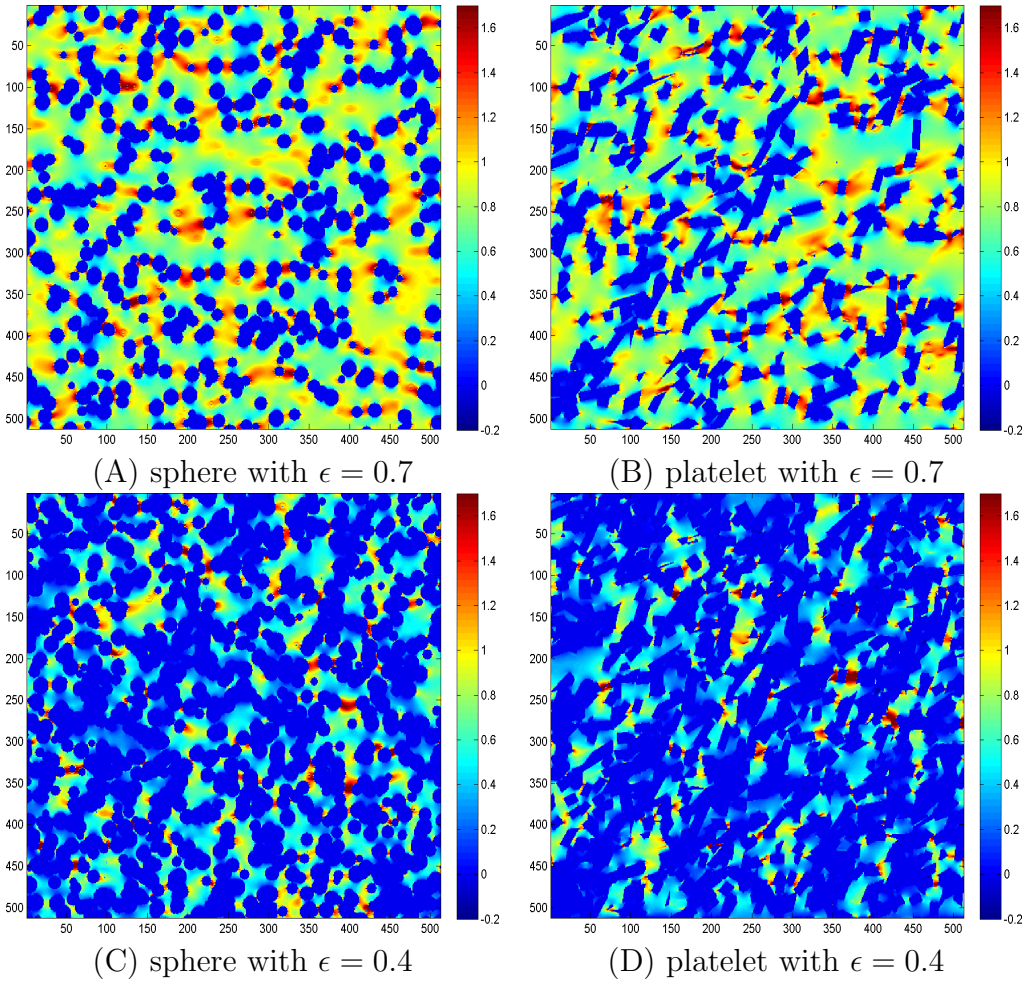

(A) sphere with $\epsilon = 0.7$ (B) platelet with $\epsilon = 0.7$

(C) sphere with $\epsilon = 0.4$ (D) platelet with $\epsilon = 0.4$

Figure 11.2: 2D sections of the first component of the flux field J_1 in the plane $z = 256$ obtained by FFT method on the Boolean models.

and platelets. The platelets have the same size and shape as the identified model in Sec. 8.5. The orientations of the platelets are isotropic. The microstructure volume is 512^3 voxel. The radius of spheres is 20 voxel. In order to study the relation between pore volume fraction and the tortuosity factor (as indicated in Eq. 11.6), microstructures of different pore volume fractions are generated.

A macroscopic concentration gradient is applied between the two faces along the first axis: $\overline{\mathbf{E}} = [1, 0, 0]$. The diffusion flux is in the complementary of the grains. When the algorithm converges, the steady concentration field is obtained, together with the flux field. An example of the first component of the flux fields J_1 are shown in Fig. 11.2.

The effective diffusion coefficients and the tortuosities estimated by Eq. 11.19 are respectively shown in Fig. 11.3 and in Fig. 11.4. The effective diffusion coefficients satisfy the Hashin-Shtrikman upper bound. Compared to the Boolean model of spheres, the Boolean model of isotropic platelets have lower diffusion coefficients and higher tortuosity factors. The shape of elongated prism increases the tortuosity of the porous phase. The shape effect is more important for media of low porosity, as shown in Fig. 11.2 (C) and (D).

The value of p in Eq. 11.6 is obtained by curve fitting using linear least squares with $\epsilon \geq 0.5$. For the Boolean model of spheres, $p = 0.74$. For the Boolean model of

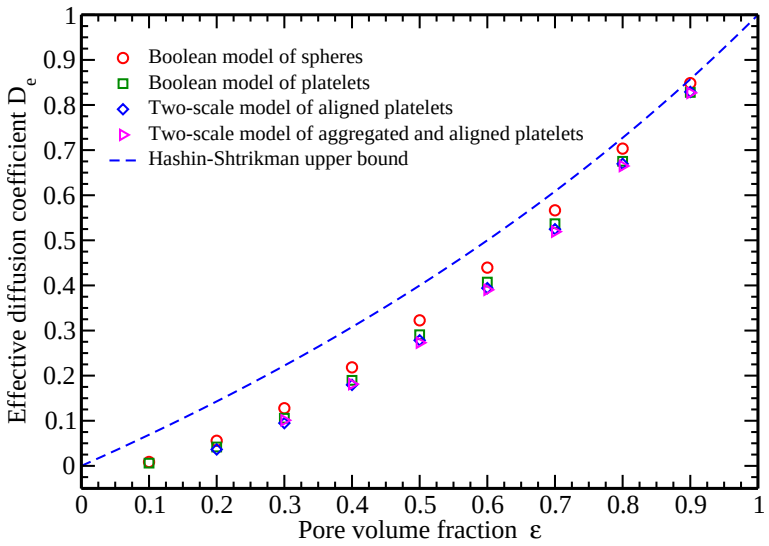

Figure 11.3: Effective diffusion coefficients of random models in function of pore volume fraction.

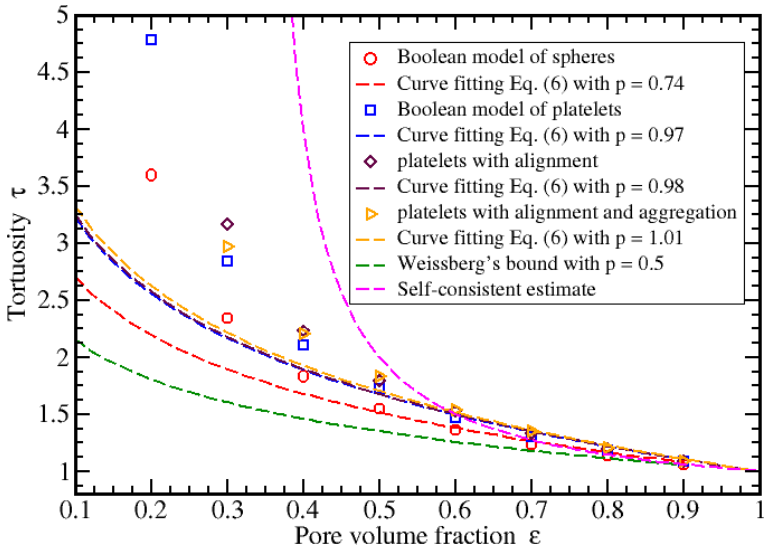

Figure 11.4: Tortuosity in function of porosity.

platelets, $p = 0.97$. The estimated tortuosity factors satisfy the Weissberg's lower bound with $p = 0.5$ for Boolean model of spheres.

11.3.2 Two-scale model of platelets

We study the effects of platelet alignment and platelet aggregation on the effective diffusion coefficient and on the tortuosity factor. The two-scale model of platelets is considered. First, the platelet density inside the aggregates p_{A1} is set to the same as the overall solid volume fraction $1 - \epsilon$. The volume fraction of spherical alignment zones is set to be 50%. In this microstructure, half of the platelets are aligned, but not aggregated. Second, the aggregation effect is added into the microstructure by setting p_{A1} higher than the overall solid volume fraction. A quadratic function of the pore volume fraction is used: $p_{A1} = 1 - \epsilon^2 > 1 - \epsilon$. The fractions of aligned and isotropic platelets are both maintained at 50% by setting $p_S p_{A1} = 0.5(1 - \epsilon)$. The

Platelets organization	Platelets (nm) D_1	D_2	D_3	D_4	Aggregates p_{A1}	p_S	$r_S(nm)$	Figure
Isotropic	14.3	2.4	2.0	3.3	0	0	0	Fig. 11.2 (B) (D)
Aligned	14.3	2.4	2.0	3.3	$1-\epsilon$	0.5	30	Fig. 11.5 (A)
Aligned and aggregated	14.3	2.4	2.0	3.3	$1-\epsilon^2$	$\frac{0.5}{1+\epsilon}$	30	Fig. 11.5 (B)

Table 11.3: Parameter table of the microstructures of the random models of platelets.

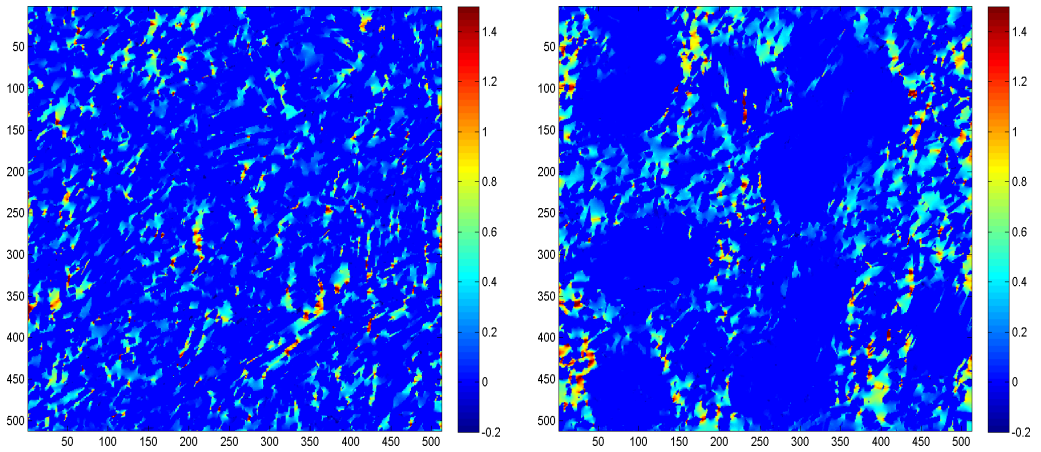

(A) Aligned platelets (B) Aligned and aggregated platelets

Figure 11.5: 2D sections of the first component of the flux field J_1 in the plane $z = 256$ obtained by FFT method on the two-scale models in Fig. 11.4 at $\epsilon = 0.3$.

parameters of the microstructures of platelets are shown in Tab. 11.3.

As shown in Fig. 11.3 and Fig. 11.4, the platelet alignment decreases the diffusivity and increases the tortuosity, compared to the isotropic platelets. The platelet aggregation has little influence on the diffusivity and tortuosity factor at high porosity. At low porosity, e.g. $\epsilon = 0.3$, the aggregation decreases the tortuosity factor. This is because the aggregation enlarges the pores outside the aggregates. The aggregation effect is shown in Fig. 11.5. The value of p in Eq. 11.6 is obtained by curve fitting using linear least squares with $\epsilon \geq 0.6$. For the microstructure with aligned platelets, $p = 0.98$. For the microstructure with aligned and aggregated platelets, $p = 1.01$.

11.3.3 Effects of aggregation density on tortuosity

The effects of fraction of aligned platelets on the tortuosity is considered. We set the overall pore volume fraction ϵ constant at 0.31, and let $t = p_{A1}p_S/(1-\epsilon)$ vary between 0 and 1.0 with step 0.1. The platelet density inside the aggregates is set $p_{A1} = 1-\epsilon^2$, higher than the platelet density outside the aggregates. When $t = 0$, no alignment is in the microstructure and it is equivalent to the Boolean model of isotropic platelets. When $t = 1$, all the platelets are aligned and contained in the aggregates. The parameters of the microstructures are shown in Tab. 11.4.

The tortuosity of above microstructures are estimated with the FFT method, and are shown in Fig. 11.6.When $0.1 < t < 0.4$, the tortuosity slightly decreases with increasing fraction of aggregations. However, when t is greater than 0.4, the higher the fraction of aggregated platelet is, the higher the tortuosity factors are.

Platelets organization	Platelets (nm) D_1	D_2	D_3	D_4	Aggregates p_{A1}	p_S	$r_S(nm)$	Figure
Aligned and aggregated	14.3	2.4	2.0	3.3	$1-\epsilon^2$	$\frac{t}{1+\epsilon}$	30	Fig. 11.7

Table 11.4: Parameters of the microstructures with varying aggregation density p_S, where $\epsilon = 0.31$ and $t \in \{0.1, 0.2, ..., 1.0\}$.

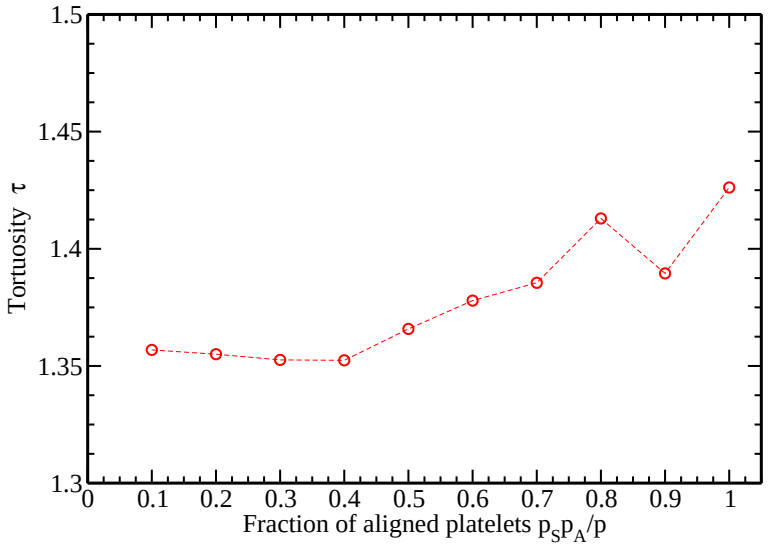

Figure 11.6: Tortuosity in function of volume fraction of aligned and aggregated platelets t. The parameters of the microstructures are shown in Tab. 11.4.

The 2D sections of the flux field with $t = 0.4$ and $t = 1.0$ are shown in Fig. 11.7.

Note that when the value of t is high ($0.8 \leq t \leq 1$), the representativities of the microstructures decrease, and the variance of estimates is high.

11.4 Modeling of hindered diffusion from identified models

We consider two identified models of platelets for mesoporous alumina – the two-scale model identified with the correlation function of TEM images of sample 1 (see details in Sec. 8.5) and the three-scale model identified with the nitrogen porosimetry isotherms of sample 1, including both the adsorption and the desorption branches (see details in Sec. 10.5). The parameters of the two microstructures are shown in Tab. 11.5.

The volume of the microstructures are 300^3 nm^3, with resolution 0.33 nm per voxel. The global pore volume fraction is set to be 0.69 (the same as sample 1). A

Microstructure	Platelets (nm) D_1	D_2	D_3	D_4	Aggregates p_{A1}	p_S	r_S	Exclusions r_m (nm)	r_c (nm)	k
Two-scale	14.3	2.4	2.0	3.3	0.3	0.2	30	0	0	0
Three-scale	14.3	2.4	2.0	3.3	0.47	0.2	30	5.5	6	1.3

Table 11.5: Parameter table of the identified random models of mesoporous alumina.

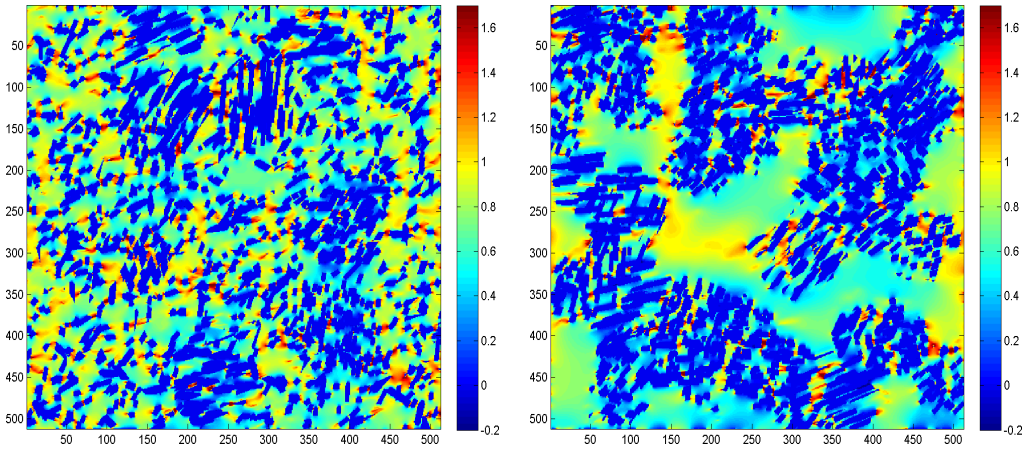

(A) $p_S p_A = 0.4p$ (B) $p_S p_A = 1.0p$

Figure 11.7: 2D sections of the first component of the flux field J_1 in the plane $z = 256$ obtained by FFT method on the two-scale models shown in Fig. 11.6.

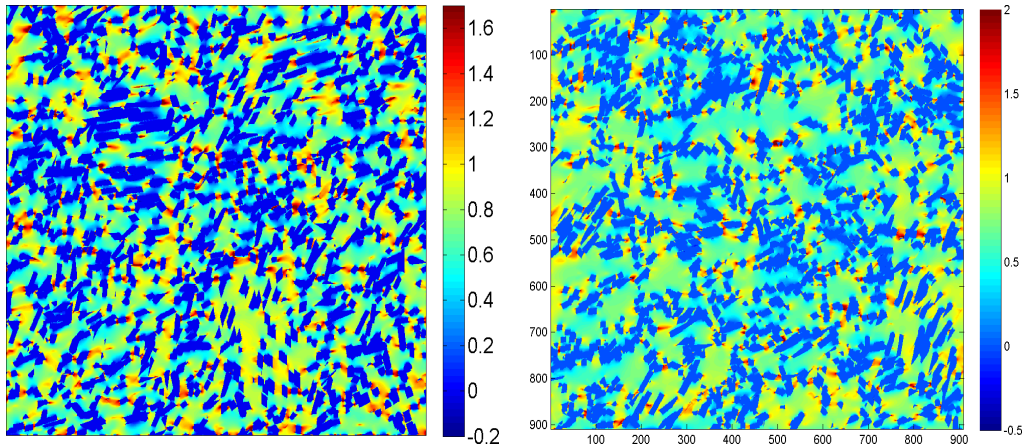

(A) Two-scale (B) Three-scale

Figure 11.8: 2D sections of the first component of the flux field $\mathbf{J}_1$ in the plane $z = 256$ obtained by FFT method on the identified random models of platelets with parameters shown in Tab. 11.5.

concentration gradient is imposed between the two faces along the $\mathbf{e}_1$ axis. The diffusion flux is computed using FFT method on the two models. The first components of the flux fields are shown in Fig. 11.8.

The effective diffusion coefficient is obtained by averaging $\mathbf{J}_1$ over the domain. The relative error of the estimates are analysis by the representative volume element. The variance of estimates $D^2(V')$ in function of domain volume V' is shown in Fig. 11.9. The relative error of the two estimates are obtained by:

$$e_r = \frac{2\sqrt{D^2(V_0)}}{\langle \mathbf{J}_1 \rangle} \tag{11.22}$$

where V_0 is the volume of the microstructure and $D^2(V_0)$ is obtained by curve fitting (Fig. 11.9). The relative errors of the estimates on the two-scale model and the three-scale model are 0.86% and 0.81% respectively.

The comparison between numerical computation and NMR measurements is

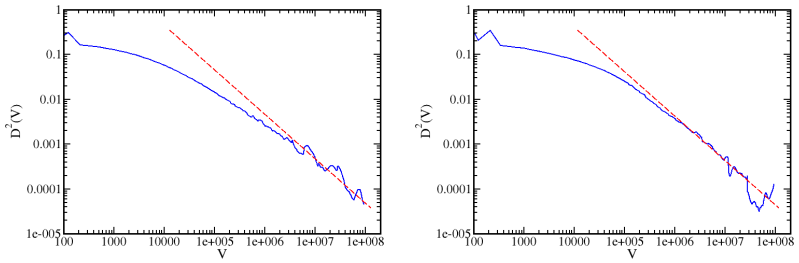

(A) Two-scale (B) Three-scale

Figure 11.9: Variance $D^2(V')$ computed over the first component of the flux field $\mathbf{J}_1$. Linear curve fitting for large V' by $1/V'$ is in red.

Table 11.6: Comparison of effective diffusion coefficients from numerical computation and NMR measurements.

Microstructure	D_e	D_0	$\tau = \frac{D_0}{D_e}$	D'_e	$\tau' = \frac{D_0}{D'_e}$
	$10^{-9}\,\mathrm{m}^2/\mathrm{s}$	$10^{-9}\,\mathrm{m}^2/\mathrm{s}$		$10^{-9}\,\mathrm{m}^2/\mathrm{s}$	
Sample 1		2.40	2.29		
Two-scale	0.51 ± 0.0022	1	1.96	0.46	2.19
Three-scale	0.50 ± 0.0020	1	2.00	0.45	2.23

shown in Tab. 11.6. The two-scale model and the three-scale model of platelets have similar effective diffusion coefficients. The ratio $\frac{D_0}{D_e}$ is about 20% lower than the experimental result. This is because in the numerical computation of Fick's diffusion, the molecule size is neglected, and the hindering effects (the drag effect and the partition effect) are not taken into account.

The Eq. 11.4 and the Eq. 11.3 are used to compensate the hindering effect by $D'_e = K_p K_d D_e$. The compensated tortuosity factor $\tau' = \frac{D_0}{D'_e}$ is then estimated, shown in the last column in Tab. 11.6. The tortuosity factors of the two-scale model (2.19) and of the three-scale model (2.23) are close to the NMR measurement result (2.29), respectively with relative error 4.4% and 2.6%.

11.5 Conclusion

In this chapter, the hindered diffusion in mesoporous alumina has been numerically estimated. The diffusion coefficients of toluene in the alumina samples were measured by PFG-NMR. The tortuosity factors were estimated as the ratio of free and confined diffusion coefficients. We modeled the tortuosity factors in Boolean models of spheres and isotropic platelets using numerical FFT-Fick's diffusion computation. The Boolean model of spheres has higher diffusion coefficient than that of platelets. The mixture of isotropic and aligned platelets was also studied, with or without aggregation. The platelet alignment decreases the diffusion coefficient and increases the tortuosity factor. The platelet aggregation increases the diffusion coefficient at low pore volume fraction, while at high pore volume fraction the effect is weak. At a fixed pore volume fraction, the tortuosity factor increases with increasing fraction of aggregated platelets, when the fraction of aggregated platelets is higher than 0.4.

We computed numerically the Fick's diffusion flux on the two-scale and three-

scale models of platelets for mesoporous alumina. The effective diffusion coefficients and the tortuosity factors were estimated. The hindering effects were estimated by Renkin's equation and cylindrical pore assumption, and were used to correct the effective diffusion coefficient numerically computed. The tortuosity factors of the random models are close to the experimental result, with relative error less than 4.4%.

Chapter 12

Other physical properties of mesoporous alumina

12.1 Permeability

12.1.1 Reminder: homogenization of Stokes flow

We consider the steady-state flow of an incompressible Newtonian fluid in mesoporous alumina. The flux velocity $\mathbf{u}(\mathbf{x})$ in the porous phase is described by the Stokes equation:

$$\mu \Delta u_i(\mathbf{x}) = \partial_i p(\mathbf{x}), \qquad \partial_i u_i(\mathbf{x}) = 0 \quad (\mathbf{x} \in P) \tag{12.1}$$

where μ is the fluid viscosity, p the pressure field and P the compact set for the porous phase. No-slip boundary condition is applied on the solid interface:

$$\mathbf{u}(\mathbf{x}) = 0 \quad (\mathbf{x} \in \partial S \bigcup S) \tag{12.2}$$

where S is the compact set for the solid phase. Periodic boundary condition is applied for the fluid velocity on the domain boundaries:

$$\mathbf{u}(\mathbf{x} \pm \mathbf{e}_k L) \equiv \mathbf{u}(\mathbf{x}) \tag{12.3}$$

where L is the side length of the cubic domain and $\mathbf{e}_k, k \in 1, 2, 3$ the basis vector. A macroscopic pressure gradient of intensity δP along the direction $\mathbf{E}$ is applied on the domain:

$$\langle \partial_i p(\mathbf{x}) \rangle = \delta P E_i, \qquad |\mathbf{E}| = 1, \tag{12.4}$$

where $\langle \cdot \rangle$ means average over the domain. The boundary condition for the pressure field satisfies the periodic fluctuation $p*$ (Ene & Sanchez-Palencia, 1975):

$$p*(x) = p(x) - \delta P(\mathbf{x} \cdot \mathbf{E}) = p*(\mathbf{x} \pm L\mathbf{e}_k) \tag{12.5}$$

The permeability κ_{ij} is defined by the Darcy's law:

$$\langle u_i(\mathbf{x}) \rangle = -\frac{\kappa_{ij} E_j}{\mu} \delta P. \tag{12.6}$$

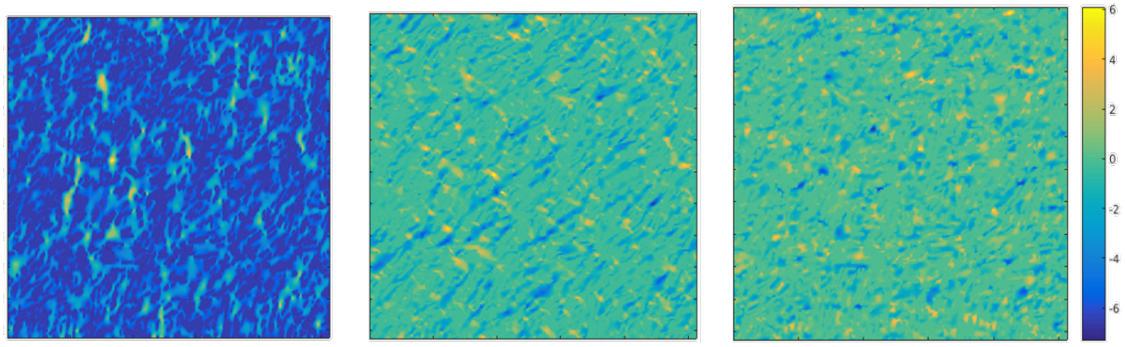

(A) u_1 (B) u_2 (C) u_3

Figure 12.1: 2D section of the velocity field components in the porous phase: x-direction (vertical on the map), y-direction (horizontal on the map) and z-direction (normal to the map) on top-right, bottom-left and bottom-right resp.

Mesoporous alumina is macroscopically isotropic. In this work, we choose $\mathbf{E} = \mathbf{e}_1$, so that the permeability tensor κ is identified with the first component $\kappa = \kappa_{11}$ and:

$$\kappa = -\frac{\mu \langle u_1(\mathbf{x}) \rangle}{\delta P} \tag{12.7}$$

For analytical permeability estimation, the Carman-Kozeny estimates (Carman, 1937; Kozeny, 1927) is considered:

$$\kappa^{CK} = \frac{f^3}{c\gamma^2} \tag{12.8}$$

where γ is the specific surface area, f the porosity.

12.1.2 Numerical solution of local fields

We use the FFT method (Wiegmann, 2007) to solve numerically the Eq. 12.1 – 12.5. By convention, we set the pressure gradient $\delta P = -1\,\text{Pa}$ and the viscosity $\mu = 1\,\text{Pa}\,\text{s}$. The algorithm converges, and we obtain the steady-state velocity field. A 2D section of the velocity field is shown in Fig. 12.1. The permeability is obtained directly by averaging the velocity field:

$$\kappa_e = \langle u_1(\mathbf{x}) \rangle \tag{12.9}$$

The effective permeability estimated on the two-scale model of platelets is $1.45\,\text{nm}^2$, larger than the Carman-Kozeny estimate of $0.95\,\text{nm}^2$. The estimation result cannot be validated because no experiment has been performed to measure the permeability on our mesoporous alumina samples.

12.1.3 Representative volume element

The representativity of the estimated effective permeability is analyzed using the variance $D^2_\kappa(V)$ of estimates over n random realizations of volume V. In practice, a single large realization of volume V is sufficient. The volume is divided into disjoint subdomains of volume V'. When $V \gg V'$ and $V' \to \infty$, the asymptotic expansion reads (Matheron, 1971):

$$D^2_\kappa(V') \propto \frac{D^2_\kappa A^\kappa_3}{V'} \tag{12.10}$$

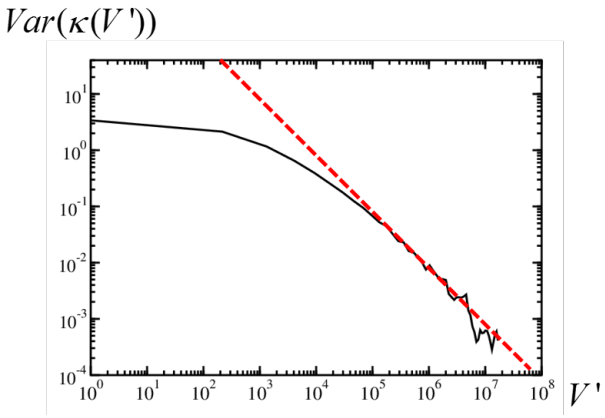

Figure 12.2: Variance $D^2_\kappa(V')$ computed over the first component of the velocity field u_1. Linear curve fitting for large V' by $1/V'$ is in red.

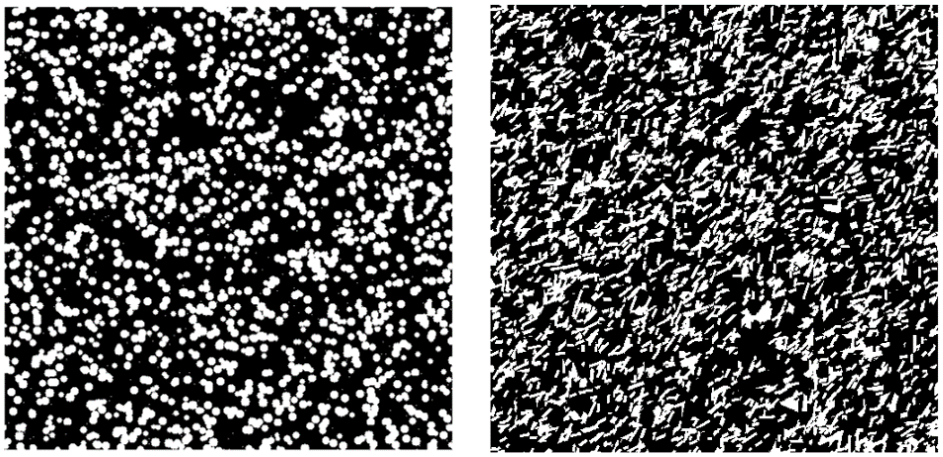

(A) Spheres (B) Platelets

Figure 12.3: 2D sections of microstructures of Boolean models of spheres and of isotropic platelets.

where D^2_κ is the point variance, and A^κ_3 is the integral range.

The variance $D^2_\kappa(V')$ computed over the velocity field is shown in Fig. 12.2. The curve fitting satisfies the reciprocal of V'. The variance $D^2_\kappa(V)$ at domain volume V is estimated by extending the fitting line. The relative error of the permeability estimation is:

$$\frac{2\sqrt{D^2_\kappa(V)}}{\kappa_e} = 0.98\% \tag{12.11}$$

12.1.4 Effects of prism shape on permeability

To study the effects of prism shape on the permeability, we compare the permeabilities of a Boolean model of spheres and a Boolean model of isotropic platelets. The pore volume fractions of the two microstructures are the same 0.69. The platelet size is the same as the identification in Sec. 8.5. The sphere radius is 10 nm. The 2D sections of the microstructures and of the velocity fields are shown in Fig. 12.3 and Fig. 12.4 respectively.

The effective permeability of the Boolean model of spheres is 2.96 nm^2, while

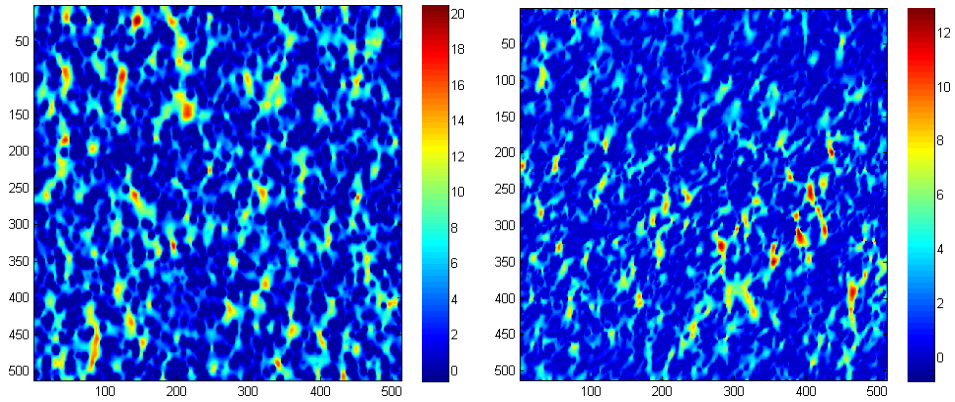

(A) Spheres (B) Platelets

Figure 12.4: 2D sections of velocity fields in Boolean models of spheres and of isotropic platelets.

$1.43\,\mathrm{nm}^2$ for the Boolean model of platelets. The elongated prism shape is not favorable for the improvement of permeability in Boolean models.

12.2 Elastic response of the 3D model of platelets

The rigidity of the catalyst support at high porosity is of the industry's interest. We use the FFT method to compute the elastic response of the 3D microstructures, and estimate the effective elastic moduli.

12.2.1 Reminder: linear elasticity homogenization

The constitutive behavior follows an isotropic, compressible linear elastic law, such that the stress and strain tensors are related by the local elastic tensor C:

$$\sigma(x) = C : \varepsilon(x) \tag{12.12}$$

where σ and ε are the local stress and strain tensors, respectively. The material has an isotropic local elastic tensor C that reads:

$$C_{ijkl} = \lambda(x)\delta_{ij}\delta_{kl} + \mu(x)(\delta_{ik}\delta_{jl} + \delta_{il}\delta_{jk}) \tag{12.13}$$

where δ is Kronecker symbol and $\lambda(x)$ and $\mu(x)$ are constant-per-phase Lamé's first and second coefficients. For a 3D media, the local bulk modulus is $\kappa = \lambda + 2/3\mu$. In the porosity, both $\lambda(x)$ and $\mu(x)$ equal to zero.

The strain derives from the displacement field u. Assuming small deformation, this reads:

$$\varepsilon_{ij} = \frac{1}{2}(\partial_i u_j + \partial_j u_i) \tag{12.14}$$

Symmetrically, the stress field satisfies an "equilibrium equation", in the absence of external forces:

$$\partial_i \sigma_{ij} = 0 \tag{12.15}$$

Periodic boundary conditions are applied with the material subjected to an overall strain loading $\bar{\varepsilon}$. The effective properties are computed by taking averages over

the elementary cell Ω. It is assumed that isotropy is recovered at the macroscopic scale:

$$\varepsilon_0 = \langle\varepsilon\rangle, \qquad \sigma_0 =< \sigma >= \widetilde{C} : \varepsilon_0 \tag{12.16}$$

where $\varepsilon_0 = \bar{\varepsilon}$ and σ_0 are the macroscopic strain and stress respectively, $< . >$ denotes the spatial mean over Ω, and $\widetilde{C}$ is the resulting effective elastic tensor.

The FFT method is based on the Lippmann-Schwinger equation. It makes use of an iterative fixed-point algorithm derived from the periodic equation (Moulinec & Suquet, 1994):

$$\varepsilon_{ij}(x) = \bar{\varepsilon}_{ij} - G_{ij,kl}(x) * \tau_{kl}(x), \qquad \tau_{ij}(x) = \sigma_{ij}(x) - C^0_{ij,kl} : \varepsilon_{kl}(x) \tag{12.17}$$

In Eq. 12.17, a homogeneous reference elasticity tensor C^0 is introduced, together with its associated polarization field τ and Green operator G. In Fourier domain, the Green operator has the form (Kanaun & Levin, 2008):

$$G_{ij,kl}(\mathbf{q}) = \{q_i \left[q_m C^0_{mj,kn} q_n\right]^{-1} q_l\}_{sym} \tag{12.18}$$

where $\mathbf{q} \neq 0$. If the reference elasticity tensor C^0 is symmetric, positive and isotropic, when $\mathbf{q} \neq 0$, the Green operator has the form:

$$G_{ij,kl}(\mathbf{q}) = \frac{1}{\mu^0}\left[(\frac{q_i q_l}{|\mathbf{q}|^2}\delta_{jk})_{sym} - \frac{\lambda^0 + \mu^0}{\lambda^0 + 2\mu^0}\frac{q_i q_j q_k q_l}{|\mathbf{q}|^4}\right] \tag{12.19}$$

The "direct scheme" (Moulinec & Suquet, 1994) applies the equation 12.17 iteratively:

$$\varepsilon^{k=0} = \bar{\varepsilon}, \qquad \varepsilon^{k+1} = \bar{\varepsilon} - G * [(C - C^0) : \varepsilon^k], \qquad (k \geq 0) \tag{12.20}$$

The convolution product is then computed in Fourier domain, using Fast Fourier Transform. Refined FFT algorithms with modified Green operators have also been proposed, in order to improve the convergence rate. In this work, we use the accelerated scheme (Eyre & Milton, 1999). The convergence rate of the scheme is influenced by the choice of reference elasticity tensor.

12.2.2 Numerical solution of local fields

The two-scale model of platelets identified with the correlation function of TEM images (see details in Sec. 8.5) is used. The microstructure volume is 512^3 voxel (3D view in Fig. 12.5 A). The Young's modulus of the solid phase is set to be 253 GPa (Gallas et al., 1994), while the porous phase 0 GPa. Staub (2014) took 0.22 as the macroscopic Poisson coefficient of unimodal and bimodal γ-alumina. The Poisson coefficient of alumina grains at the nanoscale should be a bit higher than the macroscopic value (Willot & Jeulin, 2011). Therefore, the Poisson coefficient of alumina grains is empirically set as 0.24.

An overall hydrostatic strain loading is imposed to the microstructure. The algorithm converges, and the stress field σ and the strain field ε are obtained. A 3D view of the stress field component σ_{xx} is shown in Fig. 12.5 (B). The 2D sections of the three main components of the stress field are shown in Fig. 12.6.

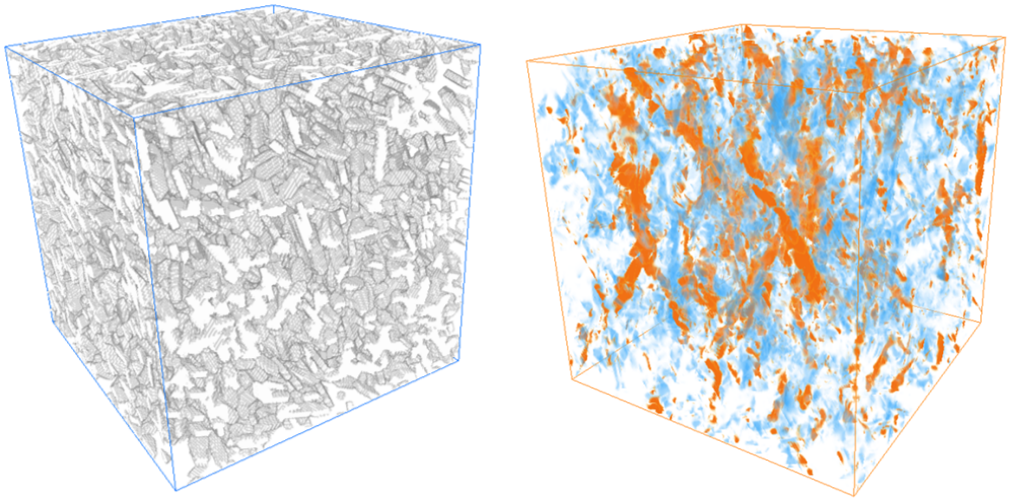

(A) (B)

Figure 12.5: 3d views of (A) the microstructure of mesoporous alumina and (B) stress field component σ_{xx}. The direction of e_x orients from the upper face to the lower face. Warm colors correspond to high positive stress zones, while cold colors for weak negative zones.

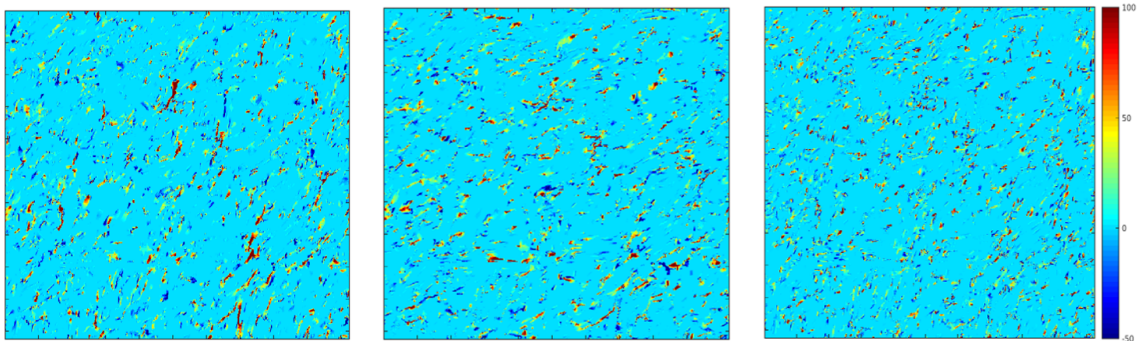

(A) σ_{xx} (B) σ_{yy} (C) σ_{zz}

Figure 12.6: 2D section of the stress field components in the solid: xx-direction (vertical on the map), yy-direction (horizontal on the map) and zz-direction (normal to the map) on top-right, bottom-left and bottom-right resp.

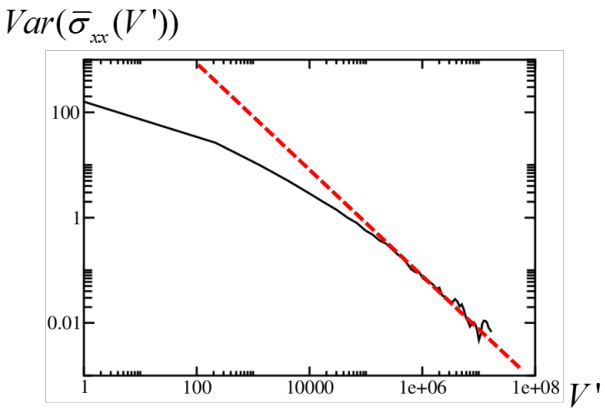

Figure 12.7: Variance $D_\sigma^2(V')$ computed over the first component of the stress field σ_{xx}. Linear curve fitting for large V' by $1/V'$ is in red.

12.2.3 Representative volume element

The representativity of the estimated effective elastic moduli is analyzed using the variance $D_\sigma^2(V)$ of estimates over n random realizations of volume V. In practice, a single large realization of volume V is sufficient. The volume is divided into disjoint subdomains of volume V'. When $V \gg V'$ and $V' \to \infty$, the asymptotic expansion reads (Matheron, 1971):

$$D_\sigma^2(V') \propto \frac{D_\sigma^2 A_3^\sigma}{V'} \tag{12.21}$$

where D_σ^2 is the point variance, and A_3^σ is the integral range.

The variance $D_\sigma^2(V')$ computed over the stress field is shown in Fig. 12.7. The linear curve fitting satisfies the asymptotic expansion. The variance $D_\sigma^2(V)$ at domain volume V is estimated by extending the fitting line. The relative error of the estimated $\langle \sigma_{xx} \rangle$ is:

$$\frac{2\sqrt{D_\sigma^2(V)}}{\langle \sigma_{xx} \rangle} = 3.02\% \tag{12.22}$$

12.2.4 Comparison with literature

The effective elastic moduli are calculated by eq. 12.16, and are shown in Tab. 12.1. The results satisfy the Hashin-Shtrikman upper bound. However, they cannot be validated because no experiment has been performed on elastic response of our mesoporous alumina samples. The results are compared with some elastic moduli of similar materials in literature.

Source	Method	ϵ	grain properties		effective properties	
			E (GPa)	ν	E (GPa)	ν
(Staub, 2014)	experiment	66.5%			6.4	
(Staub, 2014)	experiment	72.5%			3.6	
(Gallas et al., 1994)	experiment		253			
	HS upper bound	69%	253	0.24	41.5	0.24
	FFT	69%	253	0.24	1.65	0.19

Table 12.1: Comparison between elastic moduli computed by numerical methods and of similar materials in literature. Staub's sample of $\epsilon = 66.5\%$ is unimodal γ-alumina, and the sample of $\epsilon = 72.5\%$ is bimodal γ-alumina.

Part VII

Conclusions of the thesis

Chapter 13

Conclusion and perspectives

13.1 Conclusion

The study aims at enriching our knowledge on the relation between the morphology of the microstructure and the transport properties of mesoporous alumina. The goal of this thesis is to develop morphological models of the microstructure that are representative of the material, and to predict its transport properties which include sorption property and diffusion property.

Our approach consists of three steps: microstructure modeling constrained by TEM images, morphological simulation of sorption properties and homogenization on diffusion property. Accordingly, the thesis manuscript is organized focusing on the three problematics.

In Part III, the TEM images of 300 nm thick and 70 nm thick specimens were processed. The noise in the TEM images were identified, and the drift of the electron detectors was removed. The correlation functions of the 2D projections of the alumina microstructures were estimated.

In Part IV, based on the preliminary study by (Pietrasanta, 2013) on the Boolean model of isotropic platelets and the two-scale model of aligned platelets, we identified the size of the platelets and the spatial organization of the aggregates. The resulting two-scale model has a specific surface area much higher than the BET area by porosimetry, because the high-frequency noise biases the identification of platelet size. The noise and carbon membrane were then taken into account in the TEM image simulation. The re-identified model has platelets of size consistent with experimental observations, and was validated with the BET specific surface area.

In Part V, a procedure was proposed to simulate the capillary condensation and evaporation in porous media. The capillary condensation is simulated by a closing operator, while the evaporation is simulated by a closing operator followed by a hole-filling operator. The method is entirely geometrical, and the meniscus formed satisfies the Kelvin equation. The method was validated on simple geometries like slit pore and ink-bottle pores, in agreement with literature. When applied to random models of porous media, boundary effects introduce strong finite-size effects on the desorption branch. These effects were corrected by the percolation threshold analysis of the vapour phase. The main advantage of the method is the computation efficiency in large microstructures.

The method was then applied on various random models of porous media.

Isotherms are not sensitive to the shape of obstacles in Boolean models. The union or intersection of models of different scales combines their features in pore size distribution. A smooth pore size distribution was reproduced with a union of Boolean model of spherical exclusions. Ink-bottle effects were reproduced by the union of pores of distinct scales. By implementing hardcore spherical exclusions, the desorption threshold was controlled.

In order to reproduce the full range of the isotherms of nitrogen porosimetry on mesoporous alumina, the multilayer adsorption at low pressure was simulated by a dilation operator. The simulated isotherms of the two-scale model of platelets identified in Part IV indicated that its average pore size is smaller than experiment result. To enlarge the pores, a three-scale model with hardcore exclusions was proposed. This model reproduced the experimental isotherm with the full range simulation of nitrogen porosimetry.

The limitation of the method was also addressed: the spherical structuring element simplifies the local geometry during adsorption, and further underestimates the condensation pressure. The spherical structuring element is more coherent with the vapour-liquid interface during desorption. When watching only the desorption branch, the two-scale model of platelets identified with TEM images has close isotherms with experimental result. It indicates the consistency between the TEM images and the porosimetry isotherms.

In Part VI, the diffusion coefficients of toluene in the alumina samples were measured by PFG-NMR. The diffusion coefficients of Boolean models of spheres and of isotropic platelets were estimated using numerical FFT-Fick's diffusion computation, together with their tortuosity factors. Comparison indicated that platelets are less favorable than spheres for a high diffusion coefficient. The mixture of isotropic and aligned platelets was also studied, with or without aggregation. The platelet alignment decreases the diffusion coefficient and increases the tortuosity factor. The platelet aggregation increases the diffusion coefficient at low pore volume fraction, while at high pore volume fraction the effect is weak.

We computed numerically the Fick's diffusion flux on the two-scale and three-scale models of platelets for mesoporous alumina. With cylindrical pore assumption, the hindering effects were estimated by Renkin's equation, and were added in the effective diffusion coefficient estimation. The tortuosity factors of the two models are close to the experimental result, with relative errors 4.4% and 2.6% respectively. Numerical computations on elastic response and Stokes flow were also performed on the two-scale model of platelets. The effective elastic moduli and effective permeability have been predicted, but further experimental validation is required.

In summary, we modeled the 3D microstructure of mesoporous alumina with a random model of platelets. The model incorporates the information extracted from the XRD (by platelet shape) and the TEM images (by platelet size and aggregate organization). After parameter identification, the model reproduces the covariance of TEM images, the desorption branch of nitrogen porosimetry (including the specific surface area, the pore size distribution and the desorption threshold), and the effective diffusion coefficent measured by PFG-NMR. The effects of platelet size and aggregate organization on gas sorption properties have been studied. The effects of platelet shape, alignement and aggregation on the diffusion property have been studied.

13.2 Perspectives

The three samples of mesoporous alumina studied in this work were not distinct enough in texture. They have similar porosimetry isotherms and diffusion properties. Even so, differences in platelet aggregation scale have been observed visually in the TEM images. A preliminary work in the segmentation of primary grains and the quantification of local alignment has been shown in Sec 7.5. These information can be further explored and be quantified for the microstructure modeling and identification. This work may lead to models of better precision for each sample. If more samples with distinct textures are available, comparisons between them will help us to better understand the effects of microstructure morphology on the transport properties.

The morphological simulation of capillary condensation is not perfect: the solid-vapour interfaces are complex. Using a spherical structuring element to probe the curvature of the interface is over-simplified. Closing operator adapting to the interface curvature is an alternative for improvement.

In the Fick's diffusion computation, the hindering effects are estimated using analytical or empirical equations. In fact, the effect of gyration radius can be simulated by a dilation operator. The dilation puts a repulsion distance between molecules and solid walls. This manner is more precise than the cylindrical pore assumption.

The effective elastic moduli and effective permeability predicted using the FFT method should be further validated by experiment. The effects of microstructure morphology on the elasticity and permeability of mesoporous alumina are also of great interest for the refining industry. With these knowledge, microstructure optimizations can be performed for each property or coupled properties.

Bibliography

Abdallah, B., Willot, F., & Jeulin, D. (2015) Stokes flow through a Boolean model of spheres: Representative volume element. *Transport in Porous Media* 109:3, 711-726.

Adler, P., Jacquin, C., and Quiblier, J. (1990). Flow in simulated porous-media. *International Journal of Multiphase Flow*, 16(4):691–712.

Altendorf, H., Jeulin, D. & Willot, F. (2014) Influence of the fiber geometry on the macroscopic elastic and thermal properties. *Int. J. Sol. Struct.* **51**, 3807–3822.

Azzimonti, D., Willot, F., & Jeulin, D. (2013) Optical properties of deposit models for paints: full-fields FFT computations and representative volume element. *Journal of Modern Optics* 60:7, 519-528.

Baddeley, A., Rubak, E., & Turner, R. (2015) Spatial point patterns: methodology and applications with R. CRC Press.

Bird, G. A. (1976) Molecular Gas Dynamics. *Clarendon*, Oxford.

Brunauer, S., Emmett, P.H. & Teller, E. (1938) Adsorption of gases in multimolecular layers. *J. Am. Chem. Soc.* 60, 309–319.

Barrande, M., Bouchet, R., and Denoyel, R. (2007). Tortuosity of porous particles. *Analytical chemistry*, 79(23):9115–9121.

Barrett, E.P., Joyner, L.G. & Halenda, P.P. (1951) The Determination of Pore Volume and Area Distributions in Porous Substances. I. Computations from Nitrogen Isotherms. *J. Am. Chem. Soc.* 73:1, 373–380.

Callaghan, P., MacGowan, D., Packer, K., and Zelaya, F. (1990). High-resolution q-space imaging in porous structures. *Journal of Magnetic Resonance (1969)*, 90(1):177–182.

Carman, P.C. (1937) Fluid flow through granular beds. *Trans. Inst. Chem. Eng.* 15, 150–166.

Chiche, D., Digne, M., Revel, R., Chanéac, C., and Jolivet, J.-P. (2008). Accurate determination of oxide nanoparticle size and shape based on X-ray powder pattern simulation: application to boehmite AlOOH. *The Journal of Physical Chemistry C*, 112(23):8524–8533.

Cimino, R., Cychosz, K.A., Thommes, M. & Neimark, A.V. (2013) Experimental and theoretical studies of scanning adsorption–desorption isotherms. *Colloids and Surfaces A: Physicochemical and Engineering Aspects* 437, 76–89.

Chiu, S. N., Stoyan, D., Kendall, W. S. & Mecke, J. (2013) Stochastic geometry and its applications. John Wiley & Sons.

Cohan, L.H. (1938) Sorption Hysteresis and the Vapor Pressure of Concave Surfaces. *J. Am. Chem. Soc.* 60:2, 433-435.

Comiti, J. and Renaud, M. (1989). A new model for determining mean structure parameters of fixed beds from pressure drop measurements: application to beds packed with parallelepipedal particles. *Chemical Engineering Science*, 44(7):1539–1545.

Couka, E., Willot, F., Jeulin, D., Achour, M.B., Chesnaud, A. & Thorel, A. (2015) modelling of the multiscale dispersion of nanoparticles in a hematite coating. *Journal of Nanoscience and Nanotechnology, American Scientific Publishers* 15:5, 3515–3521.

Darcy, H. (1856) Les fontaines publiques de la ville de Dijon. *Dalmont* Paris.

Dechadilok, P. and Deen, W. (2006). Hindrance factors for diffusion and convection in pores. *Industrial & Engineering Chemistry Research*, 45(21):6953–6959.

Deen, W. (1987). Hindered transport of large molecules in liquid-filled pores. *AIChE Journal*, 33(9):1409–1425.

Delarue, A. & Jeulin, D. (2002) Homogenization of dielectric properties of random nanocomposites. Communication to *Matériaux 2002*, 21-25 October 2002, N-12/02/MM, Paris School of Mines Publication.

Derrien, M. (1986). Selective hydrogenation applied to the refining of petrochemical raw materials produced by steam cracking. *Studies in Surface Science and Catalysis*, 27:613–666.

Diaz, I., Gonzalez-Pena, V., Marquez-Alvarez, C., and Kikkinides, E. (2004). Transmission electron microscopy combined with stochastic reconstruction methods for structural characterization of porous alumina synthesized via non-ionic surfactant-templating route. *Microporous and Mesoporous Materials*, 68(1-3):11–19.

Digne, M., Sautet, P., Raybaud, P., Euzen, P., and Toulhoat, H. (2004). Use of DFT to achieve a rational understanding of acid–basic properties of γ-alumina surfaces. *Journal of Catalysis*, 226(1):54–68.

Ene, H.I. & Sanchez-Palencia, E. (1975) Equations et phénomenes de surface pour l'écoulement dans un modele de milieu poreux. *J. Mécanique* 14:1, 73-108.

Euzen, P., Raybaud, P., Krokidis, X., Toulhoat, H., Le Loarer, J.-L., Jolivet, J.-P., and Froidefond, C. (2002). Alumina. In Schüth, F., Sing, K., and Weitkamp, J., editors, *Handbook of porous solids*, pages 1591–1677. Wiley-VCH, Weinheim.

Eyre, D.J. & Milton, G.W. (1999) A fast numerical scheme for computing the response of composites using grid refinement. *The European Physical Journal Applied Physics* 6:1, 41-47.

Fukusawa, J. & Tsujii, K. (1988) Higher-order structure formation of ultrafine boehmite particles in sols, gels, and dried materials. *J. Colloid Interface Sci.* **125**, 155–161.

Frank & Joachim (1992) Electron tomography. Springer.

Frenkel, J. (1946) Kinetic theory of liquids, Clarendon Press, Oxford.

Gallas, M.R. & Piermarini, G.J. (1994) Bulk modulus and Young's modulus of nanocrystalline γ-alumina. *J. Am. Ceram. Soc* 11:77, 2917–2920.

Garboczi, E.J. & Bentz, D.P. (1991) Digitized simulation of mercury intrusion porosimetry. *Ceram. Trans.* 16, 365–380.

Greco, A., Jeulin, D. & Serra, J. (1979) The use of the texture analyser to study sinter structure: application to the morphology of calcium ferrites encountered in basic sinters of rich iron ores. *Journal of Microscopy* 116, 199-211.

Godinez, C., Cabanes, A., and Villora, G. (1995). Experimental study of the front-end selective hydrogenation of steam-cracking C_2-C_3 mixture. *Chemical Engineering and Processing: Process Intensification*, 34(5):459–468.

Halsey, G. D. (1948) *J. Chem. Phys.* 16, 31.

Hammersley, J. & Handscomb, D. (1964) Monte carlo methods. *Methuen*, London.

Harris, K., Alexander, J., Goscinska, T., Malhotra, R., Woolf, L., and Dymond, J. (1993). Temperature and density dependence of the selfdiffusion coefficients of liquid n-octane and toluene. *Molecular Physics*, 78(1):235–248.

Hashin, Z. & Shtrikman, S. (1963) A variational approach to the theory of the elastic behaviour of multiphase materials. *Journal of the Mechanics and Physics of Solids* 11:2, 127-140.

Haynes J.M. (1973) Pore size analysis according to the Kelvin equation. *Matériaux et constructions* 6 (33), 209–213.

Hill, T. L. (1952) Theory of physical adsorption. *Adv. Catal.* 4:1.

Hollewand, M. and Gladden, L. (1995). Transport heterogeneity in porous pellets—I. PGSE NMR studies. *Chemical Engineering Science*, 50(2):309–326.

Iglesia, E., Soled, S., Baumgartner, J., and Reyes, S. (1995). Synthesis and catalytic properties of eggshell cobalt catalysts for the Fischer-Tropsch synthesis. *Journal of Catalysis*, 153(1):108–122.

Jean, A., Jeulin, D., Forest, S., Cantournet, S. & N'Guyenm, F. (2010) A multiscale microstructure model of carbon black distribution in rubber. *Journal of Microscopy* 241, 243–260.

Jean, A., Willot, F., Cantournet, S., Forest, S. & Jeulin, D. (2011) Large-scale computations of effective elastic properties of rubber with carbon black fillers. *International Journal for Multiscale Computational Engineering* 9:3, 271-303.

Jeulin, D. (1979) Morphologie mathématique et propriétés physiques des agglomérés de minerais de fer et du coke métallurgique Thèse de Docteur-Ingénieur en Sciences et Techniques Minières, Option Géostatistique, Ecole des Mines de Paris, 23 Novembre 1979.

Jeulin, D. (1987) Random structure analysis and modelling by mathematical morphology. *Proc. CMDS5*, ed. by A.J.M. Spencer (Balkema, Rotterdam), 217-226.

Jeulin, D. (1991) Modèles morphologiques de structures aléatoires et de changement d'échelle. Thèse de Doctorat d'Etat ès Sciences Physiques, *Université de Caen*, 25 Avril 1991.

Jeulin, D. (1991) Modèle de fonction aléatoires multi-variable. *Sci Terre* 30, 225-256.

Jeulin, D. (1996) modelling heterogeneous materials by random structures. *European Workshop on Application of Statistics and Probabilities in Wood Mechanics*, Bordeaux, 22–23 March 1996, N-06/96/MM, Paris School of Mines Publication.

Jeulin, D. (2000) Random texture models for material structures. *Statistics and Computing* 10, 121–132.

Jeulin, D. & Moreaud M. (2008) Segmentation of 2D and 3D textures from estimates of the local orientation. *Image Anal Stereol* 27, 183–192.

Jeulin, D. (2011) Variance scaling of Boolean random varieties. *hal.archives-ouvertes.fr/hal-00618967* (accessed Sep. 4, 2014).

Jeulin, D. (2012). Morphology and effective properties of multi-scale random sets:a review. *Comptes Rendus Mécanique*, 340(4-5):219–229.

Jeulin, D. (2013) Correlation of orientations in a vector field and statistics of alignments. Internal Report, CMM, Mines ParisTech, N-02/13/MM.

Jeulin, D. (2014) A two-scales platelet random model. *Internal Report*, CMM, Mines ParisTech, N-02/14/MM.

Joshi, M.Y. (1974) A class of stochastic models for porous media. PhD thesis, University of Kansas.

Kainourgiakis, M.E., Kikkinides, E.S., Galani, A., Charalambopoulou, G.C. & Stubos A.K. (2005) Digitally reconstructed porous media: transport and sorption properties. *Transp Porous Med* 58, 43–62.

Kanaun, S. & Levin, V. (2008) Self-consistent methods for composites. *Springer*, Dordrecht, The Netherlands.

Kanit, T., Forest, S., Galliet, I., Mounoury, V. & Jeulin, D. (2003) Determination of the size of the representative volume element for random composites: statistical and numerical approach. *International Journal of Solids and Structures* 40, 3647–3679.

Khodakov, A.Y., Griboval-Constant, A., Bechara, R. & Zholobenko, V. (2002) Pore size effects in Fischer-Tropsch synthesis over Cobalt-supported mesoporous silicas. *Journal of Catalysis* 206, 230–241.

Kierlik, E., Monson, P. A., Rosinberg, M. L., Sarkisov, L. & Tarjus, G. (2001) Capillary Condensation in Disordered Porous Materials: Hysteresis versus Equilibrium Behavior. *Phys. Rev. Lett.* 87:5, 055701.

Kim, P., Kim, Y., Kim, C., Kim, H., Park, Y., Lee, J.H., Song, I.K. & Yi, J. (2003) Synthesis and characterization of mesoporous alumina as a catalyst support for hydrodechlorination of 1,2-dichloropropane: effect of catalyst preparation method. *Catalyst letters* 89, 3–4.

Kirchner, T., Shakhov, A., Zeigermann, P., Valiullin, R., and Kärger, J. (2012). Probing mesopore connectivity in hierarchical nanoporous materials. *Carbon*, 50(13):4804–4808.

Klimov, O.and Leonova, K., Koryakina, G., Gerasimov, E., Prosvirin, I., Cherepanova, S., Budukva, S., Pereyma, V., Dik, P., Parakhin, O., and Noskov, A. (2014). Supported on alumina Co-Mo hydrotreating catalysts: Dependence of catalytic and strength characteristics on the initial AlOOH particle morphology. *Catalysis Today*, 220:66–77.

Koch, K., Ohser, J., & Schladitz, K. (2003). Spectral theory for random closed sets and estimating the covariance via frequency space. *Advances in Applied Probability*, 603–613.

Koci, P., Stepanek, F., Kubicek, M., and Marek, M. (2006). Meso-scale modelling of CO oxidation in digitally reconstructed porous Pt/gamma-al_2o_3 catalyst. *Chemical Engineering Science*, 61(10):3240–3249.

Koci, P., Stepanek, F., Kubicek, M. & Marek, M. (2007) Pore-scale modelling of non-isothermal reaction phenomena in digitally reconstructed porous catalyst. *Molecular Simulation* 33:4-5, 369–377.

Koci, P., Novak, V., Stepanek, F., Marek, M., and Kubicek, M. (2010). Multi-scale modelling of reaction and transport in porous catalysts. *Chemical Engineering Science*, 65(1):412–419. 20th International Symposium on Chemical Reaction Engineering, Kyoto, JAPAN, Sep 7-10, 2008.

Kohout, M., Collier, A.P. & Stepanek, F. (2004) Effective thermal conductivity of wet particle assemblies. *International Journal of Heat and Mass Transfer* 47:25, 5565–5574.

Kosek, J., Stepanek, F. & Marek, M. (2005) modelling of transport and transformation processes in porous and multiphase bodies. *Advances in Chemical Engineering* 30, 137-203.

Kortunov, P., Vasenkov, S., Kärger, J., Valiullin, R., Gottschalk, P., Fé Elía, M., Perez, M., Stöcker, M., Drescher, B., McElhiney, G., Berger, C., Gläser, R., and Weitkamp, J. (2005). The role of mesopores in intracrystalline transport in USY zeolite: PFG NMR diffusion study on various length scales. *Journal of the American Chemical Society*, 127(37):13055–13059.

Kosek, J., Stepanek, F., and Marek, M. (2005). Modeling of transport and transformation processes in porous and multiphase bodies. In Marin, G., editor, *Multiscale Analysis*, volume 30 of *Advances in Chemical Engineering*, pages 137–203. Elsevier.

Kozeny, J. (1927) Ueber kapillare leitung des wassers im boden. *Sitzungsber Akad Wiss Wien* 136, 271–306.

Krüger, G. and Weiss, R. (1970). Diffusionskonstanten einiger organischer Flüssigkeiten. *Zeitschrift für Naturforschung A*, 25(5):777–780.

Langmuir, I. (1918) The adsorption of gases on plane surfaces of glass, mica and platinum. *J. Am. Chem. Soc.* 40:9, 1361–1403.

Lantuejoul, C. (1991) Ergodicity and integral range. *Journal of Microscopy* 161, 387–403.

Lee, J., Jeon, H., Oh, D., Szanyi, J., and Kwak, J. (2015). Morphology-dependent phase transformation of γ-Al_2O_3. *Applied Catalysis A: General*, 500:58–68.

Levitz, P. (1993) Knudsen diffusion and excitation transfer in random porous media. *J. Phys. Chem.* 97, 3813–3818.

Libby, B. & Monson, P. A. (2004) Adsorption/Desorption Hysteresis in Ink-bottle Pores: A Density Functional Theory and Monte Carlo Simulation Study. *Langmuir* 20:10, 4289–4294.

Lindblad, J. (2005) Surface area estimation of digitized 3D objects using weighted local configurations. *Image and Vision Computing* 23, 111–122.

Lippens, B. C., Linsen, B. G. & de Boer, J. H., (1964) Studies on pore systems in catalysts I. The adsorption of nitrogen; apparatus and calculation. *Journal of Catalysis* 3:1, 32–37.

Liu, H., & Seaton, N.A. (1994) Determination of the connectivity of porous solids from nitrogen sorption measurements—III. Solids containing large mesopores. *Chemical Engineering Science* 49:11, 1869–1878.

Matheron, G. (1967) Eléments pour une théorie des milieux poreux, Masson, Paris.

Matheron, G. (1987) Composition des perméabilité en milieu poreux hétérogène: critique de la règle de pondération géomètrique. *Rev. IFP* 23:2, 201-218.

Matheron, G. (1971) The theory of regionalized variables and its applications. *Ecole National Superieure des Mines de Paris*, Fontainebleau.

Matheron, G. (1989) Estimating and Choosing, Springer-Verlag, Berlin.

Maurer, J., Calvin, R., Qi, R. & Raghavan, V. (2003) A linear time algorithm for computing exact Euclidean distance transforms of binary images in arbitrary dimensions. *Pattern Analysis and Machine Intelligence* IEEE Transactions on 25.2, 265–270.

Merdrignac, I., Roy-Auberger, M., Guillaume, D., and Verstraete, J. (2013). Hydroprocessing and hydroconversion of residue fractions. In Toulhoat, H. and Raybaud, P., editors, *Catalysis by Transition Metal Sulfides*. Editions TECHNIP, Paris France.

Meyer, R.R., & Kirkland, A.I. (2000) Characterisation of the signal and noise transfer of CCD cameras for electron detection. *Microsc. Res. Tech.* 49:3, 269–80.

Misra, C. (1986) Industrial Alumina Chemicals. *ACS Monograph 184, ACS, Washington.*

Moreaud, M. (2006) Propiétés morphologiques multi-échelles et prévision du comportement diélectricque de nanocomposites. Doctoral thesis, Centre de Morphologie Mathématique, ENSMP.

Moreaud, M., Celse, B. & Tihay, F. (2008) Analysis of the accessibility of macroporous alumino-silicate using 3D-TEM. *Materials Science and Technology*, October 5-9, Pittsburgh, PA.

Moreaud, M., Revel, R., Jeulin, D. & Morard V. (2009) Size of boehmite nanoparticles by TEM images analysis. *Image Anal Stereol* 28, 187–193.

Moreaud, M., Jeulin, D., Morard, V. & Revel, R. (2012) TEM image analysis and modelling: application to boehmite nanoparticles. *Journal of Microscopy* 245, 186–199.

Moreland, K., Avila, L. & Fisk, L.A. (2007) Parallel unstructured volume rendering in ParaView. *Proceedings of IS&T SPIE Visualization and Data Analysis 2007*, San Jose, CA.

Morin, C. (2014) Préparation d'alumine à porosité contrôlée: étude de l'interaction de la boehmite dans des solvants et des propriétés fonctionnelles des matériaux résultants. PhD thesis, *IFP Energies Nouvelles.*

Moulinec, H. and Suquet, P. (1994). A fast numerical method for computing the linear and nonlinear mechanical properties of composites. *Comptes rendus de l'Académie des sciences. Série II, Mécanique, physique, chimie, astronomie*, 318(11):1417–1423.

Mu, D., Liu, Z.-S., Huang, C., and Djilali, N. (2007). Prediction of the effective diffusion coefficient in random porous media using the finite element method. *Journal of Porous Materials*, 14(1):49–54.

Mu, D., Liu, Z., Huang, C. & Djilali, N. (2008) Determination of the effective diffusion coefficient in porous media including Knudsen effects. *Microfluid Nanofluid* 4, 257–260.

Münch, B. & Holzer, L. (2008) Contradicting geometrical concepts in pore size analysis attained with electron microscopy and mercury intrusion. *Journal of the American Ceramic Society* 91 (12), 4059–4067.

Nelder, J. & Mead, R. (1965) A simplex method for function minimization. *Computer Journal* 7, 308–313.

Papadopoulos, G. (1993) Study of adsorption, diffusion and gas relative permeability in mesoporous alumina membranes, in relation to their porous and macroscopic structure. Ph.D. thesis (in Greek), University of Athens.

Pardo, P., Montoya, N., and Alarcón, J. (2015). Tuning the size and shape of nanoboehmites by a free-additive hydrothermal method. *CrystEngComm*, 17(10):2091–2100.

Pellegrini, Y. P., & Willot, F. (2012). Generalized two-body self-consistent theory of random linear dielectric composites: an effective-medium approach to clustering in highly-disordered media. *arXiv preprint arXiv*: 1206.0857.

Pickup, S. and Blum, F. (1989). Self-diffusion of toluene in polystyrene solutions. *Macromolecules*, 22(10):3961–3968.

Pietrasanta, A. (2013) Mathematical morphology applied to mesoporous alumina: construction of a 3D random model through the analysis of 2D TEM images. Master thesis, University of Milan.

Prakash, A. & Lebensohn R. (2009) Simulation of micromechanical behavior of polycristals: finite element versus fast Fourier transforms. *Modelling and Simulation in Materials Science and Engineering* 17:6, 064010.

Prasher, B. and Ma, Y. (1977). Liquid diffusion in microporous alumina pellets. *AIChE Journal*, 23(3):303–311.

Prieto, G., Shakeri, M., de Jong, K.P. & de Jongh, P.E. (2014) Quantitative relationship between support porosity and the stability of pore-confined metal nanoparticles studied on $CuZnO/SiO_2$ methanol synthesis catalysts. *ACS Nano* 8:3, 2522–2531.

Radon, J. & Parks, P.C. (1986) On the determination of functions from their integral values along certain manifolds. *IEEE Transactions on Medical Imaging* 5:4, 170-176.

Rana, M.S., Ancheyta, J., Maity, S.K. & Rayo, P. (2011) Hydrotreating of Maya crude oil: I. effect of support composition and its pore-diameter on asphaltene conversion. *Petroleum Science and Technology* 25:1-2, 187–199.

Reimer, L. & Kohl, H. (2008) Transmission electron microscopy: physics of image formation. Springer, 36.

Reyes, S. and Iglesia, E. (1991). Effective diffusivities in catalyst pellets: new model porous structures and transport simulation techniques. *Journal of Catalysis*, 129(2):457–472.

Rigby, S. and Gladden, L. (1999). The prediction of transport properties of porous media using fractal models and NMR experimental techniques. *Chemical Engineering Science*, 54(15-16):3503–3512. 15th International Symposium on Chemical Reaction Engineering (ISCRE 15), Newport Beach, CA, Sep 13-16, 1998.

Rozita, Y., Brydson, R., Comyn, T., Scott, A., Hammond, C., Brown, A., Chauruka, S., Hassanpour, A., Young, N., Kirkland, A. Sawada, H., and Smith, R. (2013). A study of commercial nanoparticulate γ-Al_2O_3 catalyst supports. *ChemCatChem*, 5(9):2695–2706.

Rozman, M. and Utz, M. (2001). Efficient reconstruction of multiphase morphologies from correlation functions. *Physical Review E*, 63(6):066701.

Sahimi, M. (1993). Flow phenomena in rocks: from continuum models to fractals, percolation, cellular automata, and simulated annealing. *Reviews of Modern Physics*, 65(4):1393–1534.

Santos, F., Nieto de Castro, C., Dymond, J., Dalaouti, N., Assael, M., and Nagashima, A. (2006). Standard reference data for the viscosity of toluene. *Journal of physical and chemical reference data*, 35(1):1–8.

Satterfield, C., Colton, C., and Pitcher, W. (1973). Restricted diffusion in liquids within fine pores. *AIChE Journal*, 19(3):628–635.

Seaton N.A. (1991) Determination of the connectivity of porous solids from nitrogen sorption measurements. *Chemical Engineering Science* 46 (8), 1895–1909.

Serra, J. (1968) Les fonction aléatoires de dilution. Note interne, Centre de Morphologie Mathématique, ENSMP.

Serra J. (1982) *Image analysis and mathematical morphology.* Academic Press, Inc.

Staub, D. (2014) Etude du comportement mécanique à rupture des alumines de forte porosité: application aux supports de catalyseurs d'hydrotraitement des résidus. PhD thesis, *L'institut national des sciences appliquées de Lyon*, France.

Štěpánek, F. and Ansari, M. (2005). Computer simulation of granule microstructure formation. *Chemical engineering science*, 60(14):4019–4029.

Štěpánek, F., Soos, M. & Rajniak, P. (2007) Characterization of porous media by the virtual capillary condensation method. *Colloids and Surfaces A: Physicochem. Eng. Aspects* 300, 11–20.

Sing, K. S. W., Everett, D. H., Haul, R. A. W., Moscou, L., Pierotti, R. A., Rouquerol, J., & Siemieniewska, T. (1985) Reporting physisorption data for gas/solid systems with special reference to the determination of surface area and porosity. *Pure Appl. Chem.* 57:4, 603–619.

Soille P. (1999) *Morphological Image Analysis: Principles and Applications.* Springer Science & Business Media, 11.

Takei, T., Chikazawa, M. & Kanazawa, T. (1997) Validity of the Kelvin equation in estimation of small pore size by nitrogen adsorption. *Colloid and Polymer Science* 275:12, 1156–1161.

Tanner, J. (1970). Use of the stimulated echo in NMR diffusion studies. *The Journal of Chemical Physics*, 52(5):2523–2526.

Tayakout, M., Ferreira, C., Espinat, D., Arribas Picon, S., Sorbier, L., Guillaume, D., and Guibard, I. (2010). Diffusion of asphaltene molecules through the pore structure of hydroconversion catalysts. *Chemical Engineering Science*, 65(5):1571–1583.

Thommes, M., Kohn, R. & Froba, M. (2000) Sorption and pore condensation behavior of nitrogen, argon and krypton in mesoporous MCM-48 silica materials. *J. Phys. Chem. B* **104**, 7932–7943.

Thovert, J.F., Salles, J. & Adler, P.M. (1993) Computerized characterization of the geometry of real porous media: their discretization, analysis and interpretation. *Journal of Microscopy* 170 (1), 65–79.

Tran, V.D., Moreaud, M., Thiebault, E., Denis, L. & Becker, J.M. (2014) Inverse problem approach for the alignment of electron tomographic series. *Oil and Gas SCi. and Technology* OGST, 69:2, 279–291.

Trimm, D.L. & Stanislaus, A. (1986) The control of pore size in alumina catalyst supports: a review. *Applied Catalysis* 21, 215–238.

Valiullin, R. and Kärger, J. (2011). The impact of mesopores on mass transfer in nanoporous materials: evidence of diffusion measurement by NMR. *Chemie Ingenieur Technik*, 83(1-2):166–176.

Wang, H., Pietrasanta, A., Jeulin, D., Willot, F., Faessel, M., Sorbier, L., & Moreaud, M. (2015) Modelling mesoporous alumina microstructure with 3D random models of platelets. *Journal of Microscopy* 260(3), 287–301.

Weissberg, H. (1963). Effective diffusion coefficient in porous media. *Journal of Applied Physics*, 34(9):2636–2639.

Wernert, V., Bouchet, R., and Denoyel, R. (2010). Influence of molecule size on its transport properties through a porous medium. *Analytical chemistry*, 82(7):2668–2679.

Wiegmann, A. (2007) Computation of the permeability of porous materials from their microstructure by FFF-Stokes. *Fraunhofer-Institut für Techno-und Wirtschaftsmathematik*, Fraunhofer (ITWM).

Williams, D.B. & Carter, C.B. (2009) Transmission Electron Microscopy. Springer.

Willot, F. & Jeulin, D. (2009) Elastic behavior of composites containing Boolean random sets of inhomogeneities. *International Journal of Engineering Science* 47:2, 313-324.

Willot, F. & Jeulin, D. (2011) Elastic and electrical behavior of some random multiscale highly contrasted composites. *International Journal of Multiscale Computational Engineering* 9:3, 305-326.

Willot, F., Abdallah, B. & Pellegrini Y. (2013) Fourier-based schemes with modified Green operator for computing the electrical response of heterogeneous media with accurate local fields. *International Journal for Numerical Methods in Engineering* 98:7, 518-533.

Willot, F., Gillibert, L. & Jeulin, D. (2013) Microstructure-induced hotspots in the thermal and elastic responses of granular media. *International Journal of Solids and Structures* 50:10, 1699-1709.

Willot, F. (2015) Fourier-based schemes for computing the mechanical response of composites with accurate local fields. *Comptes Rendus – Mécanique* 343:3, 232-245.

Willot, F., Abdallah, B., and Pellegrini, Y.-P. (2014). Fourier-based schemes with modified Green operator for computing the electrical response of heterogeneous media with accurate local fields. *International Journal for Numerical Methods in Engineering*, 98(7):518–533.

Wood, J. and Gladden, L. (2003). Effect of coke deposition upon pore structure and self-diffusion in deactivated industrial hydroprocessing catalysts. *Applied Catalysis A: General*, 249(2):241–253.

Wu D.H., Chen A.D. & Johnson C.S. (1995). An Improved Diffusion-Ordered Spectroscopy Experiment Incorporating Bipolar-Gradient Pulses. *Journal of Magnetic Resonance Series A*, 115(2):260-264.

Yeong, C. & Torquato, S. (1998) Reconstructing random media. *Physical Review E* 57:1, 495-506.

Youssef, S., Rosenberg, E., Gland, N., Kenter, J., Skalinski, M., and Vizika, O. (2007). High resolution CT and pore-network models to assess petrophysical properties of homogeneous and heterogeneous carbonates. In *SPE/EAGE Reservoir Characterization and Simulation Conference*.

Zecevic, J., de Jong, K.P. & de Jong, P.E. (2013) Progress in electron tomography to assess the 3D nanostructure of catalysts *Current Opinion in Solid State and Materials Science* 17:3, 115–125.

Ziegel, J. & Kiderlen, M. (2010) Estimation of surface area and surface area measure of three-dimensional sets from digitizations. *Image Vision Comput.* **28**, 64–77.

Résumé

Dans ce travail réalisé au Centre de Morphologie Mathématique and IFPEN, on s'intéresse à la microstructure et aux propriétés physiques d'alumines mésoporeuses. Il s'agit d'un support de catalyseur utilisé notamment dans les procédés industriels de raffinage du pétrole. Fortement poreux, ce matériau est formé de ''plaquettes'' distribuées de manière désordonnée à l'échelle de la dizaine de nanomètres. Les propriétés de transport de masse du support de catalyseur sont fortement influencées par la morphologie de la microstructure poreuse. Ce travail porte sur la modélisation de la microstructure et des propriétés de transport des alumines mésoporeuses, à l'aide d'outils numériques et théoriques dérivés de l'analyse d'image et de la théorie des ensembles aléatoires. D'une part, on met en place des méthodes de caractérisation et de modélisation des microstructures, qui s'appuient sur, entre autre, des images obtenues par microscopie électronique en transmission (MET) et des courbes de porosimétrie azote. D'autre part, on utilise des méthodes d'homogénéisation numérique à champs complets par transformées de Fourier rapide (FFT).

Dans un premier temps, le matériau est caractérisé expérimentalement par porosimétrie azote et résonance magnétique nucléaire à gradient de champ pulsé (RMN-GCP). Les images MET sont obtenues sur des échantillons d'épaisseur variable, filtrées et caractérisés par des fonctions de corrélation, notamment. Le bruit à haute fréquence issu de la membrane de carbone est identifié et pris en compte dans la modélisation de l'imagerie MET. À partir des images MET 2D, un modèle aléatoire à deux échelles est proposé pour représenter la microstructure 3D. Il prend en compte la forme des plaquettes d'alumine, leurs tailles, les effets d'alignement locaux et d'agrégation, qui sont identifiés numériquement. La procédure est validée à l'aide de comparaisons entre modèles et images expérimentales, en terme notamment de fonctions de corrélation et de surface spécifique mesurées par porosimétrie azote.

Dans un deuxième temps, une méthode de simulation des courbes d'isotherme de porosimétrie dans des milieux poreux périodiques ou aléatoires est développée. Basée sur des opérations morphologiques simples, elle étend un travail antérieur sur la porosimétrie au mercure. L'adsorption multicouche à basse pression est simulée à l'aide d'une dilatation tandis que les ménisques de l'interface vapeur-liquide intervenant pendant l'adsorption sont simulés à l'aide de fermetures de la phase solide par des éléments structurants sphériques. Pour simuler la désorption, une combinaison de fermetures et de bouchages de trou est utilisée. Le seuil de désorption est obtenu par une analyse de la percolation de la phase gazeuse. La méthode, d'abord validée sur des géométries simples, est comparée à des résultats antérieurs. Elle prédit une hystérésis et les distributions de pores associées à la porosimétrie. Nous l'appliquons aux modèles de microstructures 3D d'alumines mésoporeuses et proposons un modèle à trois échelles afin de rendre compte du seuil de pression pendant la désorption. En plus de la courbe de désorption, ce modèle reproduit les fonctions de corrélation mesurées sur les images MET.

Dans un troisième temps, la diffusion de Fick, la perméabilité de Darcy, et les propriétés élastiques sont prédites à l'aide de calculs de champs complets par FFT sur des réalisations des modèles d'alumines mésoporeuses à deux et trois échelles. Les coefficients de diffusion effectifs et les facteurs de tortuosité sont prédits à partir de l'estimation du flux. Sont étudiés les effets de forme, d'alignement et d'agrégation des plaquettes sur les propriétés de diffusion à grande échelle. Les prédictions numériques sont validées au moyen des résultats expérimentaux obtenus par méthode RMN-GCP.

Mots Clés

Traitement de l'image, microstructure, modèle aléatoire, simulation de porosimétrie azote, condensation capillaire, FFT, diffusion restreinte

Abstract

In a work made at Centre de Morphologie Mathématique and IFPEN, we study the microstructure and physical properties of mesoporous alumina. This is a catalyst carrier used in the petroleum refining industry. Highly porous, it contains disordered "platelets" at the nanoscale. The mass transport properties of the catalyst carrier are strongly influenced by the morphology of the porous microstructure. We focus on the modeling of the microstructure and of transport properties of mesoporous alumina, using numerical and theoretical tools derived from image analysis and random sets models. On the one hand, methods are developed to characterize and model the microstructure, by extracting and combining information from transmission electron microscope (TEM) images and nitrogen porosimetry curves, among others. On the other hand, the numerical homogenization relies on full-field Fourier transform computations (FFT).

The material is first characterized experimentally by nitrogen porosimetry and pulse-field gradient nuclear magnetic resonance (PFG-NMR). TEM images, obtained on samples of various thicknesses are filtered and measured in terms of correlation function. The high-frequency noise caused by carbon membrane support is identified and integrated in the TEM image model. Based on the 2D TEM images, a two-scale random set model of 3D microstructure is developed. It takes into account the platelet shape, platelet size, local alignments and aggregations effects which are numerically identified. The procedure is validated by comparing the model and experimental images in terms of correlation function and specific surface area estimated by nitrogen porosimetry.

Next, a procedure is proposed to simulate porosimetry isotherms in general porous media, including random microstructures. Based on simple morphological operations, it extends an earlier approach of mercury porosimetry. Multilayer adsorption at low pressure is simulated by a dilation operation whereas the menisci of the vapor-liquid interface occurring during adsorption are simulated by closing the solid phase with spherical structuring elements. To simulate desorption, a combination of closing and hole-filling operations is used. The desorption threshold is obtained from a percolation analysis of the gaseous phase. The method, validated first on simple geometries, is compared to previous results of the literature, allowing us to predict the hysteresis and pore size distribution associated to porosimetry. It is applied on 3D microstructures of mesoporous alumina. To account for the pressure threshold during desorption, we propose a refined three-scale model for mesoporous alumina, that reproduces the correlation function and the desorption branch of porosimetry isotherms.

Finally, Fick diffusion, Darcy permeability, and elastic moduli are numerically predicted using the FFT method and the two-scale and three-scale models of mesoporous alumina. The hindering effects in diffusion are estimated by the Renkin's equation. The effective diffusion coefficients and the tortuosity factors are estimated from the flux field, taking into account hindering effects. The effects of platelet shape, alignment and aggregation on the diffusion property are studied. The numerical estimation is validated from experimental PFG-NMR results.

Keywords

TEM image processing, microstructure, random model, nitrogen porosimetry simulation, capillary condensation, FFT, hindered diffusion